



<https://theses.gla.ac.uk/>

Theses Digitisation:

<https://www.gla.ac.uk/myglasgow/research/enlighten/theses/digitisation/>

This is a digitised version of the original print thesis.

Copyright and moral rights for this work are retained by the author

A copy can be downloaded for personal non-commercial research or study,
without prior permission or charge

This work cannot be reproduced or quoted extensively from without first
obtaining permission in writing from the author

The content must not be changed in any way or sold commercially in any
format or medium without the formal permission of the author

When referring to this work, full bibliographic details including the author,
title, awarding institution and date of the thesis must be given

Enlighten: Theses

<https://theses.gla.ac.uk/>
research-enlighten@glasgow.ac.uk

**A CHARACTERISATION OF THE MICROMAGNETIC PROPERTIES OF
THIN FILM MAGNETIC RECORDING MEDIA BY LORENTZ ELECTRON
MICROSCOPY**

by Frank John Martin

Submitted for the degree of Ph.D. at the University of
Glasgow.

March 1991.

© 1991 Frank J. Martin

ProQuest Number: 11007973

All rights reserved

INFORMATION TO ALL USERS

The quality of this reproduction is dependent upon the quality of the copy submitted.

In the unlikely event that the author did not send a complete manuscript and there are missing pages, these will be noted. Also, if material had to be removed, a note will indicate the deletion.



ProQuest 11007973

Published by ProQuest LLC (2018). Copyright of the Dissertation is held by the Author.

All rights reserved.

This work is protected against unauthorized copying under Title 17, United States Code
Microform Edition © ProQuest LLC.

ProQuest LLC.
789 East Eisenhower Parkway
P.O. Box 1346
Ann Arbor, MI 48106 – 1346

ACKNOWLEDGEMENTS

Many people have helped me during the course of this work and at this point I would like to thank you all sincerely. The role of the supervisor is vitally important in making the Ph.D. study interesting, efficient, and enjoyable. Professor R.P.Ferrier ensured this was the case and so deserves a particular vote of thanks. I would like to thank Professor J.N.Chapman for his help and for the provision of the facilities in the Solid State Group at the University of Glasgow. Thanks are also due to the Department of Electrical Engineering at the University for the use of their facilities in the Sub-Nanometre Group. Dr.S.McVitie deserves thanks for helping to acquire some of the DPC images discussed in this thesis.

For the maintenance of the facilities at Glasgow I would like to thank the technical staff. I would also like to thank all those who helped in the preparation of this thesis.

Finally, I would not be writing these words if it had not been for the direction and support given by my parents throughout my education. No amount of thanks can express my gratitude.

DECLARATION

This thesis is a record of the work carried out by me in the Department of Physics and Astronomy at the University of Glasgow. The work herein is my own with the exception of the magnetic recording media which were provided by the General Product Division of IBM. Some of the work given in this thesis can be found in the following papers:

'Lorentz Image-Derived Film Media Noise', R.P.Ferrier, F.J.Martin, T.C.Arnoldussen, L.L.Nunnelley, IEEE Trans Magn. Vol. 24, No.6 (1988).

'The Determination of Transition Noise By Lorentz Electron Microscopy', R.P.Ferrier, F.J.Martin, T.C.Arnoldussen, L.L.Nunnelley, IEEE Trans. Magn., MAG-25, 3387 (1989).

'An Examination of Transition Noise By Lorentz Electron Microscopy', R.P.Ferrier, F.J.Martin, T.C.Arnoldussen, L.L.Nunnelley, IEEE Trans. Magn., MAG-26, 1536 (1990).

'Side Writing/Reading In Magnetic Recording', T.C.Arnoldussen, L.L.Nunnelley, F.J.Martin, R.P.Ferrier, Proc. MMM Conference, San Diego (1990). To be published in the J. Appl. Phys..

This thesis has not previously been submitted for a higher degree.

CONTENTS

ACKNOWLEDGEMENTS

DECLARATION

SUMMARY

CHAPTER ONE	1
FERROMAGNETIC MATERIALS AND THE PRINCIPLES OF MAGNETIC RECORDING	
1.1 INTRODUCTION	1
1.2 ENERGY CONSIDERATIONS IN FERROMAGNETIC MATERIALS	1
1.2.1 FERROMAGNETISM AND THE EXCHANGE INTERACTION	
1.2.2 MAGNETOCRYSTALLINE ANISOTROPY	
1.2.3 MAGNETOSTRICTIVE ENERGY	
1.2.4 MAGNETOSTATIC ENERGY	
1.2.5 DOMAIN WALLS	
1.2.6 SUMMARY OF THE ENERGY CONTRIBUTIONS	
1.3 PRINCIPLES OF LONGITUDINAL MAGNETIC RECORDING	9
1.3.1 THE HYSTERESIS LOOP	
1.3.2 THE RECORDING SYSTEM	
1.4 SUMMARY	15
CHAPTER TWO	17
CHARACTERISATION OF FERROMAGNETIC THIN FILM MEDIA BY ELECTRON MICROSCOPY	
2.1 INTRODUCTION	17
2.2 OPTICAL MICROSCOPY - FERROFLUID DECORATION	17
2.3 IMAGING BY CONVENTIONAL TRANSMISSION ELECTRON MICROSCOPY	18

2.4	ELECTRON DISPERSIVE X-RAY ANALYSIS	21
2.5	LORENTZ ELECTRON MICROSCOPY	22
2.5.1	ELECTRON BEAM - THIN FILM INTERACTION	
2.5.2	SMALL ANGLE DIFFRACTION	
2.5.3	FOUCAULT IMAGING	
2.5.4	FRESNEL IMAGING	
2.5.5	DIFFERENTIAL PHASE CONTRAST IMAGING	
2.6	SUMMARY	30
 CHAPTER THREE		 31
SPECIMEN PREPARATION		
3.1	INTRODUCTION	31
3.2	IRON COBALT CHROMIUM (FCC)	32
3.2.1	HARD DISK FABRICATION	
3.2.2	IRON COBALT CHROMIUM WRITE EXPERIMENTS	
3.2.3	PREPARATION OF THIN FILM IRON COBALT CHROMIUM SPECIMEN FROM HARD DISK	
3.2.4	RESULTS OF THIN FILM PREPARATION	
3.2.5	SUMMARY OF THE IRON COBALT CHROMIUM PREPARATION	
3.3	COBALT NICKEL CHROMIUM (CONICR)	45
3.3.1	HARD DISK FABRICATION	
3.3.2	COBALT NICKEL CHROMIUM WRITE EXPERIMENTS	
3.3.3	PREPARATION OF THIN FILM COBALT NICKEL CHROMIUM SPECIMEN FROM HARD DISK	
3.3.4	RESULTS OF THIN FILM PREPARATION	
3.3.5	SUMMARY OF THE COBALT NICKEL CHROMIUM PREPARATION	

CHAPTER FOUR	51
THE PHYSICAL AND MICROMAGNETIC CHARACTERISATION OF IRON COBALT CHROMIUM THIN FILM RECORDING MEDIUM BY ELECTRON MICROSCOPY	
4.1 INTRODUCTION	51
4.2 EXAMINATION OF THE PHYSICAL MICROSTRUCTURE	52
4.2.1 BRAGG DIFFRACTION STUDIES OF THE CRYSTALLINE STRUCTURE	
4.2.2 OBSERVATION OF THE SPECIMEN GRAIN STRUCTURE	
4.3 MICROMAGNETIC CHARACTERISATION	59
4.3.1 TRACKS WRITTEN ALONG THE EASY AXIS	
4.3.2 INVESTIGATION OF MAGNETIC INDUCTION IN THE LOCALITY OF TRACKS WRITTEN OFF THE EASY AXIS	
4.3.2.1 FERROFLUID AND FRESNEL IMAGING	
4.3.2.2 SMALL ANGLE DIFFRACTION AND DIFFERENTIAL PHASE CONTRAST IMAGING	
4.4 SUMMARY	75
CHAPTER FIVE	78
THE PRELIMINARY CHARACTERISATION OF COBALT NICKEL CHROMIUM THIN FILM RECORDING MEDIUM BY ELECTRON MICROSCOPY	
5.1 INTRODUCTION	78
5.2 OBSERVATION OF THE GRAIN STRUCTURE	78
5.3 INVESTIGATION OF THE RECORDED MICROMAGNETIC DOMAIN STRUCTURES	80
5.3.1 FRESNEL AND DIFFERENTIAL PHASE CONTRAST IMAGING	
5.3.2 SMALL ANGLE DIFFRACTION STUDIES	

5.4	SUMMARY	86
CHAPTER SIX		88
QUANTITATIVE ESTIMATION OF A.C. ERASED MEDIUM FLUX NOISE POWER BY LORENTZ ELECTRON MICROSCOPY		
6.1	INTRODUCTION	88
6.2	THE RELATIONSHIP BETWEEN THE MEDIUM MICROMAGNETISATION AND THE MEDIUM FLUX NOISE POWER	89
6.3	ELECTRONIC MEASUREMENT OF THE ELECTRONIC NOISE POWER	94
6.4	PREPARATION OF MEDIUM MAGNETISATION MAPS AND THE CALCULATION OF LORENTZ DERIVED NOISE SPECTRA BY FAST FOURIER TRANSFORM COMPUTATION	95
6.5	ESTIMATION OF THE A.C. ERASED MEDIUM FLUX NOISE POWER	102
6.6	SUMMARY	108
CHAPTER SEVEN		110
INVESTIGATION OF TRANSITION NOISE FROM SQUARE WAVE WRITTEN TRACKS BY LORENTZ ELECTRON MICROSCOPY		
7.1	INTRODUCTION	110
7.2	ELECTRONIC MEASUREMENT OF TRANSITION NOISE POWER	111
7.3	BINARY REPRESENTATION OF THE MEDIUM MAGNETISATION FROM LORENTZ IMAGES	112
7.4	THE PERIODOGRAM TECHNIQUE OF ESTIMATING TRANSITION NOISE POWER	114
7.4.1	FFT COMPUTATION INVOLVING PERIODIC SIGNALS	
7.4.2	FFT COMPUTATION OF THE MEDIUM FLUX NOISE	

	POWER FROM TRACK PERIODOGRAMS	
7.4.3	RESULTS OF THE PERIODOGRAM APPROACH	
7.4.4	SUMMARY	
7.5	ANALYSIS OF INDIVIDUAL TRANSITIONS	128
7.5.1	A TRACK MODEL IN TERMS OF INDIVIDUAL TRANSITIONS	
7.5.2	FFT EFFECTS WITH ISOLATED TRANSITION NOISE FUNCTIONS	
7.5.3	THE FORM OF THE TRACK MAGNETISATION AND THE ASSUMPTIONS OF THE READ MODEL	
7.5.4	RESULTS OF THE INDIVIDUAL TRANSITION ANALYSIS	
7.5.5	SUMMARY	
CHAPTER EIGHT		141
CONCLUSIONS AND FUTURE WORK		
REFERENCES		148

SUMMARY

This thesis describes the electron microscope based analysis of two thin film magnetic recording media: iron cobalt chromium and cobalt nickel chromium. In particular, Lorentz electron microscopy was employed to characterise the micromagnetic domain structures of square wave written tracks recorded on to these two media. From the images obtained from this examination of the medium a computational technique was developed to calculate the transition noise power spectra for written tracks from Lorentz images of their domain structure. These Lorentz derived spectra can then be directly compared to the spectra measured electronically from the readback signal measured from the hard disk.

As an introduction chapter one presents the basic energy considerations associated with ferromagnetic materials. The second half of the chapter briefly reviews the relevant aspects of longitudinal magnetic recording.

Electron microscopy provides the means through which the media can be both physically and micromagnetically characterised. The appropriate techniques are therefore described in chapter two, with particular emphasis on qualitatively describing the imaging methods of Lorentz electron microscopy.

To obtain thin films of a recording medium on which tracks have been written three stages of preparation are required. Chapter three describes these processes

in detail.

The bulk of the electron microscope analysis is contained in chapters four and five. Chapter four begins by reporting the characteristics of the physical structure of the iron cobalt chromium thin film and proceeds to describe the micromagnetic characterisation of tracks written on to the medium both along and off the easy axis.

A breakthrough in the preparation of the isotropic cobalt nickel chromium thin film medium from hard disk came in the latter stages of this Ph.D. study. The success of the technique on what is a new medium for analysis was thought worthy of inclusion; hence chapter five reviews the first images of the physical and micromagnetic structures of this medium.

There has been little or no work done to try and quantitatively relate the micromagnetic domain structures observed in Lorentz images of a recording medium with the corresponding noise performance of the medium. Chapter six describes estimation of the noise spectrum from a.c. erased iron cobalt chromium from Lorentz images and how this spectrum compares favourably with that measured electronically for the a.c. erased medium. The successful estimation of the a.c. erased noise enabled the same method of noise estimation to be employed to characterise the transition noise spectra from square wave written tracks. Chapter seven discusses the limited success of analysing sections of track (≤ 10 periods in length) and describes the evolution of a second method based on

analysing individual magnetisation reversals.

Chapter eight contains the conclusions drawn from the results of chapters four through seven along with an indication of possible future work.

CHAPTER ONE

FERROMAGNETIC MATERIALS AND THE PRINCIPLES OF LONGITUDINAL MAGNETIC RECORDING

1.1 INTRODUCTION

A full description of the phenomenon known as ferromagnetism is neither the aim nor within the scope of this chapter. Instead a summary reviewing the origins, energetics, and the application of ferromagnetic thin films to magnetic recording media is presented as a foundation to the subsequent chapters.

1.2 ENERGY CONSIDERATIONS IN FERROMAGNETIC MATERIALS

1.2.1 FERROMAGNETISM AND THE EXCHANGE INTERACTION

The characteristic feature which defines ferromagnetic materials is that below a critical temperature T_c - the Curie Temperature - there is spontaneous alignment of the atomic spins within the sample in the absence of an applied external magnetic field. Coupling of the microscopic magnetic moments in this way implies forces strong enough to overcome any thermal agitation intent on disrupting the assembly of spins. The temperature dependence of the magnetisation of a ferromagnetic material is shown in figure 1.1.

The spontaneous magnetisation decreases with increasing temperature from a maximum at absolute zero, vanishing

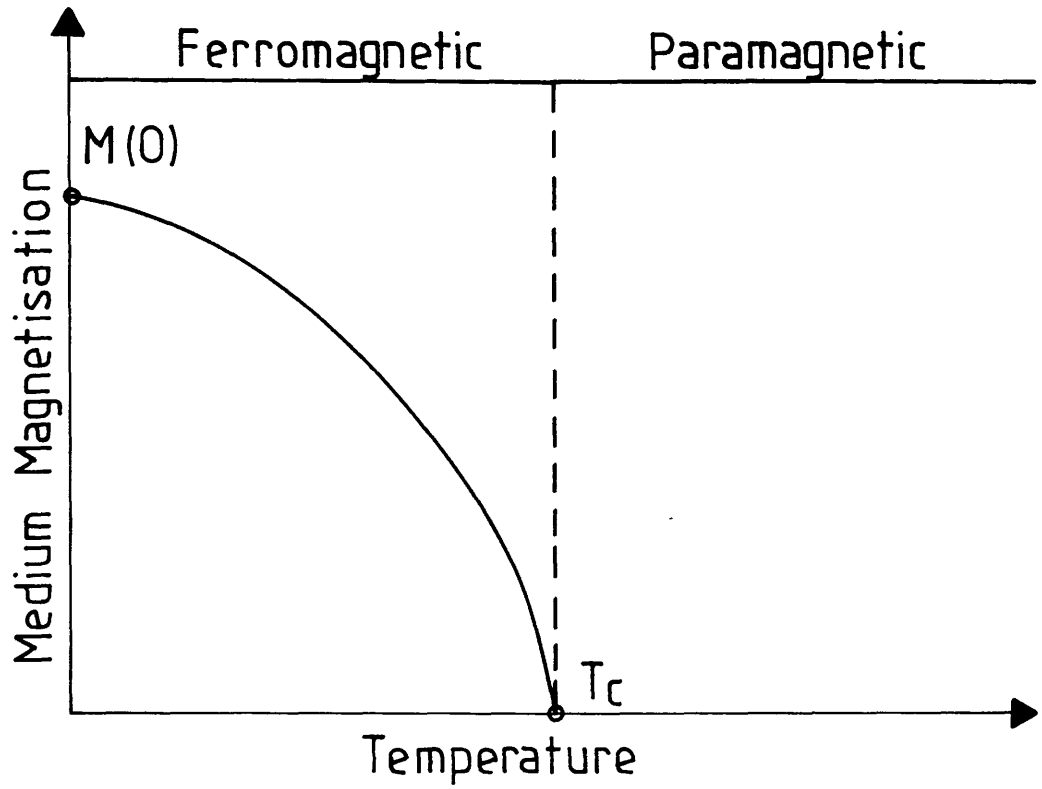


Figure 1.1 - Graph of medium magnetisation against temperature for a ferromagnetic material.

at the Curie Temperature T_c , above which the medium behaves paramagnetically. Typical values of the Curie Temperature for known ferromagnetic elements are $\approx 630\text{K}$ for nickel, $\approx 1040\text{K}$ for iron and $\approx 1400\text{K}$ for cobalt.

If the origin of the force responsible for this alignment is magnetic then the magnitude of the field can be estimated from the fact that the thermal agitation energy is approximately equal to the Zeeman energy of a magnetic moment in the field at the Curie Temperature, thus for $T_c = 300\text{K}$

$$H \approx \frac{k_B \cdot T_c}{\mu_B} \approx 4.5 \times 10^6 \text{ Oe} \quad (1.1)$$

with μ_B the Bohr Magneton (the magnetic moment of the electron spin), and Boltzmann constant k_B .

The dipolar Lorentz field was initially considered as a possible source of the alignment, this field however is typically the order of 10^3 Oe and therefore far too small to account for the required field strength.

Although aware of this disparity, Weiss [1] developed a successful theoretical treatment of ferromagnetism by assuming the existence of a hypothetical field proportional to the magnetisation; it was however Heisenberg [2] who produced a physical explanation of the 'Weiss Molecular Field' - relating ferromagnetism to the quantum mechanical exchange interaction.

The 'exchange energy' E_{ex} between two atoms i and j with vector spins S_i and S_j respectively is given by

$$E_{\text{ex}} = -2J(S_i \cdot S_j) \quad (1.2)$$

where J is known as the exchange integral and ultimately determines whether or not the ferromagnetic

state is energetically favourable within a material.

The value of the exchange integral relates the difference in Coulomb energy between spins aligned parallel or anti-parallel. It is a consequence of the Pauli Exclusion Principle in quantum mechanics that atomic electron charge distributions cannot be altered without introducing a corresponding change to the relative direction of the spins. Hence, the system will reduce its overall energy to a more stable equilibrium through the exchange interaction by altering the spatial charge distribution in the overlap region of the two atoms to produce an atomic spin configuration compatible with an exchange energy reduction.

Generally J is negative, favouring anti-parallel alignment which produces non-ferromagnetic or anti-ferromagnetic behaviour. For certain metals such as iron, cobalt and nickel the radius of the 3d electron orbit and the interatomic lattice spacing yields a positive exchange integral J , producing ferromagnetism.

The exchange interaction greatly influences the nature of the medium magnetisation but other micromagnetic energy contributions are also present within a magnetic material, all of which contribute to the overall equilibrium magnetisation configuration.

1.2.2 MAGNETOCRYSTALLINE ANISOTROPY

Experimentally it is observed that the energy required to magnetise ferromagnetic single crystals depends upon the direction of the applied magnetic field relative to the crystallographic axes, the magnetisation of the crystal preferring to lie along certain directions (easy axes). This anisotropic behaviour is termed magnetocrystalline anisotropy and has an associated anisotropic energy function E_k [10].

The crystalline lattice influences the electronic charge distributions of atomic constituents through the geometry of the lattice structure. Consider an isolated atom from a ferromagnetic material, the 3d atomic electrons responsible for the magnetic behaviour of the medium have a set of possible orbital states of equal energy, the degeneracy inherent in the orbital angular momentum quantum number. In a crystal lattice such atoms can no longer be considered isolated but are constrained under the electrostatic crystal field - the form of which is dependent on the geometry of the crystal, breaking the degeneracy in the orbital angular momentum states and imposing orientations in which the 3d electrons will preferentially orbit. The preferential occupation of these orbital states in turn produces a change in the atomic spin or magnetic moment. Hence the crystal structure, via the agency of the orbital angular momentum, is seen to influence directly the directions in which the magnetisation within the medium prefers to lie.

For a crystal with cubic symmetry, such as iron and nickel, the anisotropic energy density can be written as

$$E_K = K_1 (\alpha_1^2 \alpha_2^2 + \alpha_2^2 \alpha_3^2 + \alpha_3^2 \alpha_1^2) + K_2 \alpha_1^2 \alpha_2^2 \alpha_3^2 \quad (1.3)$$

where the α_i are the direction cosines of the magnetisation with respect to the cube edges; the anisotropy constants K_1 and K_2 are material dependent, for example at room temperature

$$K_1(\text{Fe}) = 4.2 \cdot 10^5 \text{ erg/cm}^3$$

$$K_1(\text{Ni}) = -0.56 \cdot 10^5 \text{ erg/cm}^3$$

Uniaxial anisotropy is the term used to describe a material that has one definite easy or preferred magnetisation axis. The induced easy axis can lie in or out of the plane of the medium and these materials are of practical importance in the design of magnetic recording media. For example, thin film cobalt has a hexagonal close packed crystal structure in which uniaxial anisotropy gives an easy axis parallel to the hexagonal c-axis. The associated anisotropic energy term is given by

$$E_K = K_1 \cdot \sin^2 \theta + K_2 \cdot \sin^4 \theta + K_3 \cdot \sin^6 \theta + \dots \quad (1.4)$$

where θ is the angle the magnetisation makes with the c-axis, and K_1 , K_2 , K_3 , etc are the cobalt anisotropy constants. For cobalt the first two terms are sufficient to describe the anisotropic energy function:

$$E_K = K_1 \cdot \sin^2 \theta + K_2 \cdot \sin^4 \theta \quad (1.5)$$

At room temperature

$$K_1 = 4.1 \times 10^6 \text{ erg/cm}^3$$

$$K_2 = 1.0 \times 10^6 \text{ erg/cm}^3$$

1.2.3 MAGNETOSTRICTIVE ENERGY

A deformation of the crystal lattice by the application of stress induces a further anisotropic energy contribution to ferromagnetic materials, namely magnetostrictive energy E_{ms} .

This magnetostrictive energy arises from the change in the spatial distribution of electrons and is magnetostatic in origin. As the geometric spacing between atomic or ionic constituents distorts in a particular direction the re-distribution of electronic charge within the crystal produces a change in the medium magnetisation. Conversely, a change in medium magnetisation has in the simplest case an associated sample length change, $\lambda = \delta l / l$, known as the magnetostriction coefficient.

1.2.4 MAGNETOSTATIC ENERGY

The two energy contributions discussed above suggest that the equilibrium configuration of the magnetisation within a ferromagnetic material would correspond to a situation with the magnetic moments aligned parallel (exchange) to an easy axis (anisotropy) throughout the sample. The experimental observations, however, show that at room temperature most specimens of iron ($T_c \approx 1040K$), which have not lately been placed in a magnetic field, have no observable spontaneous

magnetisation.

Weiss first proposed an explanation for this, suggesting that although on a microscopic scale all magnetic moments are parallel, the specimen is macroscopically sub-divided into regions or domains in which the magnetisation is constant, but pointing in different directions throughout the sample. The resultant net magnetisation from the entire sample is very small. Figure 1.2 illustrates this schematically. This concept of domain structure originates from a classical magnetostatic interaction. With a magnetisation of \mathbf{M} the sample will produce a magnetic field \mathbf{H} , resulting in a magnetostatic potential energy

$$E_{\mathbf{H}},$$

$$E_{\mathbf{H}} = \frac{1}{2} \int \mathbf{M} \cdot \mathbf{H} \, dV \quad (1.6)$$

Figure 1.3a illustrates the situation of a uniformly magnetised sample. At points distant from the sample the field \mathbf{H} approximates to a dipole field,

$$\mathbf{H} = \frac{\mu}{r^3} \quad ; \quad \mu = \mathbf{M} \cdot V_{\text{SAMPLE}} \quad (1.7)$$

Hence at large distances the field

$$\mathbf{H} = \frac{+V_{\text{SAMPLE}} \cdot |\mathbf{M}|}{r^3} \quad (1.8)$$

determines the amount of magnetostatic energy stored.

Consider figure 1.3b, the magnetic field distant from the sample is no longer given by the dipole field of equation (1.8) but rather the field from a quadrupole arrangement:

$$H_{\mathbf{Q}} \propto \frac{1}{r^4} \quad (1.9)$$

This field falls off more rapidly than that from the

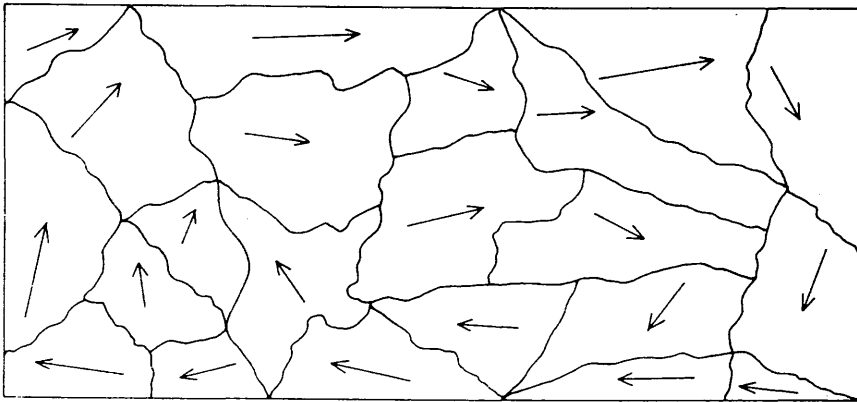


Figure 1.2 - An example of the type of domain structure possible in an unmagnetised ferromagnetic specimen - the effect is a small resultant net magnetisation.

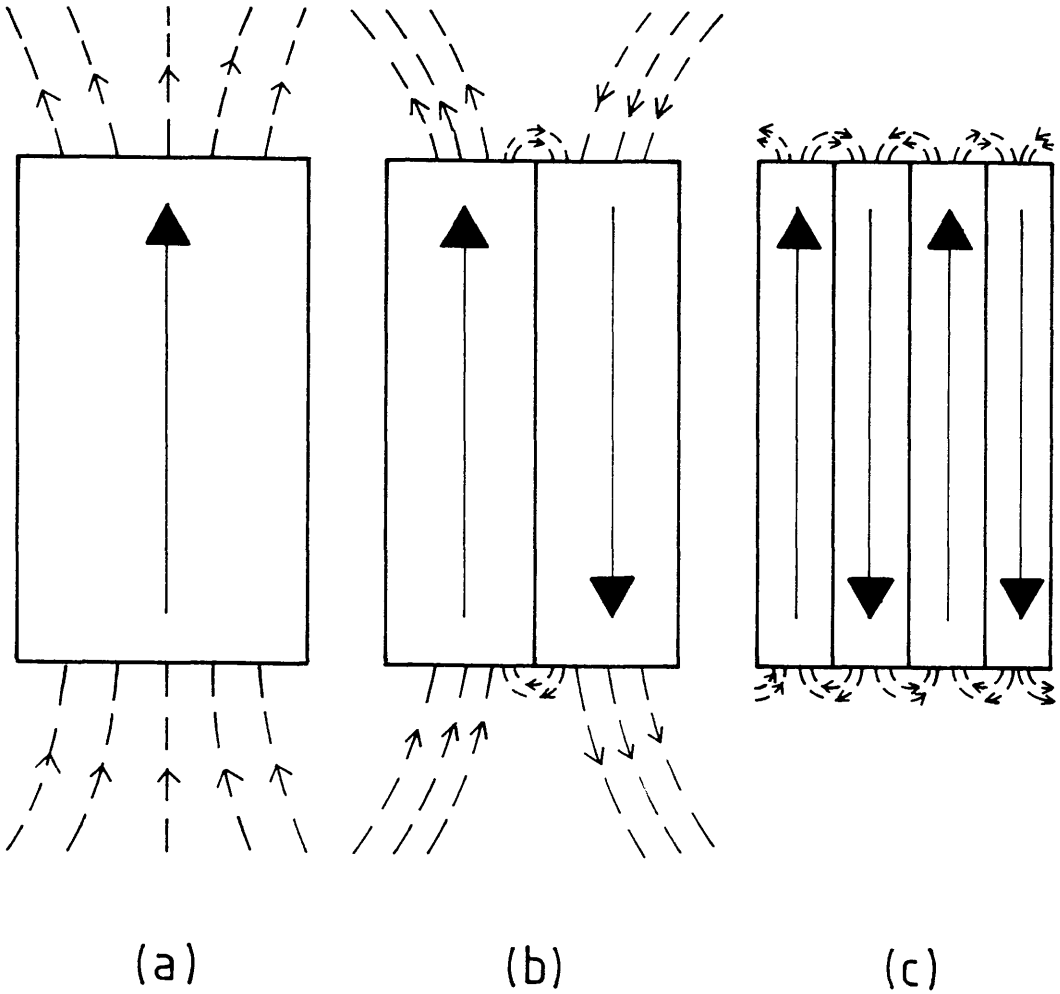


Figure 1.3 - The schematic diagram of the stray fields produced by the different domain structures illustrated.

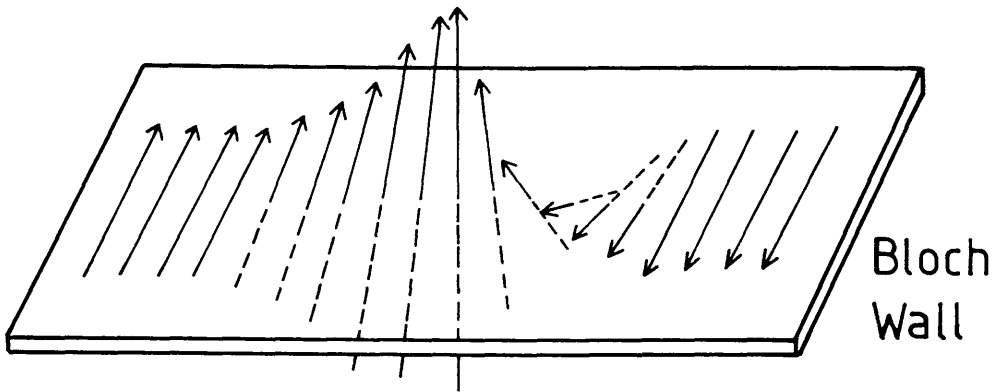
uniformly magnetised sample of figure 1.3a, hence confining the magnetic field to regions close to the free pole surface, and reducing the magnetostatic energy. Figure 1.3c describes a system with a further reduction in magnetostatic energy; additional splitting will reduce the overall system energy, but by diminishing amounts. A stable domain configuration is obtained when the reduction in magnetostatic energy is offset by an increase in other micromagnetic energy contributions. This 'trade-off' in energy terms is important in defining domain characteristics and normally contains a significant contribution from both the exchange interaction and magnetocrystalline anisotropy.

1.2.5 DOMAIN WALLS

The transition region between domains of different magnetisation is referred to as the domain wall. The thickness of the domain wall is determined by a balance between the exchange and anisotropy energies. Exchange would favour a gradual variation of vector magnetisation across the wall while the magnetocrystalline anisotropy energy favours an abrupt transition to reduce the number of magnetic moments magnetised away from the easy axis. The compromise between these two energy contributions results in walls typically 100-1000 atomic spacings wide.

Figure 1.4 illustrates the two most widely recognised

(a)



(b)

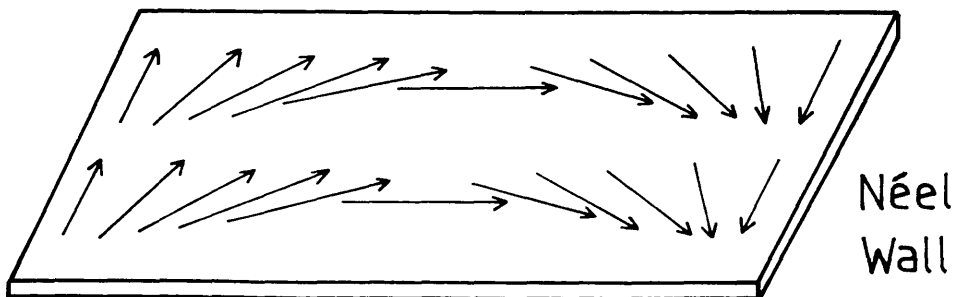


Figure 1.4 - (a) The variation in direction of the medium magnetisation across a Bloch Wall transition; (b) the variation in direction of the medium magnetisation across a Néel Wall transition.

transition wall models, the Bloch [3] and Néel [4] walls. As illustrated, the magnetisation across a Bloch wall rotates out of the medium plane. The Néel wall is characterised by an in-plane rotation of the magnetisation confining the magnetisation reversal to lie within the medium plane.

1.2.6 SUMMARY OF THE ENERGY CONTRIBUTIONS IN A FERROMAGNETIC MEDIUM

The energy terms discussed above combine to give the total micromagnetic energy of the ferromagnetic system

$$E_T = E_{EX} + E_K + E_M + E_{MS} \quad (1.10)$$

The particular characteristics of the micromagnetisation of a medium are determined by the form of the balance between these energy contributions.

1.3 PRINCIPLES OF LONGITUDINAL MAGNETIC RECORDING

1.3.1 THE HYSTERESIS LOOP

When a ferromagnetic material is subjected to an external magnetic field the medium magnetisation tends to align itself with the applied field. Upon removing this field the medium exhibits some non-zero magnetisation, and is said to be permanently magnetised. It is this ability to retain a

magnetisation representative of the nature of the applied external field that allows ferromagnetic media to be employed in data storage technology applications. Figure 1.5 describes a set of possible domain configurations that a single crystal of ferromagnetic material can develop as an externally applied magnetic field is increased in magnitude (the actual form of these domain structures were chosen to illustrate the process of magnetising the material and not to represent the domain structures found practically in ferromagnetic materials). Consider figure 1.5a. This illustrates a possible domain configuration of an unmagnetised single crystal of ferromagnetic material, the orientations of the domain magnetisations are such that the net magnetisation of the sample is zero. A small magnetic field H is applied (figure 1.5b), enhancing certain magnetisation directions by extending the appropriately magnetised domains, causing the domain walls to move. The combined domain magnetic vectors now produce a non-zero magnetisation in the direction of the applied field H .

Initially only a few domains change, but as H is increased some of the domain walls disappear, and the aligned domains increase in size. The net field from these aligned domains helps align still more domains. Thus, initially, a small increase in the applied field causes a rapid increase in the net sample magnetisation (figure 1.5c). Eventually, further increase in H produces little change in the magnetisation, since the majority of the medium is already aligned, figure 1.5d.

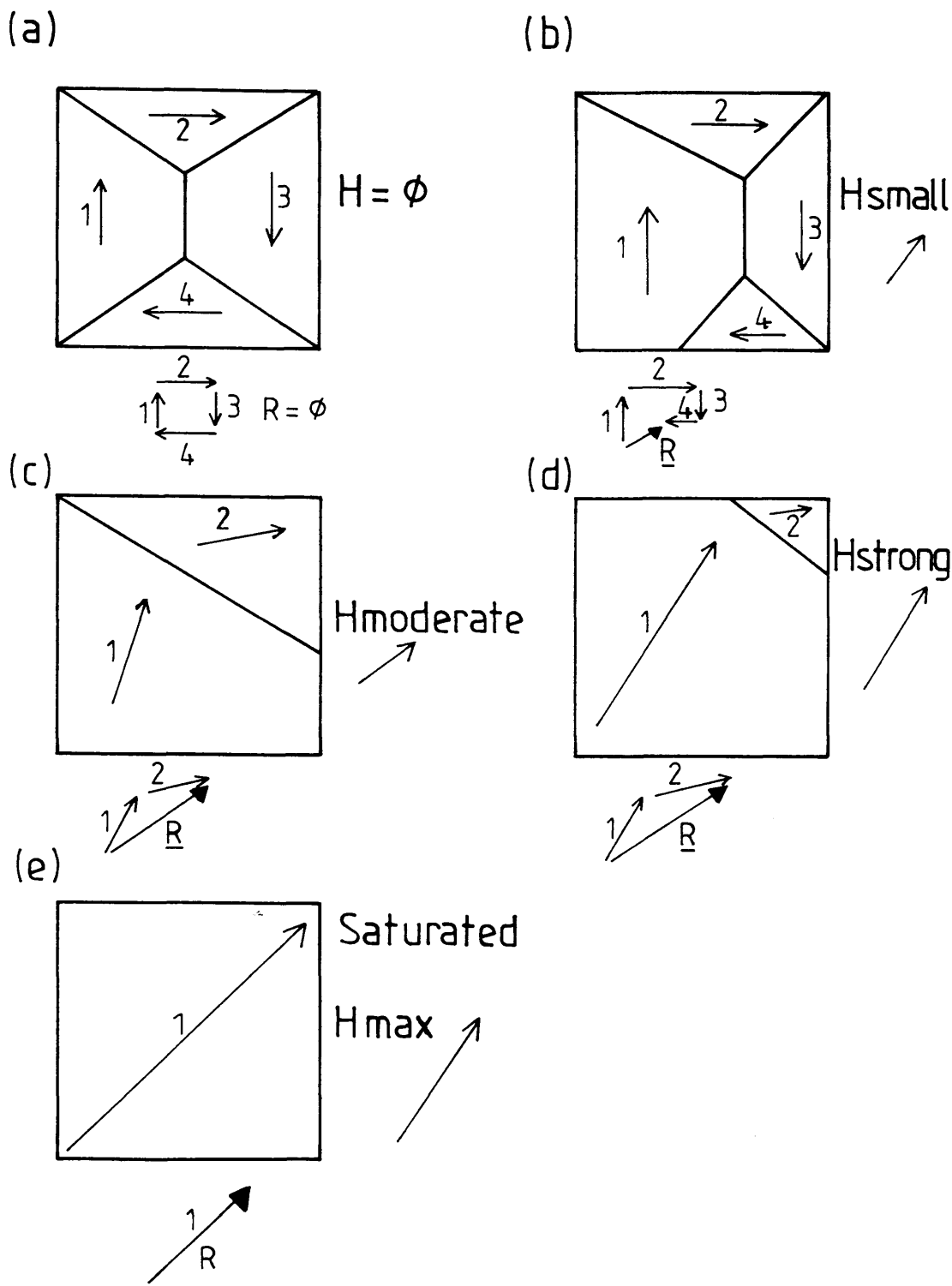


Figure 1.5 - The variation of the net medium magnetisation as the applied magnetic field H is increased: (a) no applied field; (b) small applied field; (c) moderate applied field; (d) strong applied field; (e) maximum, saturating applied field.

Finally, all the domains are combined to form one single domain in which the magnetisation lies parallel to the applied field (figure 1.5e), and the medium has reached magnetic saturation, M_s .

Upon removing the applied field the sample does not return to the unmagnetised state, but relaxes to some intermediate configuration, such as figure 1.5d. The sample is now said to be permanently magnetised, and the net magnetisation called the 'remanence magnetisation', M_R .

Since increasing H produces an increase in the medium magnetisation M which depends upon the previous magnetisation of the sample, the relationship between M - H is non-linear and dependent upon the magnetic history of the sample.

The direction of the applied H field can be reversed: varying the external field first from zero to positive H_{MAX} , then through zero to negative H_{MAX} , and finally negative H_{MAX} through zero back to positive H_{MAX} produces figure 1.6. This cyclic variation of the H field traces out a medium magnetisation plot which is known as the major hysteresis loop or simply the hysteresis loop.

There are three important parameters to note from the hysteresis loop: the saturation magnetisation M_s ; the remanent magnetisation M_R ; and the coercivity H_c , the coercivity being the field required to reduce the permanent magnetisation to zero. These three quantities describe the suitability of a particular material for potential applications.

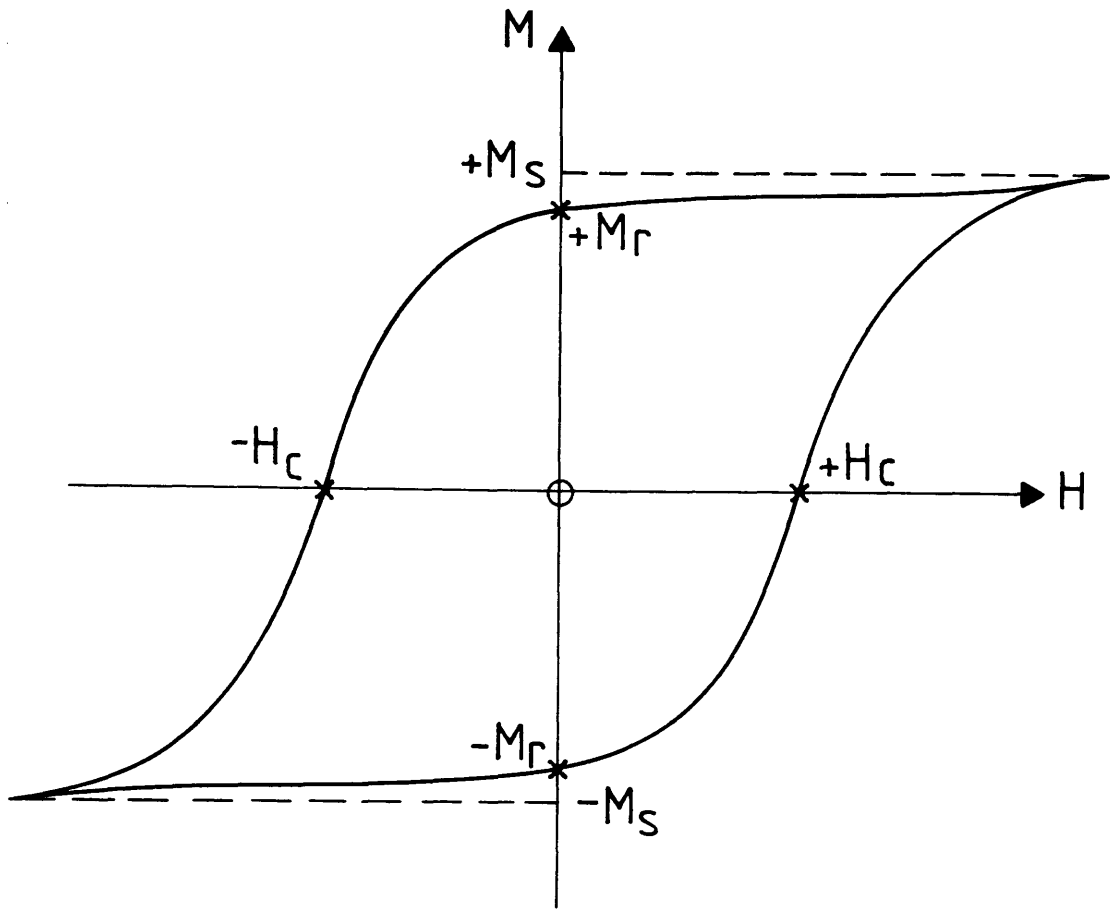


Figure 1.6 - The Hysteresis loop.

A material with a narrow major hysteresis loop is called a soft magnetic material - low coercivity characterising a medium in which the magnetisation can be reversed by small external fields. A hard magnetic material has a wide loop - showing both a high remanent magnetisation and coercivity. Media used for data storage in magnetic recording have a high remanence M_R with a coercivity large enough to retain magnetisation indefinitely yet low enough to allow magnetisation reversal when recorded upon using the lowest possible write field.

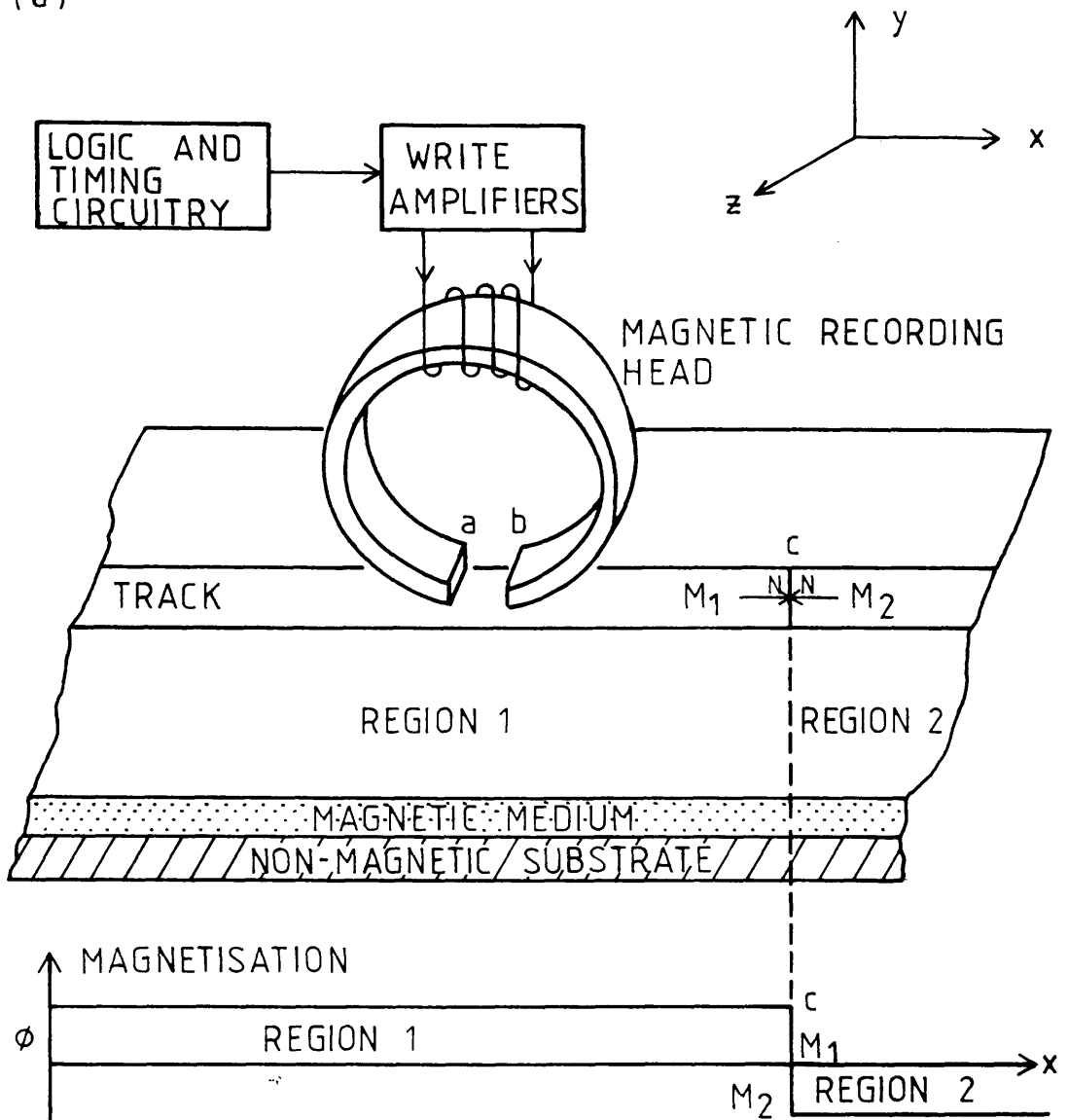
1.3.2 THE RECORDING SYSTEM

This section describes a basic longitudinal magnetic recording system - discussing both the writing and reading of data.

(A) INFORMATION STORAGE - WRITING

A schematic diagram describing the write process is shown in figure 1.7. This consists of logic and timing circuitry, write amplifiers, a magnetic recording head, and a recording medium. The medium moves with velocity v with respect to the head, and is generally supported by some non-magnetic substrate. Associated with the head is a write gap g across which a fringe magnetic field develops when the head is driven by the write current. The direction of this fringe field is

(a)



(b)

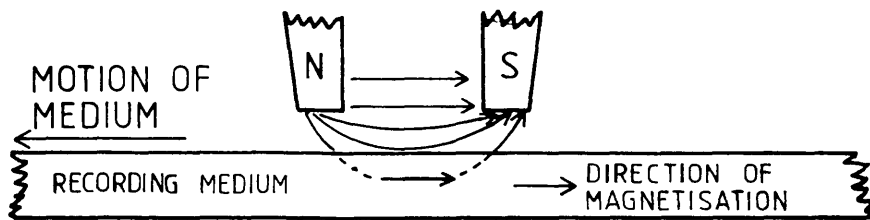


Figure 1.7 - (a) A schematic diagram of the write system; (b) the write field produced in the medium by the write head.

determined by the direction of the head current, but in any case the coupling of the write field with the medium depends upon the height at which the head flies above the medium.

If the resultant head-medium coupling produces a saturating field in the medium, then the magnetisation will be aligned parallel to this fringe field. As the medium leaves the head field the magnetisation relaxes to the remanent value. Controlling the temporal variation of the write signal records a spatial variation of the magnetisation within the medium representative of the write signal.

For longitudinal recording the system requires a two-pole write head, such as that shown in figure 1.7b, and a material in which the magnetisation lies in plane. Materials which are commonly used have uniaxial longitudinal anisotropy where the write process yields recorded magnetisation parallel or anti-parallel to the easy axis.

(B) INFORMATION RETRIEVAL - READING

If the recorded transitions are assumed to lie perpendicular to the direction of track motion then the fringe magnetic field produced by the discontinuity in the magnetic dipole density at the magnetisation reversal would be similar to the situation illustrated in figure 1.8. This stray field can be detected by the recording head as the medium travels past the pole pieces, figure 1.9. The voltage induced in the

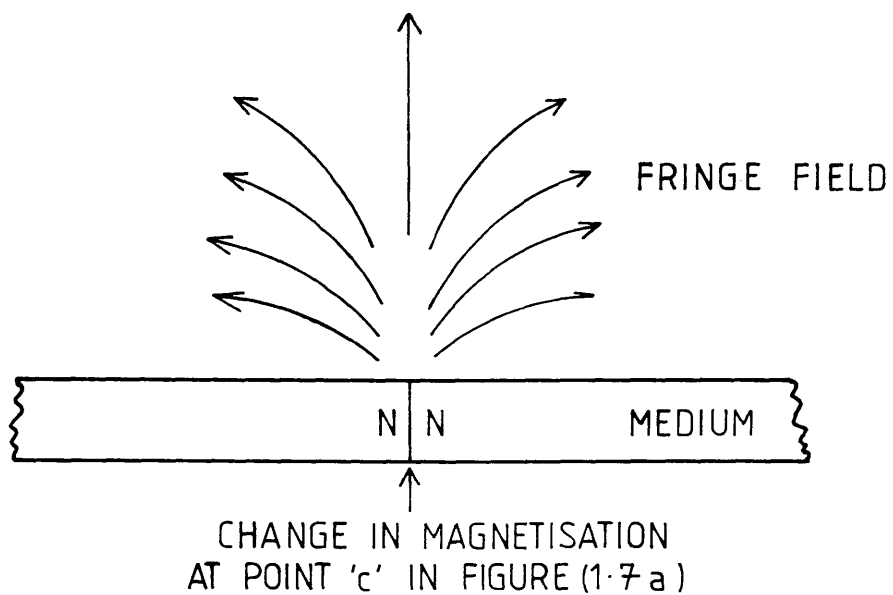


Figure 1.8 - The fringe or stray magnetic field produced at a discontinuity in the medium magnetisation.

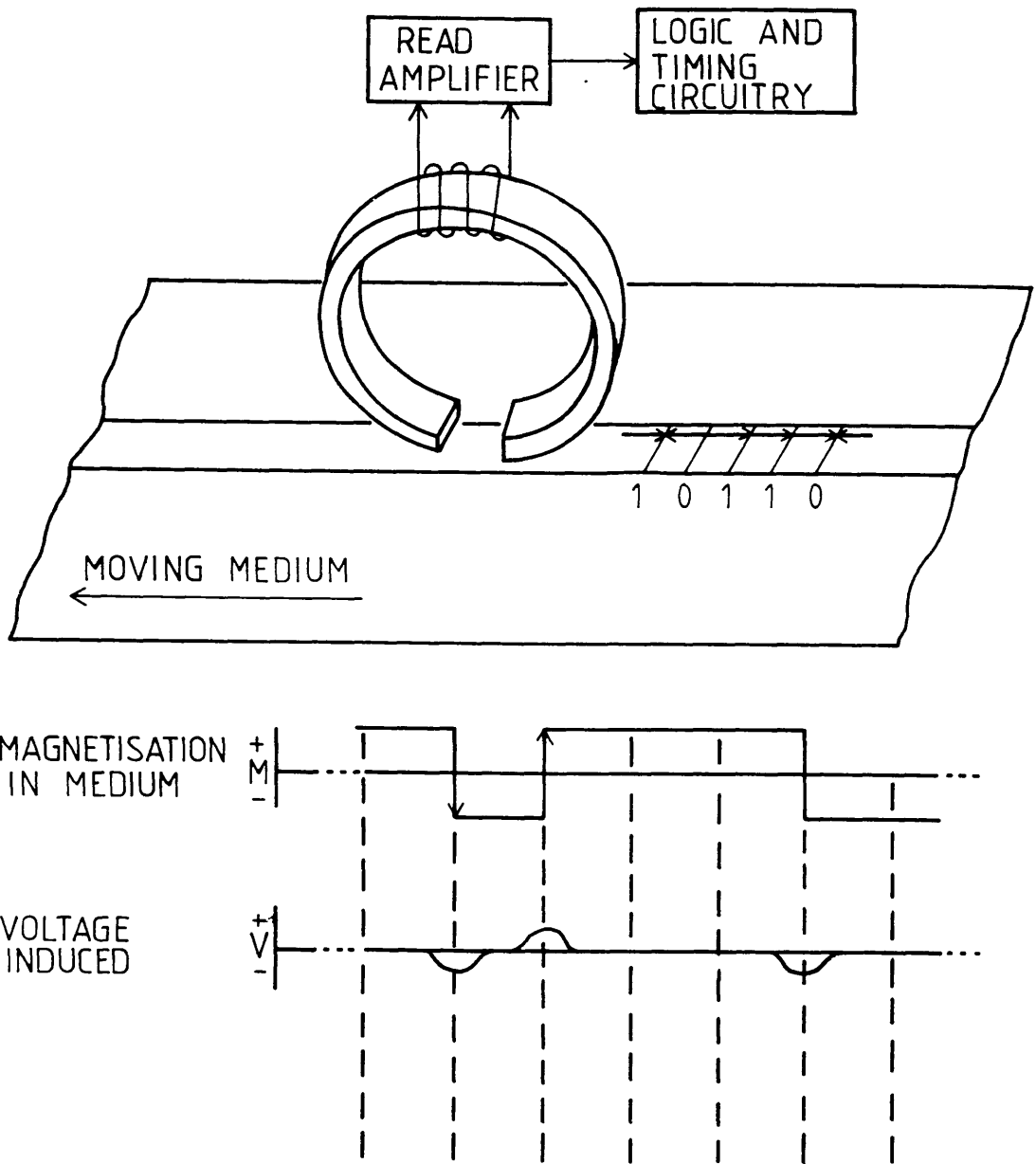


Figure 1.9 - The readback system in which changes in the medium magnetisation induce voltage signals in the head as they pass under the head pole pieces.

windings of the head is given by Faradays Law of Magnetic Induction as

$$e(t) = -n \cdot \epsilon \cdot \frac{\partial \Phi}{\partial t} \quad (1.11)$$

where Φ is the magnetic flux coupled into the head, t is time, n is the number of head turns or windings, and ϵ the head efficiency.

The Reciprocity model of reading [5] yields an expression describing the spatial variation of the readback signal. It is based upon the reciprocity relationship of electromagnetism. The theorem of reciprocity states that the coefficients describing the 'mutual inductance' between two coils are equal:

$$K_{12} = K_{21} \quad (1.12)$$

where K_{IJ} describes the coupling of flux from coil I into coil J. The theorem can be derived from a consideration of the potential energy of a current loop in a magnetic field [6]. Here, however, we will assume it is correct and not derive it.

The temporal dependence of the readback signal, equation (1.11), can be transformed to a spatial relationship by noting

$$\frac{\partial \Phi}{\partial t} = \frac{\partial x}{\partial t} \cdot \frac{\partial \Phi}{\partial x} = v \cdot \frac{\partial \Phi}{\partial x} \quad (1.13)$$

where v is the relative head-medium velocity.

Hence, equation (1.11) becomes

$$e(x) = -n \cdot \epsilon \cdot v \cdot \frac{\partial \Phi}{\partial x} \quad (1.14)$$

The Reciprocity Model [5] derives the magnetic flux Φ as

$$\Phi(x_0) = \mu_0 \cdot \int_{-w/2}^{+w/2} dz \int_d^{d+b} dy \int_{-\infty}^{+\infty} dx \cdot h_x(x, y, z) \cdot m_x(x - x_0, y, z) \quad (1.15)$$

where $m(x,y,z)$ is the magnetisation within the medium and $m_x(x,y,z)$ is the component in the x direction, x_0 is the along track co-ordinate of a magnetisation reversal, $h(x,y,z)$ is the head sensitivity function with x component $h_x(x,y,z)$, μ_0 is the permeability of free-space, W is the track width, b is the magnetic film thickness, and d is the head-medium spacing. See figure 1.10.

Combining equation (1.14) with equation (1.15), the Reciprocity Model states the signal measured by the head as

$$e(x_0) = -\mu_0 \cdot n \cdot \epsilon \cdot v \cdot \frac{\partial}{\partial x} \int_{0-w/2}^{+w/2} dz \int_d^{d+b} dy \int_{-\infty}^{+\infty} dx \cdot h_x(x,y,z) \cdot m_x(x-x_0,y,z) \quad (1.16)$$

This expression for the spatial variation of the readback signal provides a basis for the media noise analysis presented in chapters six and seven of this thesis.

1.4 SUMMARY

In this chapter we have discussed the electronic quantum mechanical origins of ferromagnetism and described the energy terms important in producing the domain structures found in ferromagnetic materials.

The hysteresis loop was described, emphasising how the curve illustrates the behaviour of the magnetisation as the applied field varies with a view to the application of ferromagnetic media in magnetic recording.

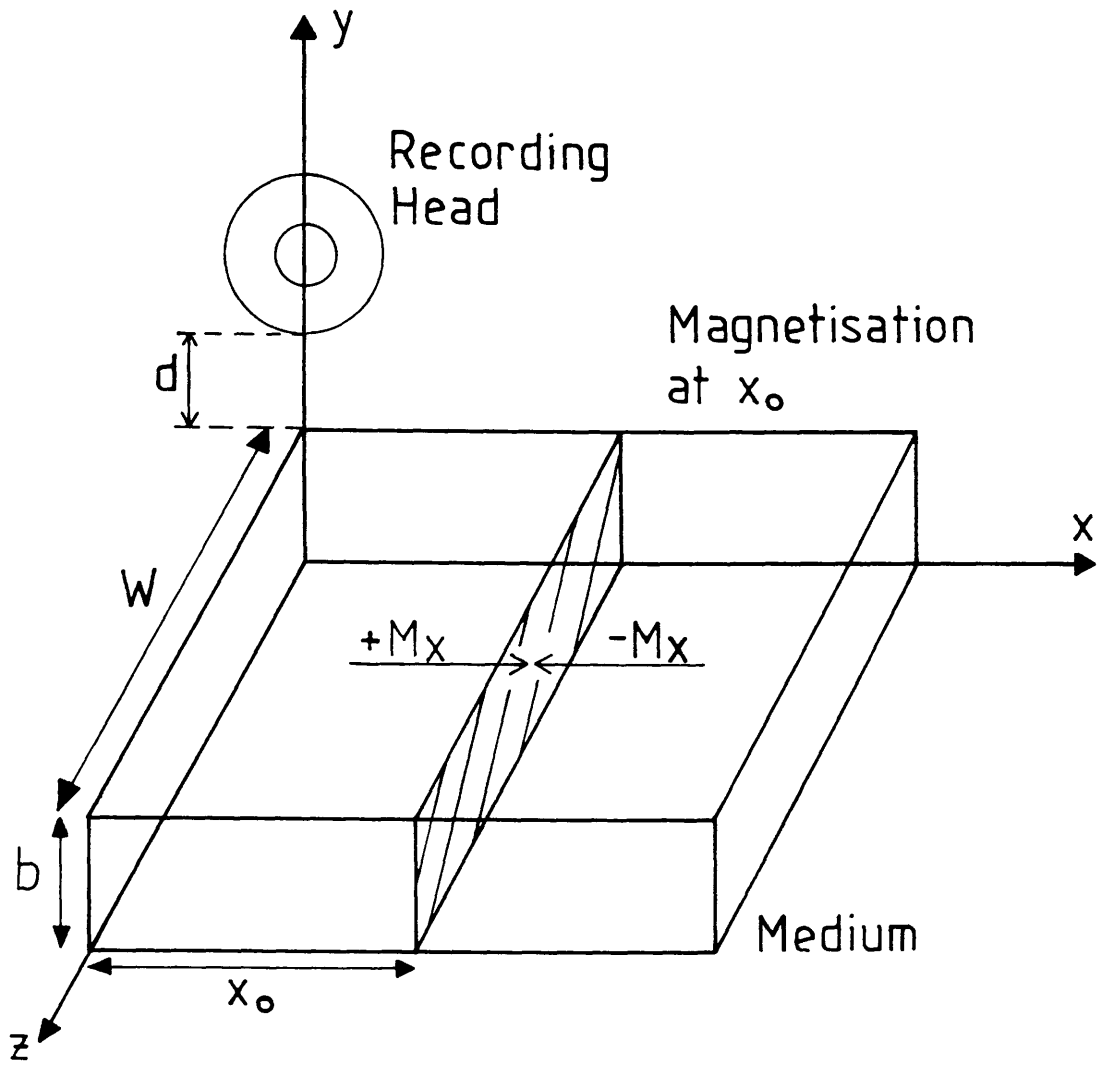


Figure 1.10 - The system geometry used in the Reciprocity Model of the read process.

Finally, the Reciprocity Model was introduced, producing an expression for the spatial variation of the readback signal detected in a longitudinal recording system.

These points provide a concise introduction to some of the underlying ideas and parameters that are of importance in subsequent chapters. A broader and more detailed account of the topics touched on here can be found in references [7,8,9], together with appraisals of the many different magnetic recording techniques and systems.

CHAPTER TWO

CHARACTERISATION OF FERROMAGNETIC THIN FILM MEDIA BY ELECTRON MICROSCOPY

2.1 INTRODUCTION

The observation of micromagnetic domain structures in ferromagnetic thin films and the interrogation of vector magnetisation within domains can in principle be accomplished using Lorentz electron microscopy. Lorentz microscopy utilises the deflection of the electron beam upon traversing the magnetic specimen to generate image contrast related to the sample magnetisation. Small-angle diffraction, Foucault and Fresnel imaging can be performed on the conventional transmission electron microscope; the differential phase contrast mode of Lorentz microscopy on a scanning transmission electron microscope.

The discussion of Lorentz microscopy is therefore the primary objective of this chapter, but consideration is also given to techniques used to characterise the physical microstructure of the specimen using electron microscopy, ferrofluid decoration, and X-ray analysis to establish specimen composition.

2.2 OPTICAL MICROSCOPY - FERROFLUID DECORATION

Magnetic structure can be imaged by optical microscopy using the Bitter technique, the modern version of which

utilises ferrofluid decoration. Although limited to optical resolutions - and also practically by the application of the ferrofluid - this method does allow a surface map of magnetisation changes to be visualised.

Ferrofluid is a colloidal suspension of ferromagnetic particles. When exposed to a magnetisation distribution the particles are free to aggregate along regions of high magnetic field gradient. Thus, applying ferrofluid to the surface of a ferromagnetic material defines the areas of high magnetic field emanation or abrupt medium magnetisation change.

In the context of this thesis this technique was used to visualise written tracks on the surface of computer hard disks. The ferrofluid congregated along written magnetisation reversals, allowing the distribution and nature of the written transitions to be imaged using an optical microscope, see figure 2.1.

2.3 IMAGING SPECIMEN BY CONVENTIONAL TRANSMISSION ELECTRON MICROSCOPY

The JEOL 1200EX and 2000FX conventional transmission electron microscopes (CTEM) were used to study the physical microstructure of the thin film recording media - identifying the grain shape and orientation through high magnification bright and dark field imaging as well as details of the crystallographic structure by diffraction techniques [1].

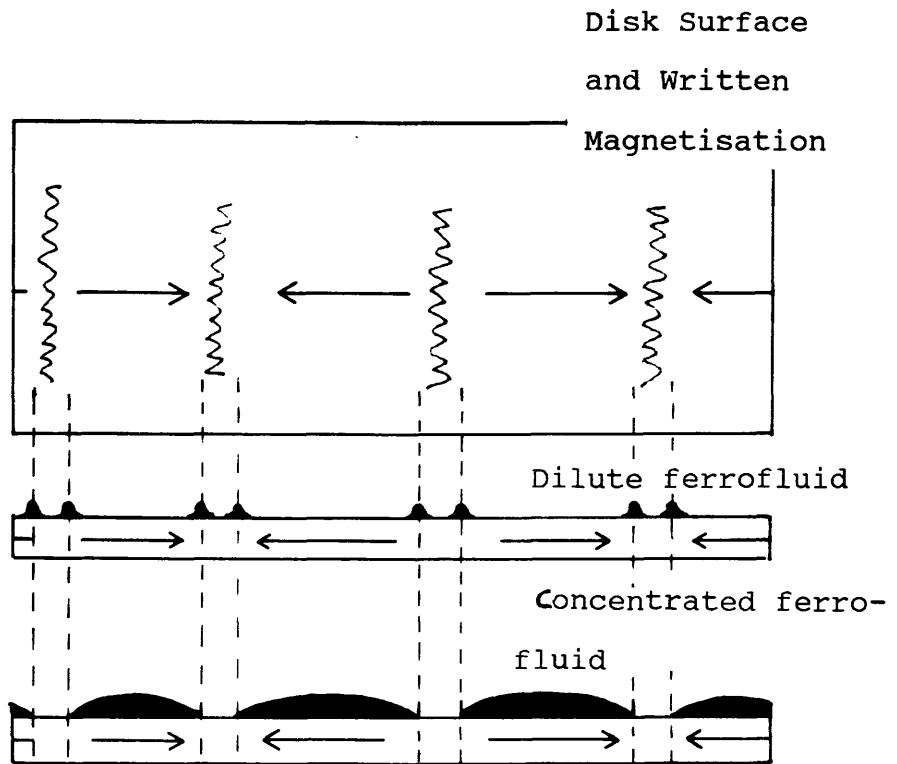


Figure 2.1 - An illustration of the two methods by which ferrofluid decoration can be used to image the written transitions.

Whatever the imaging mode considered the first component of the microscope is the electron gun, designed to produce a partially collimated electron beam, figure 2.2. The gun generates current by the thermionic emission of electrons from a heated filament. The filament is held at a negative potential with respect to the gun anode and electrons generated are accelerated via a Wehnelt electrode through a small hole in the anode. This divergent beam of electrons is normally focused to a point source in pre-specimen space by a two condenser lens system; further modification of the incident electron wave can be achieved with the various condenser apertures provided. Sources of varying coherence can thus be created by varying the strength of these condenser lenses, producing an incident beam that can be convergent, divergent, or almost plane wave in nature. An image forming or objective lens collects the scattered electron beam transmitted through the specimen, producing a diffraction pattern in the back focal plane of the lens and an image in a plane below this. The remaining post-specimen lenses combine to form a projector system, transferring the image intensity to the viewing screen.

Under normal imaging conditions the intensity projected onto the viewing plane arises from the undeflected zero order or central diffraction spot and produces a bright field image. This technique produces amplitude and phase contrast that depict the grain structure of the film, but also contains contrast originating from

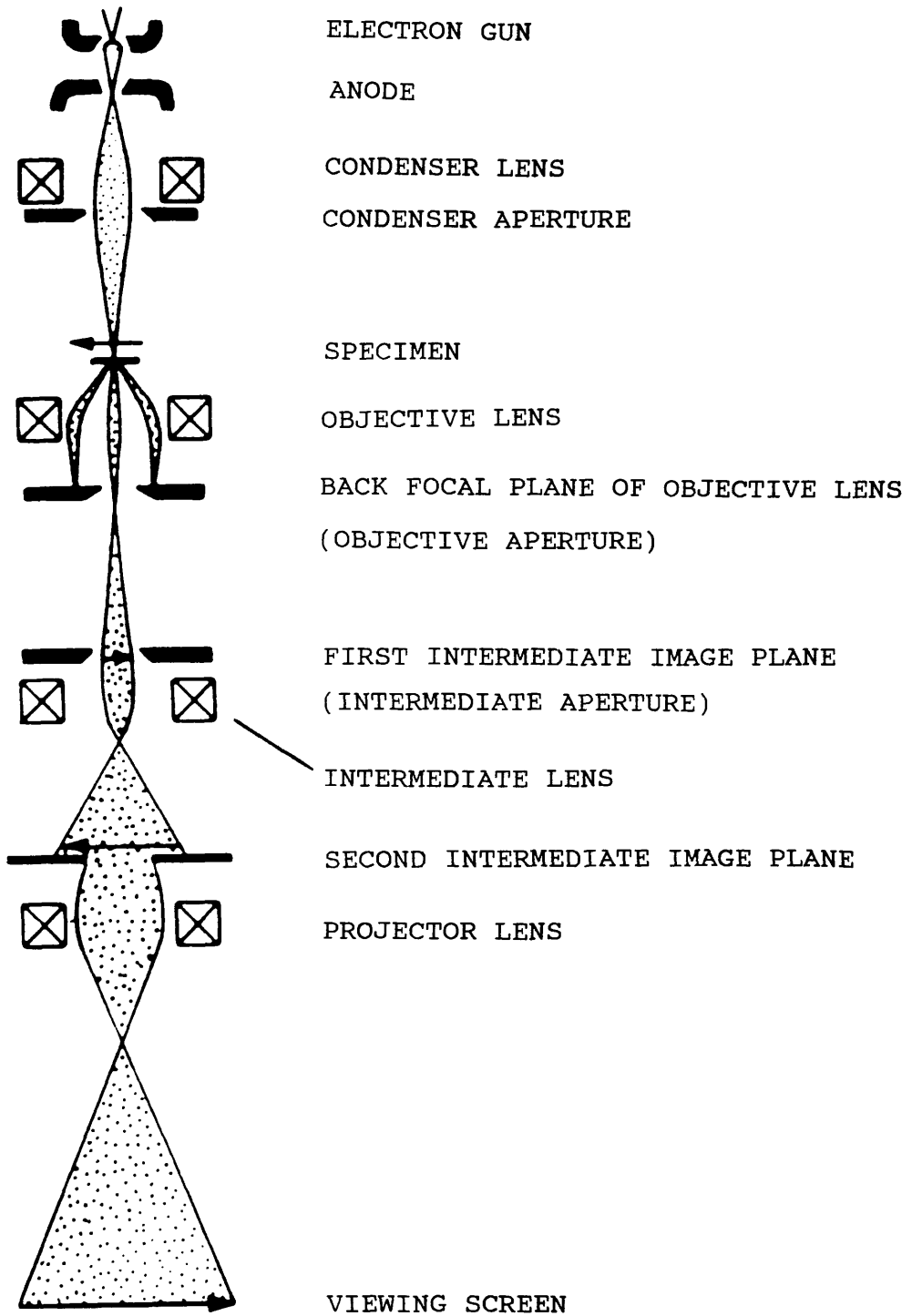


Figure 2.2 - Schematic diagram of the transmission electron microscope configuration for imaging (Thomas and Goringe [1]).

sources other than the crystallites, for example specimen debris. If the intensity from a lower order Bragg diffraction ring is used instead of the zero order beam to produce an image, a more sensitive representation of the structure of the crystallites can be obtained. This is known as dark field imaging and is achieved by shifting the specimen diffraction pattern in the back focal plane of the objective lens in a manner that projects this scattered intensity, rather than the zero order intensity, along the optic axis. The image then contains significant intensity for grains oriented preferentially to Bragg scatter into the chosen ring.

In the post-specimen region of the microscope the objective and selected area (intermediate) apertures can be used to improve the image contrast, but both apertures are also of use in diffraction studies. Figure 2.3 illustrates the electron microscope configuration for diffraction imaging. Imaging the Bragg diffraction intensity demands that the projector lenses focus upon the back focal plane of the objective lens (or the plane in which the first diffraction pattern is formed), transferring the diffraction intensity distribution to the viewing screen with a variable magnification, or camera length, dependent upon the projector lens excitations. The selected area or intermediate apertures can define the region of specimen from which the intensity within the Bragg diffraction pattern is formed.

For polycrystalline thin films diffraction studies can

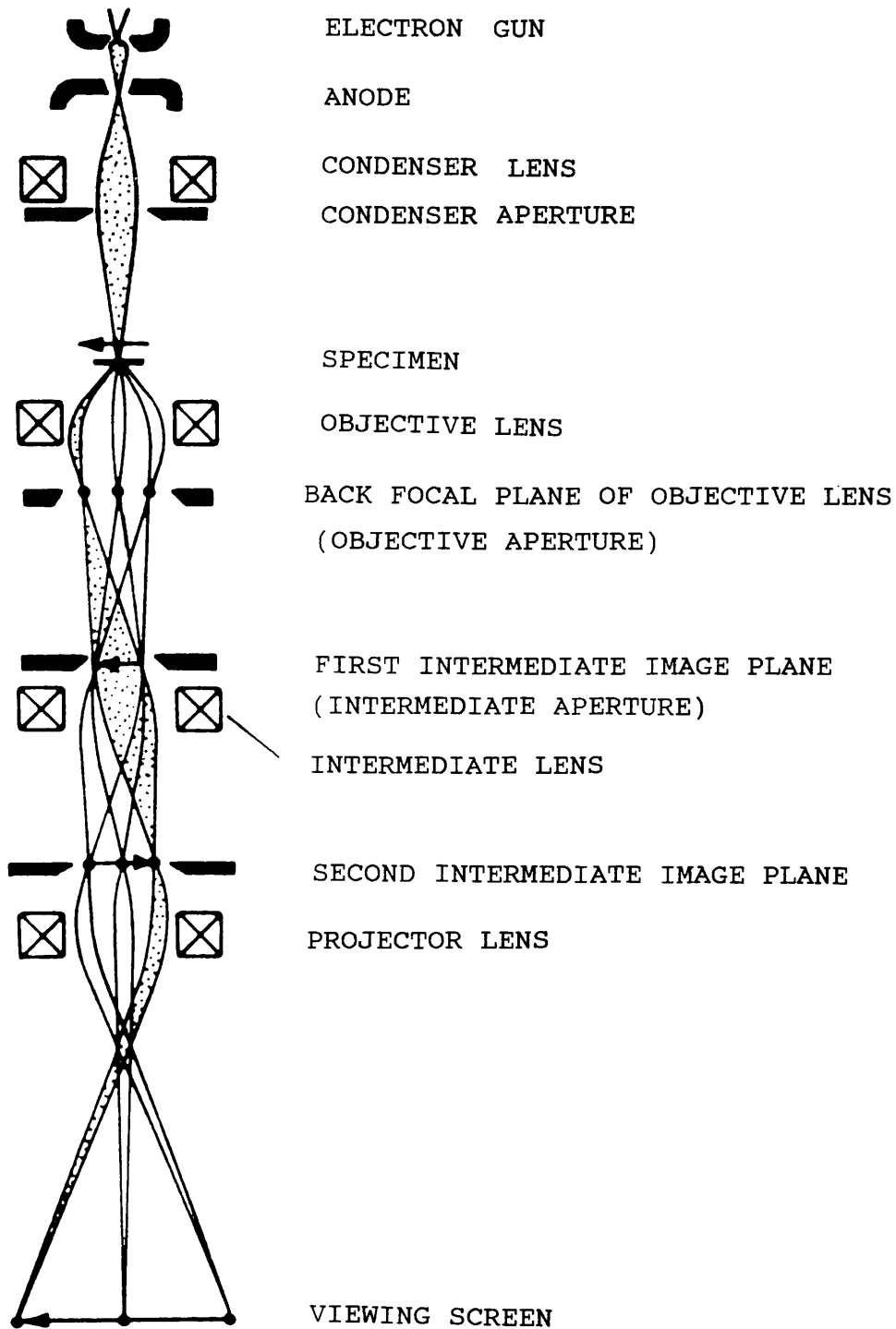


Figure 2.3 - Schematic diagram of the transmission electron microscope configuration for selected area diffraction (Thomas and Goringe [1]).

reveal details of the crystal structure to be determined. The observed Bragg diffraction patterns consist of a series of concentric rings centred around the unscattered zero-order intensity. The radii of the rings allow the crystallographic structure to be determined as well as a quantitative estimate of the lattice constant.

2.4 ELECTRON DISPERSIVE X-RAY ANALYSIS

To monitor the progress of specimen preparation methods and to determine if there is any change in the composition of the material it is important to measure the elemental concentrations of the recording media thin film alloys studied throughout the stages of specimen preparation. Energy dispersive X-ray analysis (EDX) was employed for this purpose.

The thickness of the magnetic disk specimen analysed varied from the original bulk state hard disk ($\approx 0.5\text{cm}$) to a thin film of ferromagnetic medium prepared for transmission electron microscopy ($\approx 50\text{nm}$). Consequently, because of specimen holder requirements, two different electron microscopes were used: the Hitachi S800 scanning electron microscope for bulk specimens and the JEOL 100C transmission electron microscope for thin film EDX. In both cases the X-ray detection and analysis technique is identical, see figure 2.4.

The incident electron beam excites the specimen

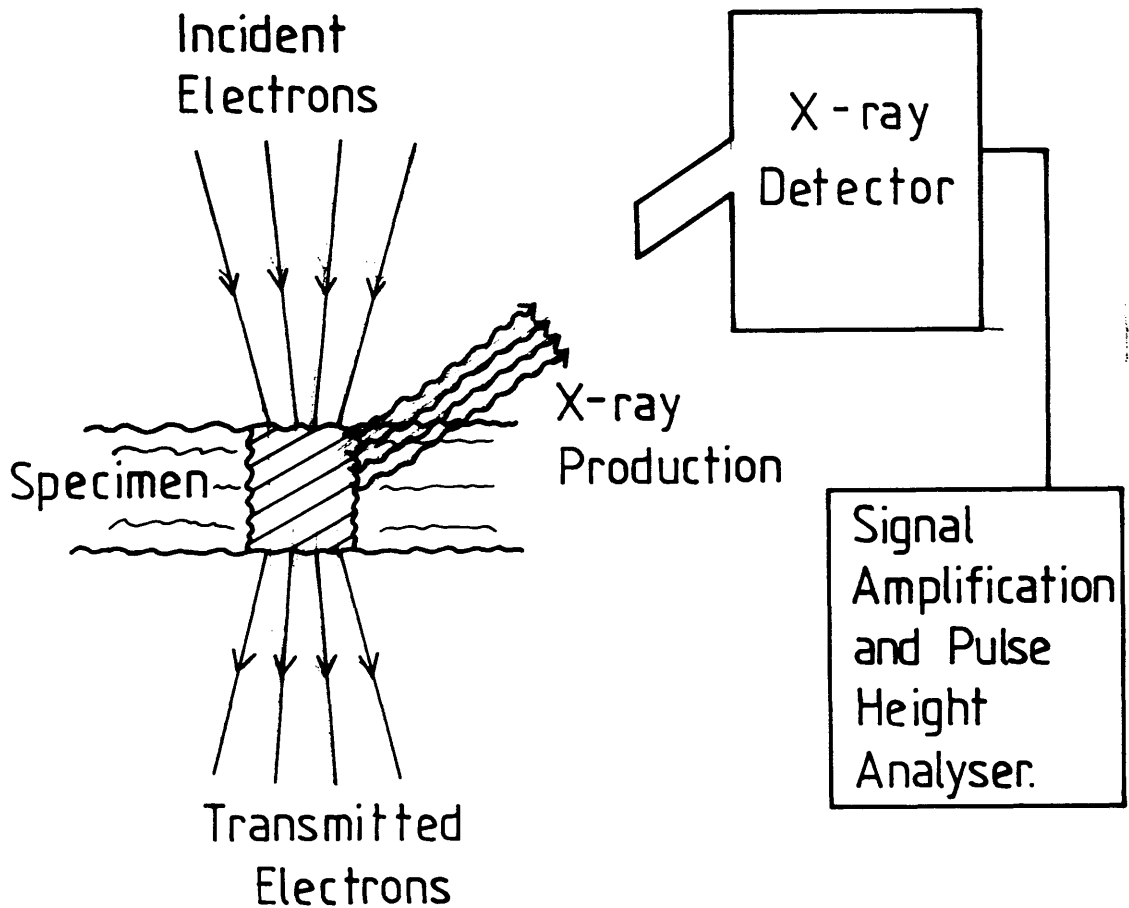


Figure 2.4 - The energies of the generated X-rays identify which elements are present; the relative intensities of the X-ray peaks in a given spectrum indicate the amount of a particular element present in the sample.

constituents, raising atomic electrons to higher energy states. These energetically unstable atoms return to equilibrium by emitting a characteristic X-ray as the excited electron reverts to its original orbit or shell. The wavelength of the emitted radiation is determined by the amount of energy released when the atom returns to equilibrium, hence identifying the excited atom. Analysis of the X-ray radiation produced by the electron-specimen interaction allows elemental concentrations to be estimated.

2.5 LORENTZ ELECTRON MICROSCOPY

2.5.1 ELECTRON BEAM - THIN FILM SPECIMEN INTERACTION

Lorentz electron microscopy [2,3] derives its name from the classical Lorentz force, which for an electron of charge e travelling with a velocity \mathbf{v} through a magnetic field of induction \mathbf{B} is given by

$$\mathbf{F} = e(\mathbf{v} \times \mathbf{B}) \quad (2.1)$$

The Lorentz force experienced by an electron as it traverses a ferromagnetic specimen in an electron microscope deflects the electron beam and for electrons of constant velocity the size and direction depends solely upon the magnitude and sense of the magnetic induction in the locality of the medium.

Consider figure 2.5; the deflection angle of the electron beam can be defined as

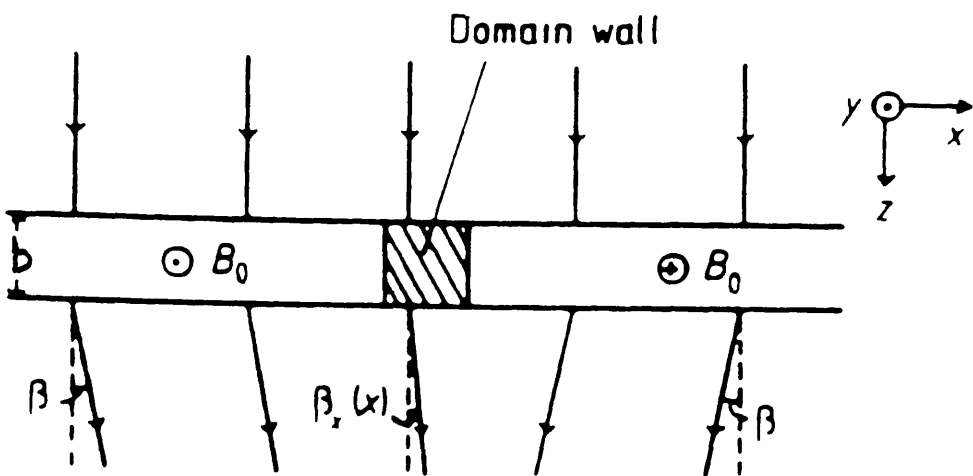


Figure 2.5 - A schematic representation of the deflection of the electron beam on traversing the oppositely magnetised domains (J.N.Chapman [2]).

$$\beta_x(x) = \frac{e \cdot \lambda}{h} \int B_y(x, z) \cdot dz \quad (2.2)$$

where $B_y(x, z)$ is the y component of magnetic induction at the point (x, z) , e is again the electronic charge, λ is the electron wavelength, and h is Planck's constant. Within the domains illustrated the induction is constant throughout the thickness of the sample, namely

$$B = \mu_0 M_s \quad (2.3)$$

where μ_0 is the permeability of free space and M_s the medium saturation magnetisation. Assuming that the effect of any stray field in the region of the sample can be neglected, the deflection angle is given by

$$\beta = \frac{e \cdot B \cdot \lambda \cdot b}{h} \quad (2.4)$$

If 100keV electrons were incident upon a film of thickness $b=50\text{nm}$ and saturation induction 1T the Lorentz deflection would be 0.06mrad, an angle much smaller than the typical first order Bragg angle of 10^{-2}rad from a crystalline specimen. Lorentz electron microscopy techniques exploit this Lorentz deflection of the electron beam in the post-specimen region of the electron microscope, allowing some aspect of the medium micromagnetics to be examined.

The classical description above provides a qualitative view of the magnetic aspects of the electron beam-specimen interaction. Although in the case of small angle diffraction [4] a quantitative estimation of the induction in the region of the specimen can be made in certain circumstances, a more rigorous quantum mechanical analysis is required if complete quantitative data acquisition is required from the

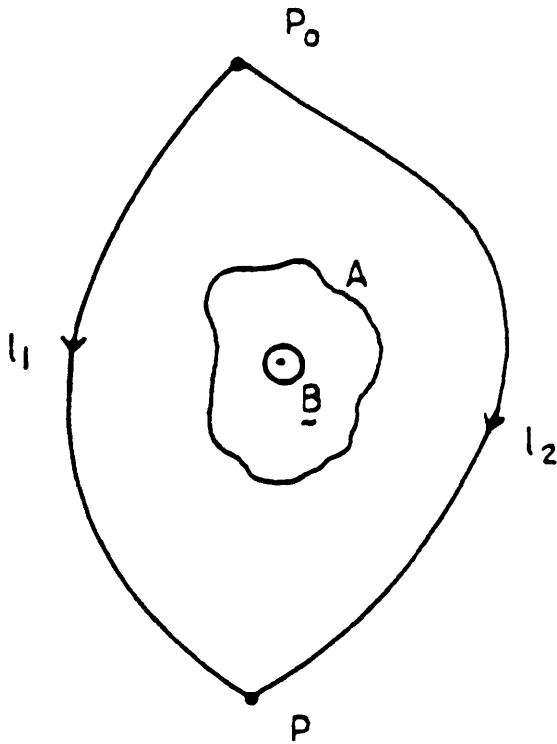
other modes of Lorentz microscopy. This was provided by Aharonov and Bohm [5], who showed that magnetic induction introduced a phase difference between the wave-functions of two electrons that reach a common destination by travelling different routes from the same origin, figure 2.6. If the two paths enclose a magnetic flux Φ then the phase shift θ can be written as

$$\theta = \frac{2.\pi.e.\Phi}{h} \quad (2.5)$$

where e and h are as previously defined - the electronic charge and Planck's constant respectively.

2.5.2 SMALL ANGLE DIFFRACTION

A conventional transmission electron microscope can be electron-optically configured to operate as a diffraction camera [4]. The intensity distribution in the back focal plane of the image forming lens describing the specimen diffraction pattern can then be observed, figure 2.3. The optical distance between this diffraction plane and the observation plane, known as the camera length, can be varied electron optically by altering the strength of the post-specimen lens magnetic fields. Extending the camera length (typically $\geq 50\text{m}$) allows the central spot of the diffraction pattern to be isolated and analysed. Although every electron experiences a magnetic deflection, those outwith the central spot are also



$$\Phi = \int_A \underline{B} \cdot d\underline{A}$$

Figure 2.6 - Idealised experimental set-up to demonstrate the Aharanov and Bohm effect.

scattered by the medium structure. The central spot comprises the unscattered electrons or those inelastically scattered by the crystal lattice and is usually the most intense feature of the diffraction pattern. The zero-order intensity, therefore, is ideal for measuring the deflection the electrons experience upon traversing the medium.

For a magnetic sample, such as that in figure 2.5, the observed zero order diffraction spot is seen to split or be composed of two sub-spots. The relative displacement of the spots is representative of the two electron deflections induced by the opposing magnetisations within the medium. A measurement of the medium magnetisation M_s can be obtained by measuring the separation of the spots Δ provided the film thickness is known. If stray field effects can be neglected then for a camera length L the medium magnetisation is given by

$$|M_s| = \frac{h \cdot \Delta}{2 \cdot e \cdot \mu_0 \cdot b \cdot \lambda \cdot L} \quad (2.6)$$

where μ_0 is the permeability of free space, b is the specimen thickness, h is Planck's constant and e and λ are the electronic charge and wavelength respectively. Practically the product of the medium magnetisation and thickness is measured - $|M_s|b$.

In practice media exhibit a more complicated vector micromagnetisation and produce zero order diffraction intensities which can be more difficult to interpret.

2.5.3 FOUCAULT IMAGING

From the above discussion it is seen that the zero order diffraction intensity peak is composed of two sub-spots representing the intensities of the respective medium magnetisations illustrated in figure 2.5. These are observed in the back focal plane of the image forming lens. The use of an aperture in this plane allows selected sub-spots to be obscured or blocked. If the remaining intensity is then projected to form an image of the specimen, figure 2.7, only the transmitted portion of the electron beam, that is, that avoiding the aperture, is present in the final image - defining the appropriately magnetised specimen domains by non-zero intensities. The magnetised areas of the specimen responsible for those sub-spots blocked in the diffraction plane are represented by reduced intensity in the final image as these electrons do not contribute to the intensity of the image. In this way an in focus image of the medium domain structure can be observed.

2.5.4 FRESNEL IMAGING

This technique allows the domain walls in the specimen to be observed, hence defining the micromagnetic domain structure. Figure 2.8 illustrates the configuration of a conventional transmission electron microscope for Fresnel imaging.

The difference between Fresnel imaging and standard

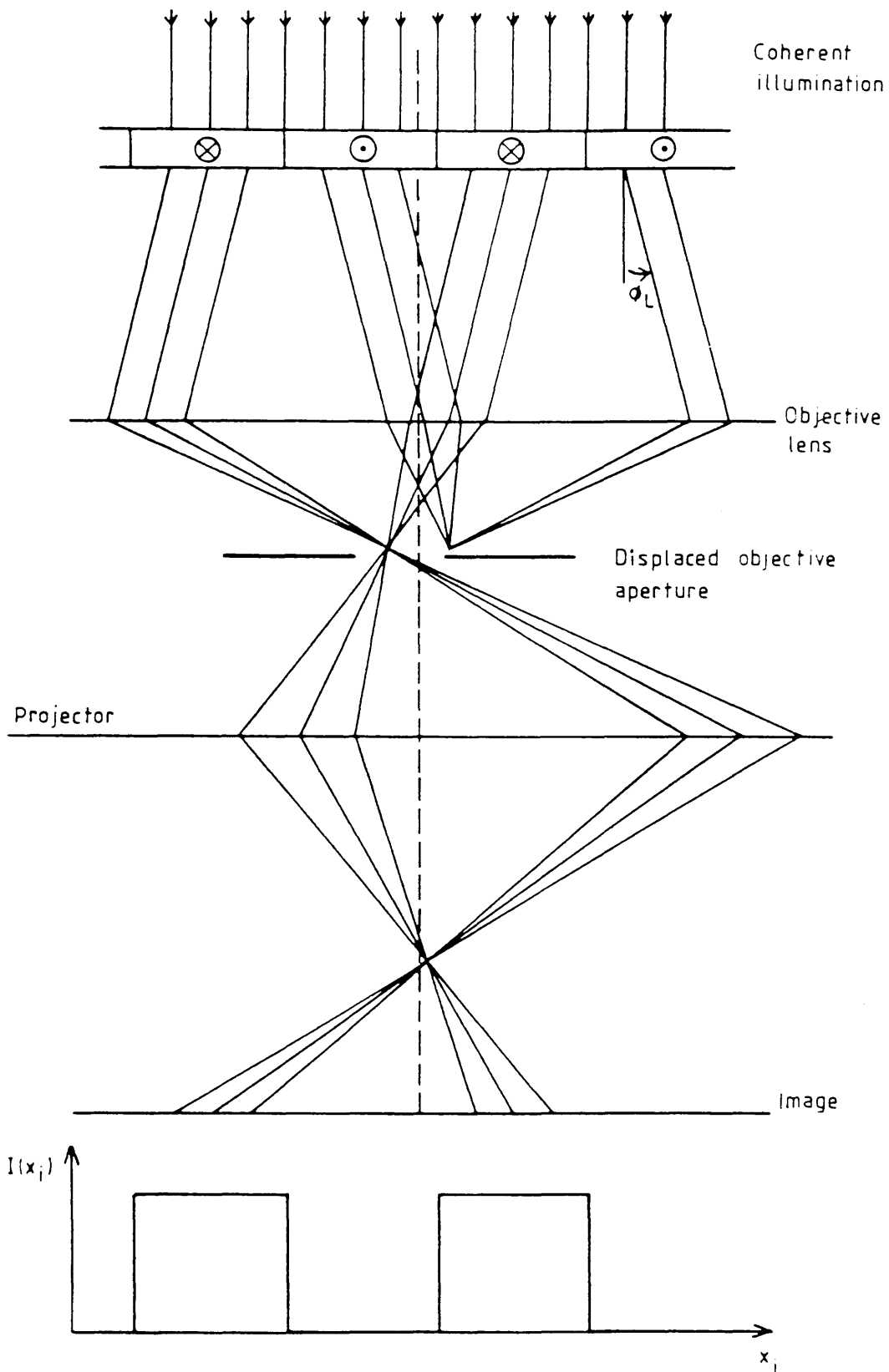


Figure 2.7 - A ray diagram illustrating the formation of a Foucault image from a ferromagnetic specimen.

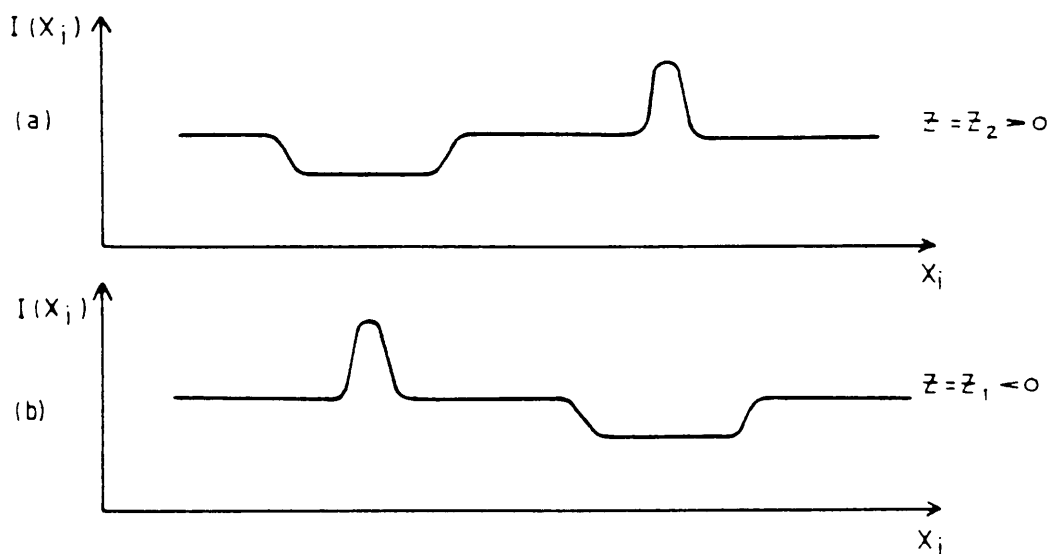
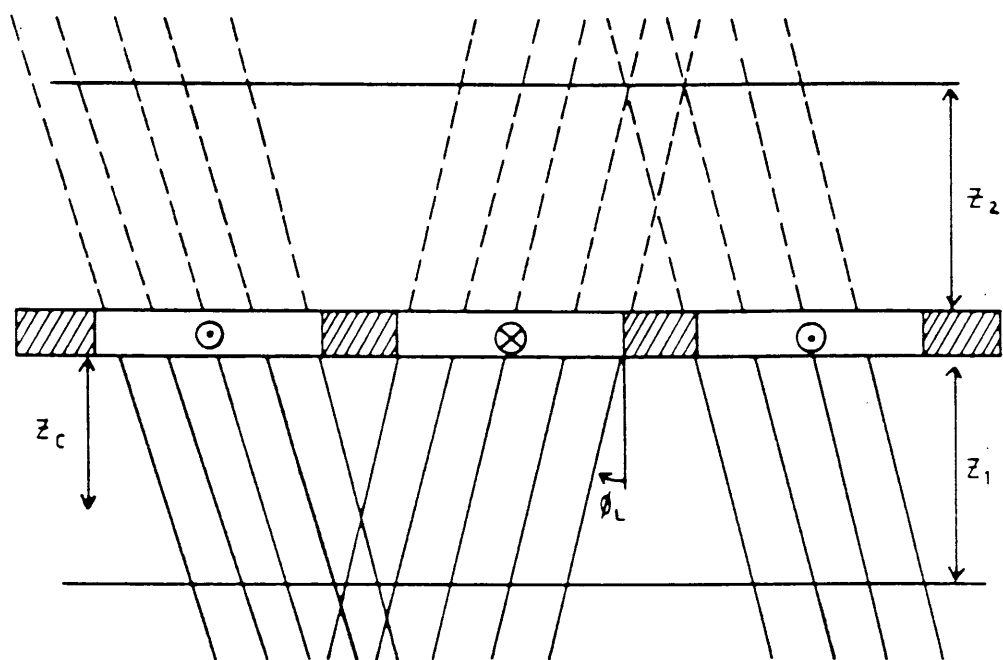


Figure 2.8 - A ray diagram illustrating the formation of a Fresnel image from a ferromagnetic specimen.

bright field imaging of the specimen structure is in the position of the plane of focus of the image forming lens. As illustrated, the micromagnetic structure is imaged by focusing on a plane either above or below rather than on the specimen. The effect of the convergence or divergence of the transmitted electrons deflected by the Lorentz force in neighbouring domains can then be observed - yielding intensity maxima and minima coincident with the domain walls. The final image obtained is then an out of focus specimen image on which the domain wall boundaries are clearly defined, thus revealing the micromagnetic domain geometry.

2.5.5 DIFFERENTIAL PHASE CONTRAST

The Lorentz techniques discussed so far are limited in their ability to characterise fully the vector nature of the medium magnetisation. Small angle diffraction identifies induction components in the region of the sample, but the interpretation of the diffraction spots in terms of the specimen induction is, in many cases, non-trivial - hence detracting too from the capabilities of Foucault imaging. Fresnel observations only define the domain geometry, yielding no information on the directionality of the magnetisation within domains unless there is a significant micromagnetic ripple within the medium.

Differential phase contrast microscopy (DPC) provides a

means by which the exact variation of magnetic induction along the trajectory of the electron beam can in principle be resolved. The technique was initially developed by Dekkers and De Lang [6], while first applied to magnetic specimens by Chapman et al [7]. Differential phase contrast cannot be obtained with conventional transmission electron microscopy; only by using a scanning transmission electron microscope (STEM) can this type of imaging be performed, figure 2.9. With the electron-optical configuration shown the pre-specimen lenses produce a focused probe of electrons on the specimen, nominally $\approx 10\text{nm}$ diameter with the VG HB5 scanning transmission electron microscope (STEM) and $\approx 35\text{nm}$ on the JEOL 2000FX CTEM modified for DPC imaging. A set of scan coils are situated in the pre-specimen region of the microscope which facilitate the raster scanning of the focused electron probe across the specimen. The transmitted electron beam is then projected onto a circular semiconductor detector in a far field plane of the microscope, the detector being divided into sections and placed symmetrically about the optic axis. The chosen camera length is determined by the amount of signal incident upon the detector - the beam diameter striking the detector is required to be less than the detector diameter for beam shift sensitivity, yet wide enough to produce an acceptable signal to noise performance. Between the specimen and the detector the diverging electron beam trajectory is modified by the de-scan or Grigson coils in a manner that ensures a

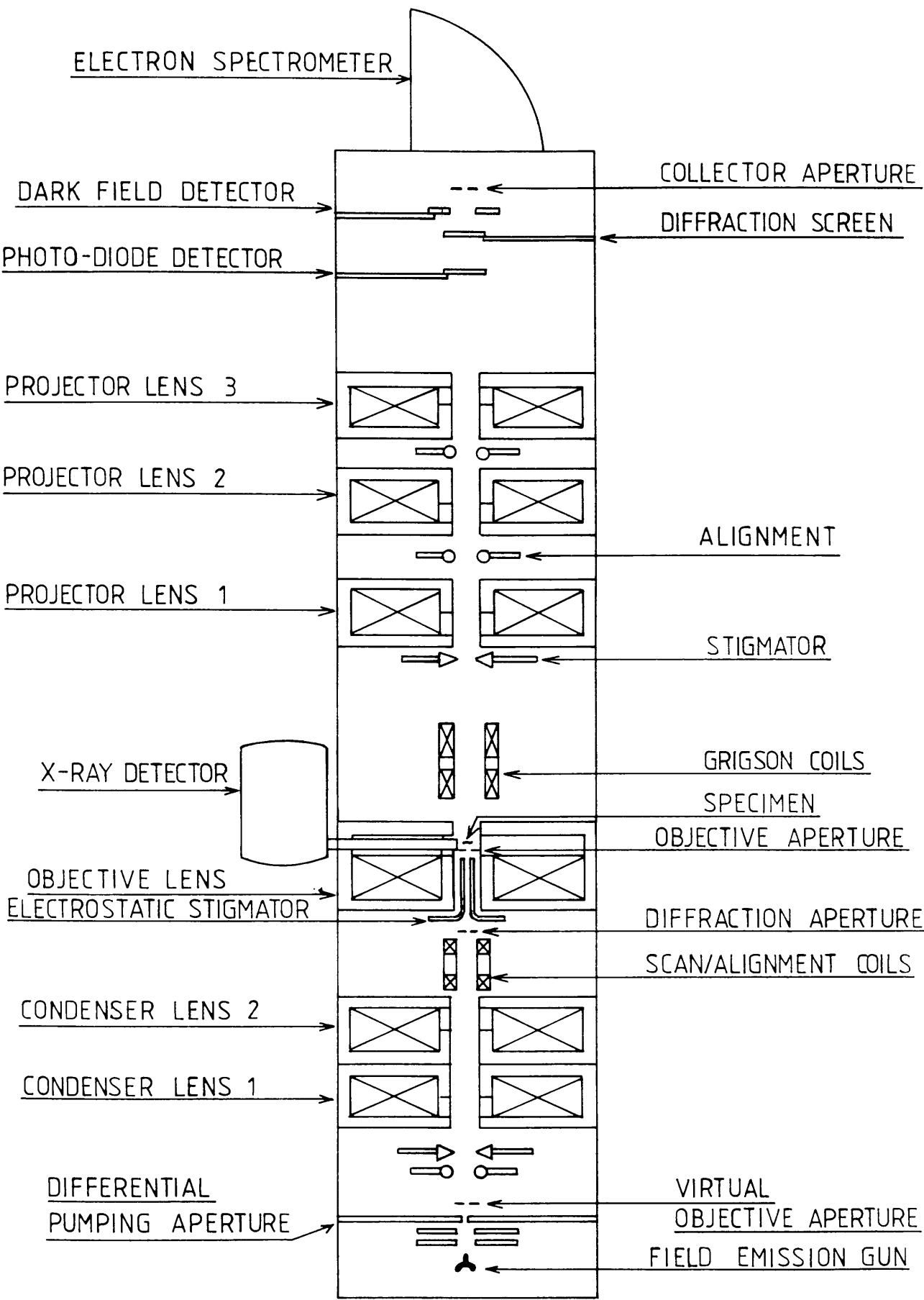


Figure 2.9 - A component diagram of the VG HB5 scanning transmission electron microscope.

uniform distribution of electrons incident upon the detector when no specimen is present. Figure 2.10 illustrates the post specimen electron beam trajectories and how the signal is collected using a split detector. The magnetic specimen induces a Lorentz deflection upon the probe as defined by equation (2.2); this produces a shift or displacement of the beam incident upon the detector surface, giving rise to unequal signals being detected by each half of the detector in figure 2.10. If the beam deflection β at the specimen is small in comparison with the probe semi-angle α then the difference between the detector segment signals provides a direct linear measurement of the local deflection angle and hence the magnetic induction B experienced by the probe for a given scan position.

This classical description of DPC signal detection has been substantiated quantum mechanically for an idealised detector by Waddell and Chapman [8] and more practically investigated by Morrison and Chapman [9].

The signal acquisition hardware and the LINK AN10 computer system used with the VG HB5 and JEOL 2000FX electron microscopes allow for the direct acquisition of the detector signals. A DPC observation is then visualised as a two-dimensional digital image in which each pixel value represents the required difference signal and hence the magnetic induction experienced by the electron probe at a given scan position. A quadrant detector extends the differentiating capabilities of the system by allowing the magnetic

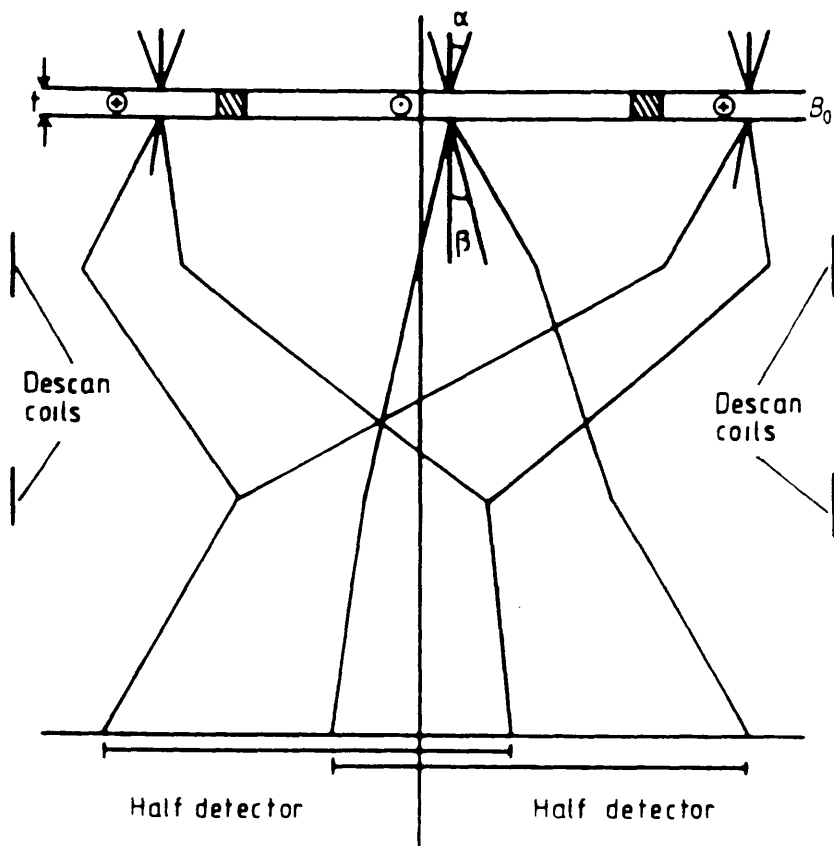


Figure 2.10 - A schematic diagram illustrating image formation in the differential phase contrast mode of Lorentz electron microscopy (J.N.Chapman [2]).

induction to be investigated in three more directions than the split detector is capable of, see figure 2.11. By using DPC the nature of the medium magnetisation can be revealed, but it must be noted that the difference signal is proportional to the magnetic induction experienced by the electron probe along the whole electron trajectory, hence stray field around the specimen can prevent an absolute characterisation of the medium micromagnetics. This is of particular practical importance when analysing written tracks where there is a high stray field component of magnetic induction.

2.6 SUMMARY

This classical description of the microscope techniques used in analysing the thin films studied provides a qualitative grounding on the acquisition of the data presented in chapters three through five. The interpretation of the medium micromagnetics from electron microscope images can thus be understood in the terms presented in this chapter.

A more rigorous, quantitative quantum mechanical approach can be found in the theses of Waddell [10], Morrison [11], and McFadyen [12].

DETECTOR CONFIGURATION

DIFFERENTIATION

IMAGE SENSITIVE
TO INDUCTION IN
THIS DIRECTION :

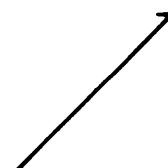
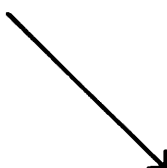
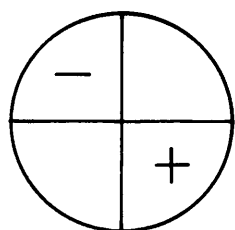
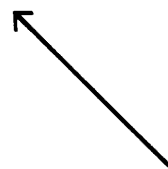
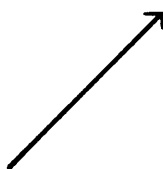
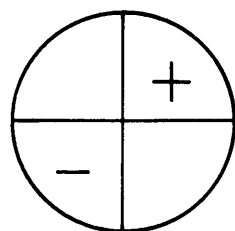
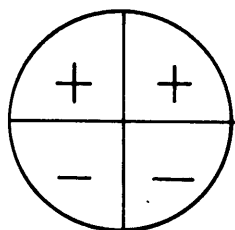
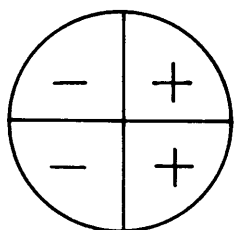
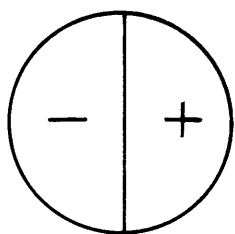


Figure 2.11 - A comparison between the differentiating capabilities of the half and quadrant semiconductor quadrant detectors used in DPC imaging.

CHAPTER THREE

SPECIMEN PREPARATION

3.1 INTRODUCTION

The overall objective of this work was the preparation of a thin film specimen of recording media that, when imaged by Lorentz electron microscopy, would reveal the micromagnetic structure of tracks written to the medium when originally it formed the recording layer of a hard disk. Three preparatory stages were involved to achieve this:

- (1) fabrication of the hard disk;
- (2) recording of experimental tracks to the disk;
- (3) isolation of the thin film recording medium from the hard disk.

Although the final step of the above process was performed completely at the University of Glasgow, facilities did not exist that would allow stages one and two to be accomplished. This work was realised through a collaboration with the laboratories of the General Products Division of IBM, San Jose, California. Two thin film recording media were prepared for electron microscope analysis: iron cobalt chromium (weight percentage Fe 42.5%: Co 42.5%: Cr 15%) and cobalt nickel chromium (weight percentage Co 72.5%: Ni 20%: Cr 7.5%). These were chosen because of their contrasting physical and magnetic properties: the iron cobalt chromium was deposited and textured to produce a medium with high magnetic anisotropy and an easy axis

in the circumferential direction of the disk; the cobalt nickel chromium medium was designed to be magnetically isotropic. It was hoped that a better understanding of the track micromagnetics associated with each film would be obtained by imaging and comparing Lorentz microscopical images from both media.

3.2 IRON COBALT CHROMIUM (FCC)

3.2.1 HARD DISK FABRICATION

For all the FCC recording experiments the disk samples originated from the same fourteen inch diameter rigid disk, a cross-section of which is shown in figure 3.1. This disk structure shall be discussed, relating the recording properties to the fabrication process. A more detailed account of the process has been given by Rossi et al [1].

The supporting disk substrate was bulk aluminium-4% magnesium. This was coated with $15\mu\text{m}$ - $20\mu\text{m}$ of electroless plated nickel phosphorus (NiP). The mechanical effect of this first overcoat was to increase the substrate hardness yielding improved wear performance, but this layer also seals the aluminum from any corrosive reaction.

Before the magnetic layer was deposited the NiP was polished in two stages. The first removed any surface topographical irregularities by a free abrasive

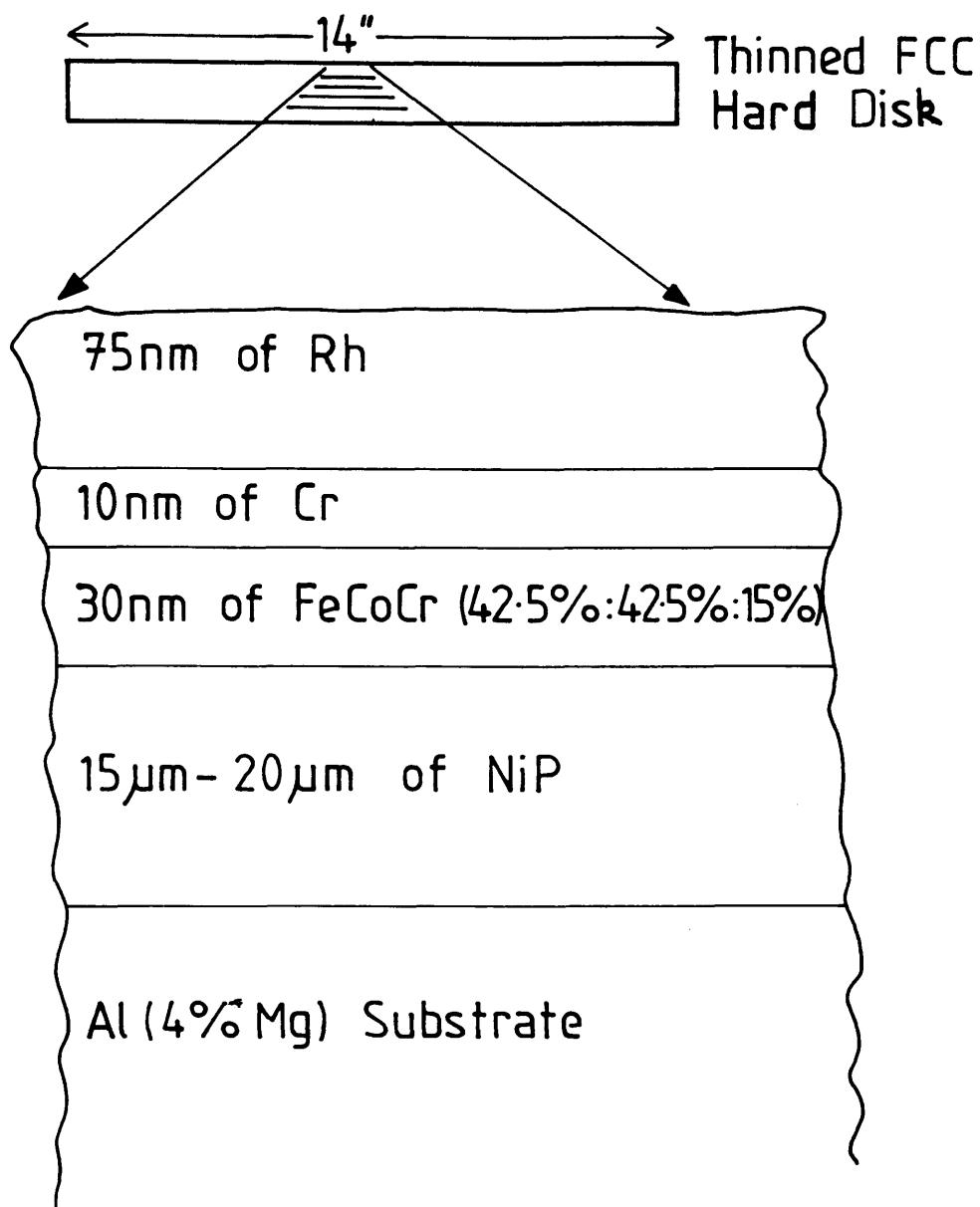


Figure 3.1 - Cross-section of the iron cobalt chromium hard disk.

polishing. To this polished surface a second, controlled abrasion was applied, producing a uniform, circumferential texture over the NiP surface. The main effects of this texturing are: a reduction of the head-disk wear or stiction; an improvement of the retention of the lubricants applied to the disk surface; an ultimate increase in the medium anisotropy and coercivity [2].

To understand why this polishing process increases the medium anisotropy consideration must be given to the deposition of the FCC recording layer. Figure 3.2 describes the film deposition by electron-beam evaporation at oblique incidence onto a rotating substrate. The process geometry induces the formation of parallel crystallite chains within the medium in a plane perpendicular to the direction of the vapour stream. This was a result of self-shadowing by the growing film, and it is at this stage that the NiP texturing may accentuate such growth. The final film deposited was seen to be highly anisotropic with a circumferential easy axis, parallel to the texture direction.

Two final overcoat layers were deposited upon the magnetic layer - 10nm of chromium and 75nm of rhodium respectively. Both of these layers were deposited by dc magnetron sputtering, the rhodium provides wear and corrosion protection while the chromium layer increases the adhesion between FCC and rhodium layers.

Figure 3.3 illustrates the hysteresis loop measurements in both the circumferential (easy axis) and radial

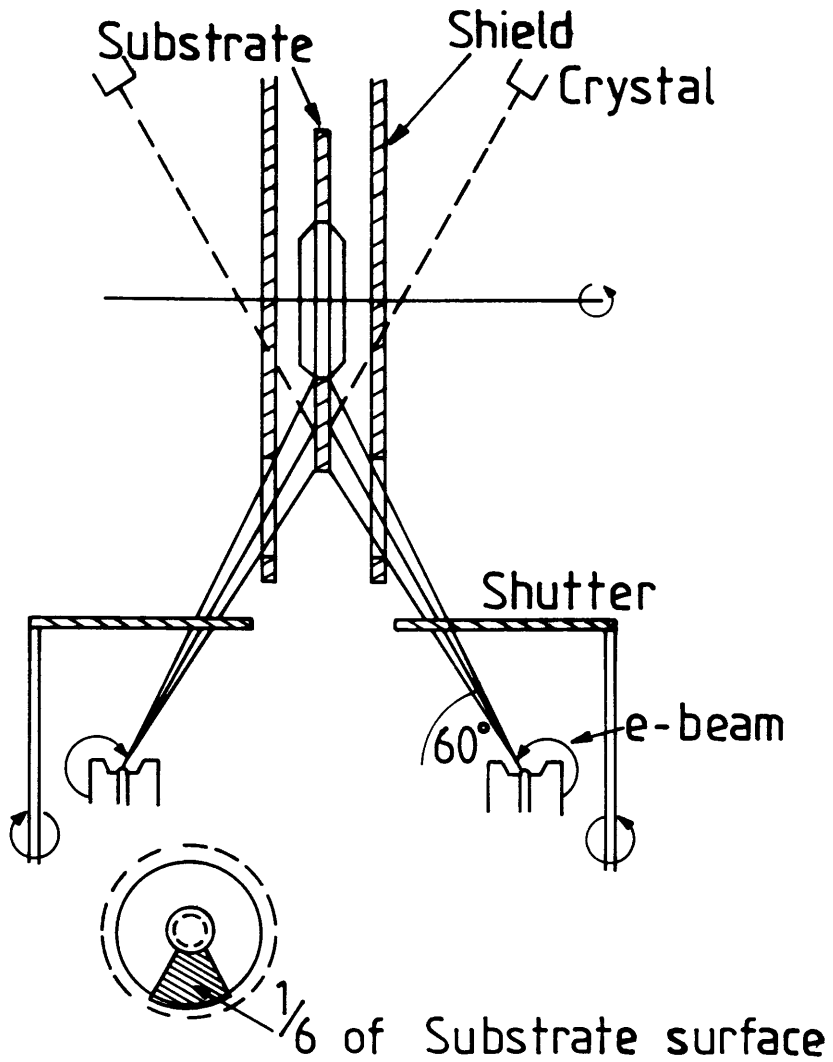


Figure 3.2 - Schematic experimental arrangement for depositing obliquely evaporated metal films on to a rotating aluminium (4% magnesium) substrate from rod-fed, electron-beam-heated sources (Rossi et al [1]).

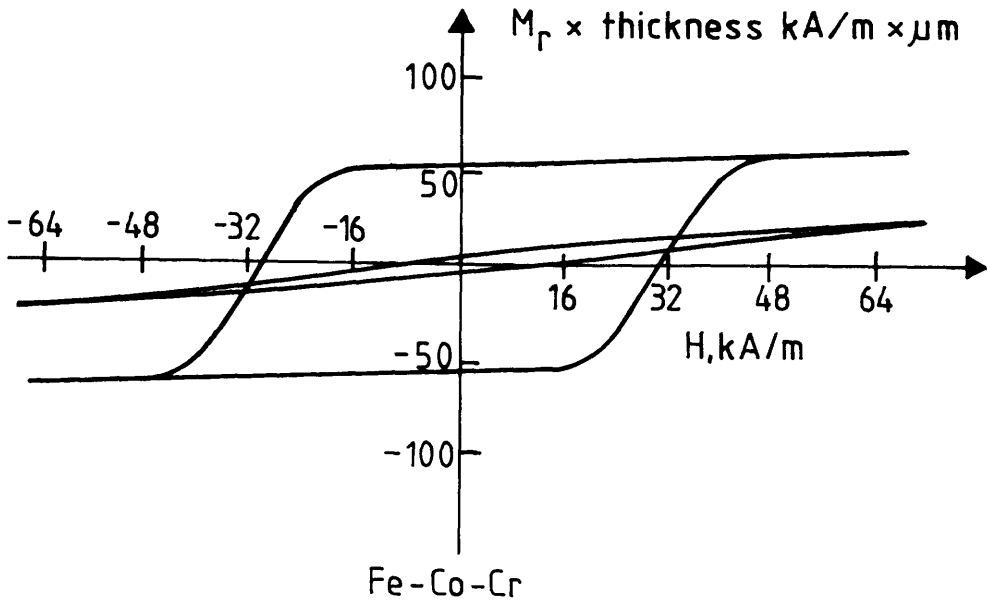


Figure 3.3 - Typical hysteresis loop measurements from the iron cobalt chromium hard disk. The larger, squarer loop is for the easy axis and the narrower loop for the transverse direction (Rossi et al [1]).

(hard axis) directions. The ratio of remanent magnetisations in these two directions is approximately 10:1. VSM measurements give the product between the circumferential remanent magnetisation and film thickness as $M_R b \approx 2.26 \times 10^{-3} \text{ emu/cm}^2$ with the circumferential coercivity $H_c \approx 350 \text{ Oe}$ and the squareness factor $S \geq 0.94$.

3.2.2 IRON COBALT CHROMIUM WRITE EXPERIMENTS

A single fourteen inch diameter iron cobalt chromium (FCC) hard disk was used in writing three different recording experiments. For each experiment similar tracks were written, allowing the behaviour of the medium to be examined for tracks of variable write frequency and current respectively. The experiments differed in the angle at which the tracks were written with respect to the medium easy axis, varying from parallel to perpendicular to the easy axis.

EXPERIMENT ONE - TRACK WRITTEN ALONG THE CIRCUMFERENTIAL OR EASY AXIS

For the purpose of this experiment the entire disk was bulk a.c. erased. This was accomplished by applying a field to the medium that alternated parallel or anti-parallel to the easy axis with diminishing amplitude.

A non-contact, two pole piece thin film head was used to write the tracks for this and all the other recording experiments. In this case an 'Evergreen' 3380E head was employed, figure 3.4a showing qualitatively the geometry of the head and the field generated between the poles while writing. The pole lengths were $12\mu\text{m}$ and $15\mu\text{m}$ respectively, and from the diagram it is seen that across the recording gap where the pole-pieces overlap the write field is essentially homogeneous. Where the longer of the two poles extends beyond the other a radically different write field is generated. This is known as 'side-writing' and produces a characteristic write effect at track edges, see figure 3.4b. The resultant track width for this head was approximately $15\mu\text{m}$.

There were three sets of tracks written to the disk to examine different aspects of the recorded medium micromagnetics. The first involved reducing the write current from a value that produced a field which saturated the recording medium to values giving non-saturation recording. Here the write frequency was held constant at 6MHz ($\lambda=6.35\mu\text{m}$) over a group of five tracks whilst the peak-peak head write current was reduced from a saturation value of 65mA through 20mA, 16mA, 14mA, to 12mA in successive tracks.

Generally the objective of recording medium development is to increase the areal storage density of a medium while maintaining a significant signal to noise ratio. The second set of tracks written investigated this by examining how the medium track micromagnetics behaved

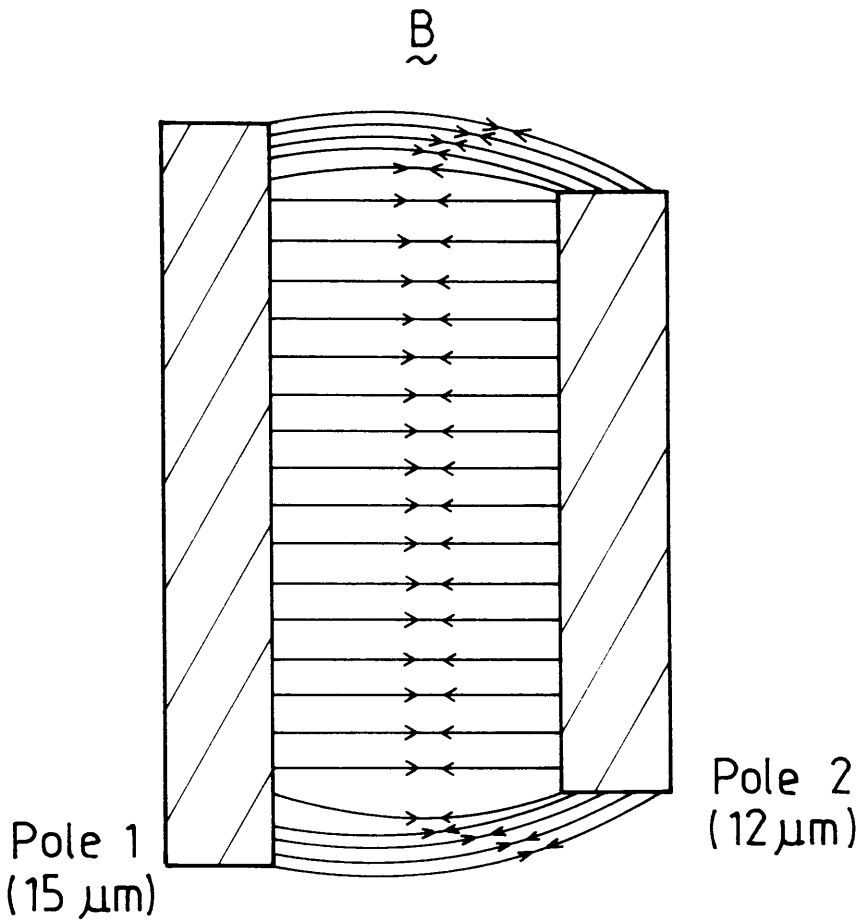
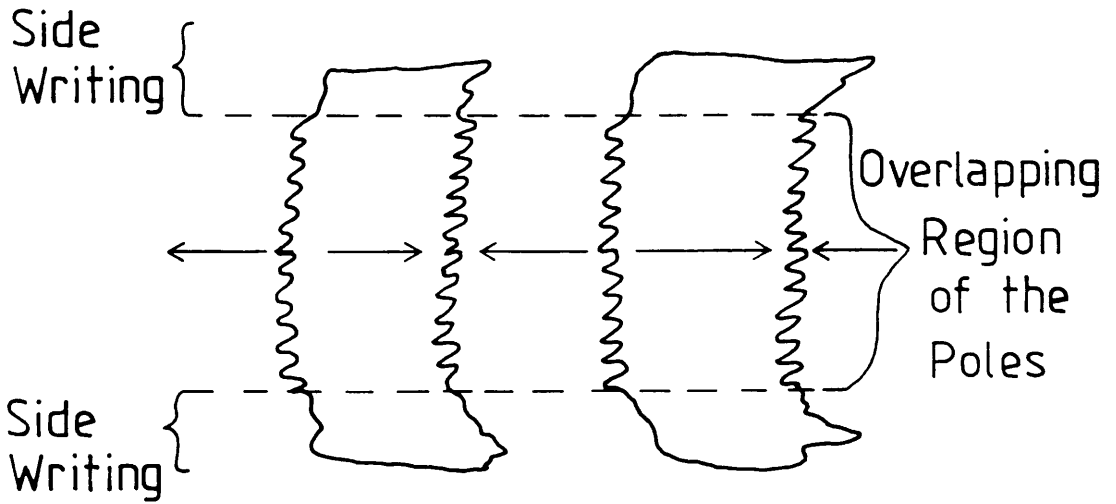


Figure 3.4 - (a) Schematic diagram of the write field generated between the pole tips of the write head;



(b) an illustration describing how side-writing manifests itself in the recorded track domain structure.

as the write frequency was increased. A head-disk speed of 38ms^{-1} and a constant write current of 65mA were set. Frequencies between 0.5MHz ($\lambda=76\mu\text{m}$) and 20MHz ($\lambda=1.9\mu\text{m}$) were written.

Finally a third group of tracks was written to examine how well a track could be overwritten by a signal of higher frequency. The procedure was to write the low frequency track but only partially step the head off the track. Writing now with a higher frequency signal produced an overlap region in which the low was overwritten by the high frequency. This region is then bordered on one side by the low frequency track and on the other by the higher of the two written signals.

Collectively these tracks - saturation, variable frequency and overlap writing - formed a set that was recorded six times. On three occasions the tracks were written directly onto the a.c. erased medium. The remaining three groups were recorded only after each track was d.c. erased with the head prior to writing, giving alternative write conditions under which the micromagnetics could be studied.

EXPERIMENT TWO - TRACK WRITTEN OFF THE EASY AXIS USING A LINEAR TESTER

This experiment was designed to investigate the medium micromagnetics when tracks were written at an angle to the easy axis of the magnetic thin film.

A circular coupon, one inch in diameter, was removed

from the original disk, see figure 3.5a. The coupon was d.c. erased by placing it between the poles of a VSM magnet with the easy axis aligned with the applied field. A maximum field of 5000 Oe was applied, then reduced to zero before the specimen was removed.

A linear coupon tester was used to write tracks using a non-contact IBM 3380 'Coronado' head, producing a track width of $\approx 26\mu\text{m}$. This test rig allowed straight lengths of tracks ($\approx 6\text{mm}$) to be written on the coupon at a given angle to the easy axis. Figure 3.5b illustrates the track pattern geometry recorded on to the coupon, showing sequences at zero, fifteen, thirty, and forty five degrees to the easy axis.

Towards the ends of each track the head velocity falls to zero, but the peak velocity of the write oscillation stroke was 1.1ms^{-1} . The write frequencies varied from 35kHz to 280kHz giving a corresponding range in signal wavelength of $31.4\mu\text{m}$ to $3.93\mu\text{m}$.

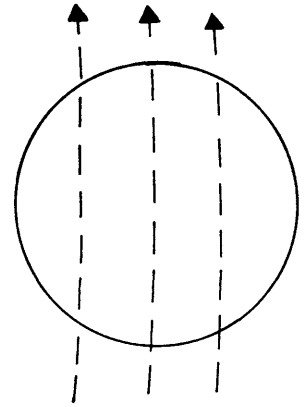
The track patterns recorded were similar to those of experiment one. A constant write frequency of 70kHz was used to observe the saturation behaviour as the track write current was reduced from 120mA to 30mA in 30mA steps. The frequency dependence of the medium magnetisation was examined at a constant write current (120mA) for frequencies of between 35kHz and 280kHz.

Original 14" FCC disk



1" FCC coupon

1" FCC coupon removed

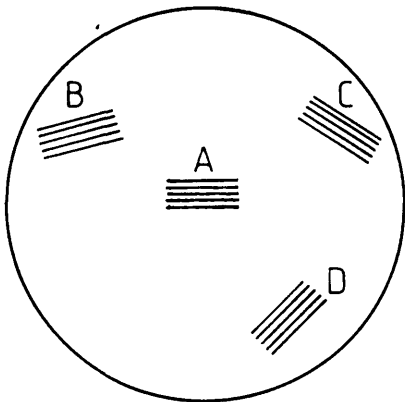


The original easy axis is essentially uniformly straight over the coupon

(a)

(b)

1" FCC coupon



Tracks	A	written	at	0°	to	e.a.
"	B	"	"	15°	"	"
"	C	"	"	30°	"	"
"	D	"	"	45°	"	"

Written track geometry recorded to the 1" coupon

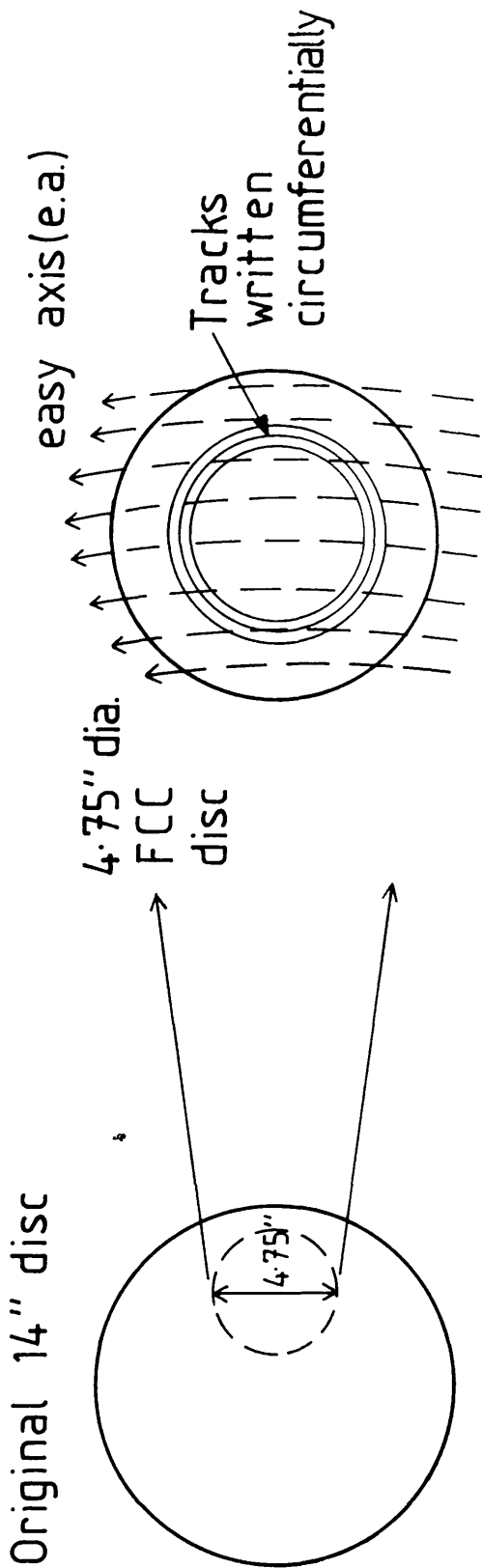
Figure 3.5 - (a) The selection of a circular coupon (one inch in diameter) from the original iron cobalt chromium hard disk; (b) the orientation of the tracks recorded to the one inch coupon.

EXPERIMENT THREE - TRACKS WRITTEN AT EVERY ANGLE TO THE EASY AXIS

A second experiment was designed to develop further the observation of tracks written off the easy axis. Firstly a 4.75 inch diameter disk was cut from the original fourteen inch FCC hard disk, this is shown in figure 3.6. The disk was initially bulk a.c. erased using a hand-held tape eraser. A non-contact thin film head was then used for recording, producing a nominal track width of $\approx 9\mu\text{m}$. The tracks were then written circumferentially around the disk to produce written tracks at every possible angle to the medium easy axis. The sequence of tracks consisted of write frequencies at one, two, four, six, and eight megahertz written with a constant saturating current ($\geq 65\text{mA}$). The head velocity was 20ms^{-1} yielding wavelengths of between $2.5\mu\text{m}$ and $20\mu\text{m}$. This set of tracks was written three times in total.

3.2.3 PREPARATION OF THIN FILM IRON COBALT CHROMIUM SPECIMEN FROM THE HARD DISK

A diagram illustrating the FCC cross-section was given in figure 3.1. From this it can be seen that to achieve FCC thin film specimen thicknesses of less than 100nm for transmission electron microscopy both the disk substrate (Al/NiP) and rhodium overcoat must be removed. The techniques used have been briefly



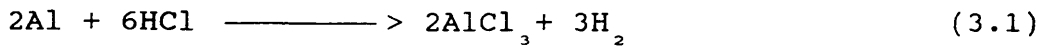
The original circumferential easy axis produces a slightly curved easy axis over the 4.75" disc.

Figure 3.6 - The selection of a 4.75 inch diameter disk from the original iron cobalt chromium hard disk.

discussed by Ferrier et al [3].

(1) Removal of Aluminium-4% Magnesium Substrate

The disk sample was first mechanically thinned to reduce the bulk Al(Mg) to a thickness of approximately 0.25mm. A hydrochloric acid etch was employed to remove the remaining Al(Mg), see figure 3.7. By immersing the sample in a boiling 50:50 solution of acid and water the layer was completely removed through the reaction



During this process the magnetic surface was protected by sellotape. This confined any acid damage to a border approximately 0.5mm wide around the periphery of the sample typically four square centimetres in extent.

(2) Reduction of the Rhodium Overcoat

The rhodium overcoat was removed by an r.f. sputter etch. The disk samples were fixed to aluminium mountings by adhesive and conducting silver dag, the latter preventing any build up of capacitance between sample and mounting. A vacuum of the order $2 \cdot 10^{-7}$ torr was maintained in the sputtering chamber and argon gas admitted, see figure 3.8. On powering the r.f. electrode arrangement the argon formed a plasma, positive argon ions and electrons, and a high negative voltage was applied to the target substrate, attracting the positive ions. The fast moving ions strike the target surface, perturbing it to such an extent that target atoms are removed. These then travel from the target and condense on other surfaces.

In order to reduce the rhodium overcoat thickness

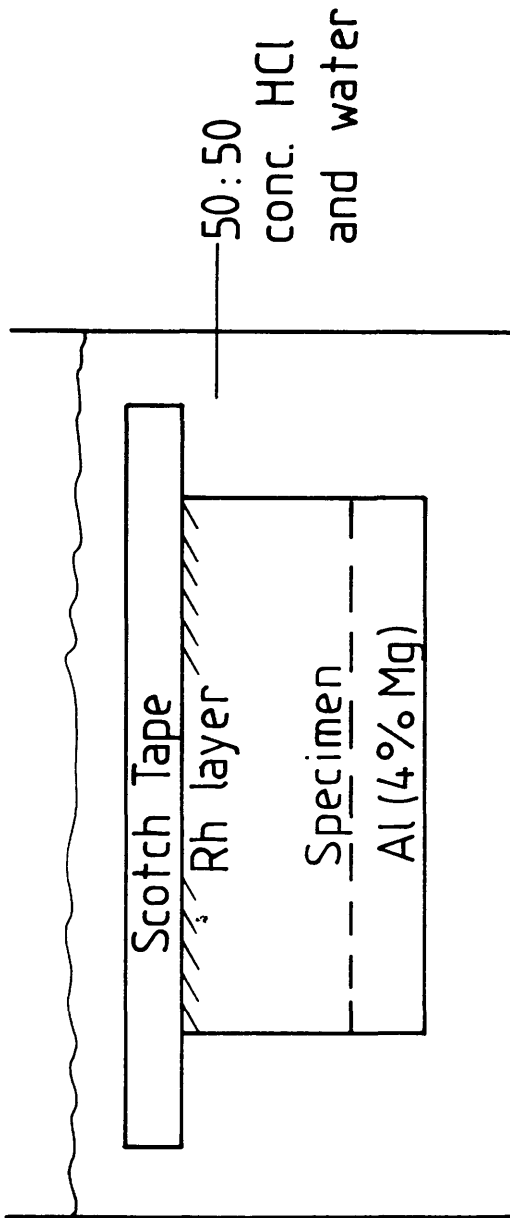
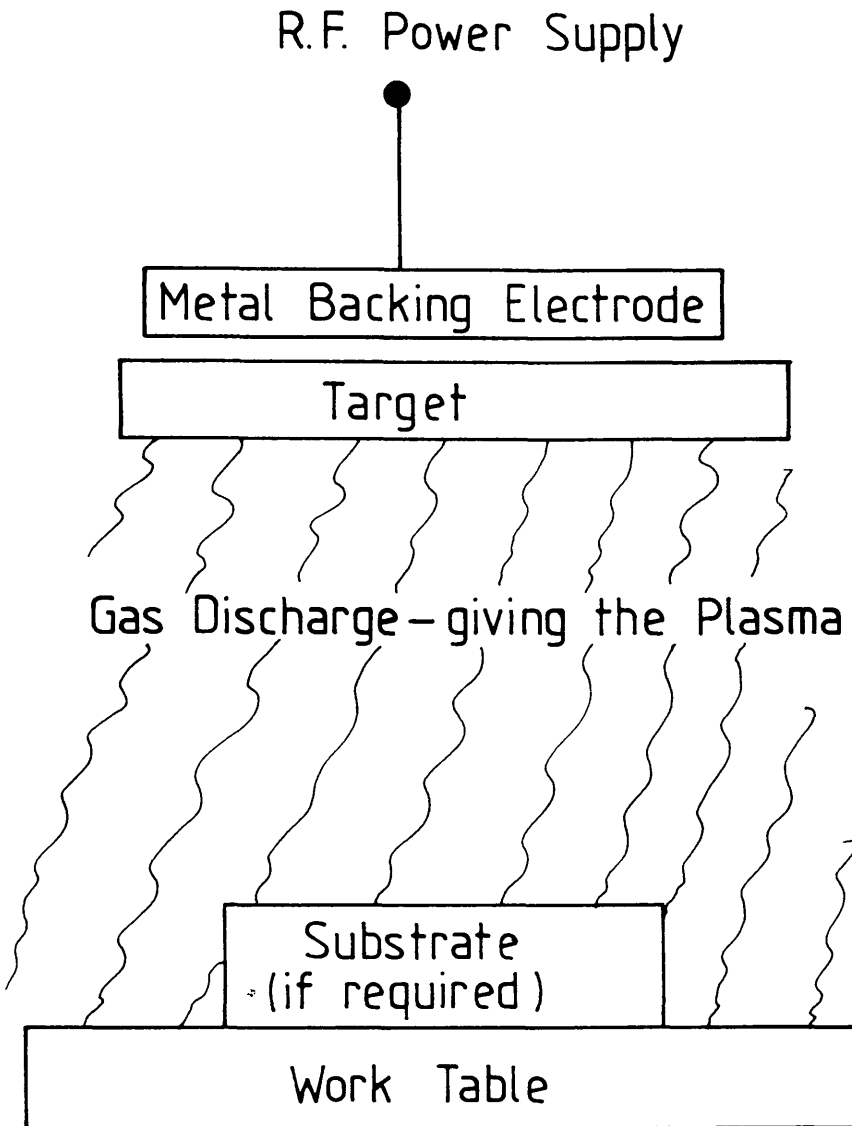


Figure 3.7 - The removal of the bulk aluminium (4% magnesium) substrate.



Material sputtered from the target forms a layer on the substrate

Figure 3.8 - Schematic diagram of the r.f. sputtering electrode arrangement. When removing the rhodium overcoat no substrate was required.

without damaging the magnetic medium the sputter etch was calibrated. Using EDX analysis on the S800 SEM the rhodium X-ray intensity was monitored as a function of sputter etch time. This was accomplished by measuring the ratios of the rhodium X-ray peak with the other elemental peaks present in the spectrum as the rhodium was etched from an original thickness of 75nm down to approximately 7nm. Figure 3.9 graphs the calibration of the rhodium sputter etch in December 1987 as an example. It is seen that the etch appears linear with time, although there may be some non-linear behaviour upon initiating the sputter that was not resolved in this plot.

(3) NiP Etch

To complete the preparation of the thin film specimen the NiP layer was etched using concentrated nitric acid, figure 3.10. The exact chemical reaction between the acid and the NiP base is variable. Both the acid strength and the exact NiP composition (unknown in this case) effect the reaction, although the products will always be a mixture of phosphoric acid in solution (either H_3PO_4 or H_3PO_3), nickel nitrate in solution ($Ni(NO_3)_2$), and nitrogen dioxide (NO_2).

By floating the specimen upon the nitric acid the exposed NiP can be monitored throughout the etch using a mirror below the glass vessel containing the acid. The appearance of the silver coloured FCC layer in place of the darker NiP indicates the completion of the etch. The complete removal of the NiP layer takes approximately three hours. Prepared thin films of FCC

Rhodium Element Ratio
against Etch Time for Plate Two

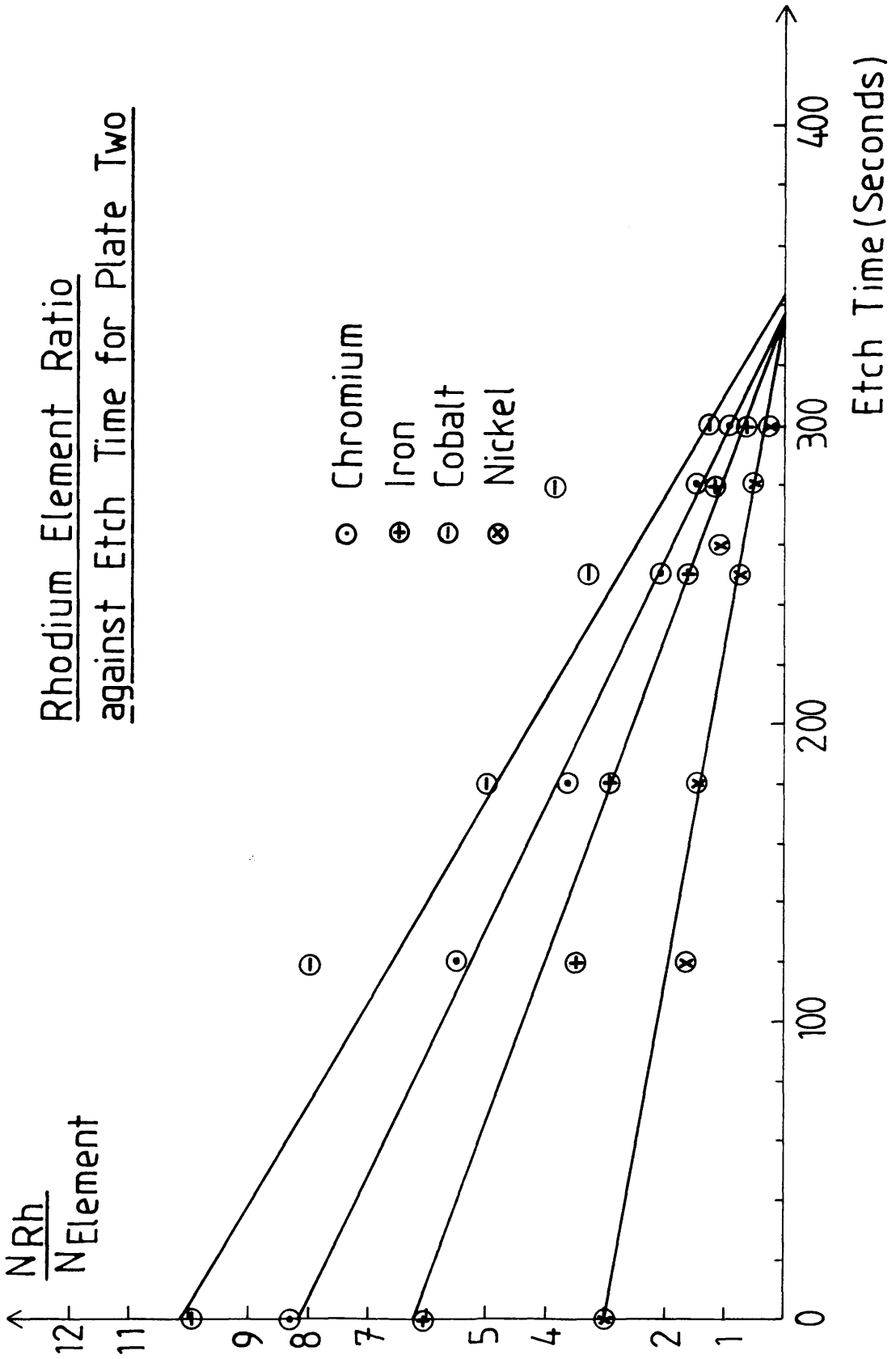


Figure 3.9 - An example of the graphical calibration of the rhodium overcoat sputter etch with time.

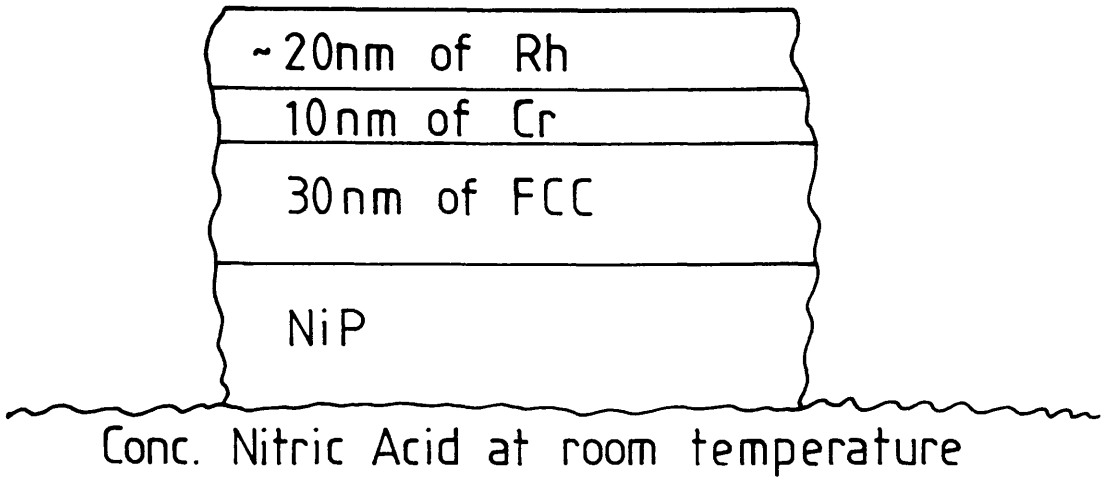


Figure 3.10 - The floatation of the iron cobalt chromium specimen on nitric acid to completely etch the NiP layer.

(<60nm thick) were collected using a non-reactive gold specimen grid. Re-floatation on a solution of sodium hydroxide first neutralised any remanent acid before a final floatation on distilled water washes the specimen.

3.2.4 RESULTS OF THE THIN FILM PREPARATION

Throughout the preparation process the presence of tracks was monitored using ferrofluid decoration. By this means tracks were imaged after both the aluminium substrate was removed and the rhodium overcoat reduced to $\approx 7\text{nm}$. An example of such an image is shown in figure 3.11.

Upon completion of the nickel phosphorus etch with nitric acid the only method with which the medium micromagnetisation could be observed was Lorentz electron microscopy. Figures 3.12 and 3.13 illustrate Fresnel images of a.c. erased and track medium for thin film specimen with $\approx 7\text{nm}$ and $\approx 20\text{nm}$ rhodium overcoats respectively.

From these images the characteristic needle-like domain structure of a.c. erase and the regular bit pattern of the written tracks can be observed for both rhodium overcoats. Images of the medium micromagnetics from the specimen with $\approx 7\text{nm}$ of rhodium however are also seen to contain large single domain regions where a.c. or track structure was expected. Further experimentation showed that these domains appeared in all specimen with

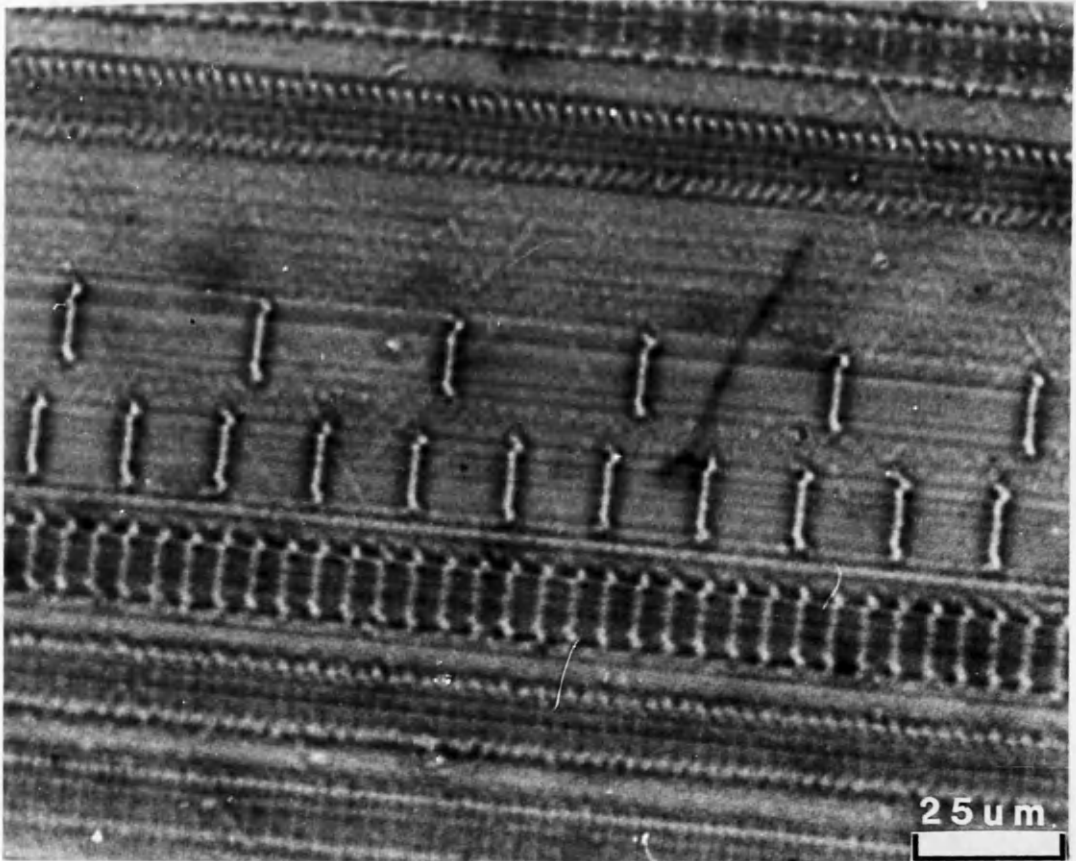


Figure 3.11 - A ferrofluid image of written tracks from the iron cobalt chromium medium after the aluminium has been removed and the rhodium overcoat thickness reduced. Tracks of different write frequency can be observed.

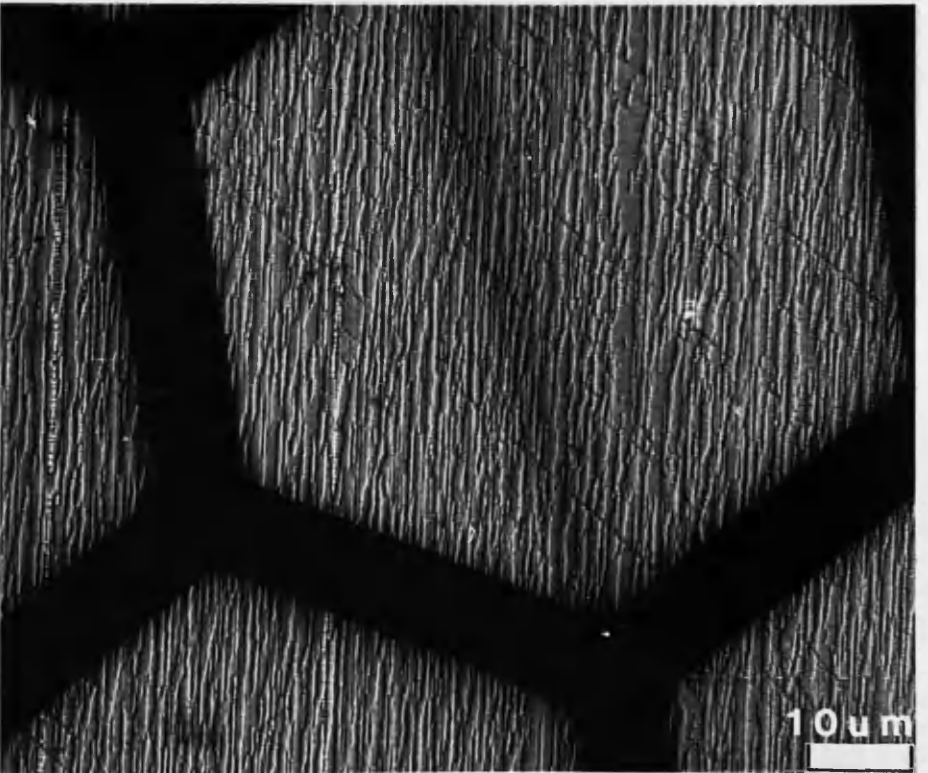
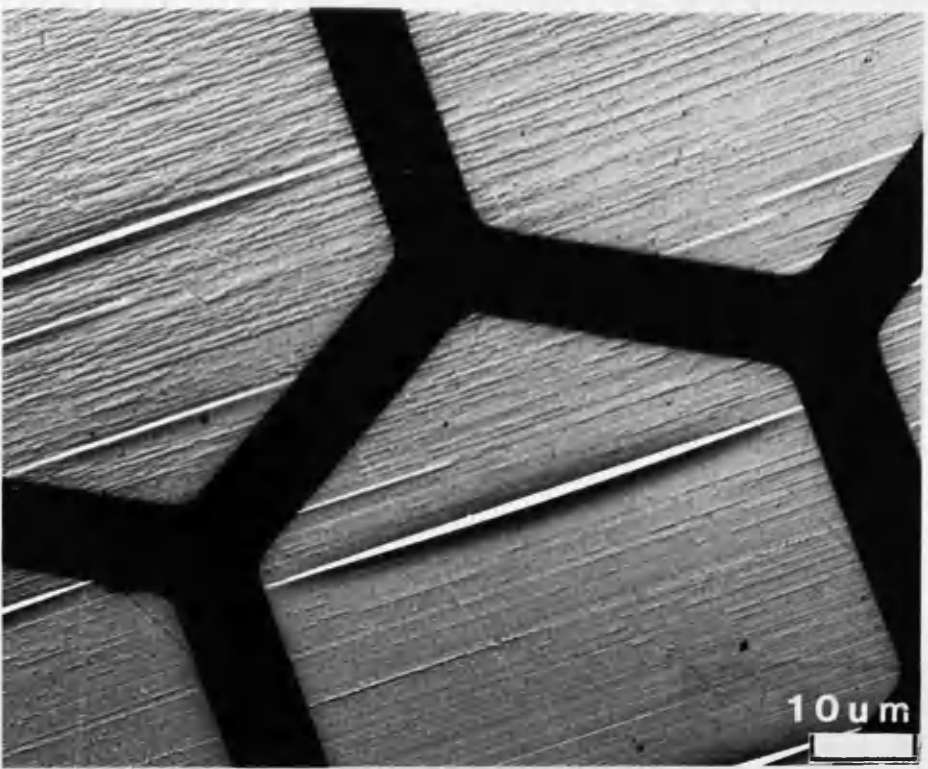


Figure 3.12 - Fresnel images of the micromagnetic domain structures from two specimens of a.c. erased medium with rhodium overcoats of 7nm and 20nm respectively. The domain contrast is seen to 'fade' in the 7nm specimen.

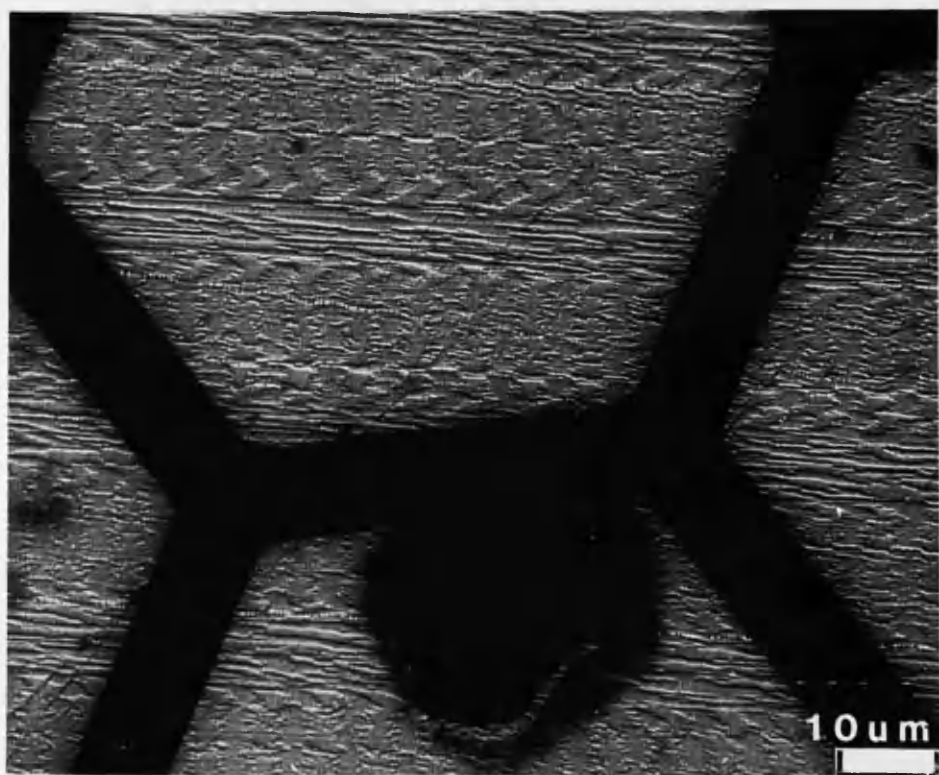
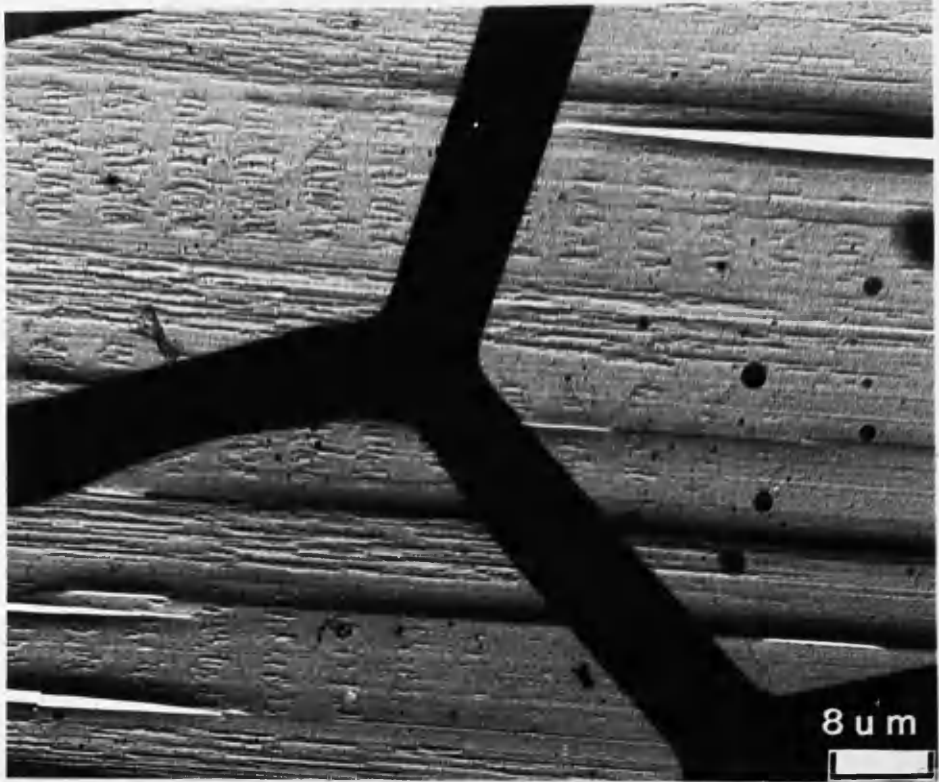


Figure 3.13 - Fresnel images of the micromagnetic domain structures from two specimens containing square-wave written tracks with rhodium overcoats of 7nm and 20nm respectively. The track domain structure is seen to 'fade' in the 7nm specimen.

less than approximately 20nm of rhodium and that their extent increased as the rhodium layer decreased.

In order to investigate if this effect was due to a variation of the magnetic medium composition through a possible reaction at the lower rhodium levels an EDX analysis of the thin film specimen with an overcoat thickness of $\approx 7\text{nm}$ was performed on the JEOL 100C conventional transmission electron microscope. Fresnel imaging allowed the selection of areas of a.c. erased and single domain contrast. Using a focused electron beam (diameter $\approx 0.5\mu\text{m}$) the elemental concentrations in both a.c. erased (AC) and single domain (SD) regions were measured. For each region five spectra were taken from within an area approximately $400\mu\text{m}^2$, giving local average values for the elemental peak ratios for the iron, cobalt, and chromium with the rhodium. This was repeated for six independent AC and SD regions of different specimen to interpret the more global behaviour.

The elemental X-ray intensities were corrected for background radiation using the AN10 acquisition software. Here an interpolated background was calculated and subtracted from elemental X-ray peaks, the intensities either side of the peak determining the background level. For each individual area analysed an estimate of any elemental ratio was given by the average of the five local measurements

$$m = \frac{\sum_{i=1}^5 r_i}{5} \quad (3.2)$$

The uncertainty associated with this value is given by

* A 5% to 10% change in these values may arise if the individual elemental partition functions, the fluorescence yields, and the K ionisation energies are accounted for when calculating the elemental ratios. This should not however change the overall result.

the best estimate of the standard error

$$\delta m = \frac{[\overline{(r_1^2)} - (\overline{r_1})^2]^{1/2}}{2} \quad (3.3)$$

A global comparison of the elemental concentration ratios for a.c. erased and single domain regions was obtained similarly by averaging the respective local regional means m_j

$$M = \frac{\sum_{j=1}^6 m_j}{6} \quad (3.4)$$

Correspondingly

$$\delta M = \frac{[\overline{(m_j^2)} - (\overline{m_j})^2]^{1/2}}{5^{1/2}} \quad (3.5)$$

Table (1) contains the values of M measured for both regions.*

Firstly it was noted that not only are each of the chromium, iron, and cobalt elemental ratios greater for the a.c. erased regions but they are so by the same amount - approximately 20% larger than the single domain areas. The uniformity of this variation indicates that none of the elements are being attacked preferentially during the etch. A second corroborative observation was the percentage composition measured spectrally for both regions:

AC Cr:Fe:Co \cong 41% \pm 3% : 29% \pm 2% : 30% \pm 2%

SD Cr:Fe:Co \cong 41% \pm 4% : 29% \pm 4% : 30% \pm 3%

For comparison with the original FCC film composition with a weight percentage of 15% : 42.5% : 42.5% in the 30nm thick magnetic medium, the 10nm chromium overcoat must be taken into account. A coarse estimate of the total elemental composition was then obtained from the

Ratio Contrast	Rh/Cr	Rh/Fe	Rh/Co
A.C.	0.42 ±0.03	0.61 ±0.04	0.57 ±0.04
S.D.	0.35 ±0.03	0.49 ±0.06	0.48 ±0.04

Table (1) - EDX measured elemental ratios for the a.c. erased (A.C.) and 'faded' or single domain (S.D.) regions of prepared specimen.

composite layer thicknesses, that is

10nm of chromium + 15% of 30nm of FCC = 14.5nm of Cr

42.5% of 30nm of FCC = 12.7nm of Fe and Co

This gave a composition estimate of

Cr:Fe:Co \approx 36% :32% :32%

which was seen to be in reasonable agreement with that measured spectrally for both a.c. and single domain regions. This implies, as expected, that the integrity of the film composition was largely maintained throughout preparation, hence detracting further from the idea of a chemical reaction between the film and the nitric acid being responsible for the onset of the single domains at low rhodium layer thicknesses.

The uniformity of the elemental ratio reduction between a.c. erased and single domain regions not only lessened the possibility of the single domains arising from a chemical reaction but suggested that in fact the rhodium layer was reduced in thickness in the locality of single domains. At lower rhodium overcoat levels the stability of the magnetic medium may become more sensitive to small rhodium thickness variations. The medium micromagnetisation would then become vulnerable to associated local stress variations through a magnetostrictive interaction, and indeed evidence of the film being stressed can be observed from figures 3.12 and 3.13 where tears in the film are seen running along the easy axis direction. The evidence therefore appeared to be in favour of a de-magnetising effect associated with local variations in the rhodium thickness at low overcoat levels (<20nm) being the

cause of the formation of single domains.

3.2.5 SUMMARY OF THE IRON COBALT CHROMIUM SPECIMEN PREPARATION

A thin film preparation technique has been developed that yields specimens in which the integrity of the magnetic recording medium remains intact throughout the process. All the tracks written to the hard disk have been imaged in the final specimen, which are approximately 60nm thick inclusive of a 20nm rhodium overcoat. This amount of rhodium was seen to be necessary to prevent medium de-magnetisation, most probably through a magnetostrictive effect attainable with low (<20nm) rhodium protection.

3.3 COBALT NICKEL CHROMIUM (CONICR)

3.3.1 HARD DISK FABRICATION

An experimental or prototype disk design was used to facilitate the preparation of thin film specimen of cobalt nickel chromium recording medium, figure 3.14 illustrates the disk cross-section. A five inch diameter disk of silicon, 0.027 inches thick, was employed as the bulk substrate onto which a 20nm thick silicon nitrate (Si_3N_4) layer was r.f. reactive

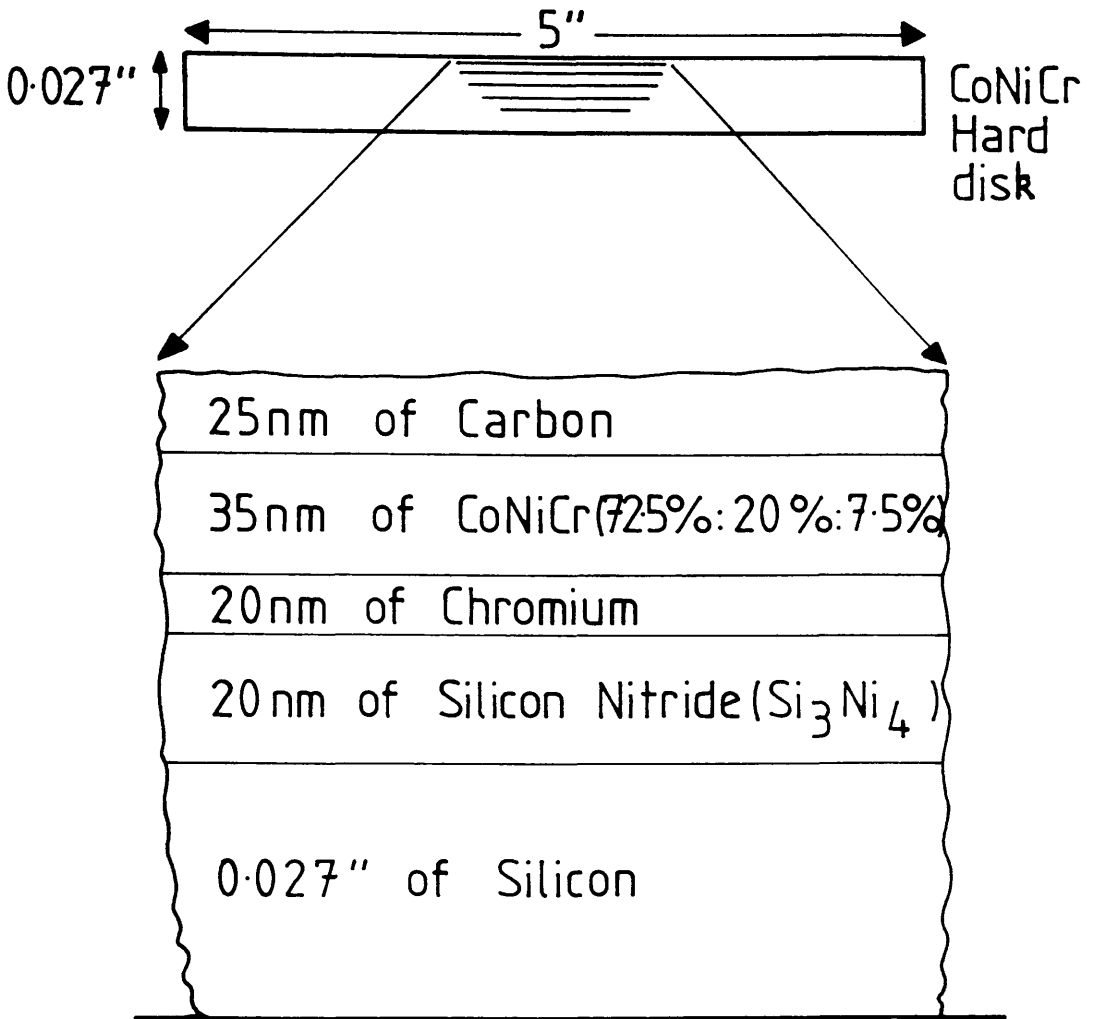


Figure 3.14 - Cross-section of the cobalt nickel chromium hard disk.

sputtered. This overcoat does not influence the magnetic properties of the recording medium, but provides a chemical barrier during the reactive processes involved in subsequent specimen preparation. Consecutive layers of chromium (20nm), CoNiCr (35nm), and carbon (25nm) were deposited by d.c. magnetron sputtering to complete the disk fabrication, the last overcoat of carbon providing wear protection. The chromium layer undercoats the magnetic medium in a manner that encourages isotropic magnetic behaviour in the CoNiCr recording layer. Chromium exhibits a characteristic columnar growth when deposited. This restricts the CoNiCr to grow only on the plateaus of these columns, reducing any inherent shape anisotropy and more importantly introducing micro-gaps between neighbouring grains, the result of which is the reduction of inter-granular exchange coupling [4]. The overall effect produced an isotropic magnetic recording layer.

Figure 3.15 graphs the hysteresis loop measurement for this disk. The ratio of the remanent magnetisations in the circumferential and radial directions was essentially 1:1, contrasting greatly with the corresponding ratio of 10:1 for the highly anisotropic iron cobalt chromium medium. VSM measurements estimated the product between the remanent magnetisation and the film thickness as $M_R b = 0.9235 \times 10^{-3}$ emu/cm² with a coercivity $H_c \approx 469$ Oe.

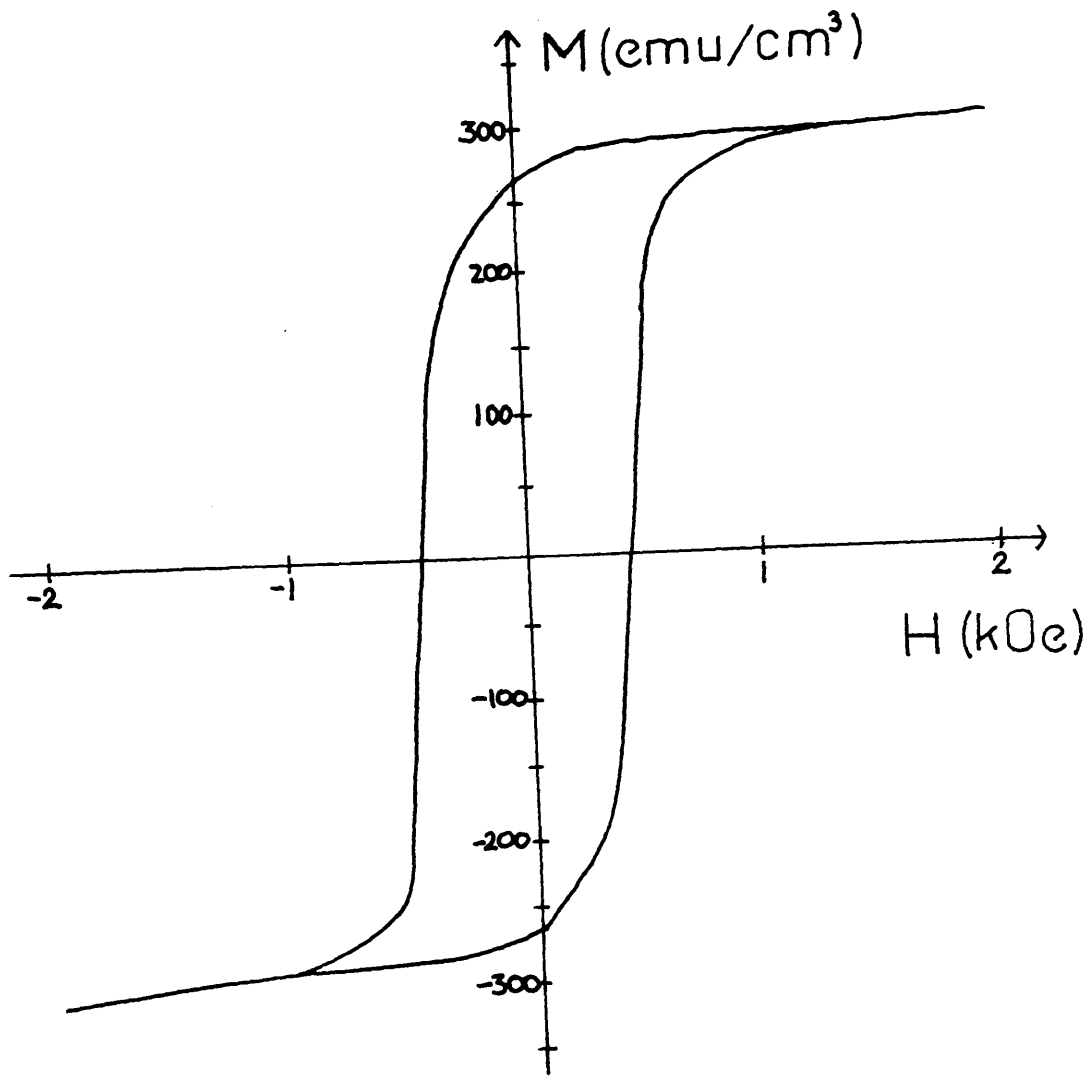


Figure 3.15 - The hysteresis loop measurement from the isotropic cobalt nickel chromium hard disk.

3.3.2 CONICR WRITE EXPERIMENTS

The original state of the disk magnetisation within the recording layer upon deposition is known as the virgin state. A non-contact Evergreen 3380 head was used to d.c. erase a radial band $\approx 2000\mu\text{m}$ wide, the intention being to write tracks in this area. Unfortunately the head was mis-placed before track recording began, giving rise to only the first eight tracks being recorded on d.c. erased medium - the remainder recorded directly onto the virgin disk.

A head-disk speed of 20ms^{-1} was chosen for recording, the head writing tracks approximately $15\mu\text{m}$ wide. A basic group of tracks was chosen to examine aspects of medium non-saturation recording, high frequency recording, and over-writing. As with the FCC disk the saturation tracks were all written at constant frequency (2MHz or $\lambda=10\mu\text{m}$) but with different write currents - namely a saturation value of 65mA followed by tracks written with currents of 20mA, 15mA, 14mA, 12mA, and 10mA. The frequency dependence of the track micromagnetisation was examined by writing constant write current (65mA) tracks at frequencies between 1MHz ($\lambda=20\mu\text{m}$) and 12 MHz ($\lambda=1.67\mu\text{m}$). Over-write tracks were written in the same manner as the iron cobalt chromium experiments. The frequency pairs were 1.5MHz/4MHz and 3MHz/8MHz respectively.

3.3.3 PREPARATION OF THIN FILM CONICR SPECIMEN

A cross-section of the disk structure was illustrated in figure 3.14. It can be seen that upon removing the silicon the resultant thin film would be 100nm thick, which can be thought of as effectively 75nm in terms of electron transmission since the carbon overcoat is essentially transparent in comparison to the other layers. This effective film thickness was acceptable for transmission electron microscopy; hence removal of the silicon became the specimen preparation.

Two stages were required to eliminate the bulk silicon. Firstly the 0.027 inch substrate was reduced to a nominal 50 μ m by hand-grinding with sand paper; a diamond paste polisher buffed the specimen to a uniform, smooth finish. Pieces of sample approximately 2mm square were then floated on a saturated solution of sodium hydroxide (NaOH) heated to between 65C and 75C. At these temperatures 50 μ m of silicon were etched in around 1.5/2.0 hours, an approximate etch rate of 0.5 μ m per minute. It was at this stage of specimen preparation that the silicon nitride layer was required to act as a barrier between the sodium hydroxide and the required thin film region. If temperatures greater than 75C were used this barrier became ineffective as the specimen were spoiled by the convection action of the warm solution submerging the samples and corrupting the magnetic surface.

Completely etched samples were collected on specimen grids and re-floated on distilled water to wash.

Because of the final specimen thickness ($\approx 100\text{nm}$) folding specimen grids were required to hold the sample securely.

3.3.4 RESULTS

Using the above technique specimens containing written tracks were successfully prepared. Figure 3.16 contains an example of a Fresnel image of track written to the virgin (not d.c. erased) medium.

Analysis by EDX of the specimen composition after the preparation process produced the following elemental ratios

$$\frac{N(\text{Cr})}{N(\text{Co})} = 1.03 \pm 0.02 \quad ; \quad \frac{N(\text{Cr})}{N(\text{Ni})} = 2.70 \pm 0.06$$

which in turn yield a percentage composition of

$$\text{Co:Ni:Cr} \cong 43\% \pm 2\% : 13\% \pm 2\% : 44\% \pm 2\%$$

The original magnetic layer was composed of 35nm of CoNiCr with a weight percentage of 72.5% : 20% : 7.5% and a 20nm chromium underlayer. This gives an approximate elemental composition of

$$\text{Co:Ni:Cr} \cong 46\% : 13\% : 41\%$$

The agreement between the spectrally measured and deposited percentage compositions indicated that the medium remains uncorrupted throughout the preparation. Pieces of debris are seen in figure 3.16. These were common to all the specimen prepared and EDX was again employed to determine their composition in order to establish their origin. Figure 3.17 illustrates two

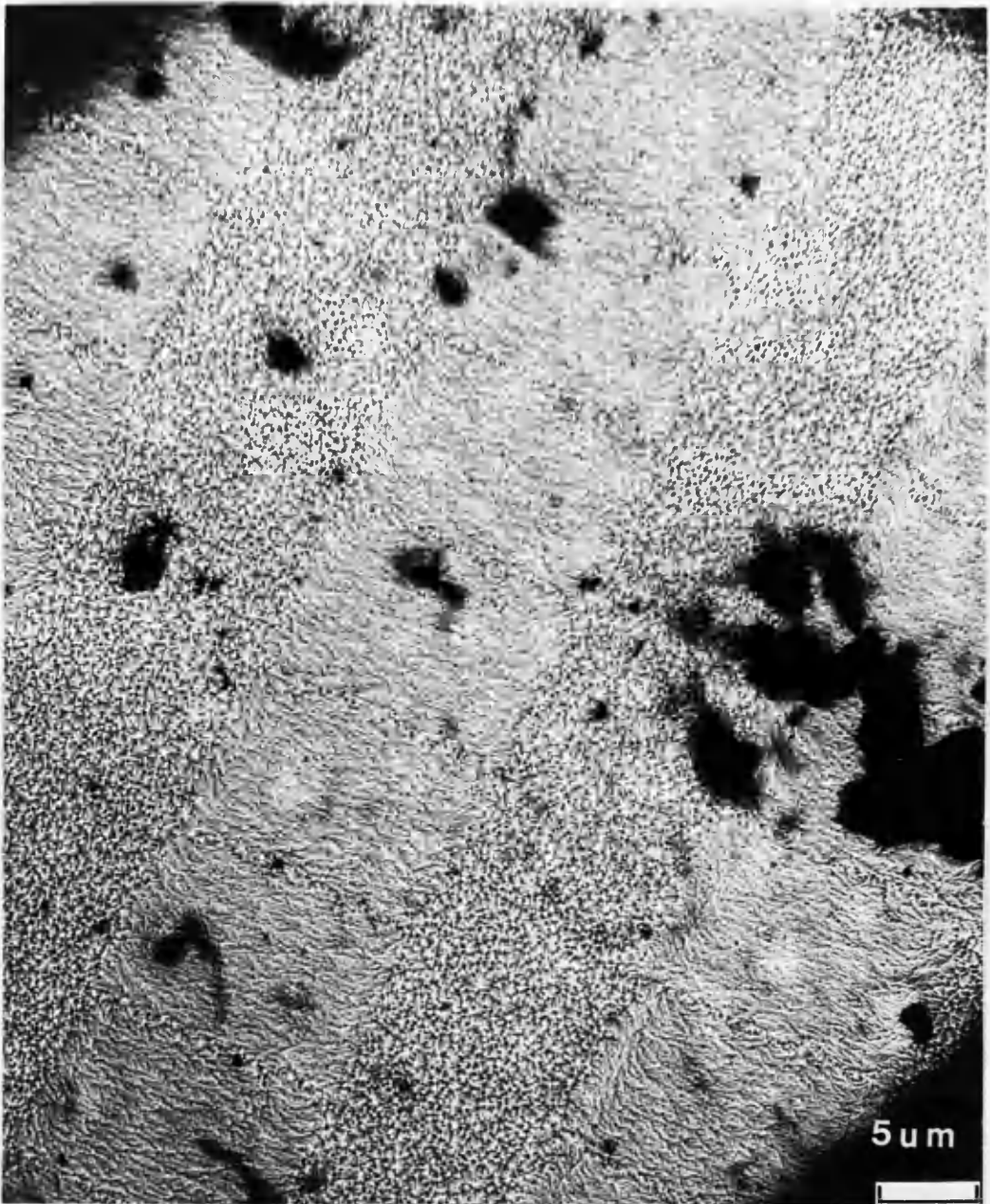


Figure 3.16 - A Fresnel image of the micromagnetic domain structure from square-wave track written to the cobalt nickel chromium medium.

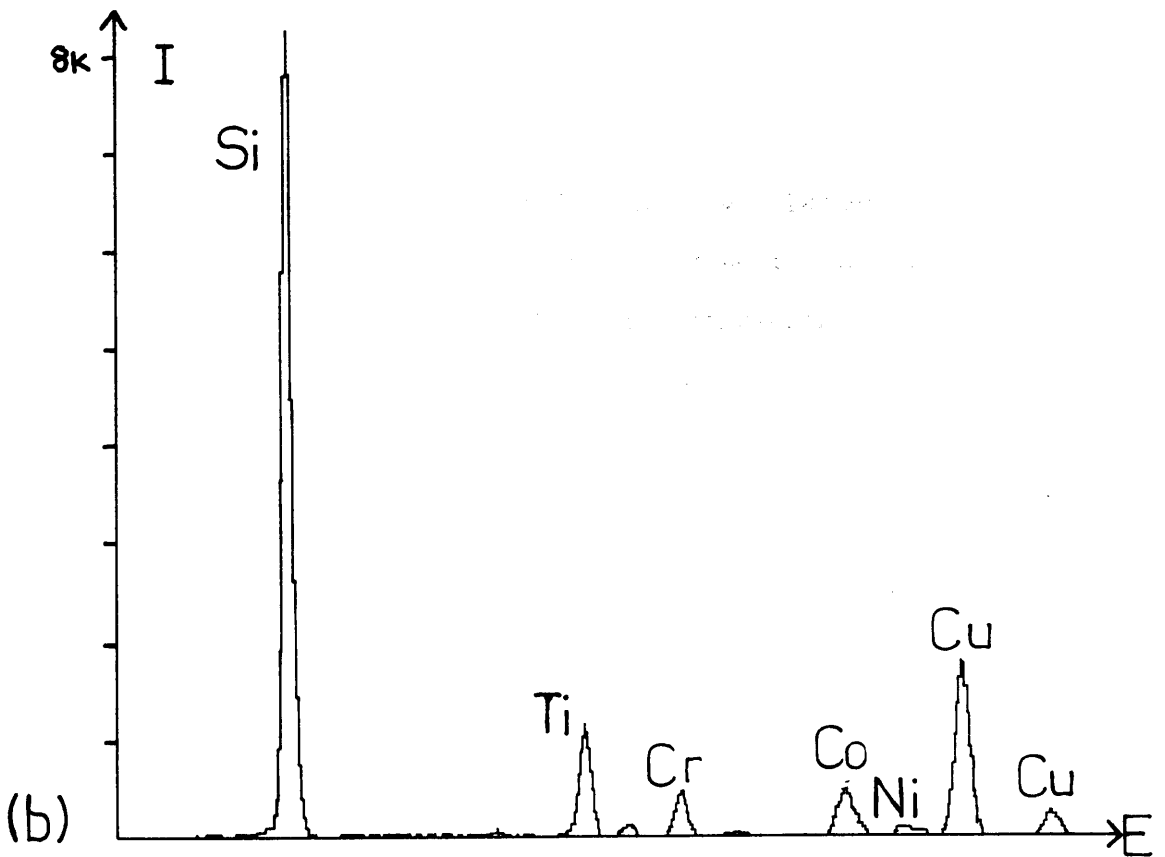
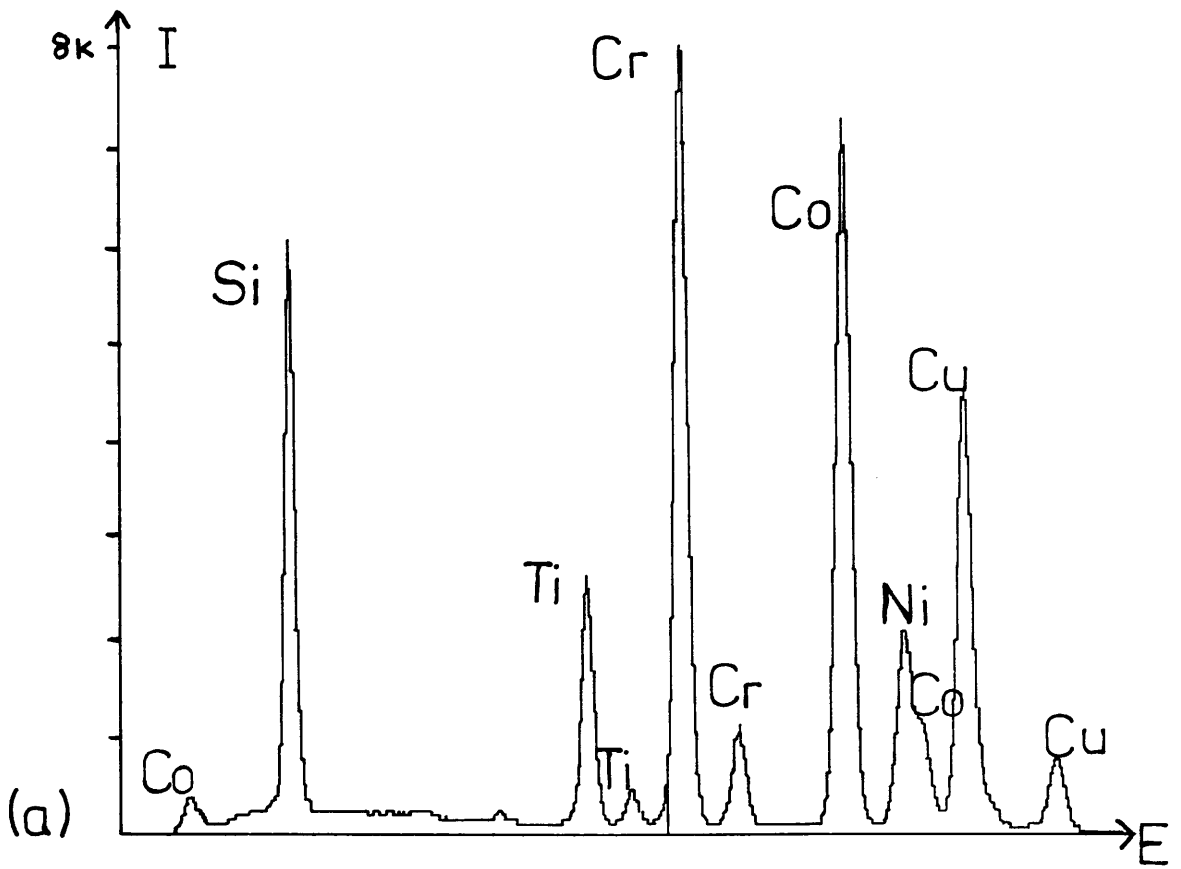


Figure 3.17 - EDX spectra from regions of the prepared cobalt nickel chromium thin film (a) without any preparation debris and (b) with preparation debris.

spectra, one each from regions of the specimen with and without debris. The increase in the silicon peak intensity with respect to the other elemental peaks present for areas with debris suggested that the debris is most likely to be un-reacted substrate silicon.

3.3.5 SUMMARY OF THIN FILM CONICR SPECIMEN PREPARATION

The use of the silicon disk substrate has simplified the preparation process of thin film specimens of cobalt nickel chromium to the removal of the substrate itself. Silicon Nitride proved an effective chemical barrier to the sodium hydroxide during the silicon etch, protecting the integrity of the final prepared film composition.

Silicon debris obscured, to varying degrees, the observation of the micromagnetic structure of the specimen. However, sufficiently large areas of specimen were clear to allow all the tracks written to be imaged by Lorentz electron microscopy.

CHAPTER FOUR

THE PHYSICAL AND MICROMAGNETIC CHARACTERISATION OF IRON COBALT CHROMIUM THIN FILM RECORDING MEDIUM BY ELECTRON MICROSCOPY

4.1 INTRODUCTION

The preparation of thin film samples of the iron cobalt chromium (FCC) recording medium from hard disk was described in the previous chapter. This produced thin film specimens approximately 65nm thick, a cross-section of which is given in figure 4.1. An energy dispersive X-ray analysis (EDX) of the prepared specimens in an electron microscope measured the percentage of chromium, iron and cobalt present as

$$\text{Cr: Fe: Co} - 41\% \pm 4\%: 29\% \pm 4\%: 30\% \pm 3\% \quad (4.1a)$$

which compared well with the elemental proportions deposited upon the original hard disk of

$$\text{Cr: Fe: Co} - 36\%: 32\%: 32\% \quad (4.1b)$$

This indicated that the magnetic layer appeared to be chemically uncorrupted by the preparation process, allowing a characterisation of the thin film specimens by electron microscopy to be representative of the state of the recording medium when part of the hard disk. The results obtained from such a microscopical analysis of the thin films are presented here, discussing both the physical microstructure and the micromagnetisation of the recording medium.

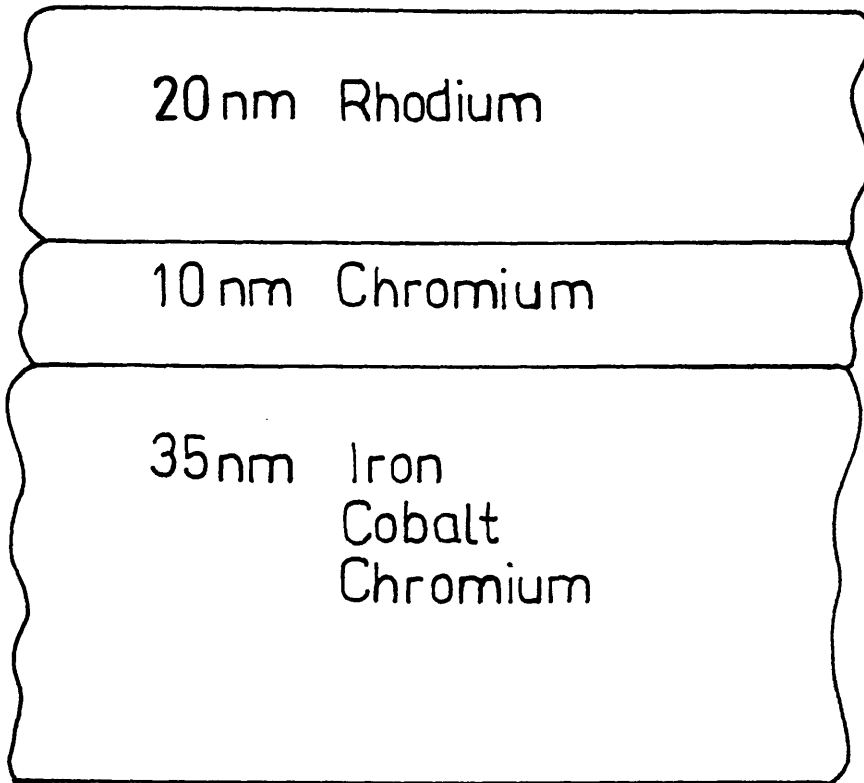


Figure 4.1 - Cross-section of the prepared iron cobalt chromium thin film specimen.

4.2 EXAMINATION OF THE PHYSICAL MICROSTRUCTURE

4.2.1 BRAGG DIFFRACTION STUDIES OF THE CRYSTALLINE STRUCTURE

A polycrystalline foil without texture structure, such as the iron cobalt chromium thin film, comprises a large number of crystallites randomly orientated with respect to the specimen axes. Plane electron waves in the monoenergetic beam of the electron microscope are diffracted by the planes of atoms in these crystals. If electrons of wavelength λ are incident upon a crystallite at a particular angle ϕ , which satisfies the Bragg equation

$$\lambda = 2.d_{hkl} \cdot \sin(\phi_{hkl}) \quad (4.2)$$

within the crystal (where d_{hkl} is the diffracting interplanar spacing for Miller indices (hkl)), some of the electrons will be scattered and will emerge from the crystals having suffered a deflection $2\phi_{hkl}$, see figure 4.2. If effectively all possible orientations of crystallites are present in the foil then the electrons will emerge from the bottom specimen surface along cones of half-angle $2\phi_{hkl}$ for all values ϕ_{hkl} permitted by the Bragg equation, equation (4.2). All emerging rays are brought to focus in the back focal plane of the objective lens on the electron microscope so as to form a series of concentric rings. The radius of any one of these rings is given by

$$r_{hkl} = 2.f.\phi_{hkl} \quad (4.3a)$$

$$= \frac{f.\lambda}{d_{hkl}} \quad (4.3b)$$

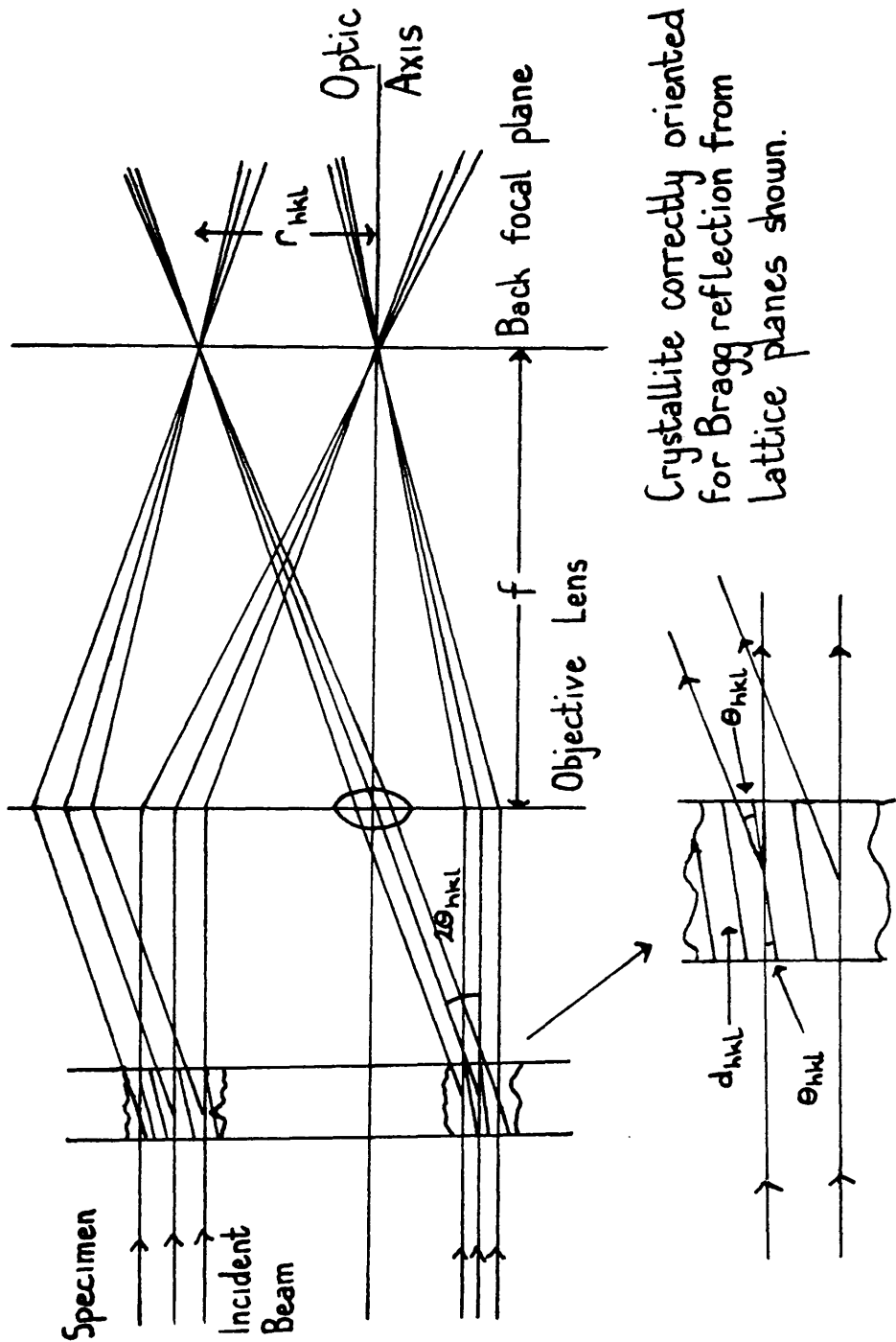


Figure 4.2 - Schematic diagram illustrating the formation of the Bragg diffraction pattern from a polycrystalline specimen.

where f is the focal length of the objective lens, all other symbols as before.

The lens system of the electron microscope projects a magnified image of the electron diffraction pattern onto a viewing screen where the diffraction intensity can be photographically recorded. The radius of any of the photographed rings is given by

$$R_{hkl} = 2.L.\phi_{hkl} \quad (4.4)$$

where L is the microscope camera length recorded for each photograph.

For cubic structures

$$d_{hkl} = \frac{a}{(h^2+k^2+l^2)^{1/2}} \quad (4.5)$$

where a is the crystal lattice parameter and (hkl) the Miller indices (all of which are integer). From equation (4.4)

$$\phi_{hkl} = \frac{R_{hkl}}{2.L} \quad (4.6)$$

which, upon substitution in equation (4.3), yields

$$r_{hkl} = \frac{f.R_{hkl}}{L} \quad (4.7)$$

If the medium is assumed to have a cubic structure, then

$$r_{hkl} = \frac{f.R_{hkl}}{L} = \frac{f.\lambda}{d_{hkl}} = \frac{f.\lambda.(h^2+k^2+l^2)^{1/2}}{a}$$

that is,

$$R_{hkl}^2 = \left(\frac{L.\lambda}{a} \right)^2 . (h^2+k^2+l^2) \quad (4.8)$$

A graph of R_{hkl}^2 against integer N is therefore seen to yield a straight line for cubic structures from which the lattice parameter a can be calculated from the

gradient g by

$$a = \frac{L \cdot \lambda}{g^{1/2}} \quad (4.9)$$

Illustrated in figure 4.3 is the characteristic Bragg diffraction intensity obtained from the thin film specimen of figure 4.1. Measurements of the ring radii squared, R_{hkl}^2 , were made from this and other similar images and plotted against integer N (the sum of the squared Miller indices) in figure 4.4. The values of N chosen for the set of R_{hkl}^2 measurements were selected by assuming a particular cubic structure and graphically trying values of N that obeyed the criteria discussed overleaf on page 55. It was seen that no single straight line could be drawn that passed through all the ring radii at integer values of N ; instead the points were seen to consist of two separate sets of data which could be represented by the two lines illustrated. A linear regression by computer analysis calculated the gradients of these lines as

$$g_1 = 385.3 \pm 1.7 \quad (4.10a)$$

$$g_2 = 176.1 \pm 3.25 \quad (4.10b)$$

For a 120 keV electron beam $\lambda=3.35\text{pm}$, the error on λ assumed negligible. Calibration of the electron microscope camera length using a nickel specimen produced a value of

$$L = 157.5\text{cm} \pm 0.3\text{cm} \quad (4.11)$$

Employment of equation (4.9) then allowed the lattice parameters for the two lines to be estimated as

$$a_1 = 2.70\text{\AA} \quad (4.12a)$$

$$a_2 = 3.975\text{\AA} \quad (4.12b)$$

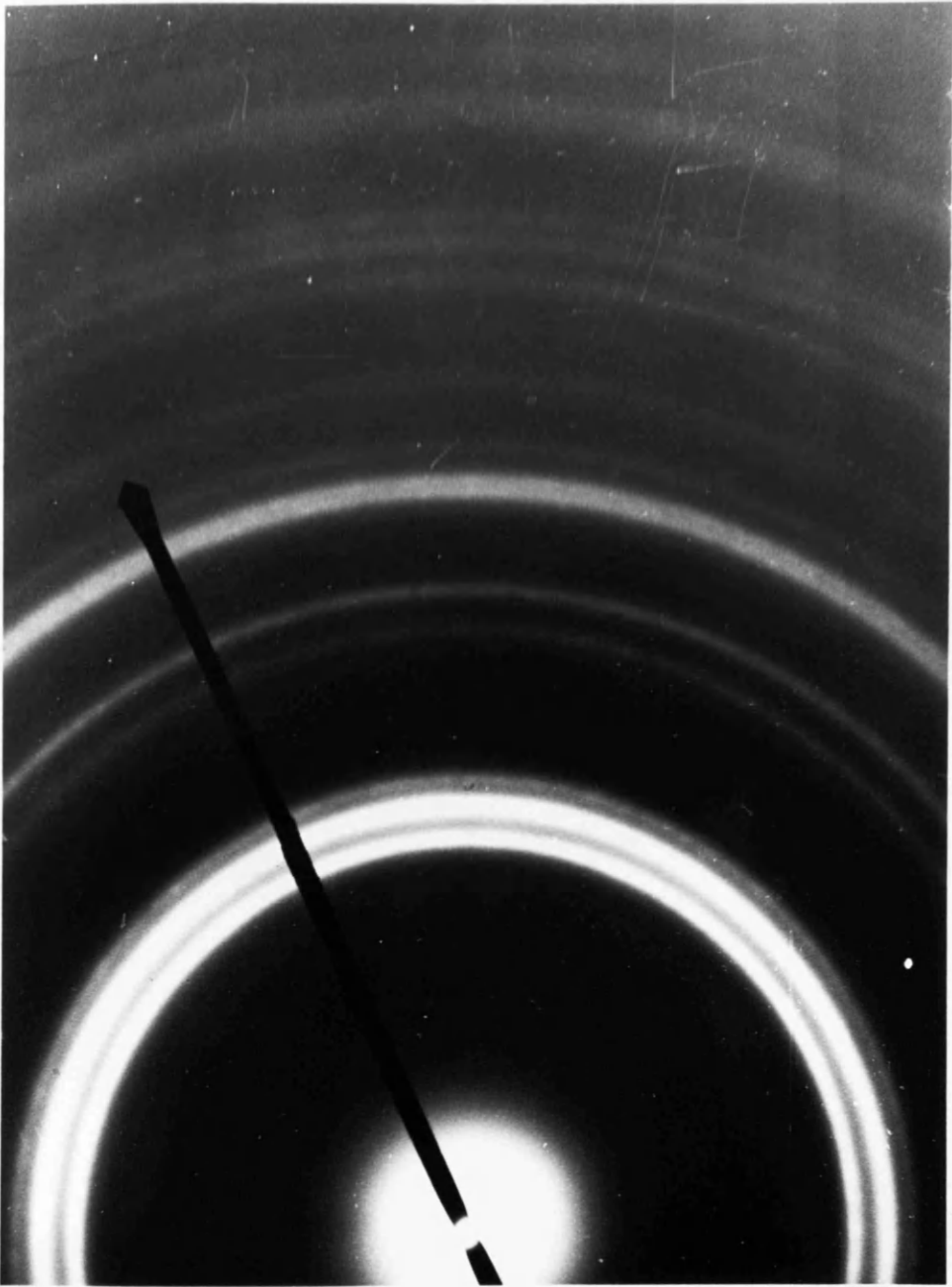


Figure 4.3 - Bragg diffraction pattern obtained from the polycrystalline iron cobalt chromium thin film specimen (camera length $\approx 160\text{cm}$).

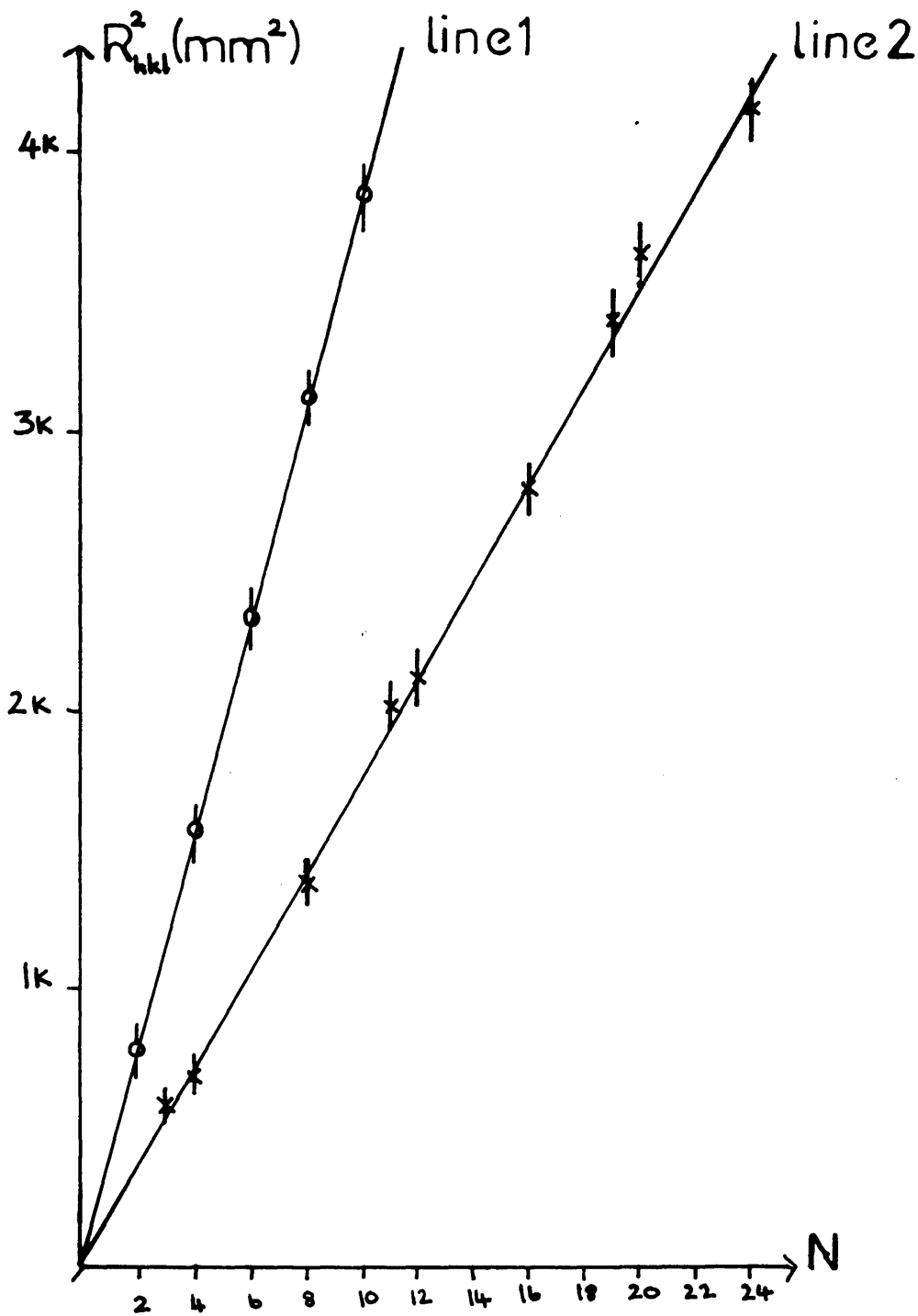


Figure 4.4 - Graph of the ring radius squared (R^2) against the sum of the squared Miller indices (N) for the iron cobalt chromium specimen.

The errors on both of these lattice parameter measurements, $\delta a_{1,2}$, were calculated from

$$\begin{aligned} \frac{\delta a}{a} &= \left(\left[\frac{\delta(g^{1/2})}{g^{1/2}} \right]^2 + \left[\frac{\delta L}{L} \right]^2 \right)^{1/2} \\ &= \left(\left[\frac{\delta g}{2 \cdot g^{1/2}} \right]^2 + \left[\frac{\delta L}{L} \right]^2 \right)^{1/2} \end{aligned} \quad (4.13)$$

Hence,

$$a_1 = 2.70\text{\AA} \pm 0.01\text{\AA} \quad (4.14a)$$

$$a_2 = 3.97\text{\AA} \pm 0.05\text{\AA} \quad (4.14b)$$

As well as providing an estimate of the cubic lattice parameter different types of cubic structures can be identified by the values of the integers of the graph points. The applicable criteria are as follows:

" for simple cubic structures all values of (hkl) are permissible; for face centre cubic (fcc) structures (hkl) must be all even or all odd; and for a body centre cubic (bcc) structure (h+k+l) must be even ".

Analysis of the two lines graphed in figure 4.4 showed they were of different characteristic cubic structures: line one complied with the conditions appropriate to a body centre cubic structure whilst line two was consistent with a face centre cubic structure. In order to identify the origins of these two diffraction intensity distributions consideration was given to the structures and lattice parameters of the elements present in the thin film sample:

chromium	- body centre cubic	- a=2.88\AA
iron	- body centre cubic	- a=2.87\AA
cobalt	- hexagonal close packed	- a=2.51\AA; c=4.07\AA
rhodium	- face centre cubic	- a=3.80\AA

The existence of only one intrinsically face centre

cubic material, rhodium, indicated that line two most probably originated from the remnants of the rhodium wear overcoat; the agreement of the measured lattice parameter with that of rhodium ($3.97\text{\AA}\pm 0.05\text{\AA}$ versus 3.8\AA) was consistent with this observation. Although these two values of the rhodium lattice parameter were in reasonable agreement, the experimentally measured 3.97\AA was surprisingly high considering the small associated uncertainty of 0.05\AA . The most probable explanation lies with the specimen position in the electron microscope. Although the nickel specimen used to calibrate the camera length and the iron cobalt chromium specimen were placed side by side in the same specimen rod and analysed consecutively, any deformation of the thin film specimen with respect to the height of the nickel specimen would produce a difference in the value of the camera length used for these two samples. This can be corrected for by carefully re-setting the eucentric height for the magnetic specimen, but this was not done in this experiment, hence in this case the result was a lattice parameter estimation that was inflated by

$$\frac{(3.97-3.8)}{3.9} \approx 5\% \quad (4.15)$$

Identification of the rhodium diffraction pattern implied that the source of the body centre cubic line was most probably the iron cobalt chromium thin film medium, the chromium layer being very much thinner. This was in agreement with the findings of Alexopoulos and Geiss [1]. An approximation of the lattice

parameter for this medium for comparison with that graphically measured can be obtained from the iron, cobalt, and chromium atomic radii when considered in the body centre cubic lattice of the iron cobalt chromium medium with weight percentage 42.5% (Fe): 42.5% (Co): 15% (Cr). If one considered the unit cell of the body centre cubic lattice to be composed of iron and cobalt atoms then an estimate of the lattice parameter would be given by

$$a(\text{Fe-Co}) \approx r_{\text{Fe}} + r_{\text{Co}} = (1/4)a_{\text{Fe}}[111] + (1/2)a_{\text{Co}}[100] \quad (4.16a)$$

where [111] and [100] represent direction vectors in the body centre cubic and hexagonal close packed lattices respectively. Similarly,

$$a(\text{Cr-Co}) \approx r_{\text{Cr}} + r_{\text{Co}} = (1/4)a_{\text{Cr}}[111] + (1/2)a_{\text{Co}}[100] \quad (4.16b)$$

$$a(\text{Fe-Cr}) \approx r_{\text{Fe}} + r_{\text{Cr}} = (1/4)a_{\text{Fe}}[111] + (1/4)a_{\text{Cr}}[111] \quad (4.16c)$$

$$a(\text{Co-Co}) \approx r_{\text{Co}} + r_{\text{Co}} = (1/2)a_{\text{Co}}[100] + (1/2)a_{\text{Co}}[100] \quad (4.16d)$$

etc

A weight $w(i-j)$ can be assigned to each possible value of $a(i-j)$ using the weight percentages, that is

$$w(i-j) = \% (i) \times \% (j)$$

For example,

$$w(\text{Fe-Cr}) = 0.425 \times 0.15 = 0.06375$$

An estimate of the lattice constant for the iron cobalt chromium medium can then be made from the weighted average of the possible $a(i-j)$:

$$a \approx \sum_{i,j=\text{Fe,Co,Cr}} w(i-j) \times a(i-j) \approx 2.5\text{\AA} \quad (4.17)$$

As was the case for the rhodium the experimentally measured value of $2.7\text{\AA} \pm 0.01\text{\AA}$ for the iron cobalt chromium foil will also be inflated. If the same

percentage discrepancy estimated from the rhodium result is assumed present on this measurement, the 'corrected' body centre cubic lattice parameter for the iron cobalt chromium medium is then $2.56\text{\AA}\pm 0.01\text{\AA}$ and in good agreement with above estimate of $\approx 2.5\text{\AA}$.

4.2.2 OBSERVATION OF THE SPECIMEN GRAIN STRUCTURE

Bright and dark field images of the iron cobalt chromium medium at magnifications of 100K and 150K are given in figure 4.5. The limitations on structural resolution in both types of image prevented an estimation of the grain size of the medium, all that was attainable from these images was the apparent dimension over which the image contrast appeared to change through some physical variation of the film structure: $\approx 15\text{nm}$. The work of Alexopoulos and Geiss [1] produced a grain size estimate from transmission electron microscopy and X-ray studies of between 5nm-10nm which, although smaller, was in reasonable agreement with the dimension estimated from figure 4.5. Clearly visible in the bright field images are the striation contours produced by the hard disk texturing process. Along these regions the grain structure appears less mottled than the intervening areas, but more importantly cracks were observed within these striations that were seen to be generally directed laterally, parallel to the medium easy axis. Arnoldussen et al [2] reported an increase in the ratio

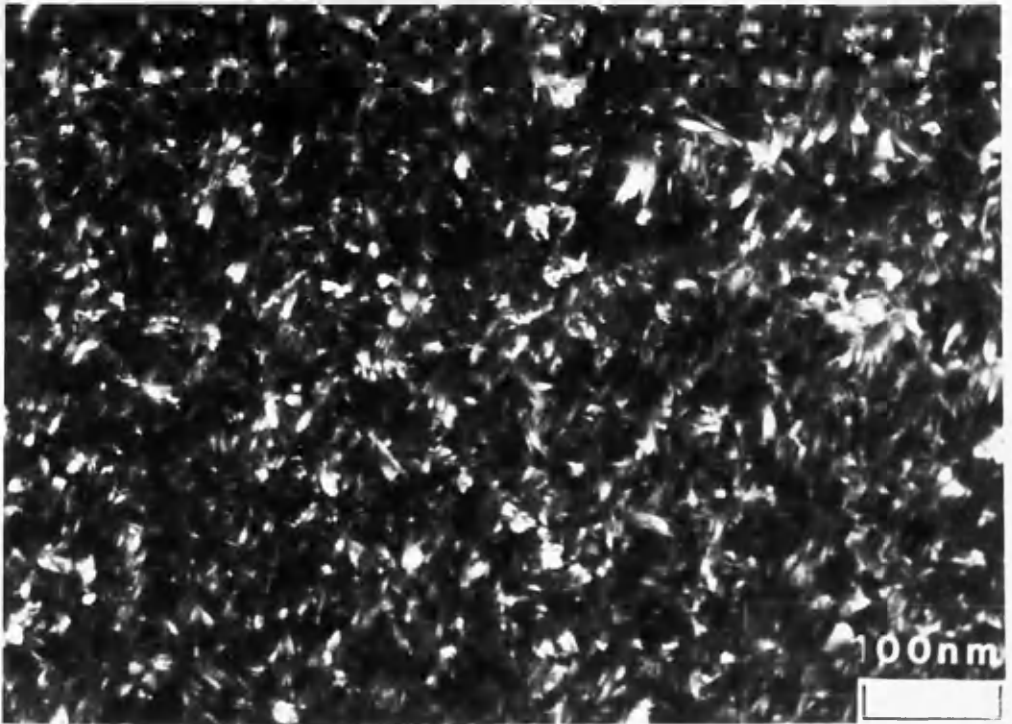
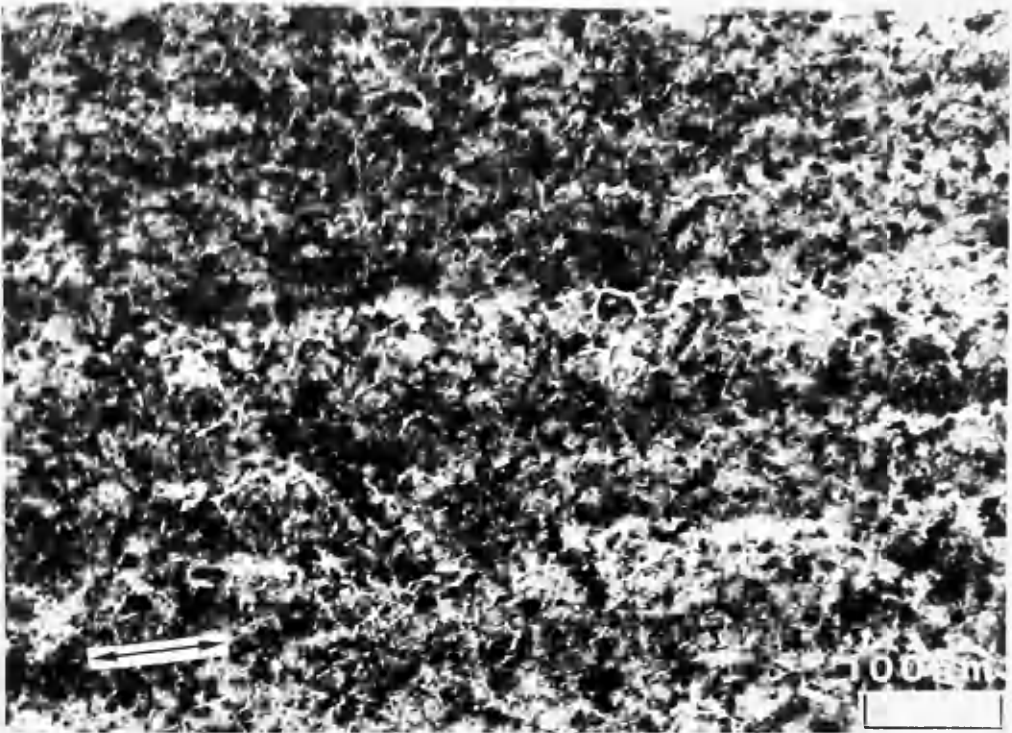
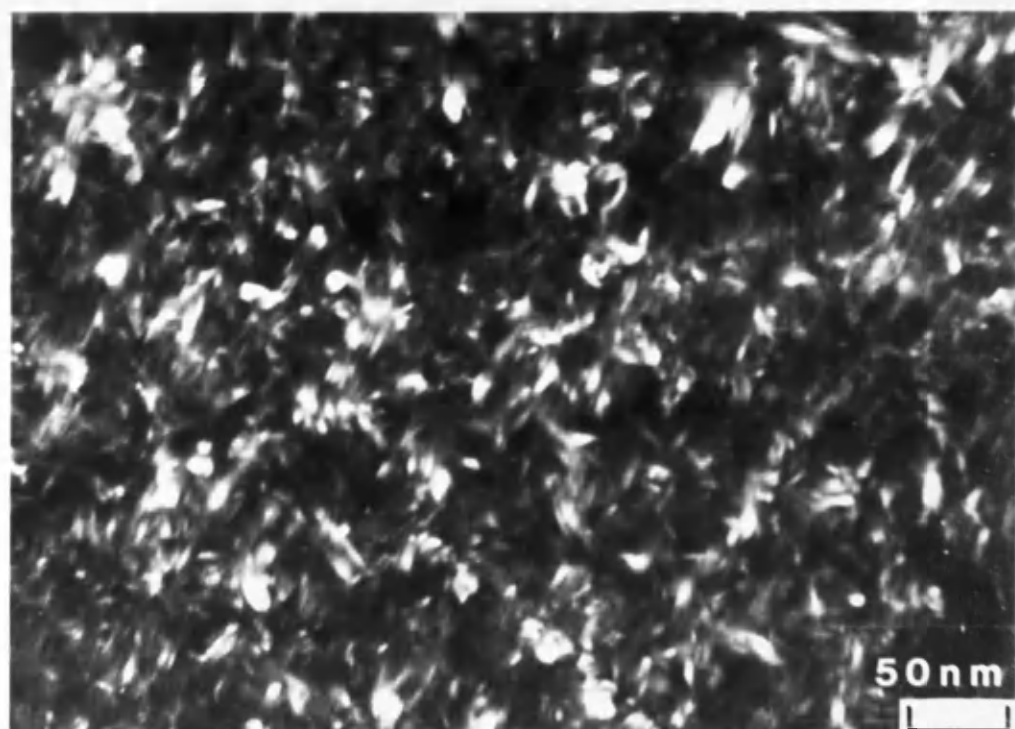


Figure 4.5 - Bright and dark field transmission electron microscope images of the iron cobalt chromium thin film at magnifications of (a) $\times 100K$



(b) $\times 150K$.

of the remanent coercivities in the easy and hard axes as a result of the uniaxial circumferential texturing process for which an explanation may be given based upon the striation structure of figure 4.5. In the striation regions, grain to grain magnetic coupling would favour a circumferential orientation of the crystallite magnetisation (parallel to the easy axis) to attain the optimum energetic configuration since any exchange and/or magnetostatic energy contributions in this direction would not incur the increase in energy across the gaps encountered between grains coupling in the radial direction or hard axis. The striations, therefore, may have the effect of increasing the easy axis coercivity at the expense of that in the hard axis.

4.3 MICROMAGNETIC CHARACTERISATION

The micromagnetic characterisation of the iron cobalt chromium foil presented here entailed examining by Lorentz electron microscopy the micromagnetic domain structures written to the medium under various write conditions. Originally tracks written along the circumferential easy axis of the highly oriented hard disk were investigated to examine the domain structures recorded as the magnitude and frequency of the head write signal varied. This has been discussed previously in papers by Ferrier et al [3], Tong et al [4] and Arnoldussen and Tong [5]. These experiments

were then extended to examine the micromagnetic domain structures of tracks when written at some angle ψ to the easy axis.

4.3.1 TRACKS WRITTEN ALONG THE EASY AXIS

Tracks written along the circumferential easy axis of the original hard disk with increasing frequencies were first studied by ferrofluid decoration, a typical image is illustrated in figure 4.6 in which the written wavelengths range from $4.76\mu\text{m}$ (T5) to $76.4\mu\text{m}$ (T1). In the lower frequency tracks (0.5MHz/T1-3MHz/T3) the transitions appeared to maintain their individuality and integrity. As the separation of neighbouring transitions decreased with higher write frequency (T4/6MHz, T5/8MHz) the transitions appeared to lose their individuality. Fresnel imaging of these recorded tracks allowed this to be examined further. Figure 4.7 illustrates the images. It was noticed first from this figure that the characteristic medium domain wall was saw-tooth or zig-zag in nature. Within domains no magnetic ripple was observed, indicating that there was essentially no variation in magnetisation direction within domains. The domain magnetisation was therefore considered as either parallel or anti-parallel to the easy axis. A decrease in written wavelength can be seen to position the recorded zig-zag magnetisation reversals closer together until, at $\approx 8\text{MHz}/\text{T5}$, the written bits were seen to be composed of 'lozenge'

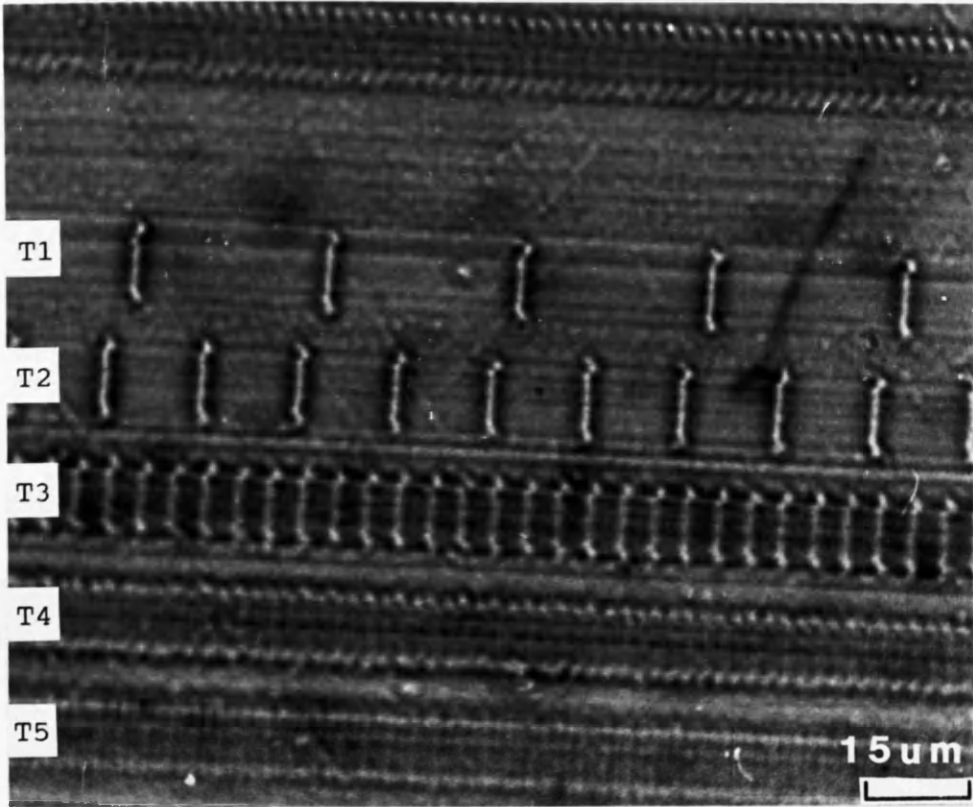


Figure 4.6 - A ferrofluid image depicting tracks of different write frequencies written along the easy axis of the medium.

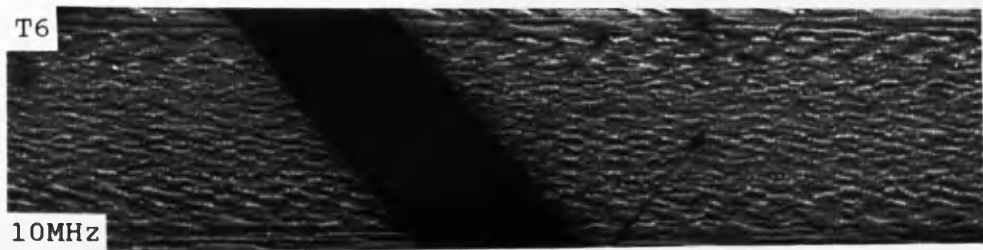
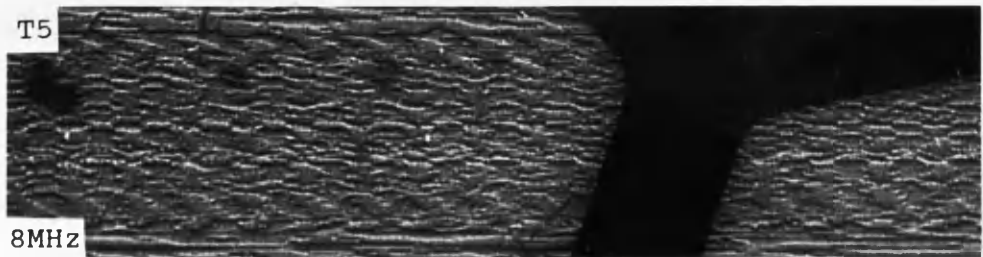
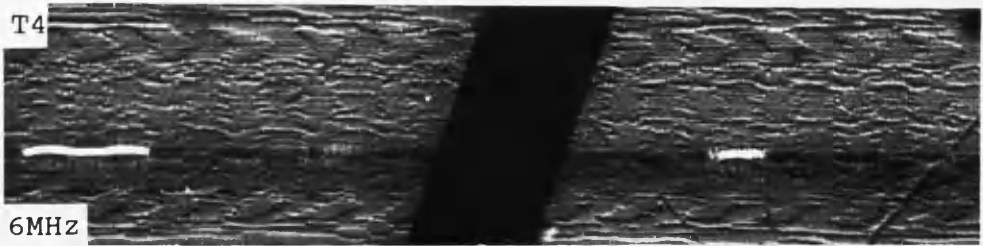


Figure 4.7 - Sections of tracks written at different frequencies along the easy axis.

shaped domains. Since a recorded signal was successfully read back from these tracks it can be deduced that the written bit may contain a minority population of lozenge domains magnetised against the direction in which the head wrote the bit. The function of the lozenge domains is most probably to minimise the micromagnetic energy of the system by reducing the magnetostatic energy produced by the free magnetic poles along the length of a written transition, the proximity of neighbouring magnetisation reversals inducing this lozenge behaviour at these higher frequencies. As can be seen, a result of this more complex lozenge domain structure was a decrease in the clarity of the written magnetisation changes between written bits. This is consistent with the work of Nunnelley [6] who measured an increase in transition noise from track medium with increasing write frequency (illustrated in figure 4.8).

Figure 4.9 describes the ferrofluid images taken from a partially over-written track. Across this track the change from the lower to higher frequency recording signal can be clearly seen, but no further details of the track can be discerned. Fresnel electron microscopy, however, was able to resolve the micromagnetic domain structure from such over-write tracks, an image of the 3MHz/8MHz experiment being given in figure 4.10. Unlike the ferrofluid image the domain structure can be seen across the full track width, showing clearly the lower of the two frequencies (3MHz) being completely over-written by a track

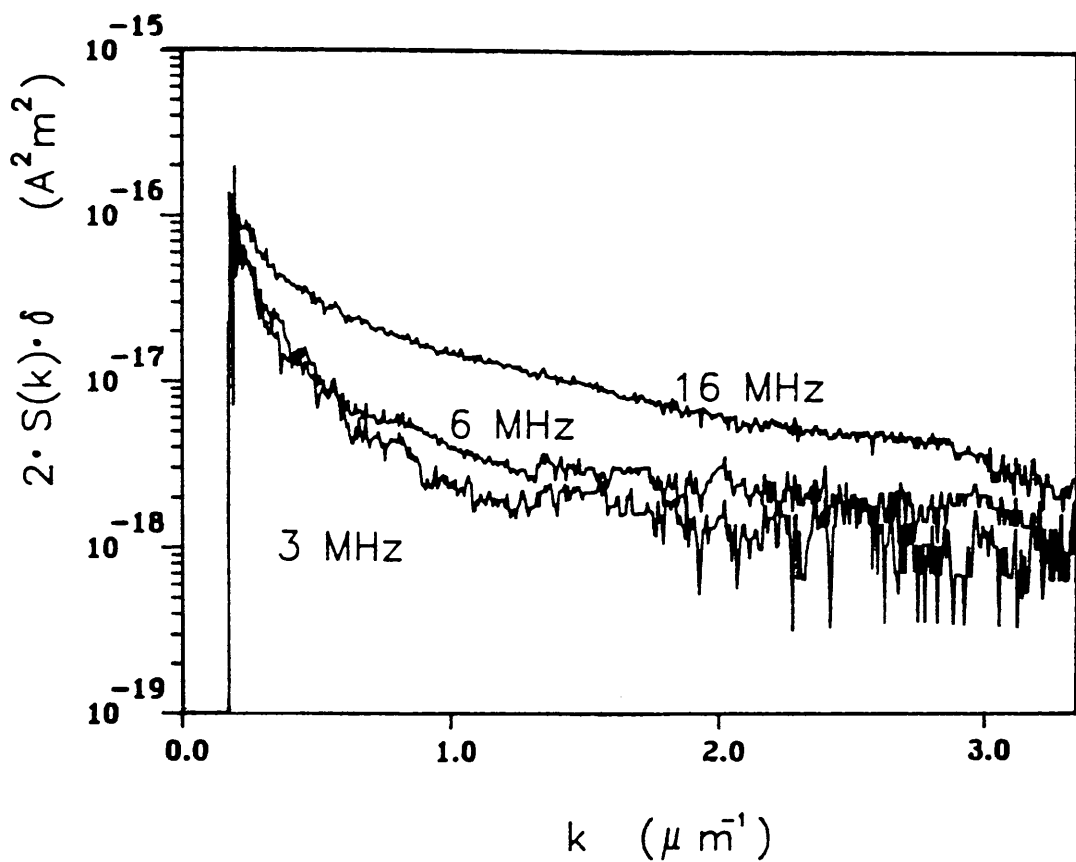


Figure 4.8 - Electronically measured noise spectra for the 3, 6, and 16 MHz square-wave written tracks.

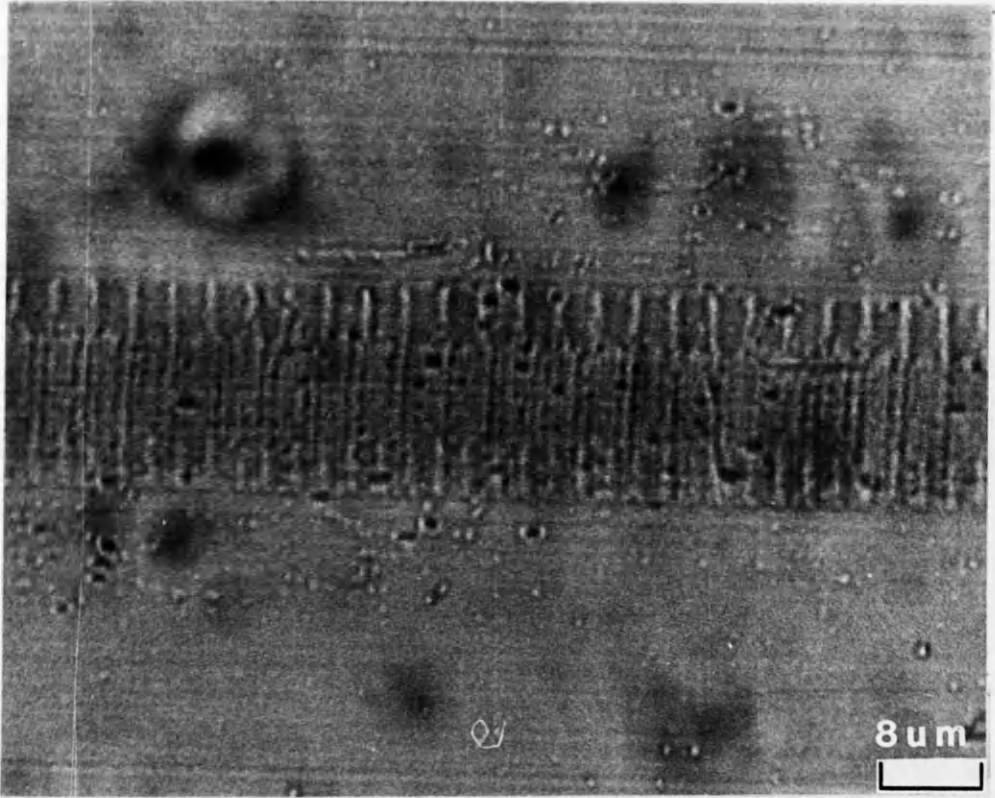


Figure 4.9 - Ferrofluid image of an over-write experiment.

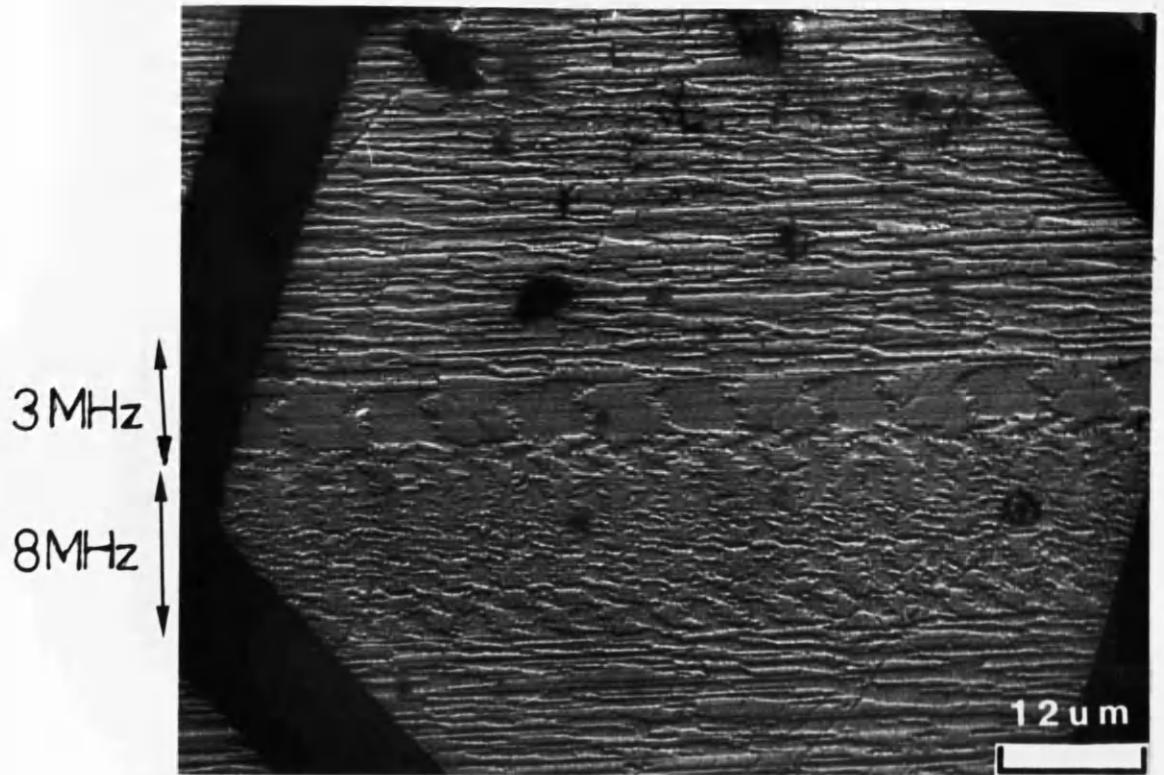


Figure 4.10 - Fresnel image of a 3MHz track over-written by an 8MHz track.

structure that was consistent with images of the 8MHz higher frequency in figure 4.7.

An examination of the five 6MHz tracks ($\lambda=6.35\mu\text{m}$) written with decreasing write current (T10/65mA, T11/20mA, T12/16mA, T13/14mA, T14/12mA) by the ferrofluid technique revealed a marked decrease in the uniformity of the magnetisation within the tracks as the write current was reduced - see figure 4.11. In the case of the weakest recording current (T14) the written track appeared to be composed of considerably less consistent written transitions. To expand upon this ferrofluid decoration these experimental tracks were again observed by Fresnel imaging - see figure 4.12. The change in form of the transition wall and the apparent dissolution of the written bits when recorded by a non-saturation current can be fully identified. Gradually the integrity of the written transitions was seen to be compromised by the decrease in write current from the saturation value of T10. The second most weakly written track, T13, was seen to be composed of domains similar to the lozenge type described above for high frequency tracks; the most weakly written track, T14, was barely distinguishable from the a.c. erased medium upon which it was written. Finally, all the Fresnel images discussed above show at the track edges the characteristic head side-writing micromagnetic domain structures. This effect caused the form of the zig-zag transition to change in character at the track edge, imposing the 'dog-bone' shape upon each bit. It was observed that this

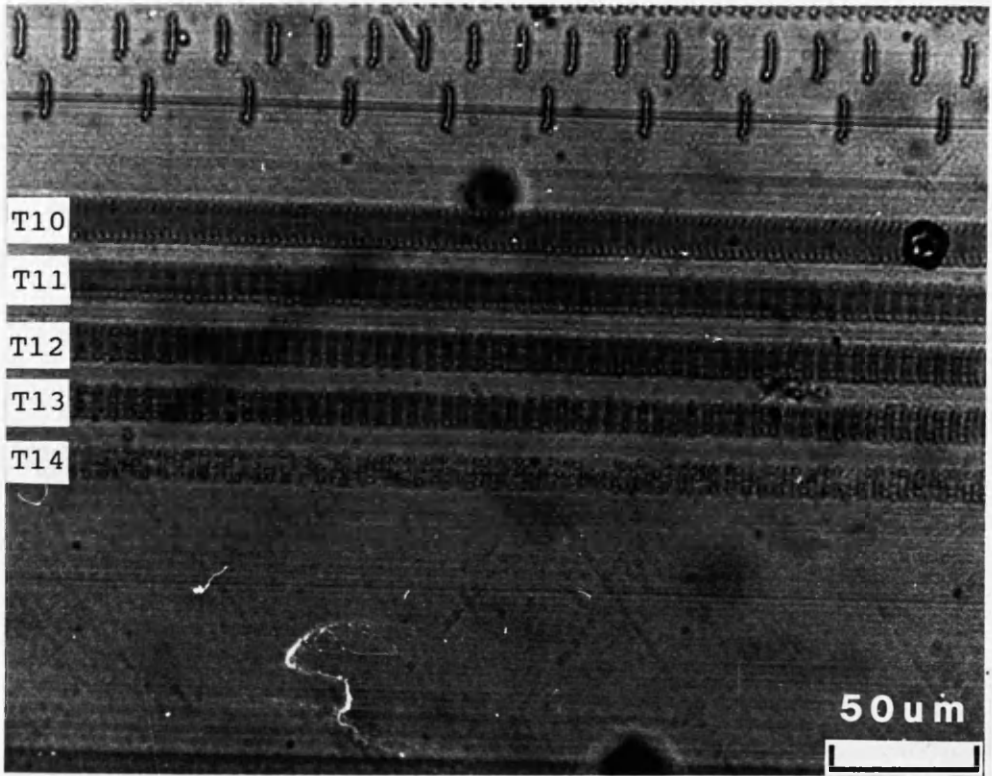


Figure 4.11 - A ferrofluid image of the experimental tracks written along the easy axis of the medium with decreasing write current.

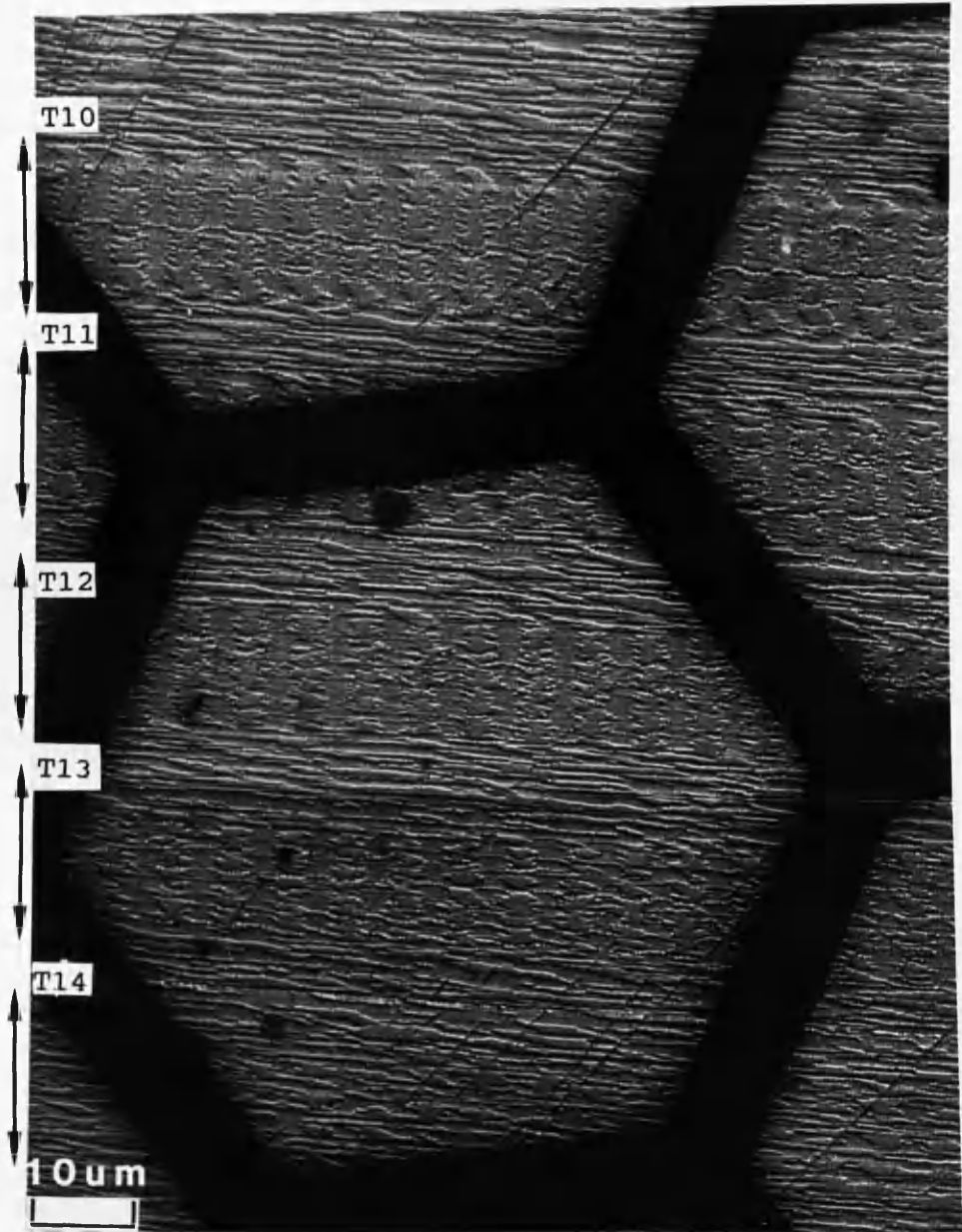


Figure 4.12 - A Fresnel image of the experimental tracks written along the easy axis of the medium with decreasing write current.

phenomenon appeared to:

(i) become more distinct as the write frequency increased, producing highly distorted bits in which the side-written lobes become the most distinguishable feature;

(ii) decrease with write current until absent from the tracks written with write signals $\leq 16\text{mA}$ (T12), indicating that the coupling between the write head and recording medium may be weaker at the edges of the head.

4.3.2 INVESTIGATION OF THE MAGNETIC INDUCTION IN THE LOCALITY OF TRACKS WRITTEN AT AN ANGLE TO THE EASY AXIS

4.3.2.1 FERROFLUID AND FRESNEL IMAGING

Ferrofluid was used to obtain images from the iron cobalt chromium coupons on which tracks were recorded at angles to the easy axis. Tracks with different write frequencies are shown in figures 4.13 and 4.14 from the d.c. and a.c. erased samples respectively. In figure 4.13 the growth or presence of some domain wall structure along the sides of the tracks (parallel to the write direction) was observed for every alternate written bit from tracks written off the easy axis of the d.c. erased coupon. Similar behaviour was observed in the images of figure 4.14, but here the growth of this 'parallel' domain wall was seen on all written bits. Although limited to the optical resolution of

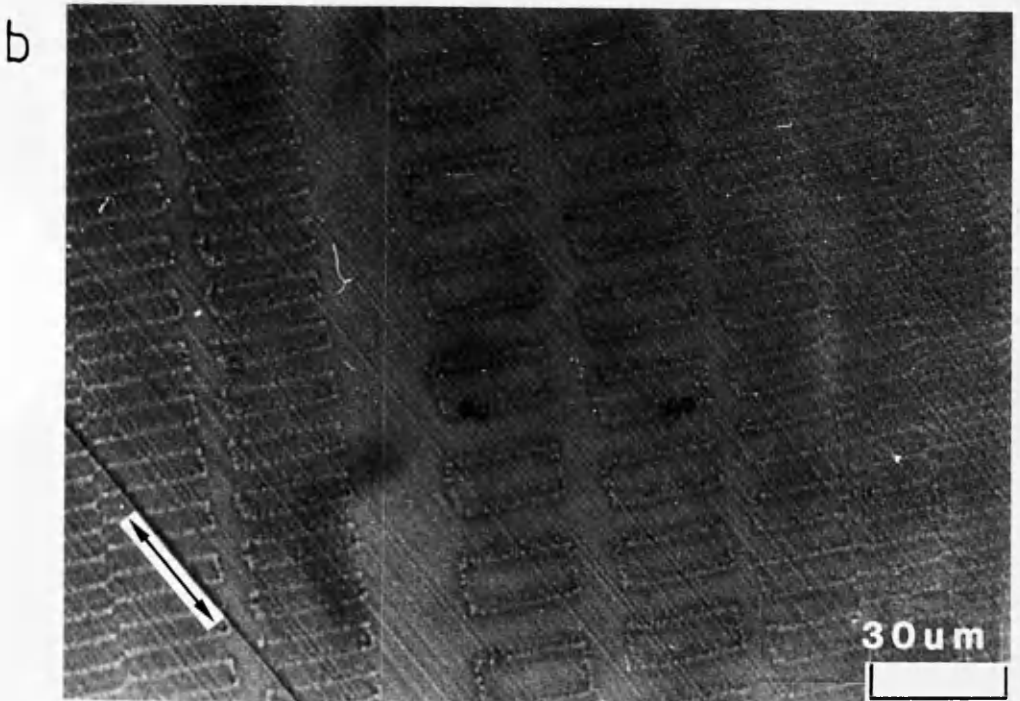
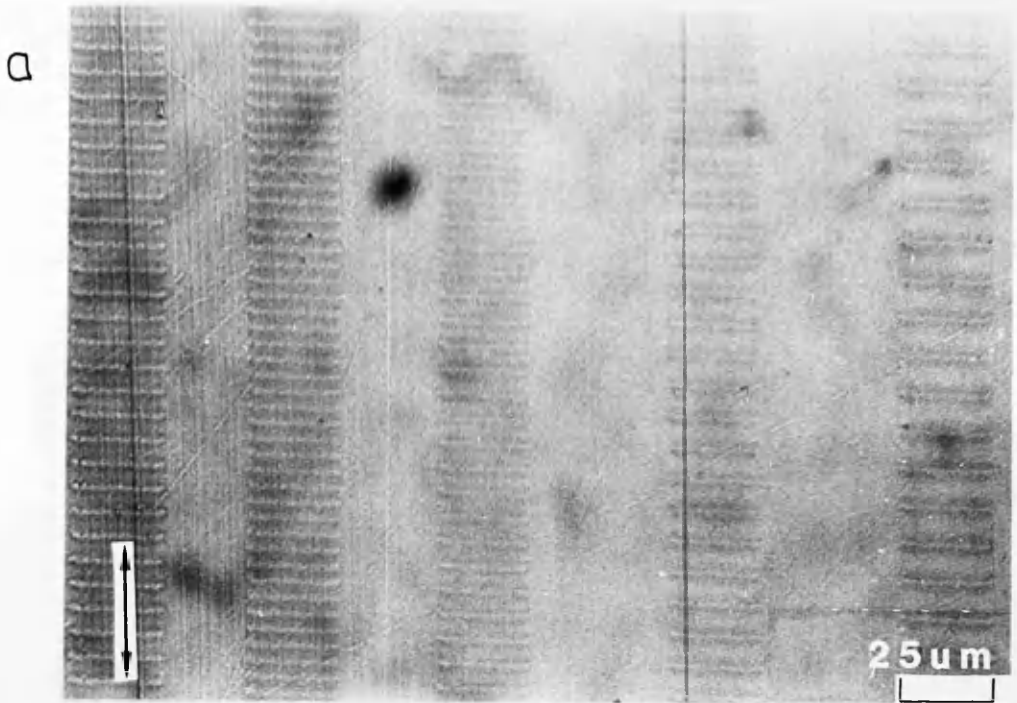
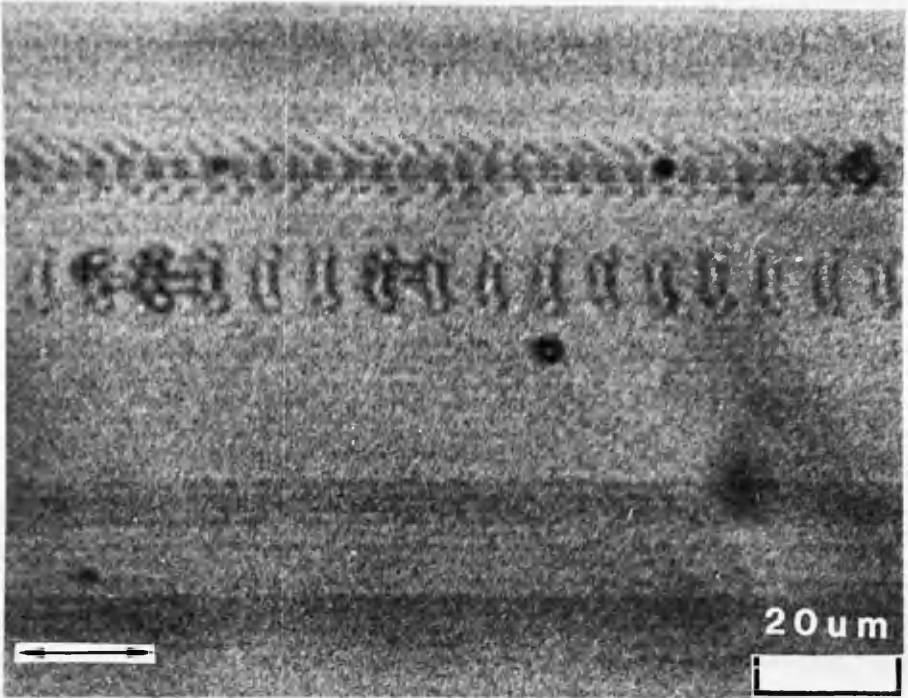


Figure 4.13 - Ferrofluid images of tracks written on the d.c. erased coupon (a) along the easy axis and (b) with a write angle of $\approx 30^\circ$ to the easy axis.

a



b

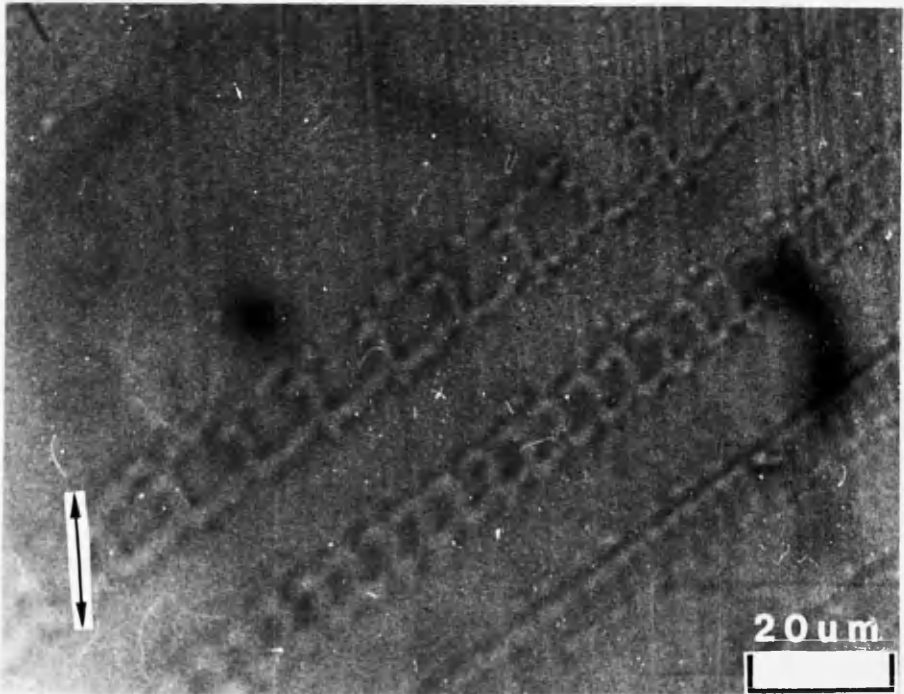


Figure 4.14 - Ferrofluid images of tracks written on the a.c. erased coupon (a) along the easy axis and (b) with a write angle of $\approx 50^\circ$ to the easy axis.

the ferrofluid technique, this initial observation suggested that the distribution of stray field gradients around the written bits are markedly different for tracks written along or off the easy axis. A comparison between the d.c. and a.c. erased coupons suggested that the form of this effect on the track domain structure was dependent upon the initial magnetic state of the medium.

As was the case for the tracks written along the easy axis Fresnel microscopy proved informative when tracks written at angles to the easy axis of the iron cobalt chromium medium were examined. Figure 4.15 contains images obtained from the d.c. erased sample while figure 4.16 illustrates the track domain structure from the a.c. erased sample. Firstly, in both figures it was observed that no matter the write angle ψ no magnetic ripple was imaged within written domains and that every saw-tooth in each domain wall transition pointed along the easy axis. This was seen to be the case for tracks written along the easy axis, suggesting that the medium magnetisation may relax along the easy axis irrespective of the write angle. Such behaviour would be consistent with the high medium magnetic anisotropy.

The track images from the d.c. erased medium illustrated the formation of zig-zag domain walls along the sides of every second recorded bit while those from the a.c. erased medium had similarly situated walls on every written bit, hence explaining the ferrofluid images from the two coupons. The Fresnel images of the

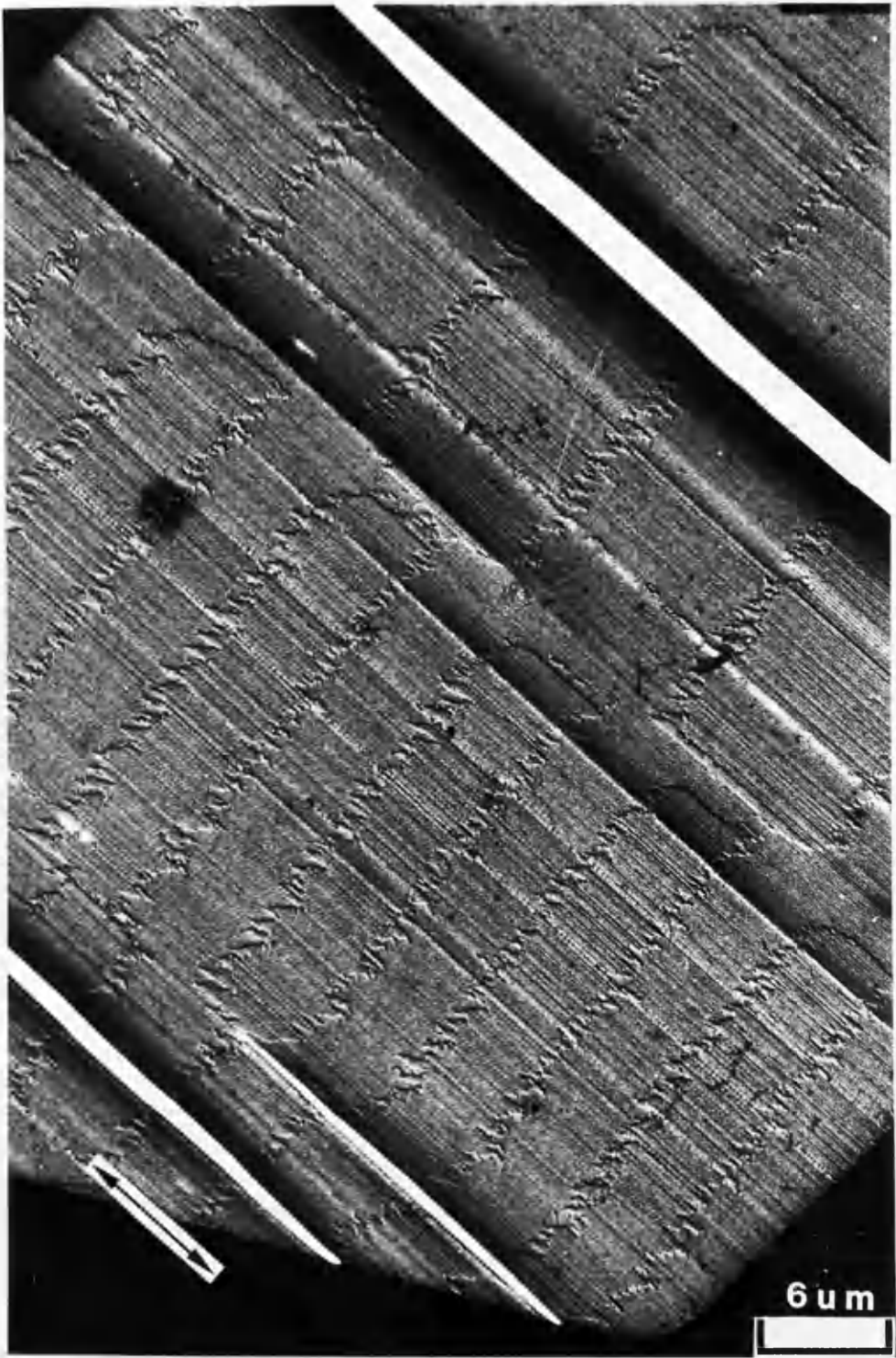
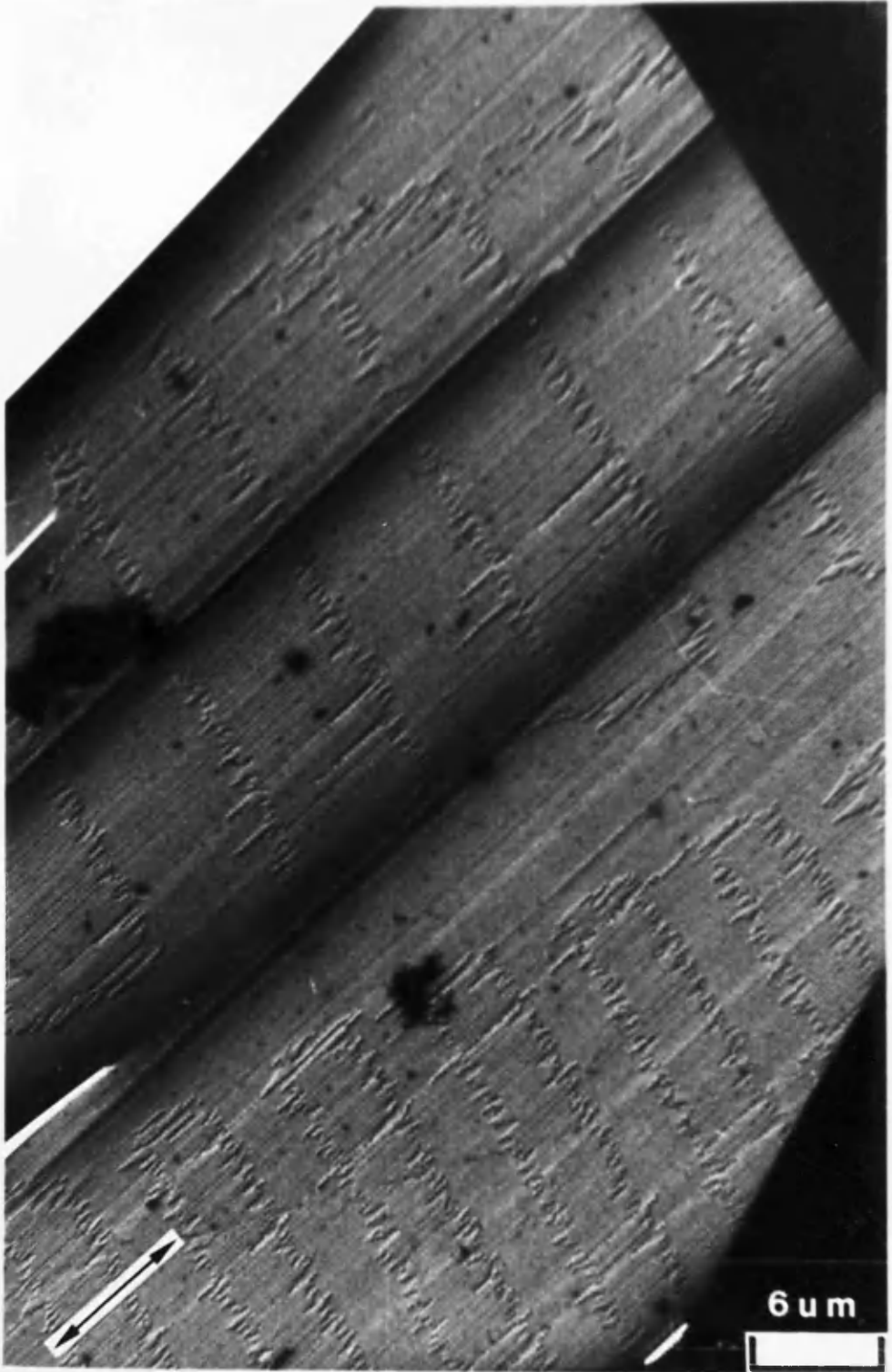


Figure 4.15 - Fresnel images of tracks written on the d.c. erased coupon at (a) $\approx 5^\circ$ to the easy axis. The arrow indicates the direction of the easy axis.



(b) $=15^\circ$ to the easy axis.



(c) $\approx 30^\circ$ to the easy axis.

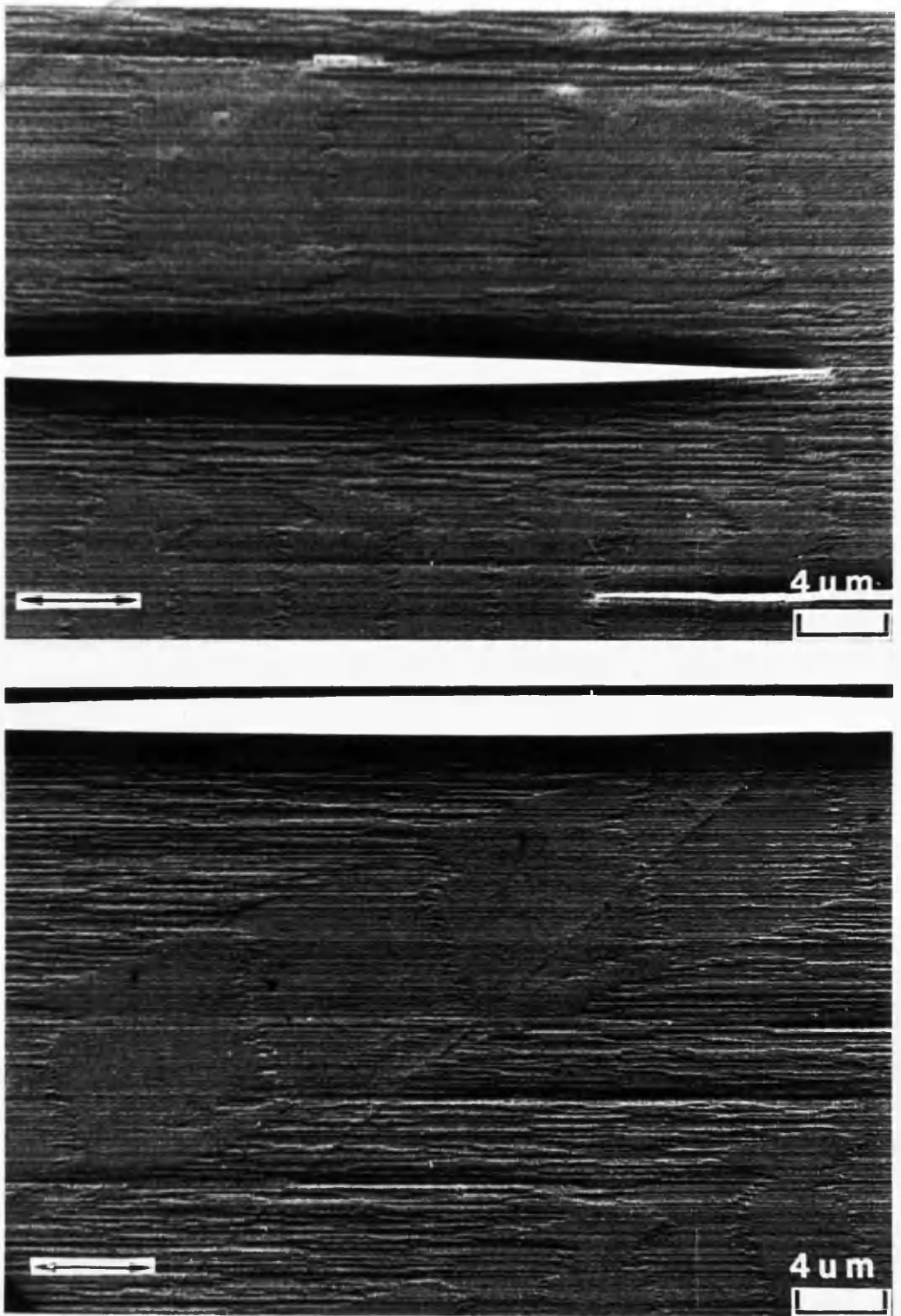
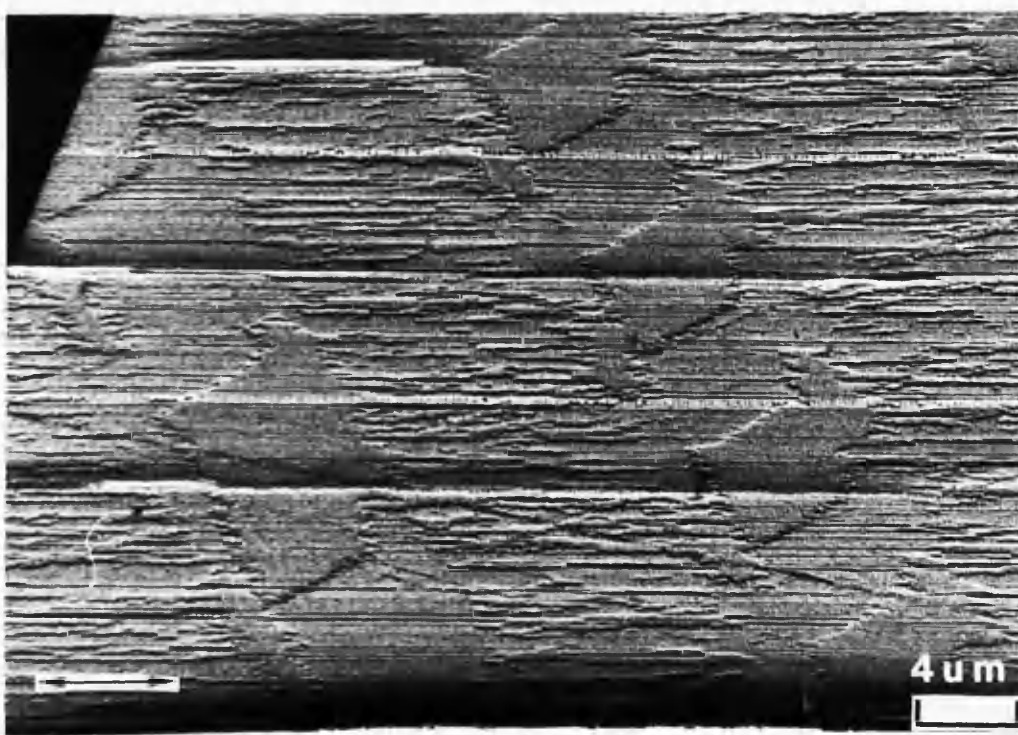
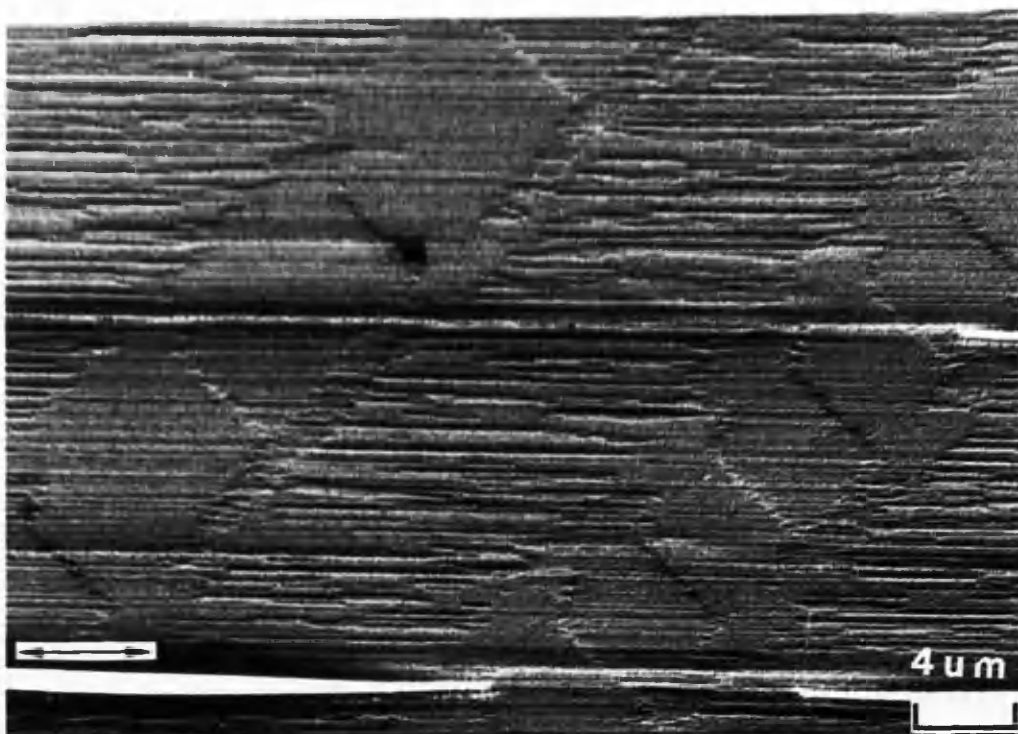
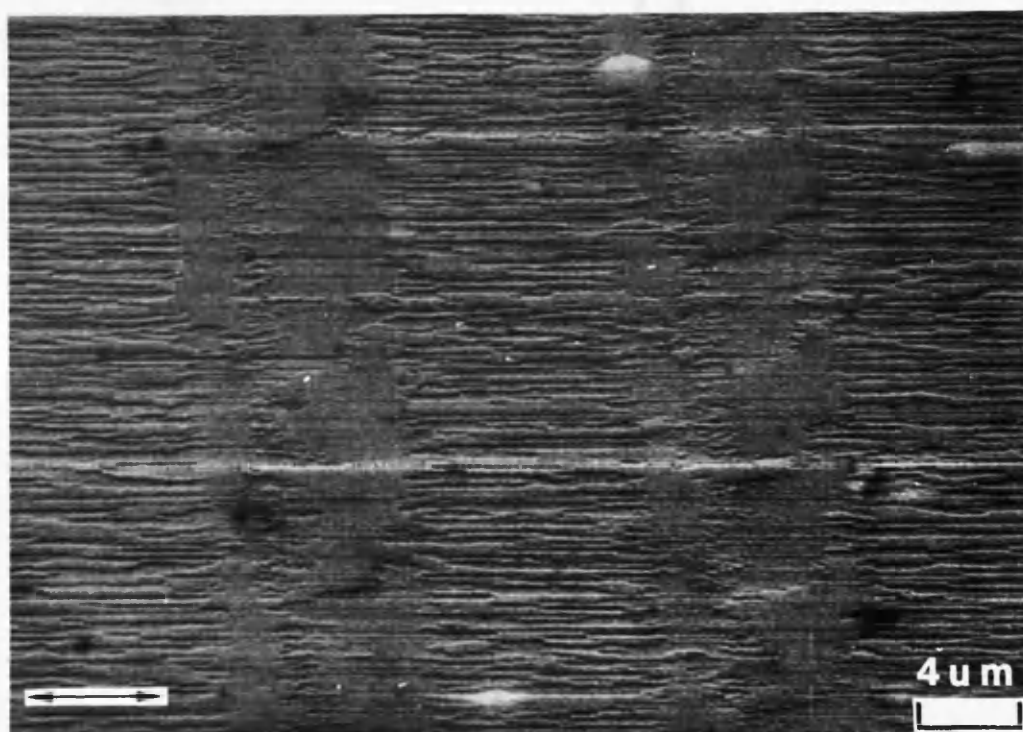
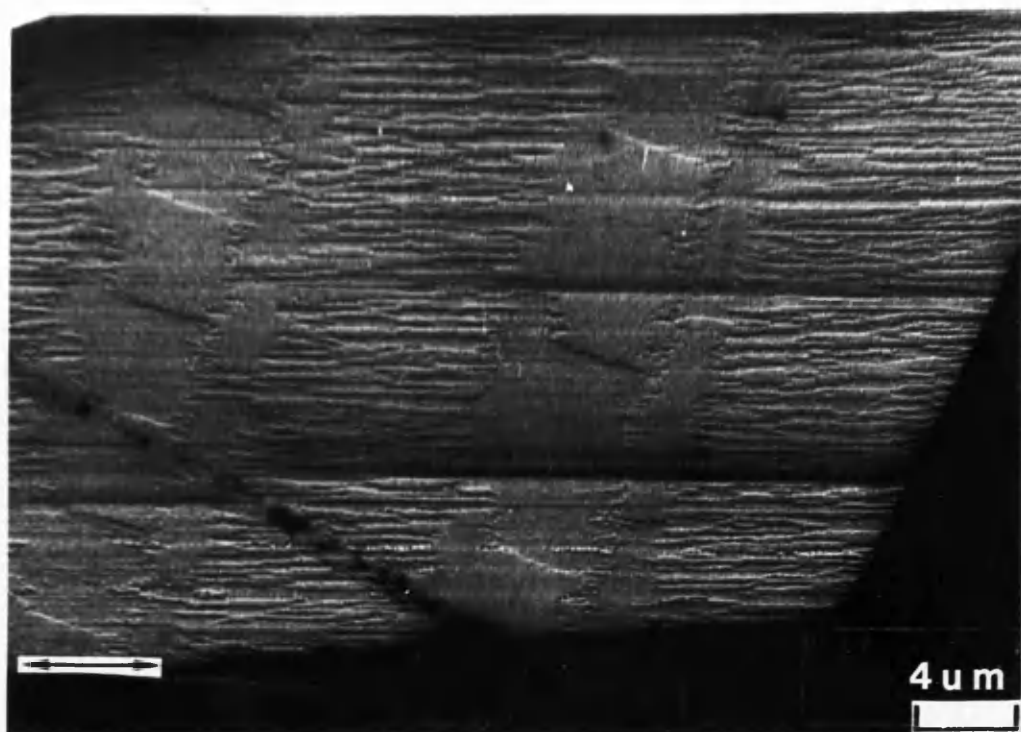


Figure 4.16 - Fresnel images of tracks written on the a.c. erased coupon at (a) $=0^\circ$ to the easy axis . The arrow indicates the direction of the easy axis. (b) $=20^\circ$ to the easy axis.



(c) -45° to the easy axis.

(d) -60° to the easy axis.



(e) $\approx 75^\circ$ to the easy axis.

(f) $\approx 85^\circ$ to the easy axis.

track domain structure also show clearly, for each type of specimen, the reduction of the zig-zag wall width between oppositely written bits as the written track rotated from the easy axis, eventually taking the form of a straight line domain wall on the a.c. erased coupon at write angles approaching 90° . For the same rotation of track write direction the domain walls at the track edges were observed to become more zig-zag in character compared to their linear form when written along the easy axis. This indicated that the free pole density or magnetic charge (indicated by the zig-zag walls) associated with a written magnetisation reversal was not only being distributed perpendicular to the write direction but also along the write direction. Such a dependency of the magnetic charge upon write angle ψ would cause the stray field induction generated over a written bit also to be a function of write angle. This relationship is discussed in detail in the next section (section 4.3.2.2).

A final separate observation was made from figure 4.16. From this image it was seen that the side-writing effects were noticeably anti-symmetric across the track. This most probably originates from some mis-alignment of the write head pole-pieces rather than any effect originating from the write angle/easy axis relationship.

4.3.2.2 SMALL ANGLE DIFFRACTION AND DIFFERENTIAL PHASE CONTRAST MICROSCOPY

Although providing excellent images of the track micromagnetic domain structure, the Fresnel mode of imaging is not capable of directly identifying the variations in the direction of the magnetic induction in and around the iron cobalt chromium medium as the write angle ψ is changed. In order to examine these fields the Lorentz techniques of small angle diffraction (SAD) and differential phase contrast (DPC) were employed to identify the directions of the medium magnetisation and associated stray fields in the locality of tracks written at angles to the easy axis. Small angle diffraction (SAD) was utilised in a qualitative manner to provide information on the direction of the net induction experienced by the electron beam traversing well defined regions of the specimen. As an example a SAD pattern obtained from a track written along the easy axis of an a.c. erased sample is given in figure 4.17. The two outer spots originate from the a.c. erased medium, whilst the essentially undeflected central spot is from the electrons traversing the track (the medium and stray field inductions cancelling to first order).

The write experiments conducted upon the d.c. erased coupon yielded tracks that appeared to be written slightly off the easy axis ($\leq 5^\circ$) rather than, as intended, along the easy axis. An example of the diffraction intensity generated from these tracks is

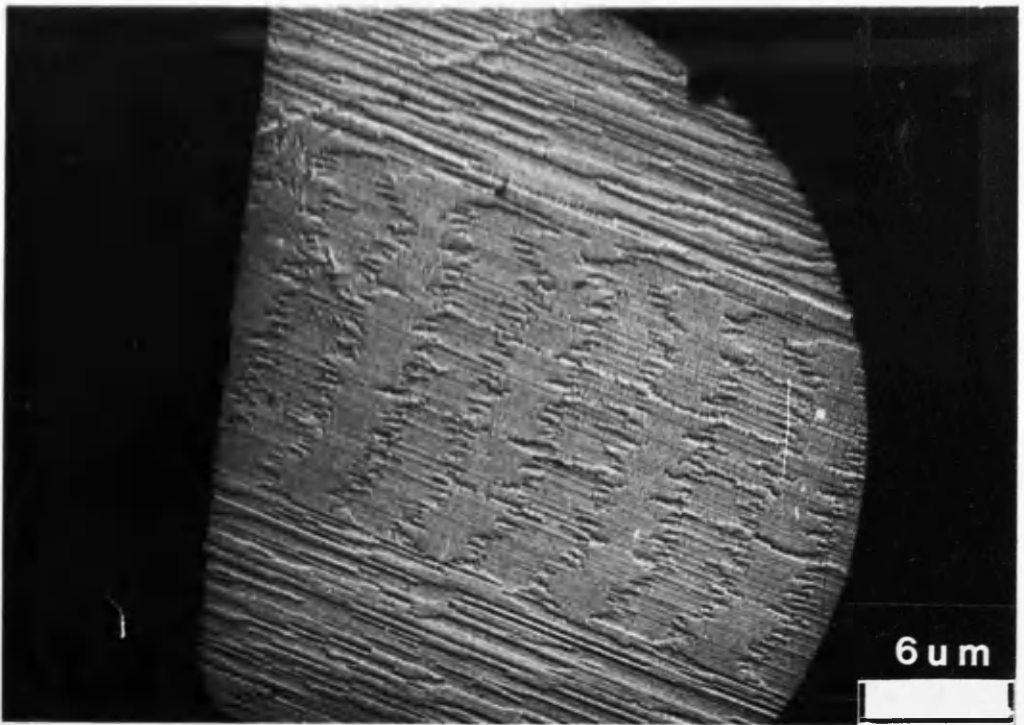


Figure 4.17 - Small angle diffraction pattern from tracks written along the easy axis of the a.c. erased medium.

given in figure 4.18. In this image: the elongated streaking intensity was produced by the striation texture of the medium; spot 'a' arose from the d.c. erasure adjacent to the track. The position of the intensity in area 'b' was consistent with that expected for the essentially undeflected track intensity, but can be seen to be composed of two separate sub-spots - one very close to the line generated by the striation structure passing through spot 'a', the other noticeably more distinct from this line. From the real space image used to produce this SAD pattern the source of these two sub-spots can only be the written track. Their existence and asymmetric placement about the striation intensity suggested that alternate bits written with or against the d.c. erasure produced two independent spots attributable to different net inductive components. The positioning of the two spots implied that these net inductions may differ slightly in magnitude and direction in alternate bits.

Tracks written at $\approx 15^\circ$ and $\approx 30^\circ$ to the easy axis of the d.c. erased coupon were analysed in an identical manner. Figures 4.19 and 4.20 describe the resultant images. A comparison of figures 4.18, 4.19, and 4.20 shows that the magnitude of the sub-spot separation progressively increased as the write angle increased from $\leq 5^\circ$ to 15° to 30° and that the direction in which the separation grew indicated a change in the components of the net magnetic induction both parallel and perpendicular to the easy axis in one of the written bits. To explain these observations one must

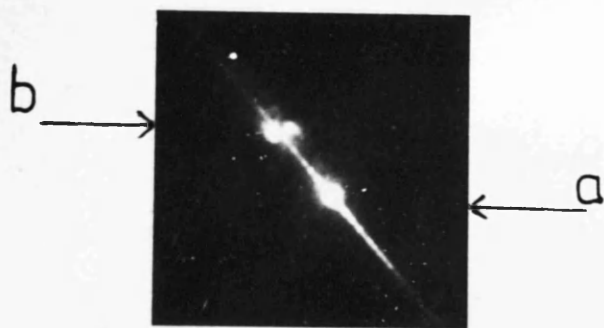
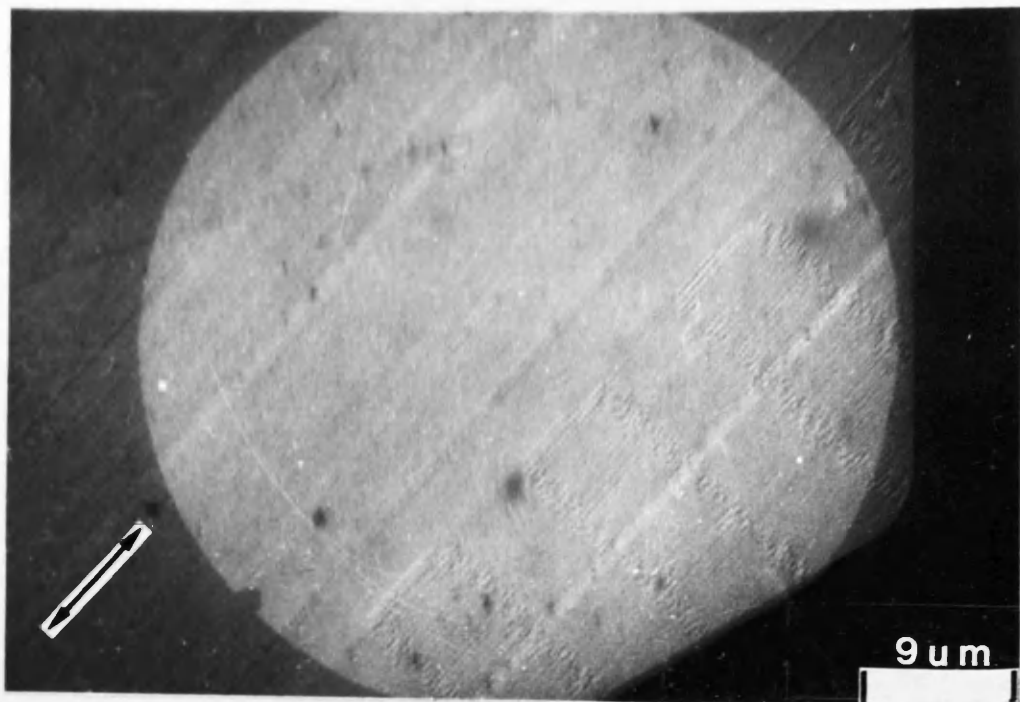


Figure 4.18 - Small angle diffraction pattern from tracks written $\leq 5^\circ$ off the easy axis of the d.c. erased coupon. (The clarity of the track image is slightly 'shaky' due to the long double exposures used to obtain this image).

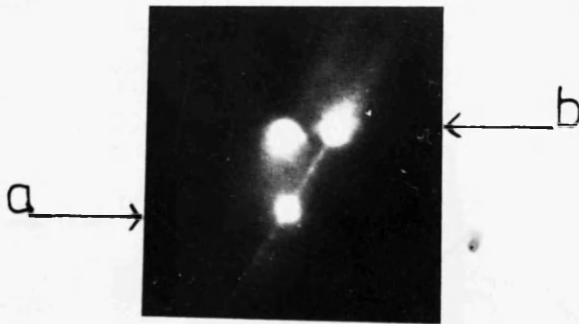
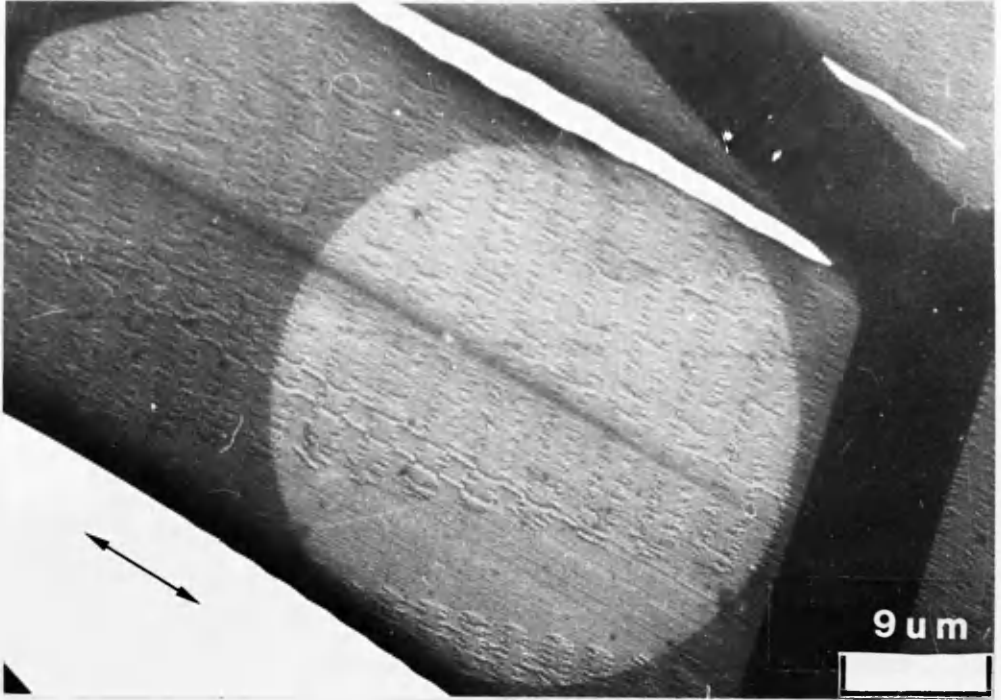


Figure 4.19 - Small angle diffraction pattern from tracks written $\approx 15^\circ$ to the easy axis of the d.c. erased coupon.

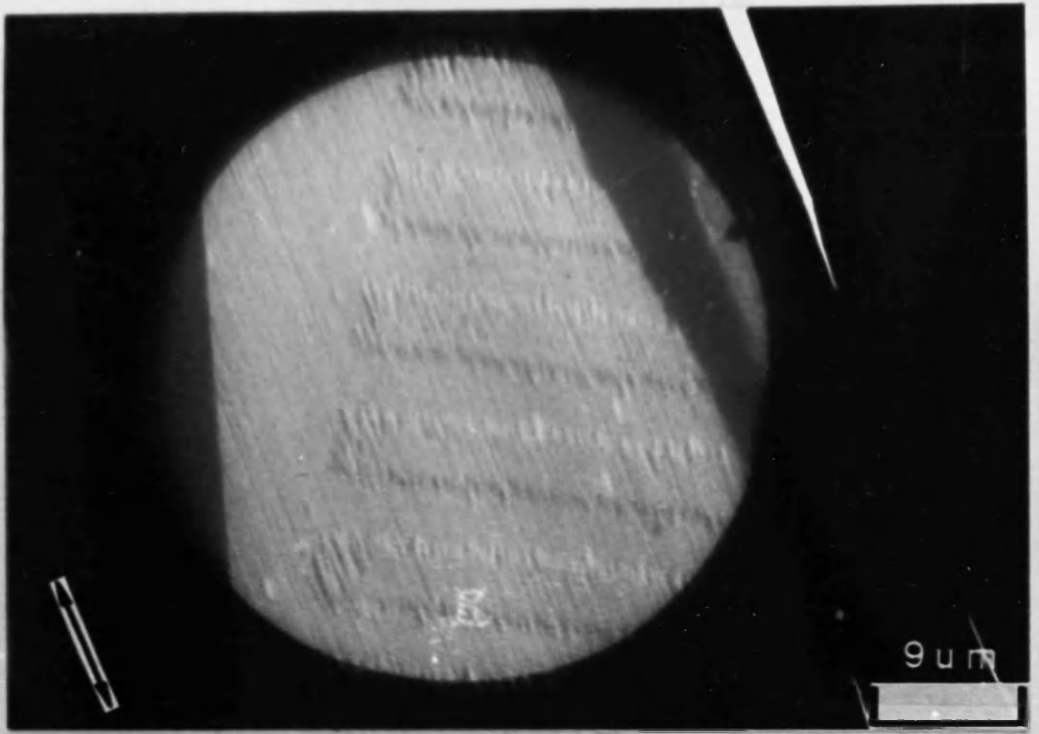


Figure 4.20 - Small angle diffraction pattern from tracks written $\approx 30^\circ$ off the easy axis of the d.c. erased coupon. (The clarity of the track image is slightly 'shaky' due to the long double exposures used)

consider the Fresnel images of the tracks illustrated in figure 4.15. As discussed, a re-distribution of the zig-zag domain walls around written bits was seen as the write angle was increased on the d.c. coupon. Such a growth of domain walls along the edges of tracks was observed to be specific to every second bit, the bits written against the d.c. magnetisation. Stray field generated across such bits would therefore be different from that over bits written with the d.c. erasure, and in particular should differ significantly in the component of stray field induction perpendicular to the easy axis. The net induction sensed by the electron beam in alternate bits would then be markedly different, producing the sub-spot separation observed. The SAD results presented have not included any from tracks written at angles to the easy axis from the a.c. erased coupon. Physical damage incurred during specimen preparation prohibited the acquisition of useful results for all of the write angles.

From the Fresnel and SAD images presented thus far the following model is proposed as a description of the behaviour of the medium and stray field inductions associated with tracks written off the easy axis. The highly anisotropic magnetic nature of the iron cobalt chromium medium was assumed sufficient to restrain the medium magnetisation to lie along the easy axis irrespective of the write angle ψ (this was reflected by the absence of magnetic ripple and the saw-teeth of the zig-zag domain walls pointing along the easy axis no matter the write direction). Figure 4.21

illustrates the stray field directions from track medium that was assumed to be initially d.c. erased; the recorded medium magnetisation within alternate bits was assumed equal with a magnitude $|\mathbf{M}_L|$. The stray field around oppositely magnetised bits was assigned \mathbf{H} and \mathbf{H}' for bits written with and against the d.c. magnetisation respectively. Both of these fields were assumed composed of a longitudinal (\mathbf{H}_L or \mathbf{H}'_L) and transverse (\mathbf{H}_T or \mathbf{H}'_T) vector component (longitudinal being parallel to the easy axis, transverse perpendicular to the easy axis):

$$\mathbf{H} = \mathbf{H}_L + \mathbf{H}_T \quad (4.18a)$$

$$\mathbf{H}' = \mathbf{H}'_L + \mathbf{H}'_T \quad (4.18b)$$

In figure 4.21a the tracks are written along the easy axis, producing a strictly longitudinal stray field if the effects of the side-written domain structure are ignored. A measure of the net induction experienced by the electrons passing through the written bits is then given by

$$\Delta\mathbf{B} = \mu_0 \cdot (\mathbf{M}_L - \mathbf{H}_L) \quad (4.19a)$$

$$\Delta\mathbf{B}' = \mu_0 \cdot (\mathbf{M}'_L - \mathbf{H}'_L) \quad (4.19b)$$

where μ_0 is the permeability of free space. Ideally this situation would produce a small angle diffraction pattern with a spot from the d.c. erasure and, since the inductions around and within written bits are assumed to cancel to first order, one other spot from the track.

A model for the induction in the locality of tracks written at angles $\leq 30^\circ$ to the easy axis is given in figure 4.21b. Here again the medium magnetisation was

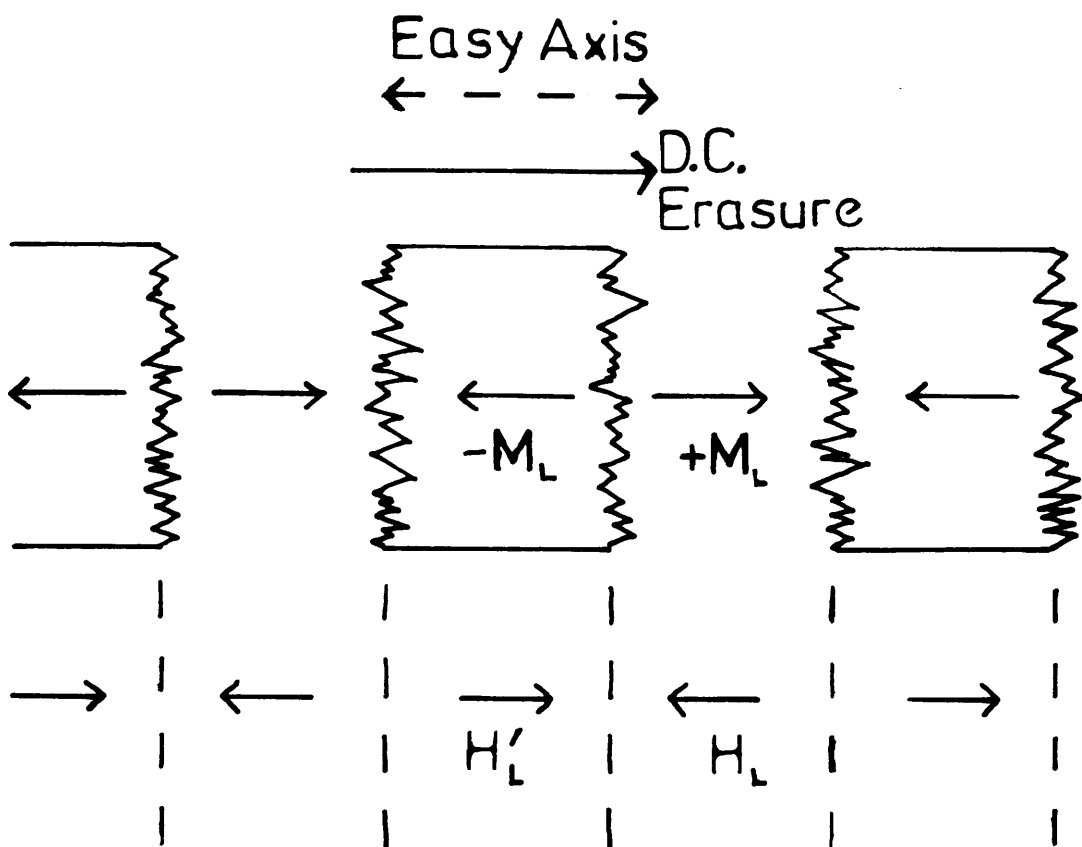
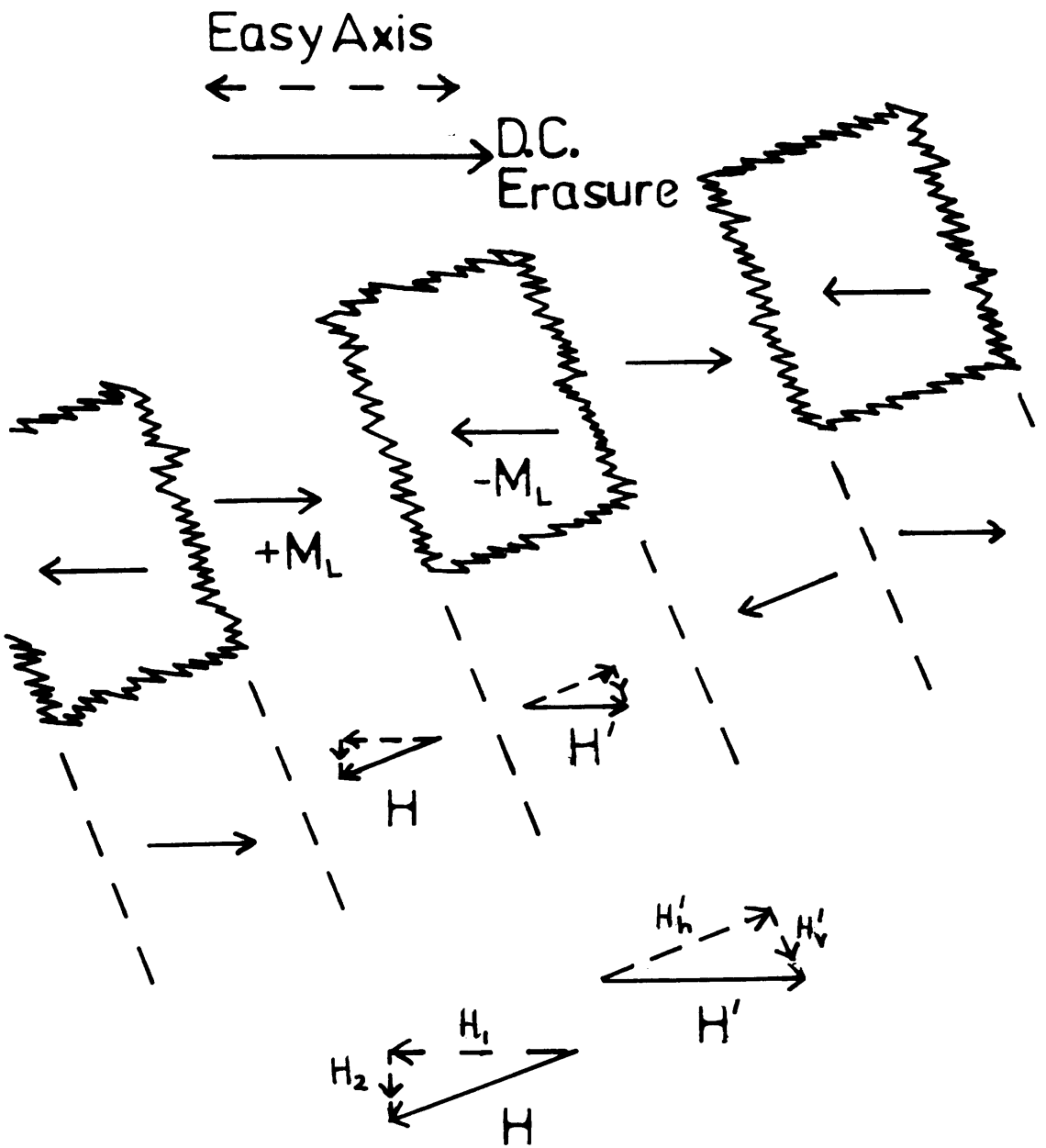


Figure 4.21 - (a) Schematic diagram describing the directions of the components of magnetisation and stray field in and around tracks written along the easy axis.



(b) Schematic diagram describing the directions of the components of magnetisation and stray field in and around tracks written off the easy axis.

assumed to have relaxed along the easy axis, but in this case the stray field appears very different to that of writing along the easy axis. The strength and direction of any stray field is dictated by the density and distribution of the free magnetic pole charge represented by the zig-zag walls. Thus far the Lorentz analysis has indicated that the micromagnetic character of the written zig-zag walls is dependent upon the write angle. They were observed to:

- (i) lie perpendicular to the write direction when writing along the easy axis;
- (ii) gradually relocate from being perpendicular to the write direction to an orientation parallel to the write direction as the write angle was increased from zero;
- (iii) finally lie parallel to the write direction when writing perpendicular to the easy axis.

In short, the zig-zag wall appears to consistently attempt to rotate or align itself perpendicular to the easy axis, resulting in the production of a strong stray field dependence on ψ . The net induction experienced by the traversing electrons in alternate written bits can be expressed as

$$\Delta B = \mu_o \cdot (M_L - H_L + H_T) \quad (4.20a)$$

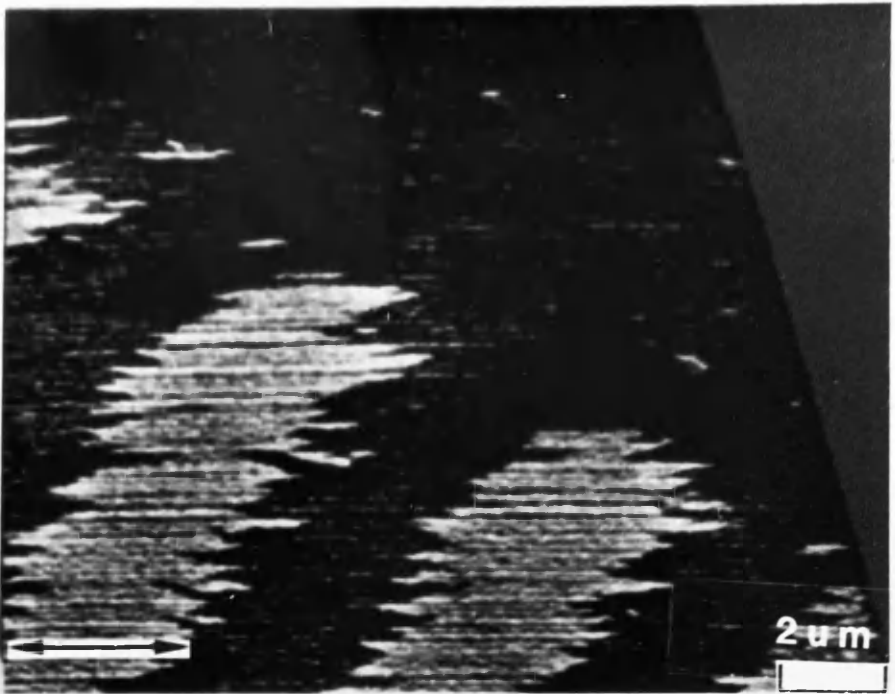
$$\Delta B' = \mu_o \cdot (M_L - H_L' + H_T') \quad (4.20b)$$

SAD observations indicated that the magnitude of one of the transverse components of the stray field from alternate bits (H_T or H_T') was non-zero for write angles ψ ($0^\circ \leq \psi \leq 30^\circ$). Consideration of the geometric distribution of the zig-zag walls in figure 4.21b indicated that the stray field components of induction

generated along (h) and across (v) the track over bits written against the d.c. erasure may add vectorially to produce a net stray field along the easy axis. The increase in transverse stray field induction observed by SAD should therefore be associated with the bits written with the d.c. erasure. DPC Lorentz electron microscopy was employed to investigate this proposed behaviour by imaging tracks written $\approx 30^\circ$ off the easy axis. Figures 4.22a and 4.22b contain DPC images sensitive to magnetic induction parallel and perpendicular to the easy axis. In figure 4.22a the distinct zig-zag walls indicate that a residual of the medium magnetic induction is being detected within the track after any stray field cancellation. This image shows the d.c. erased medium induction dark, in common with the contrast of the bits written with the d.c. erasure. The bits written against the d.c. erasure exhibit bright contrast, indicating a net induction in the opposite sense to the d.c. erased medium.

In figure 4.22b smooth sharp contrast variations indicate the detection of stray field induction. There is no net component measured from the d.c. erased medium, hence a uniform grey contrast level. The bits written against the d.c. erase are represented by the same contrast level, again indicating no net induction perpendicular to the easy axis. The bits written with the d.c. erasure, however, are represented by very dark contrast. This is consistent with the existence of a non-zero component of induction perpendicular to the easy axis and in agreement with the model proposed for

a



b

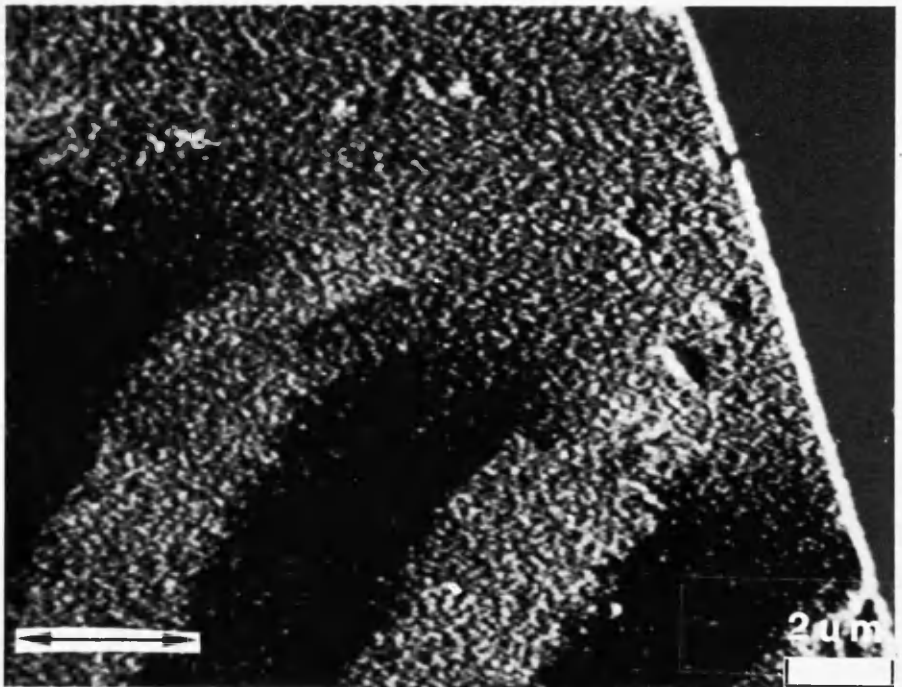


Figure 4.22 - Differential phase contrast images of a track written -30° off the easy axis of the d.c. erased coupon in which the image contrast is sensitive to induction (a) parallel to the easy axis and (b) perpendicular to the easy axis. The arrow indicates the direction of the easy axis.

the track induction from the Fresnel and SAD images presented above.

A similar model describing the stray field from tracks written between $\approx 30^\circ$ and 90° cannot be given since no SAD data was attainable at these angles. In order to characterise the micro-inductions for write angles of up to 90° , DPC was employed to analyse the a.c. erased coupon. Figures 4.23a, b, c, and d illustrate DPC images obtained by differentiating in different directions using the quadrant detector signal combinations in a manner that provides information about the inductions both parallel and perpendicular to the easy axis for tracks written at 0° , 50° , 70° , and 85° to the easy axis respectively. In all of the photographs an intensity shading can be seen across the images. This is an artifact of the DPC imaging technique and results from the scanning electron beam not being properly de-scanned in the post-specimen region of the microscope. It can be seen from figure 4.23 that this effect hampers rather than prohibits the acquisition of useful images.

Figure 4.23a(i) describes the induction parallel to the easy axis from a track written along the easy axis, figure 4.23a(ii) the induction perpendicular to the easy axis. The existence of faint a.c. erased contrast in figure 4.23a(ii) indicated that the differentiation was not exactly aligned to the easy axis but very close, thus only slightly impairing rather than prohibiting the observation of the track induction. A strong image of the characteristic medium zig-zag wall

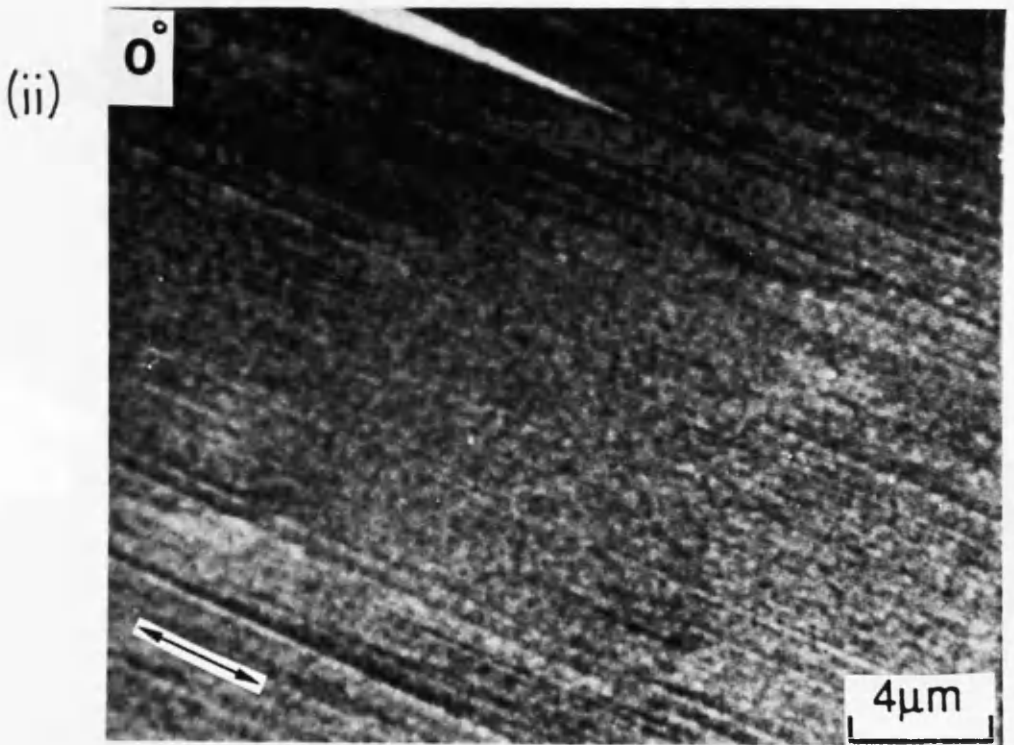
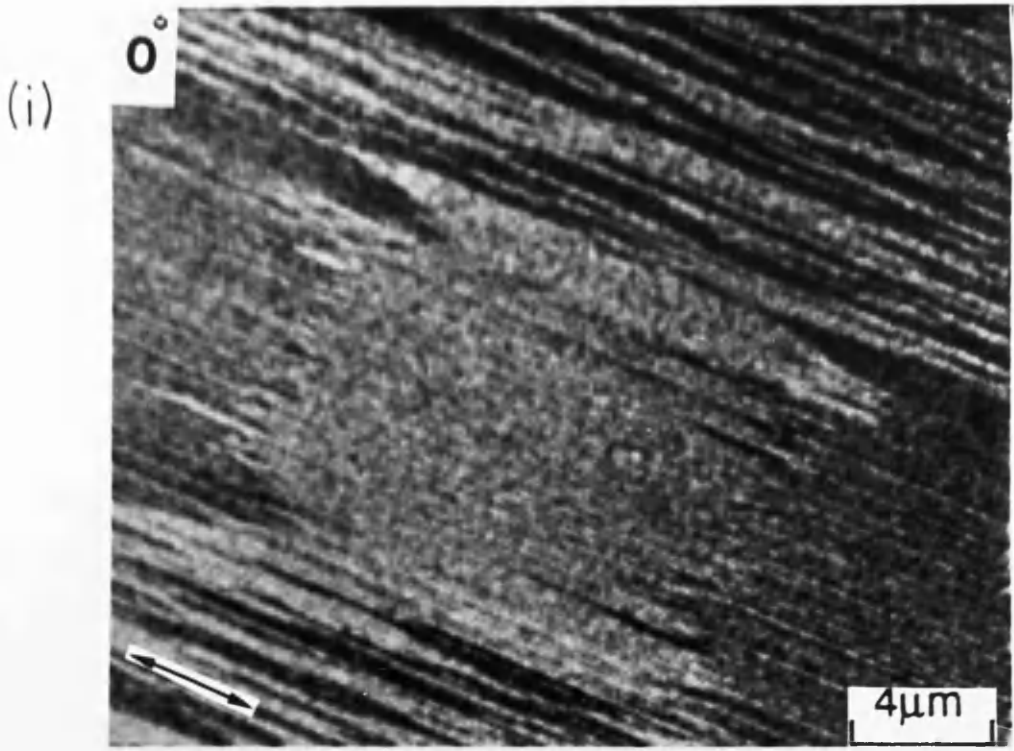


Figure 4.23 - (a) Differential phase contrast image written at $\approx 0^\circ$ off the easy axis of the a.c. erased coupon in which the image contrast is sensitive to induction (i) parallel to the easy axis and (ii) perpendicular to the easy axis. The arrow indicates the direction of the easy axis.

in figure 4.23a(i) indicated that the net longitudinal induction experienced by the traversing electrons was essentially the residual medium induction after any stray field cancellation. The image sensitive to induction perpendicular to the easy axis contained a minimal amount of image contrast (probably from the slight mis-alignment of the differentiation direction and the easy axis), implying that there was essentially no net induction in this direction and therefore confirming the assumption discussed above of there being no net transverse stray field induction when the tracks are written along the easy axis (there will be no transverse contribution to the net induction from the medium because of the strong anisotropy).

The pair of DPC images obtained from the track with write angle $\psi=50^\circ$ are described in figures 4.23b(i,ii). Growth of zig-zag walls can be seen parallel to the write direction and the change in character of the transition wall perpendicular to the easy axis towards being a straight line can be observed in figure 4.23b(i) in agreement with the Fresnel observations. Such a re-distribution of magnetic charge around the bit should induce a transverse component of induction over the written bit as discussed above. This was confirmed by the image of figure 4.23b(ii) where the outline of the written bits can be clearly seen. The smooth, sharp intensity changes indicate the detection of stray field at the transitions defining the written bit rather than medium induction. The interior of the written bits does not appear to exhibit any contrast in

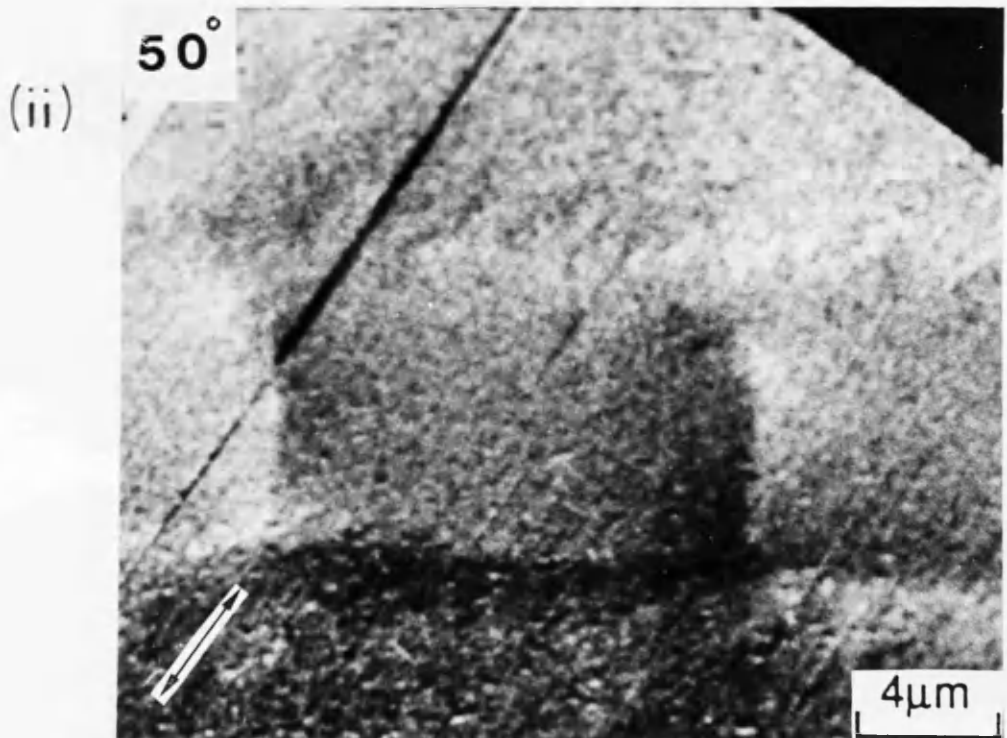
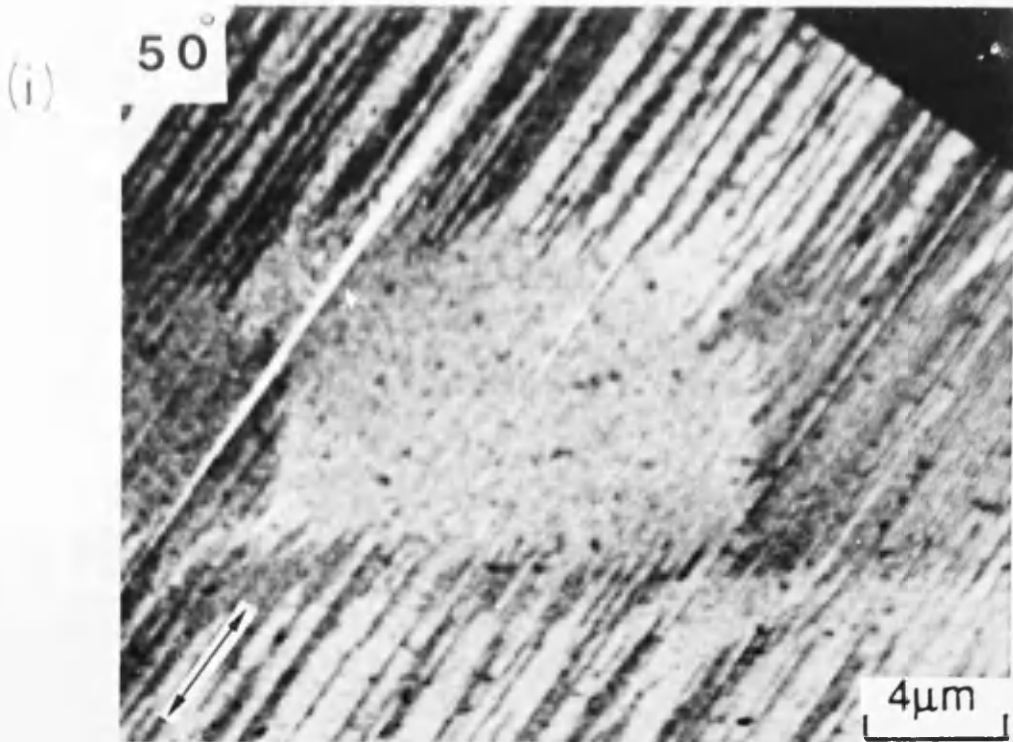


Figure 4.23 - (b) Differential phase contrast image written at $\approx 50^\circ$ off the easy axis of the a.c. erased coupon in which the image contrast is sensitive to induction (i) parallel to the easy axis and (ii) perpendicular to the easy axis. The arrow indicates the direction of the easy axis.

this image, indicating a net cancellation of any perpendicular induction in these regions. This agrees with the behaviour of the bits written against the d.c. erased medium described in figure 4.21. The DPC images of tracks with write angles of 70° and 85° showed virtually straight line domain walls perpendicular to the write direction while the walls parallel to the write direction were observed to be zig-zag. At these write angles the magnetic charge would appear to be concentrated across the track width, producing a stray field apparently parallel to the easy axis. The image sensitive to induction perpendicular to the easy axis in figure 4.23d reflected this stray field behaviour by indicating the detection of virtually no induction in this sense. The image sensitive to induction perpendicular to the easy axis from the track written at $\psi \approx 70^\circ$ to the easy axis did however appear to contain faint evidence of the smooth stray field contrast variations described for the write angle of 50° . Closer inspection indicated that some part of this contrast may in fact originate from a mis-alignment between the direction of differentiation and the medium easy axis but the smooth nature of the contrast variations within the track indicate the possible detection of stray field. The relative weakness of the contrast in this image in comparison to that in the corresponding image for a write angle ψ of $\approx 50^\circ$, figure 4.23a(ii), indicated a reduction in the transverse stray field component as the write angle increased from $\approx 50^\circ$ to $\approx 70^\circ$.

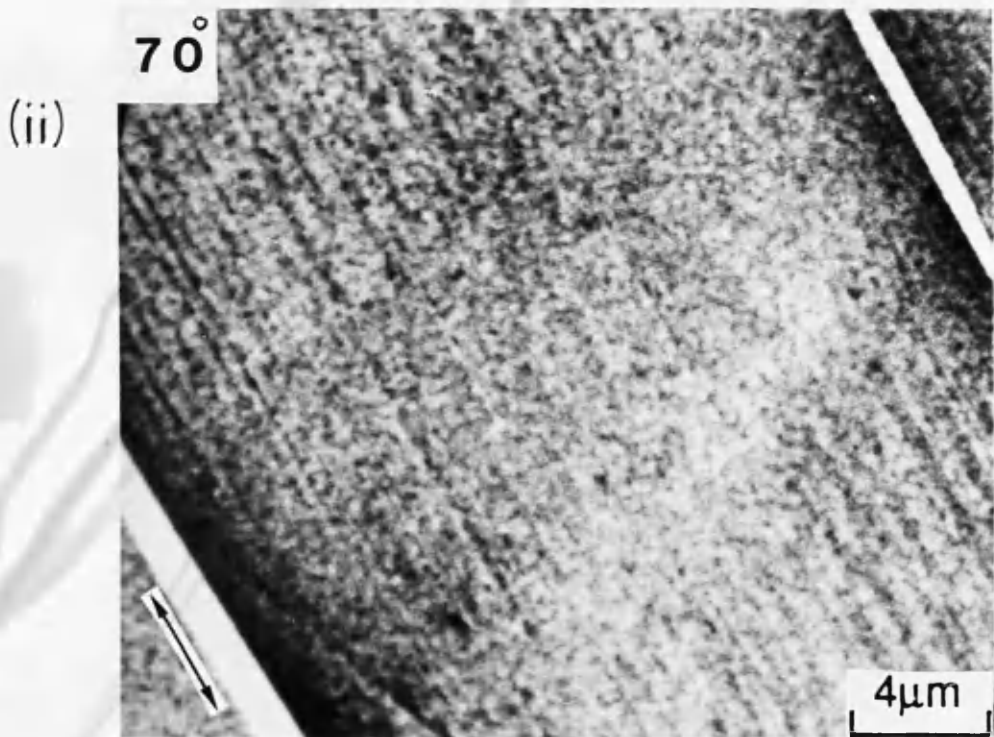
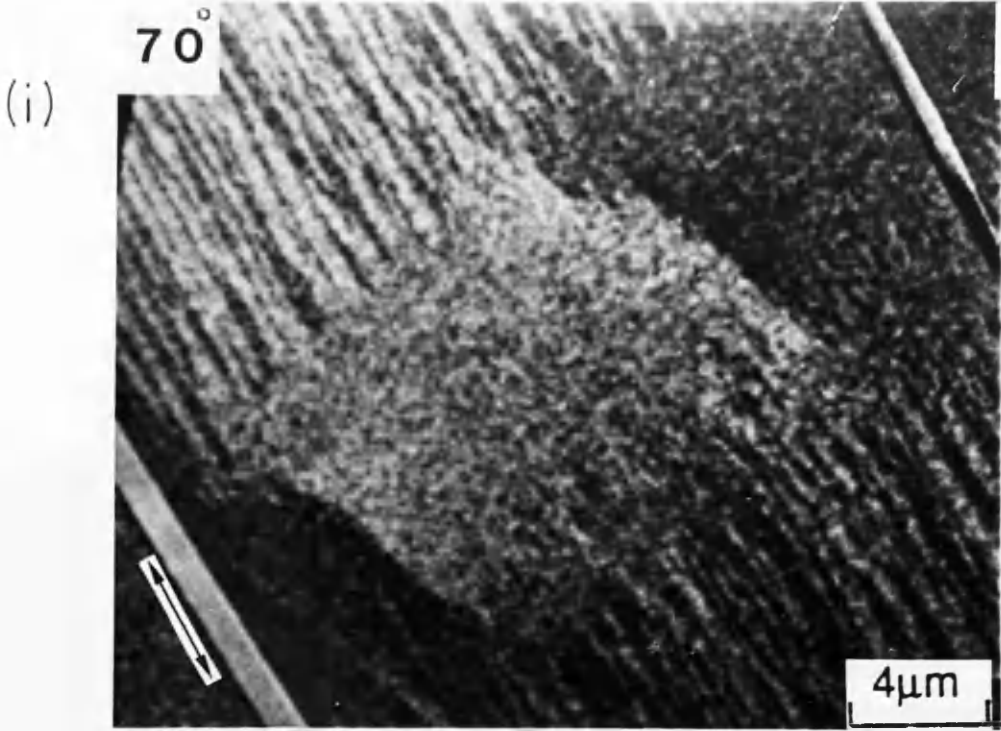
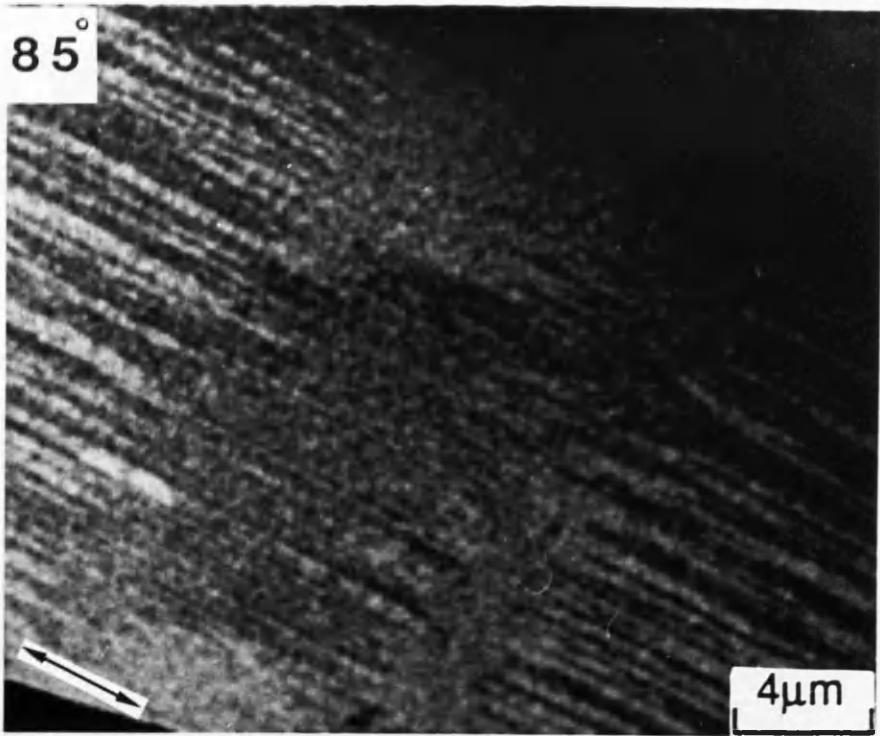


Figure 4.23 - (c) Differential phase contrast image written at $\approx 75^\circ$ off the easy axis of the a.c. erased coupon in which the image contrast is sensitive to induction (i) parallel to the easy axis and (ii) perpendicular to the easy axis. The arrow indicates the direction of the easy axis.

(i)



(ii)

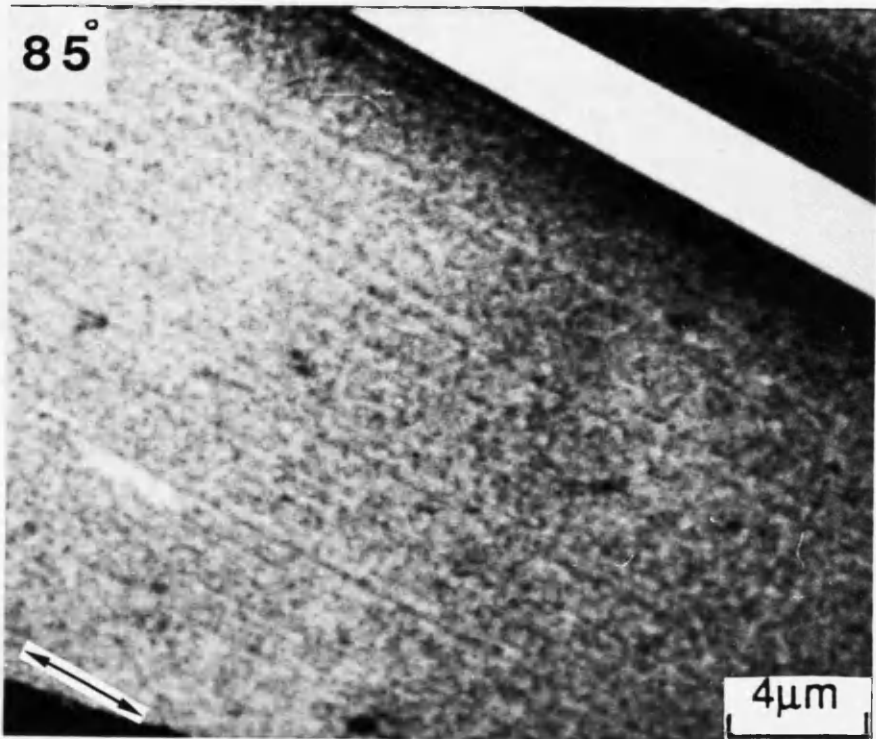


Figure 4.23 - (d) Differential phase contrast image written at -85° off the easy axis of the a.c. erased coupon in which the image contrast is sensitive to induction (i) parallel to the easy axis and (ii) perpendicular to the easy axis. The arrow indicates the direction of the easy axis.

Although limited, the DPC analysis of this a.c. erased coupon can be used to extend the proposals made from the initial studies about the local inductions around and within the medium for write angles $\leq 30^\circ$. It revealed that the component of stray field perpendicular to the easy axis appeared to increase from nothing for $\psi=0^\circ$ to being clearly observed from tracks written at a write angle $\psi \leq 50^\circ$, after which it appeared to reduce in strength to zero - indicating that the stray field may in fact re-align itself with the easy axis as the write angle ψ is increased to 90° . Consideration of the track magnetisation at a write angle of 90° suggests that any stray field generated will be very small in magnitude.

4.4 SUMMARY OF CHAPTER

The results of the microstructural analysis of the iron cobalt chromium thin film medium indicated that it had a body centre cubic crystalline structure with a lattice parameter a of $2.56\text{\AA} \pm 0.01\text{\AA}$. An estimate of the grain size was not possible, but the dimension over which the physical structure appeared to change was measured at $\approx 15\text{nm}$. These observations were consistent with those of Alexopoulos and Geiss [1].

Arnoldussen et al [2] reported that the ratio of remanent coercivities in the easy and hard axes increased upon introducing the circumferential texturing to the disk construction process. They

proposed that this treatment emphasised the growth of the parallel chains of crystallites along the easy axis which are ultimately responsible for the high medium anisotropy. The images of the film structure presented were not able to resolve clearly such chains. They did however show the presence of 'contours' associated with the texturing process which contained micro-cracks which ran parallel to the easy axis. The introduction of such cracks would favour an increase in the circumferential coercivity at the expense of that along the hard axis.

Fresnel imaging was used to observe the micromagnetic domain structures from tracks written along the easy axis of the iron cobalt chromium medium. The characteristic domain wall throughout the medium was seen to be zig-zag in character with the 'zig-zag teeth' pointing along the medium easy axis. No magnetic ripple was imaged within written domains under any write conditions, implying that the magnetisation within domains lies parallel or anti-parallel to the easy axis with a magnitude equal to the remanent magnetisation M_s .

The complete micromagnetic characterisation of the tracks written off the easy axis showed that the high magnetic anisotropy of the medium constrained the recorded track magnetisation/induction to always lie close to the easy axis no matter the angle at which a track was written. The stray field however was seen to be heavily dependent upon the write angle. The relationship between the write angle and the

distribution of the magnetic charge, defined by the zig-zag walls, was seen to rotate the stray field away from being parallel to the easy axis as the write angle ψ increased from 0° . By observing the the transverse component of the stray field using differential phase contrast microscopy it was seen that this induction was clearly observed for write angles ψ of up to $\approx 50^\circ$, after which the transverse stray field component decreased until, for write angles written approximately perpendicular to the easy axis, the stray field re-aligned itself along the easy axis with a very small magnitude. This observation reflects the high magnetic anisotropy of the medium and its subsequent desire to always align its magnetisation with the easy axis.

CHAPTER FIVE

THE PRELIMINARY CHARACTERISATION OF COBALT NICKEL CHROMIUM THIN FILM RECORDING MEDIUM

5.1 INTRODUCTION

Although a great deal of time and effort was spent developing a technique to prepare thin film specimen of isotropic recording media from hard disk the first real tangible success was only realised in the final stages of this Ph.D. study. The use of a silicon based hard disk substrate enabled chemically uncorrupted cobalt nickel chromium thin film samples to be prepared. A preliminary examination by electron microscopy was then undertaken to establish the basic micromagnetic properties of the medium. The extent of this microscopical examination was limited by the constraints of the Ph.D. time-table, but the first observations made from this work were thought worthy of inclusion as a fore-runner to any future analysis of this recording medium.

5.2 OBSERVATION OF THE GRAIN STRUCTURE

A cross-section of the thin film sample obtained from the hard disk is given in figure 5.1. Energy dispersive X-ray (EDX) analysis indicated that the chemical integrity of the cobalt nickel chromium thin film was not compromised by preparation, measuring the percentage composition of the film to be

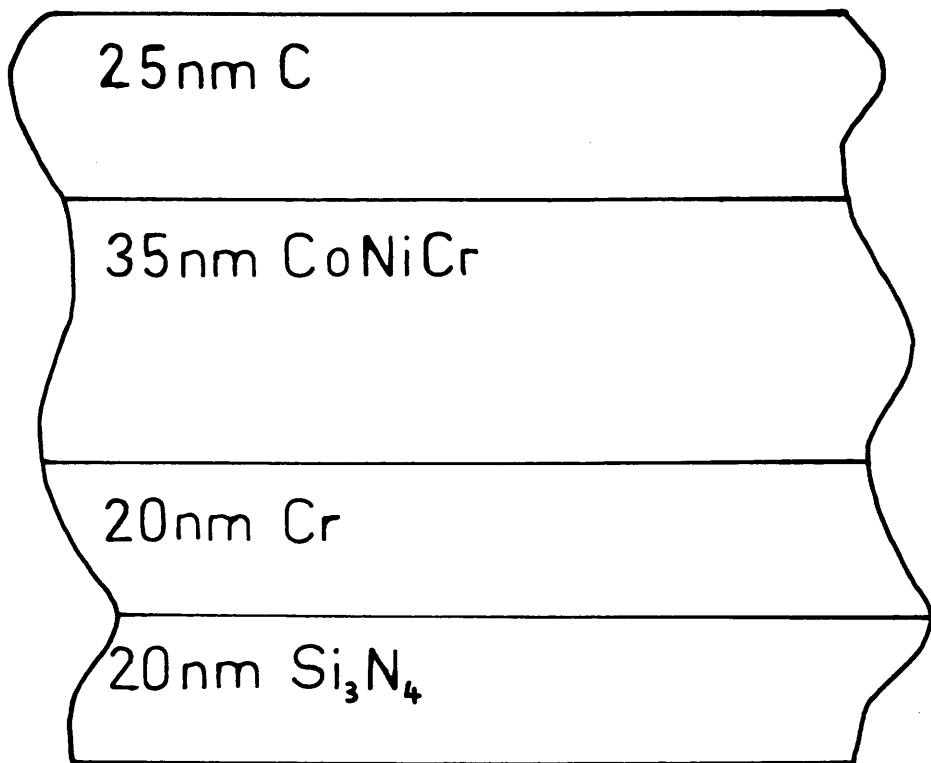


Figure 5.1 - Cross-section of the prepared cobalt nickel chromium thin film specimen.

$$\text{Co} : \text{Ni} : \text{Cr} \cong 43\% \pm 2\% : 13\% \pm 2\% : 44\% \pm 2\% \quad (5.1a)$$

and hence in good agreement with that deposited on the original hard disk,

$$\text{Co} : \text{Ni} : \text{Cr} \cong 46\% : 13\% : 41\% \quad (5.1b)$$

The JEOL 1200EX and 2000FX transmission electron microscopes were employed to investigate the physical grain structure of the thin film specimen, using both bright and dark field imaging techniques. Figure 5.2 illustrates the grain structure at a magnification of 50K \times while figure 5.3 contains the corresponding image at a magnification of 100K \times . From the bright field images the medium was seen to be composed of similarly shaped grains which were closely packed in the plane of the foil. A nominal range in grain size was estimated between 1nm and 10nm. Any cracks within the film were observed to be isotropically directed throughout the medium. The corresponding dark field images showed some streaking from the crystallite contrast. This was not due to some microscope mis-alignment while imaging, but rather some effect most probably originating from either the specimen structure or the relatively high specimen thickness of $\approx 100\text{nm}$. The reduction in image visibility due to the specimen thickness prevented useful images being obtained at magnifications higher than 100K \times .

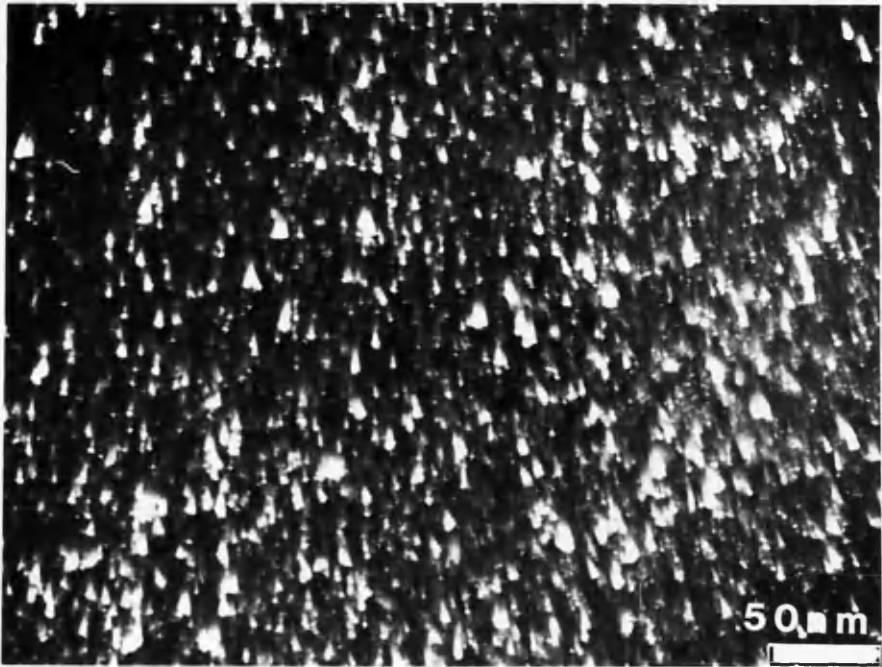
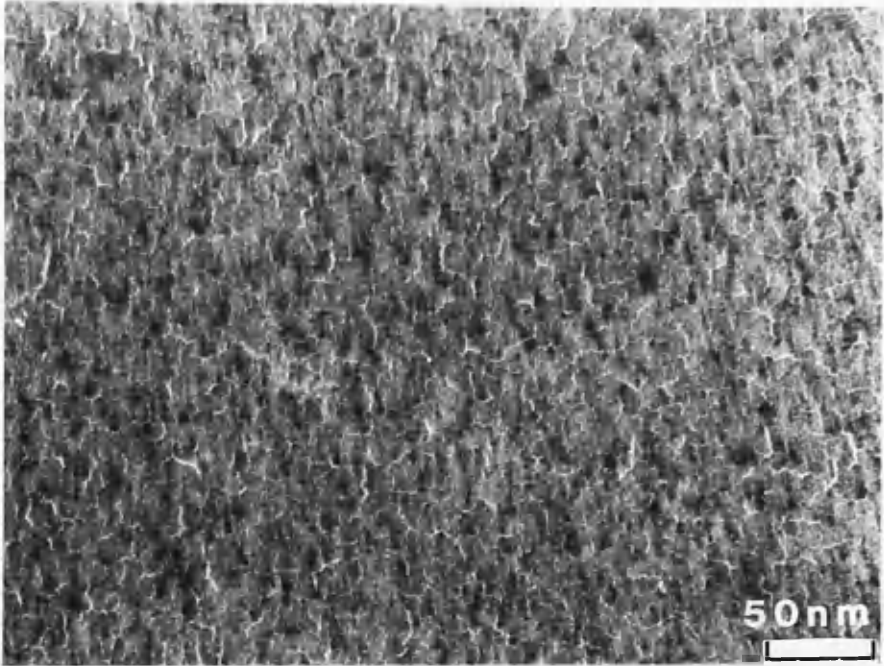


Figure 5.2 - Bright and dark field transmission electron microscope images of the cobalt nickel chromium thin film at a magnification of $\times 50K$.

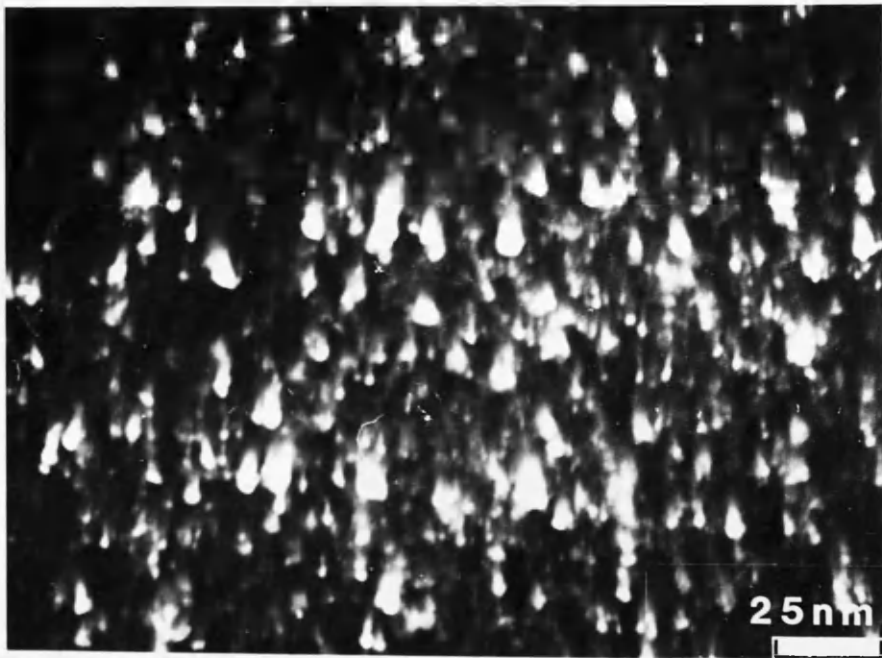
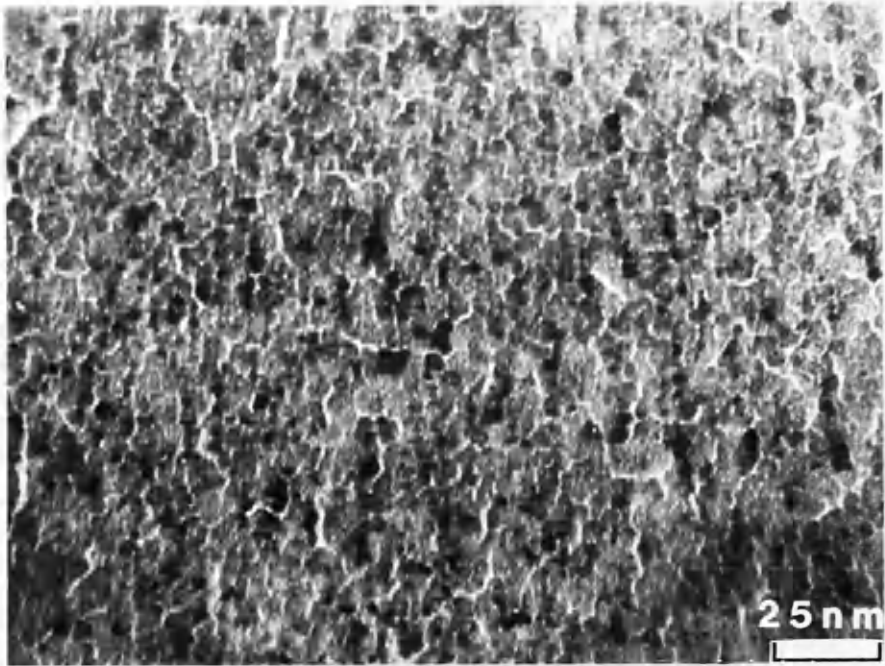


Figure 5.3 - Bright and dark field transmission electron microscope images of the cobalt nickel chromium thin film at a magnification of $\times 100K$.

5.3 INVESTIGATION OF THE RECORDED MICROMAGNETIC DOMAIN STRUCTURES

5.3.1 FRESNEL AND DIFFERENTIAL PHASE CONTRAST LORENTZ MICROSCOPY

Images of all the written tracks recorded on this thin film medium were obtained with the Fresnel mode of Lorentz electron microscopy. It was intended that the experimental tracks should be written on a region of disk which had been d.c. erased; instead it was observed that the majority of tracks were written on to the virgin disk medium (the state upon medium deposition), only eight tracks being recorded on the portion of the disk d.c. erased with the write head. The reason for this was a radial mis-placement of the head relative to the disk before the tracks were written.

Two images illustrating the micromagnetic domain structures of the virgin recording medium and the d.c. erased cobalt nickel chromium are given in figure 5.4. The virgin medium was seen to consist of a mesh of small domain walls which appeared to be oriented isotropically over the film; the most obvious features of the d.c. erased micromagnetic structure were the strong magnetic ripple contrast seen over the specimen and the array of recorded lines (see figure 5.4) running parallel to the d.c. magnetisation. Chen and Yamashita [1] described ripple contrast as originating from a minor variation in the magnetisation either side

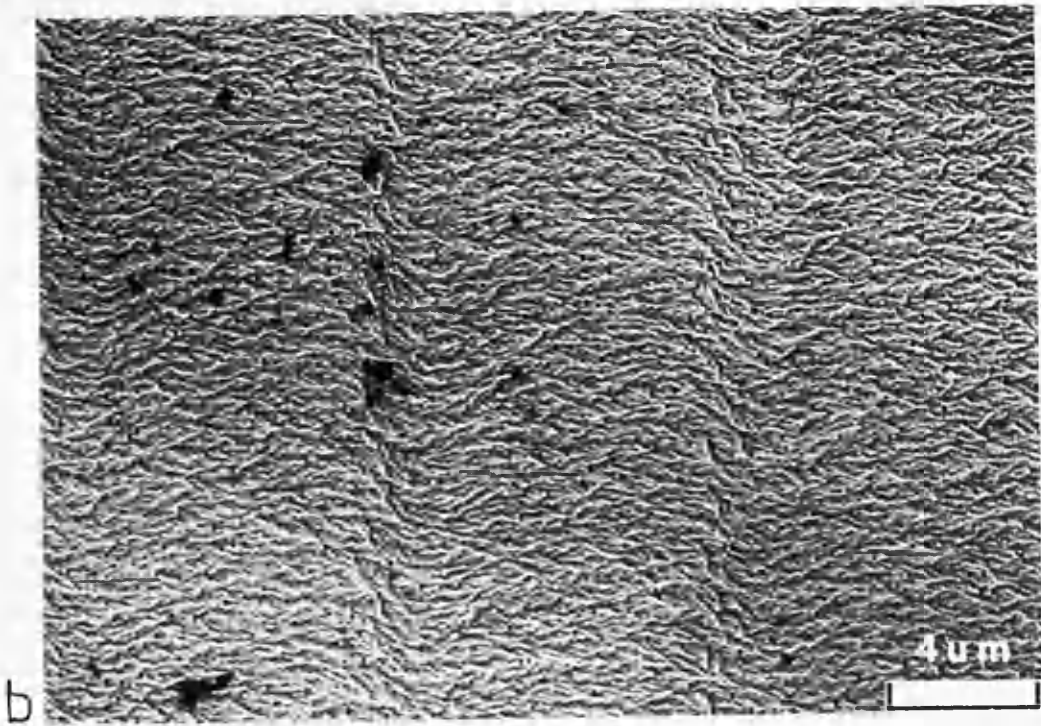
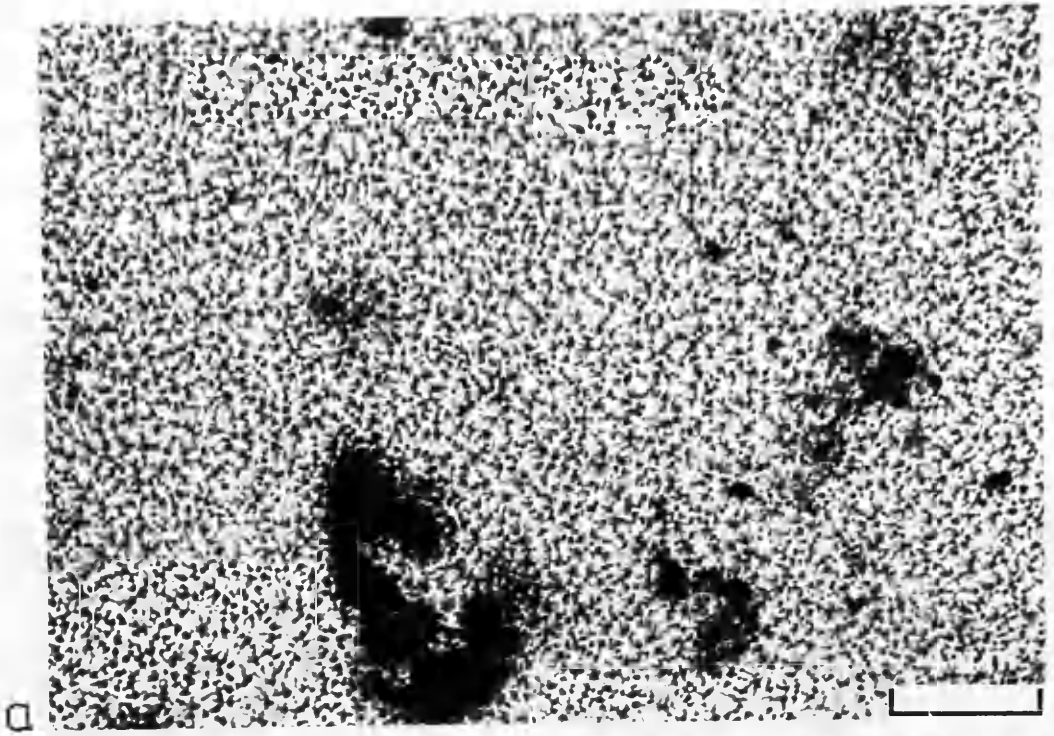


Figure 5.4 - Fresnel images of (a) the virgin medium and (b) the d.c. erased medium.

of the ripple, and stated that the magnetisation direction in this region can be thought of as approximately normal to the ripple line direction. Inspection of the ripple in the d.c. erased image then showed that the magnetisation was uniformly directed except in the regions defined by the periodic array of lines seen to run along the image. These lines arise from the side-writing effects associated with the head that was used to d.c. erase the medium. In these areas the ripple indicated that the medium magnetisation had rotated perpendicular to the apparent direction of the d.c. erasure. The ability of the medium to sustain these two perpendicular directions of magnetisation demonstrated its isotropic magnetic nature.

A track written on the virgin medium is shown in figure 5.5a. Figure 5.5b contains an image of a slightly lower frequency track written on the d.c. erased portion of the disk. Both tracks were observed to be similar in structure with written bits being composed of a dominant central block flanked by side-written wing structure. Within the bits the magnetic ripple indicated that the magnetisation in the central portion was relatively invariant, lying parallel or anti-parallel to the write direction as expected. Ripple character in the wing structure however was radically different: in these locations the ripple contours rotated rapidly at the boundary between the central bit and wing structure, producing a magnetisation in this region that appeared perpendicular to the write direction. This behaviour

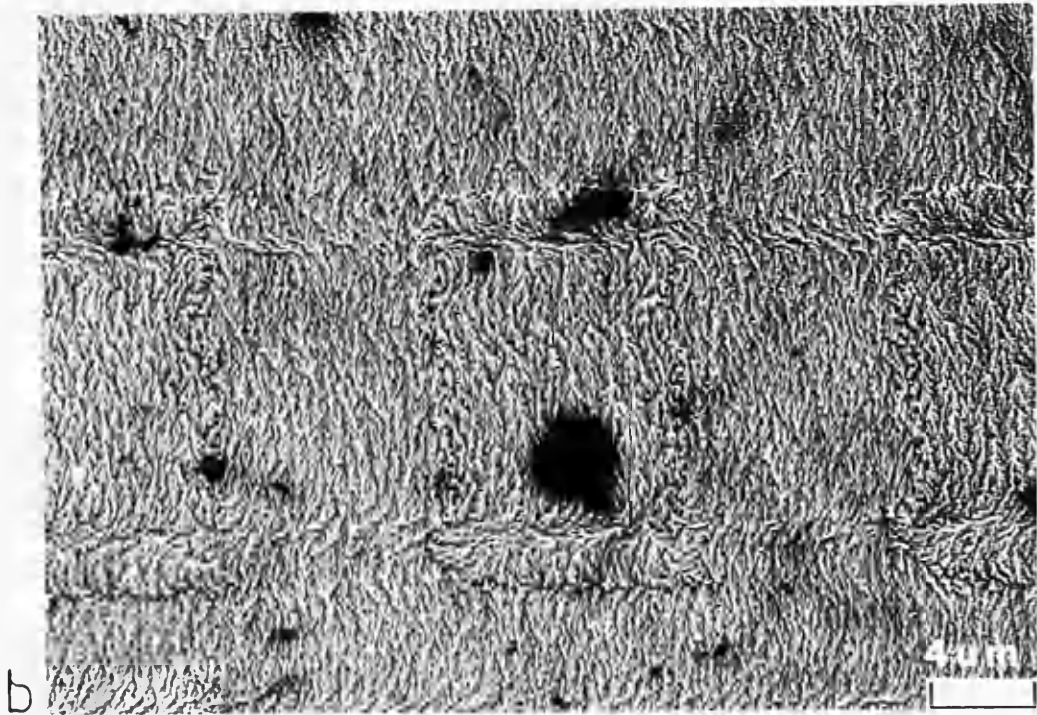
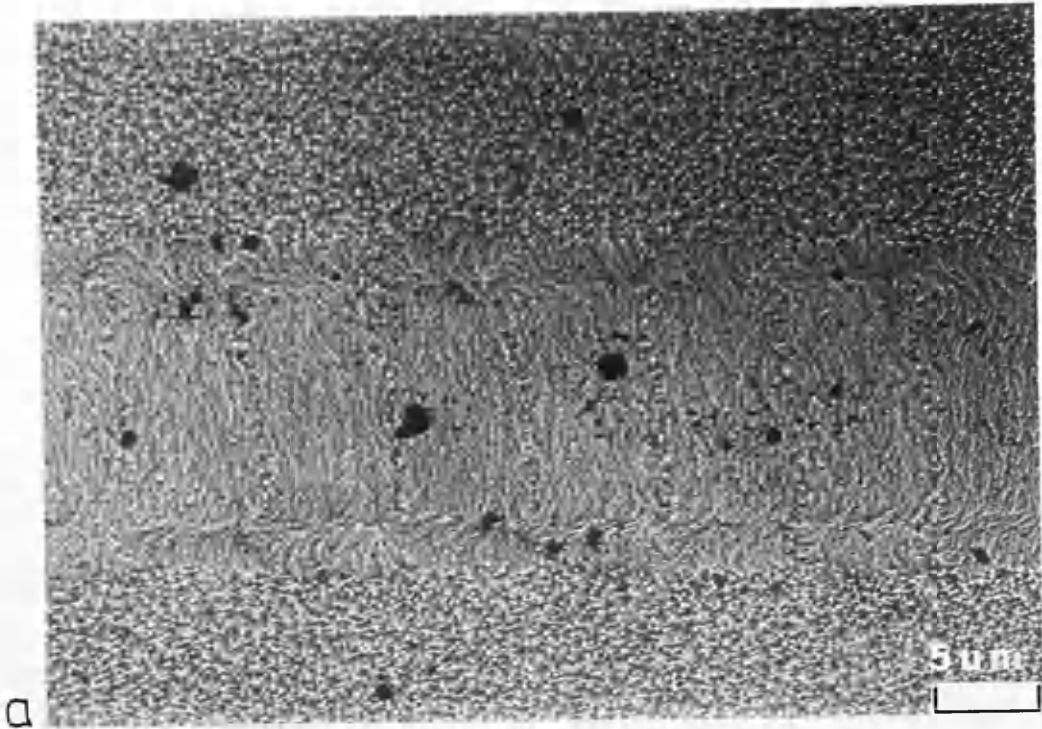


Figure 5.5 - Fresnel images of square wave written tracks written on (a) the virgin medium and (b) the d.c. erased medium.

again reflected the isotropic nature of the medium and is intimately related to the line structure observed in figure 5.4b.

Fresnel images of the micromagnetic domain structures of higher frequency tracks written on virgin material are given in figure 5.6. The observations remarked upon above regarding the structure of written bits appear to apply equally well to these tracks, but it was seen that as the write frequency increased the written transitions were placed so close together that they appear to merge and become less distinguishable, the side-written edge effects being the most visible feature visible.

A Fresnel image of an over-write experiment is given in figure 5.7 where a 3MHz track was partially over-written with a 8MHz track. The two written signals appeared consistent with the individually written tracks, exhibiting the same track domain structure discussed above for the tracks of figure 5.5. Evidence of the domain structure of one or other of the two signals was observed across the whole track width and this observation was used by Arnoldussen et al [2] to investigate the phenomenon of the side-erased bands reported at the edges of the written tracks.

In order to further characterise the magnetic microstructure of the written tracks differential phase contrast microscopy was employed using the VG HB5 scanning transmission electron microscope. One particular track was analysed to study the effects of writing on either the virgin or d.c. erased disk since

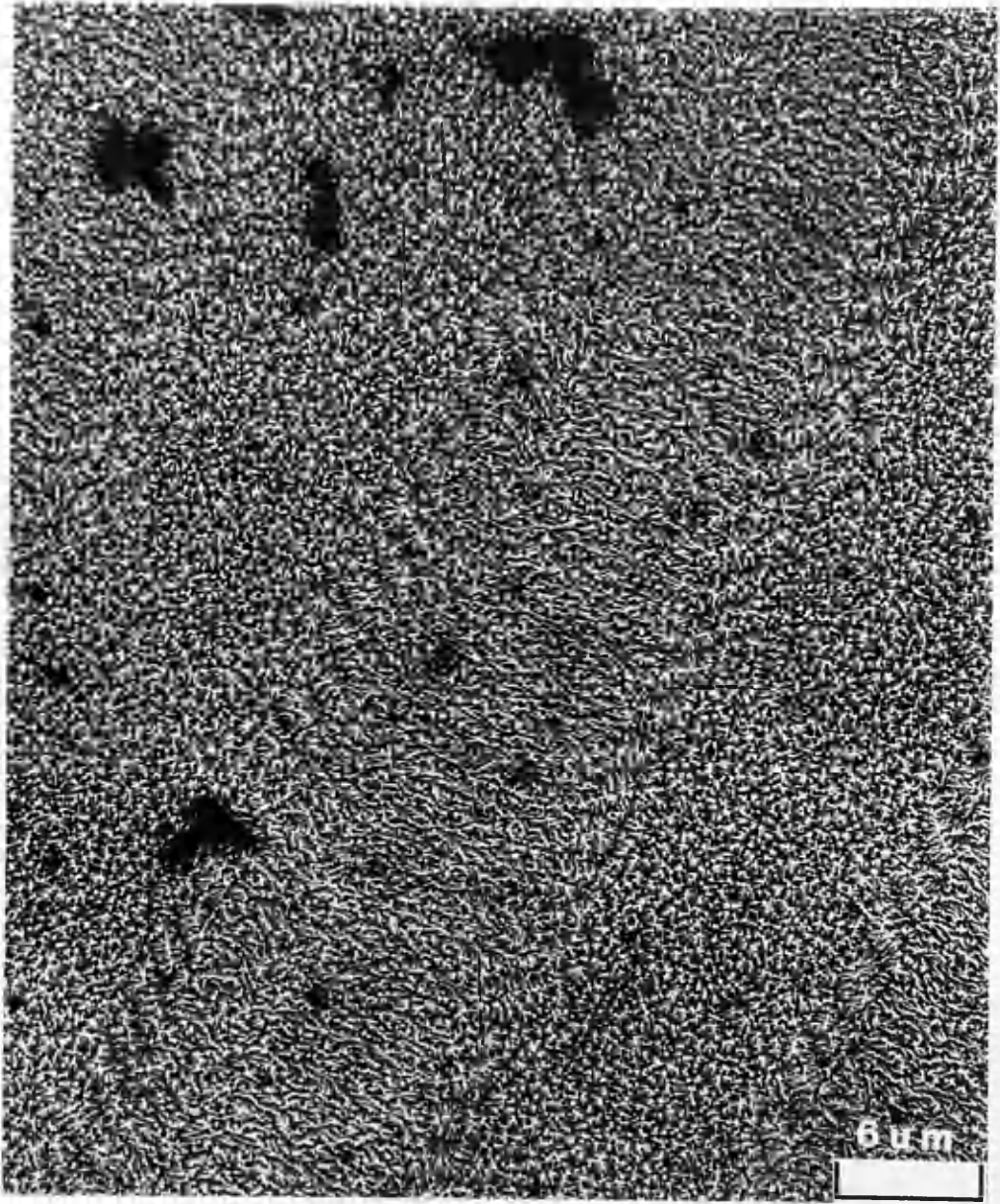


Figure 5.6 - A Fresnel image of higher frequency tracks written to the virgin medium.

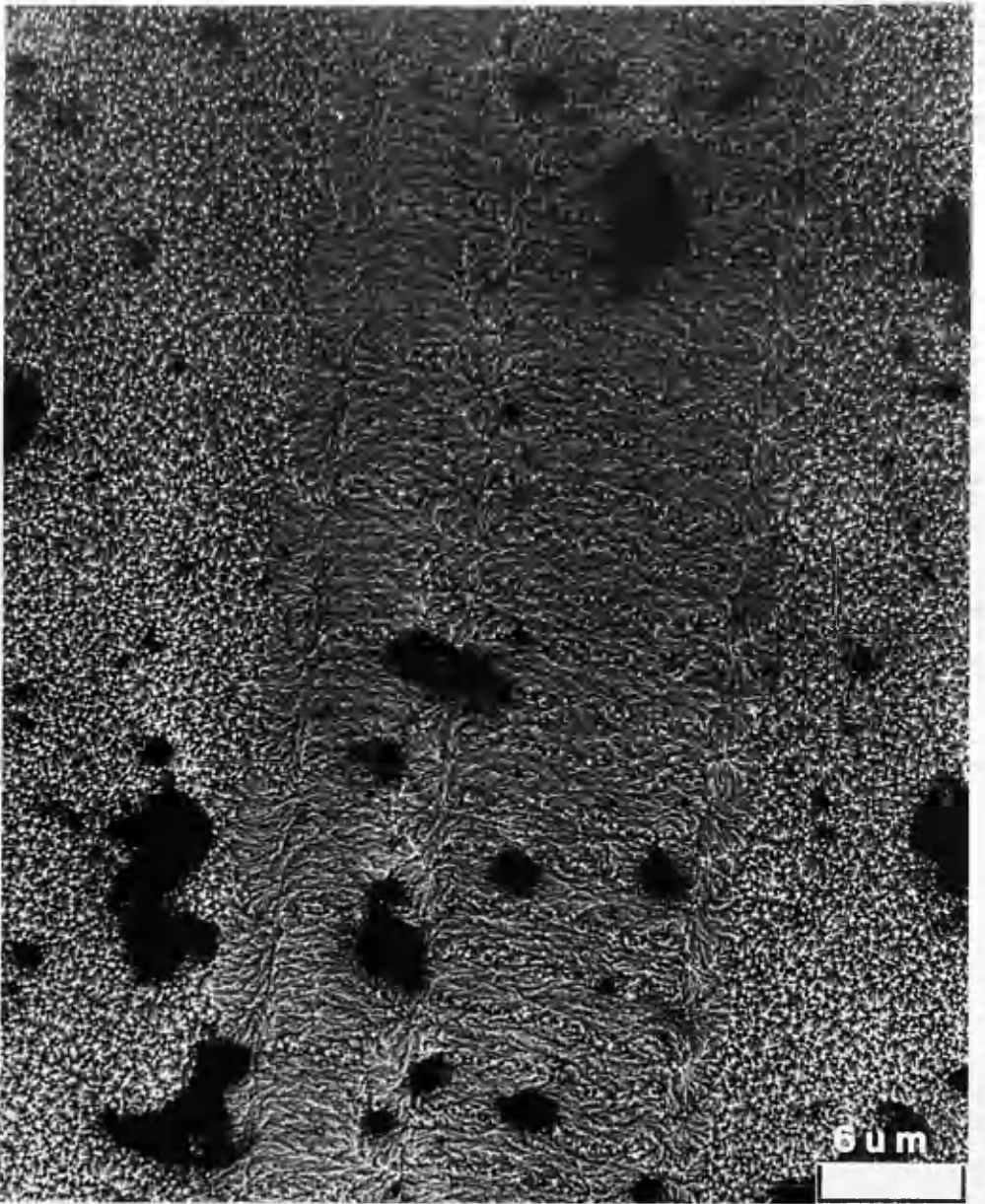


Figure 5.7 - A Fresnel image of a 3MHz track overwritten by an 8MHz track. The original medium was virgin disk.

it was written with one edge on the d.c. medium and the other on virgin disk, see figure 5.8. Images of both sides of this track were acquired separately by DPC microscopy, producing four images from each half of the track which are sensitive to induction in four different directions: parallel, perpendicular, and $\pm 45^\circ$ to the write direction. Figure 5.9 illustrates the images from the virgin side; figure 5.10 contains the images from the d.c. erased side.

From figure 5.9 it was observed that in all four images the virgin medium was seen to produce strong magnetic domain contrast, illustrating once more the isotropic character of the medium. The images sensitive to induction along the write direction, figures 5.9a and 5.10a, both show a vague outline of the domain wall structure within the track, but the low image or domain contrast suggests the difference in net induction between written bits is relatively small and therefore that the medium and stray field inductions almost cancel through the trajectory of the traversing electrons. Low DPC contrast in both figures 5.9 and 5.10 showed that this cannot be attributed to some characteristic solely associated with either of the two individual states of the medium before recording.

In the track images given and discussed above a slight curve or bend in the written transition wall can be observed and is highlighted in figure 5.11. The appearance of this feature in every written track indicated some flaw in the construction of the write head which manifests itself micromagnetically in this

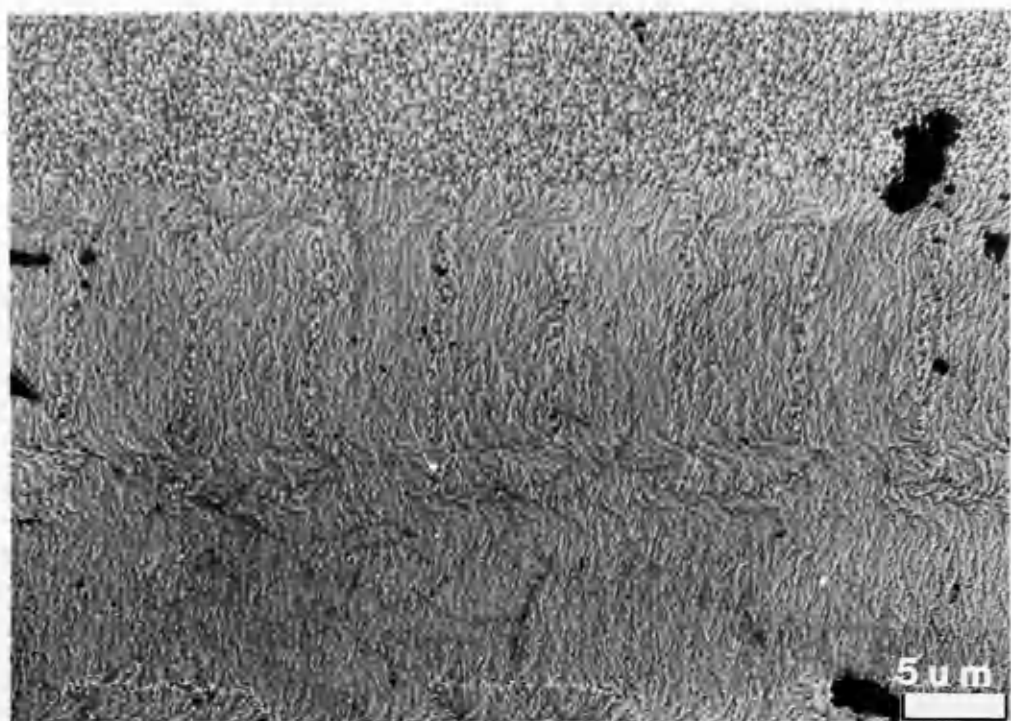


Figure 5.8 - A Fresnel image of a 2MHz ($\lambda=10\mu\text{m}$) track written partially on both the virgin and d.c. erased media.

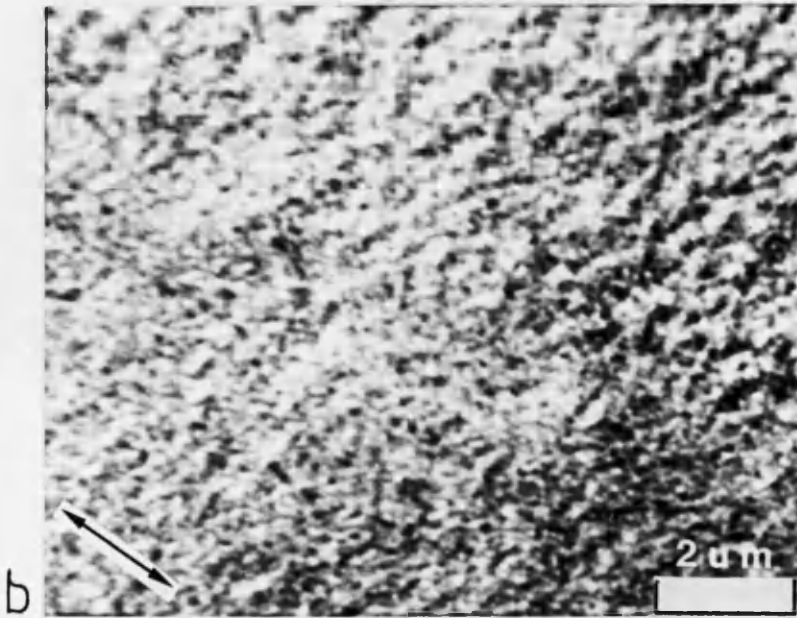
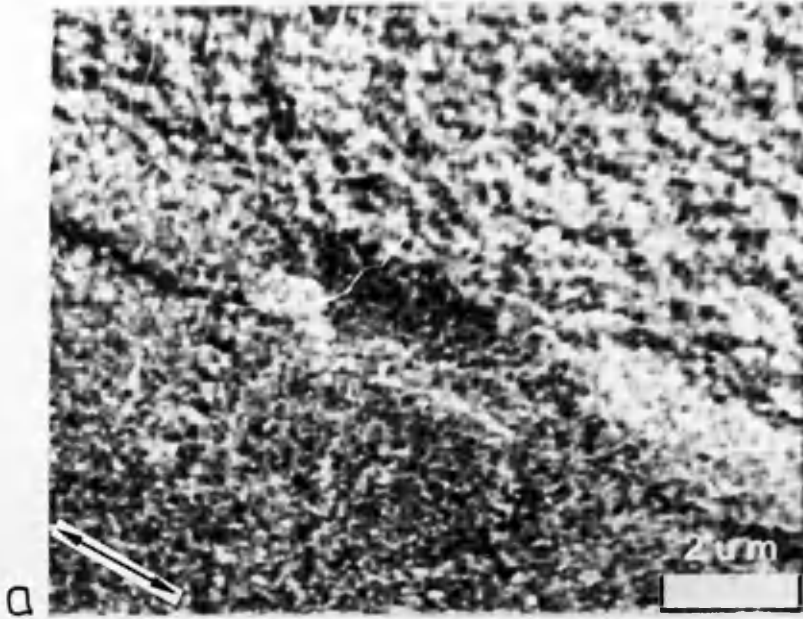
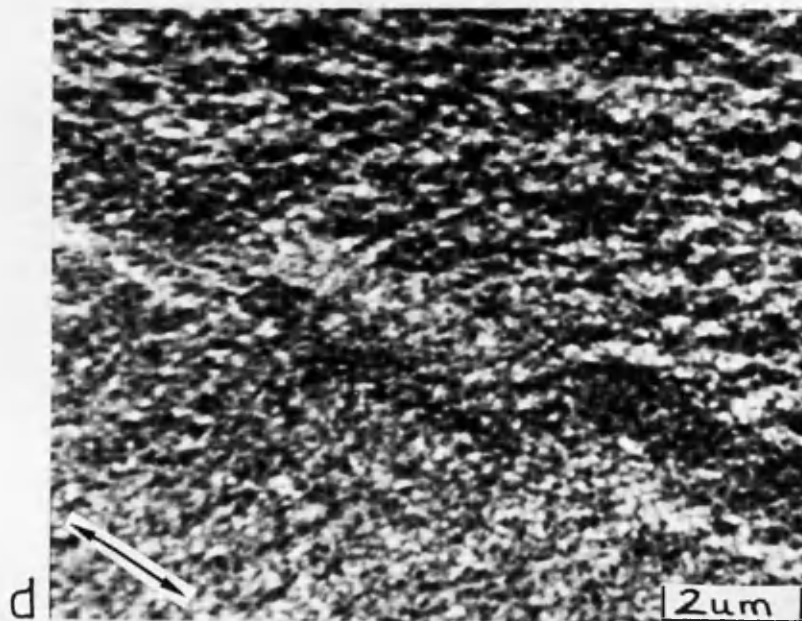
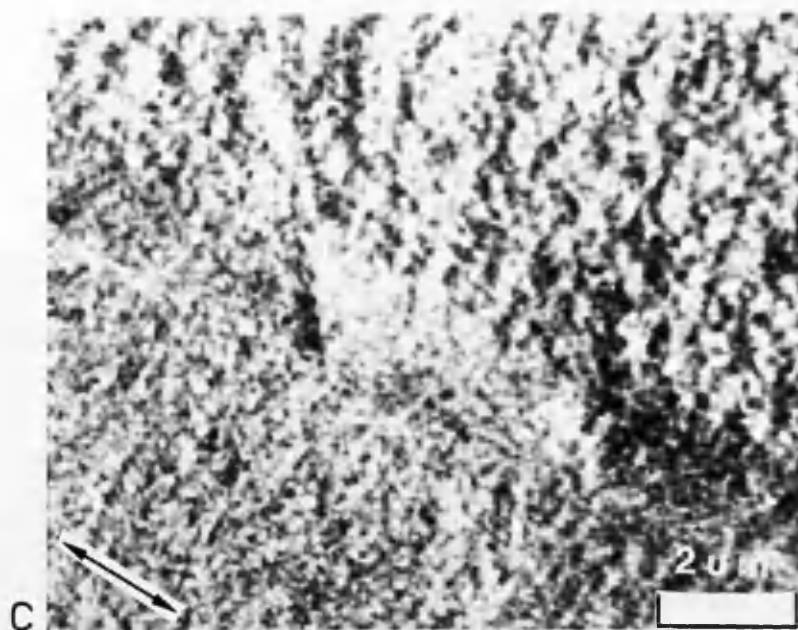


Figure 5.9 - Differential phase contrast images of the part of the track written on the virgin medium. The arrow indicates the write direction. The image contrast is sensitive to induction:
(a) parallel to the write direction;
(b) perpendicular to the write direction;



(c) $+45^\circ$ to the write direction;
(d) -45° to the write direction.

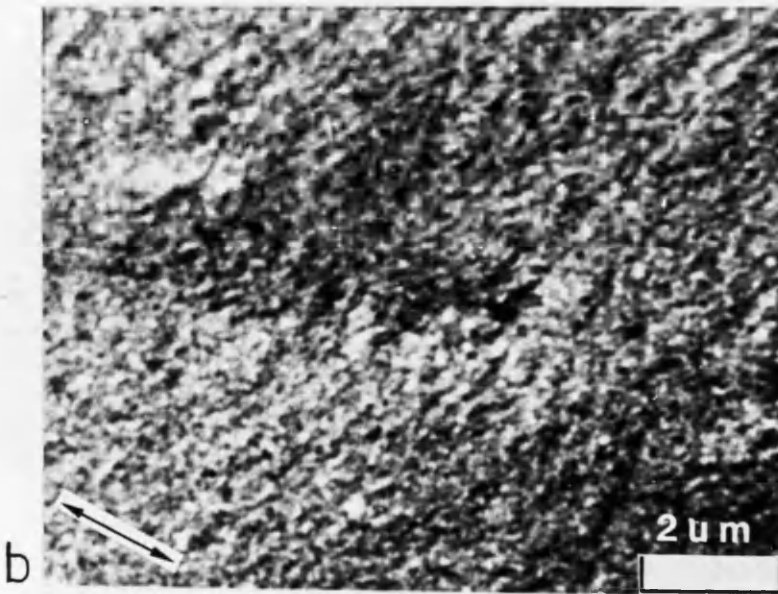
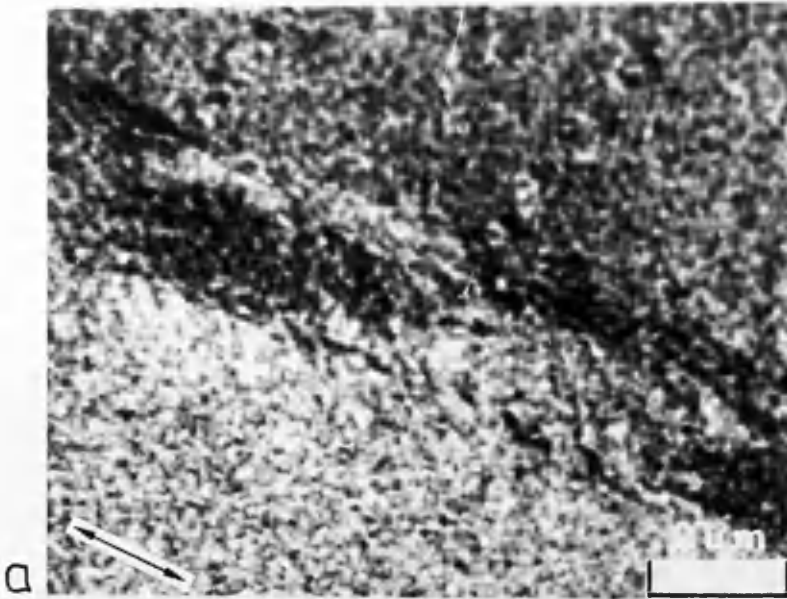
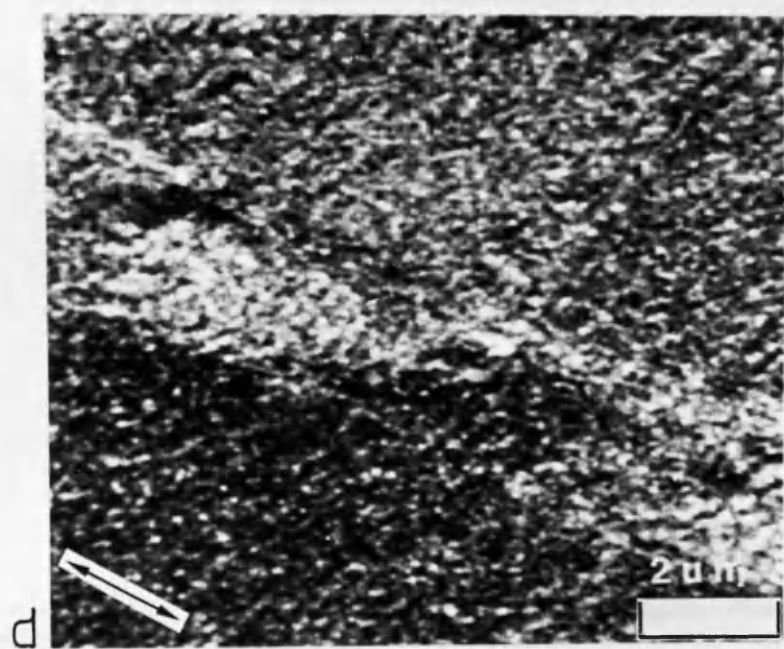
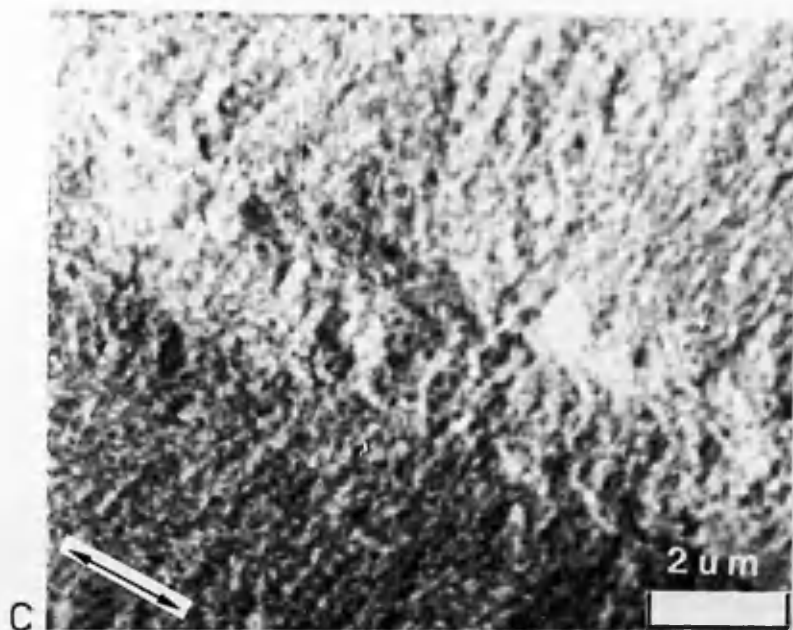


Figure 5.10 - Differential phase contrast images of the part of the track written on the d.c. erased medium. The arrow indicates the write direction. The image contrast is sensitive to induction:

- (a) parallel to the write direction;
- (b) perpendicular to the write direction;



(c) $+45^\circ$ to the write direction;

(d) -45° to the write direction.

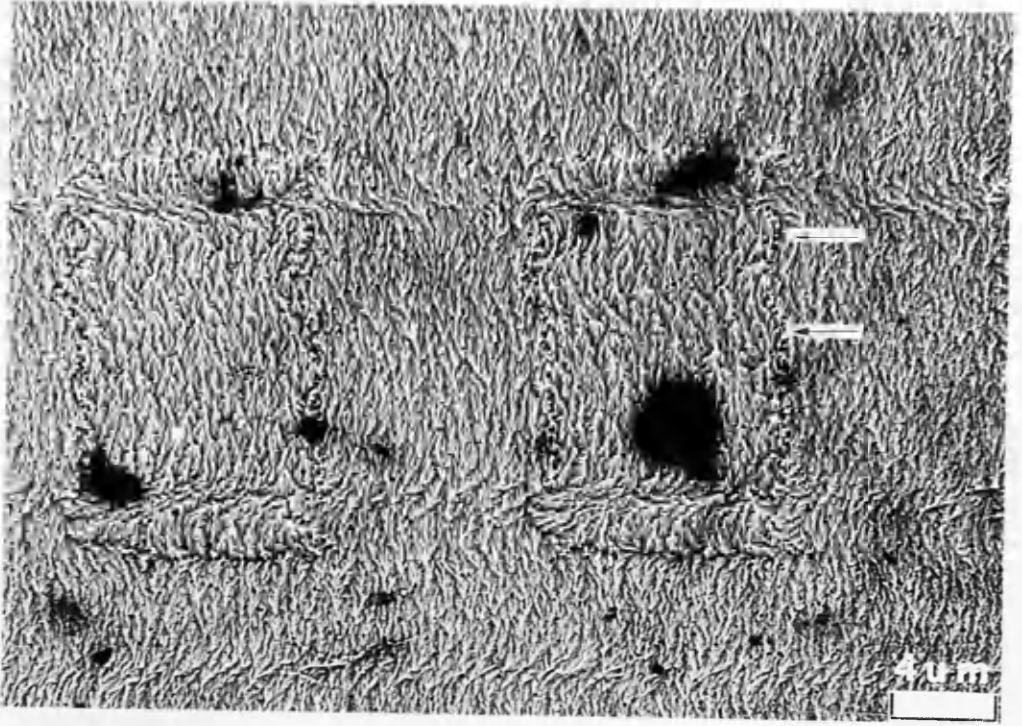


Figure 5.11 - In this Fresnel image of a track written on the d.c. erased medium the location of the transition feature is indicated.

deformation of the transition shape. Of all the tracks recorded none were seen more sensitive to the head performance than those written with decreasing write current to examine the non-saturation recording behaviour of the medium. The six tracks written to investigate this behaviour are shown in figure 5.12. It can be seen that as the current was reduced in the tracks T1 to T6:

(i) the curve associated with the write head construction gradually developed into a gap that splits the central portion of the written bits, indicating a weakness in coupling of the write field and medium relative to the rest of the central portion of the transition;

(ii) the side-written wing domain structures were observed to reduce in extent and eventually vanish, implying that the coupling between the side-writing field and the recording medium is considerably weaker than that generated in the central region of the write head. The actual value at which side-writing was no longer imaged was $\approx 15\text{mA}$;

(iii) the bits written against the d.c. erasure were seen to decompose or fragment into smaller domains at the lowest write current of 10mA .

These images illustrate clearly the variation in the character of the recorded tracks as the write current is decreased. They also highlight the sensitivity of the recording medium to any flaw in the head performance, suggesting that the medium could potentially be used to investigate the recording

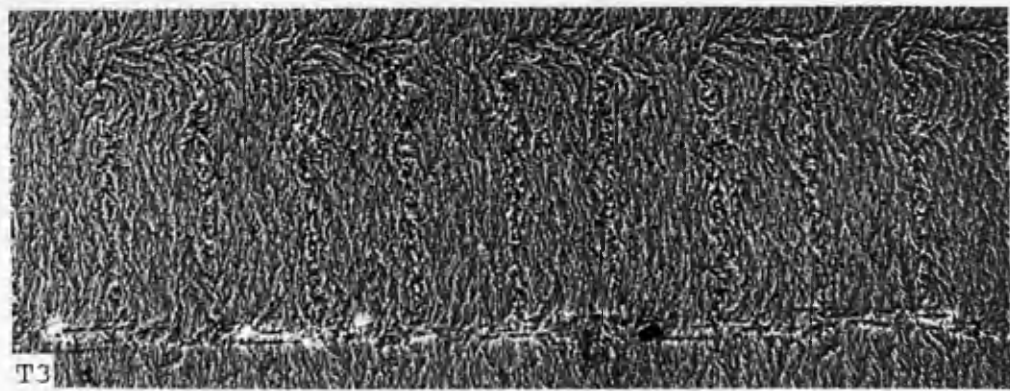
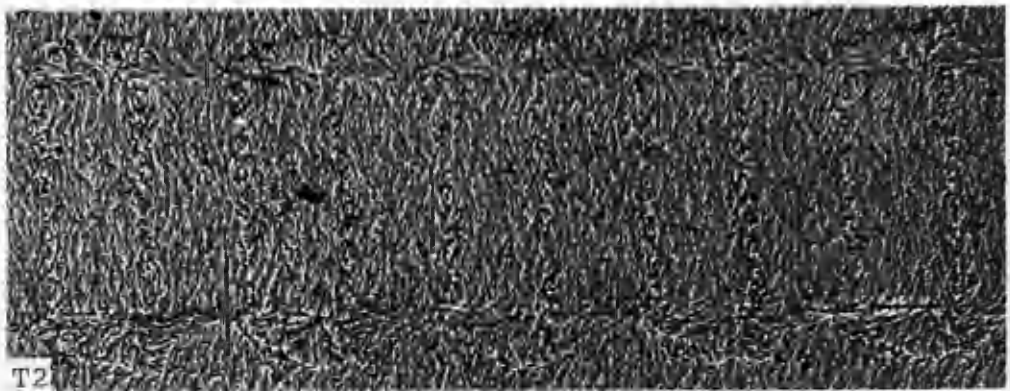
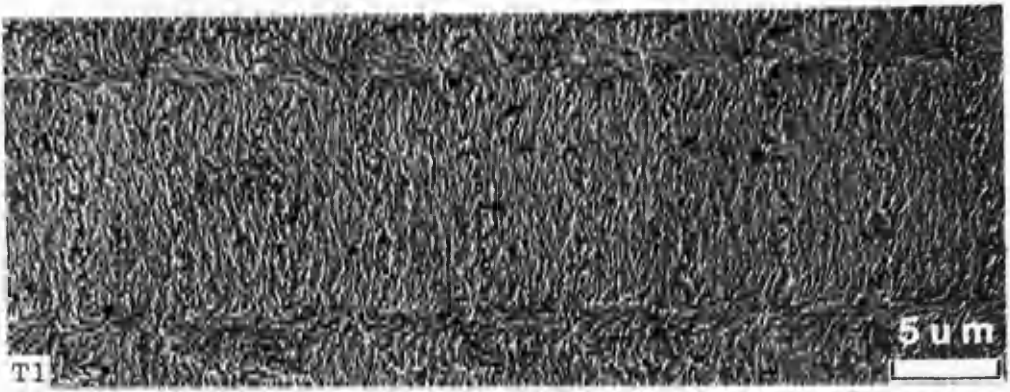
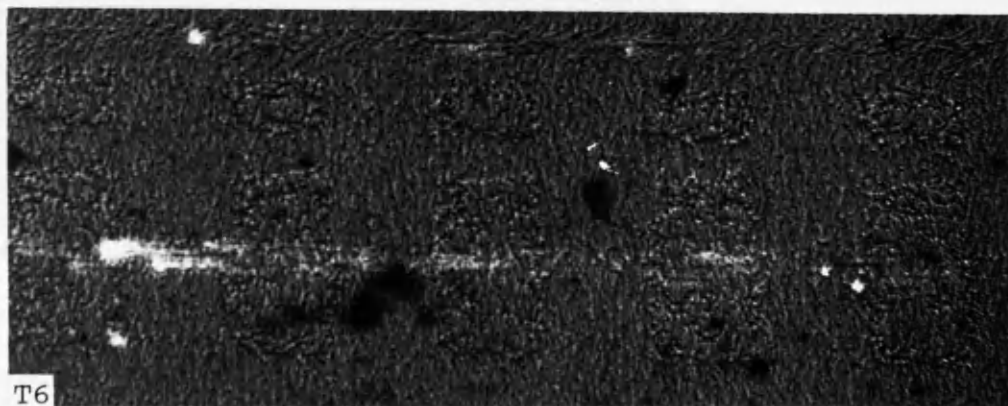
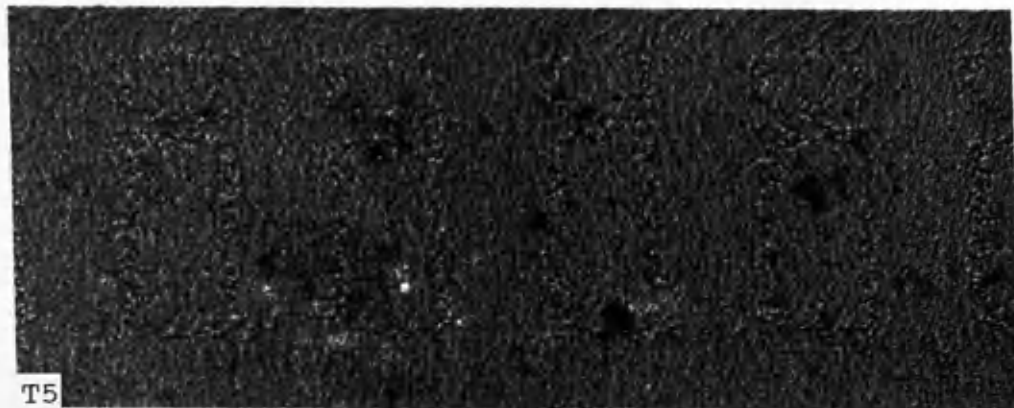
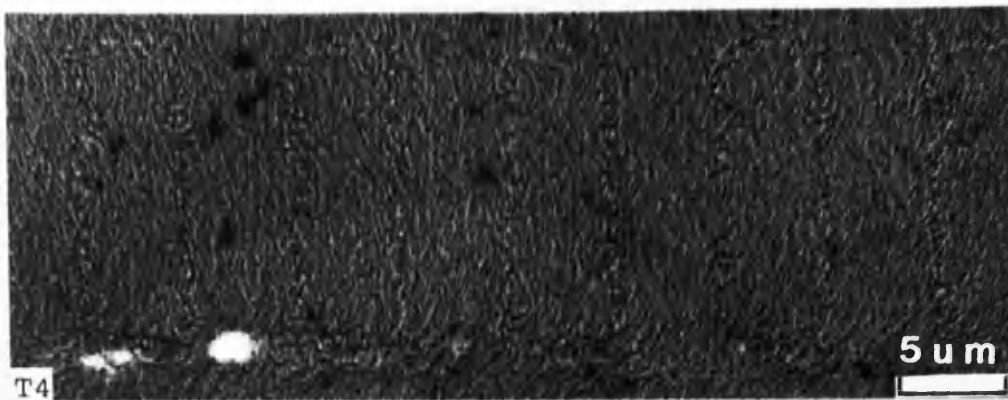


Figure 5.12 - (i) Fresnel images of tracks written with write currents of (a) 65mA-T1; (b) 20mA-T2; (c) 15mA-T3.



(ii) Fresnel images of tracks written with write currents of (c) 14mA-T4; (d) 12mA-T5; (e) 10mA-T6.

performance of write heads by correlating the various features of recorded tracks with associated changes in head construction.

5.3.2 SMALL ANGLE DIFFRACTION STUDIES

Three specific regions of the medium were examined by the technique of small angle diffraction (SAD) to investigate qualitatively the micromagnetics of the recording medium. The first of these was a region containing virgin material only, figure 5.13. If the medium magnetisation had been randomly oriented but completely in the plane of the film the observed diffraction pattern would have been a ring with a diameter generated by a Lorentz deflection equivalent to a magnetisation of $\approx 2M_s$, where M_s is the medium saturation magnetisation. The observed 'cloud' indicates that either the medium may in fact support a perpendicular component of magnetisation out of the plane of the virgin medium or that the diffuse diffraction intensity is a result of a scattering process within the film. If it is the case that there is no such scattering, this behaviour would most probably originate from the high cobalt content of the medium ($\approx 70\%$) which intrinsically exhibits an easy axis parallel to the crystallographic c-axis. A SAD image from a region in which tracks were written upon virgin disk is given in figure 5.14. Here a greater intensity was seen in the centre of the less diffuse pattern obtained, probably due to the recorded bit

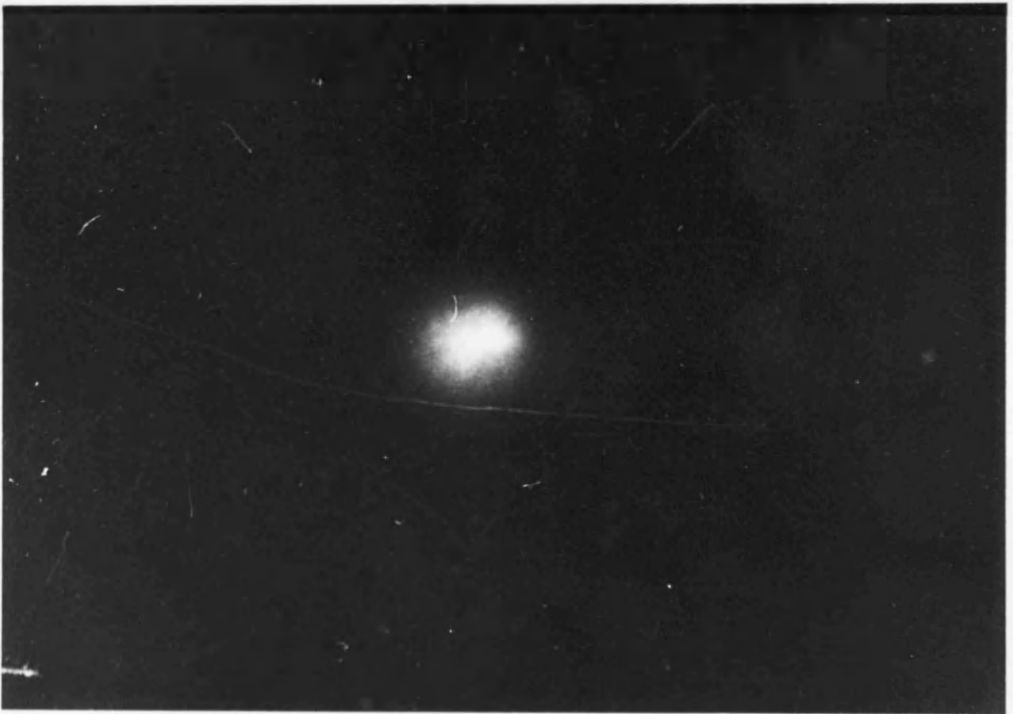
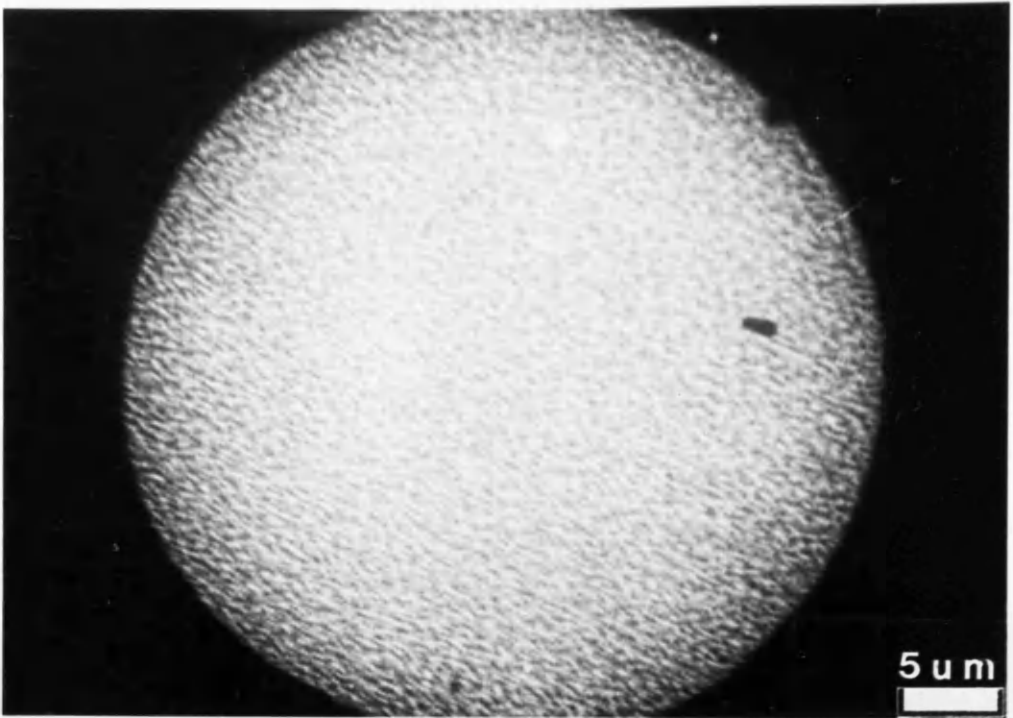


Figure 5.13 - A Fresnel image of virgin material and the corresponding small angle diffraction intensity distribution.

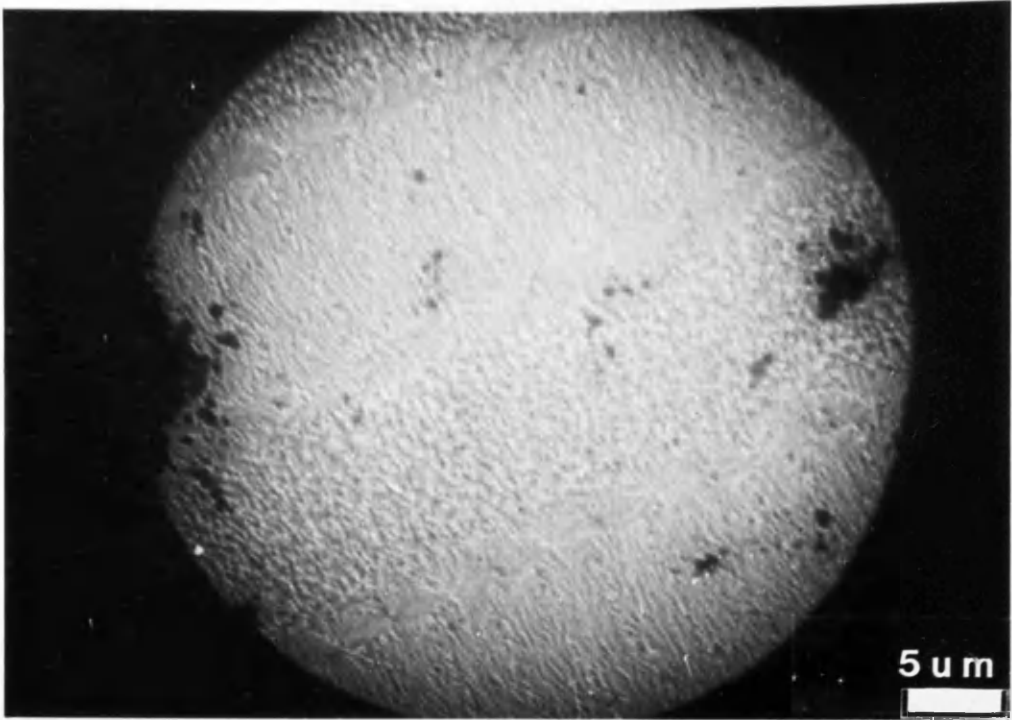


Figure 5.14 - A Fresnel image of track written on virgin material and the corresponding small angle diffraction intensity distribution.

magnetisation in the track. The final SAD experiment was performed with tracks written upon the d.c. erased medium. Figure 5.15 illustrates the observed diffraction intensity which consisted of two distinct spots, one assumed to originate from the d.c. erasure and the other from the undeflected electrons that sense little or no net induction as they pass through the written bits of the track. These experiments suggested that the in-plane d.c. erasing of the medium may have the effect of eradicating any perpendicular component of magnetisation within the medium.

5.4 SUMMARY

Transmission electron microscope images of the cobalt nickel chromium grain structure revealed it to consist of closely packed regularly shaped grains whose dimension was measured in the range 1nm-10nm. Any cracks or gaps in the film were observed not to extend in any one direction, they instead were seen to be uniformly oriented within the medium.

An initial characterisation of the medium micromagnetics by Lorentz electron microscopy provided information about the micromagnetic structure of the thin film medium. Strong magnetic ripple contrast was observed from every recorded track or d.c. erased region. This feature allowed the interpretation of the direction of magnetisation, defining regions in the side-written magnetic microstructure at the track edges

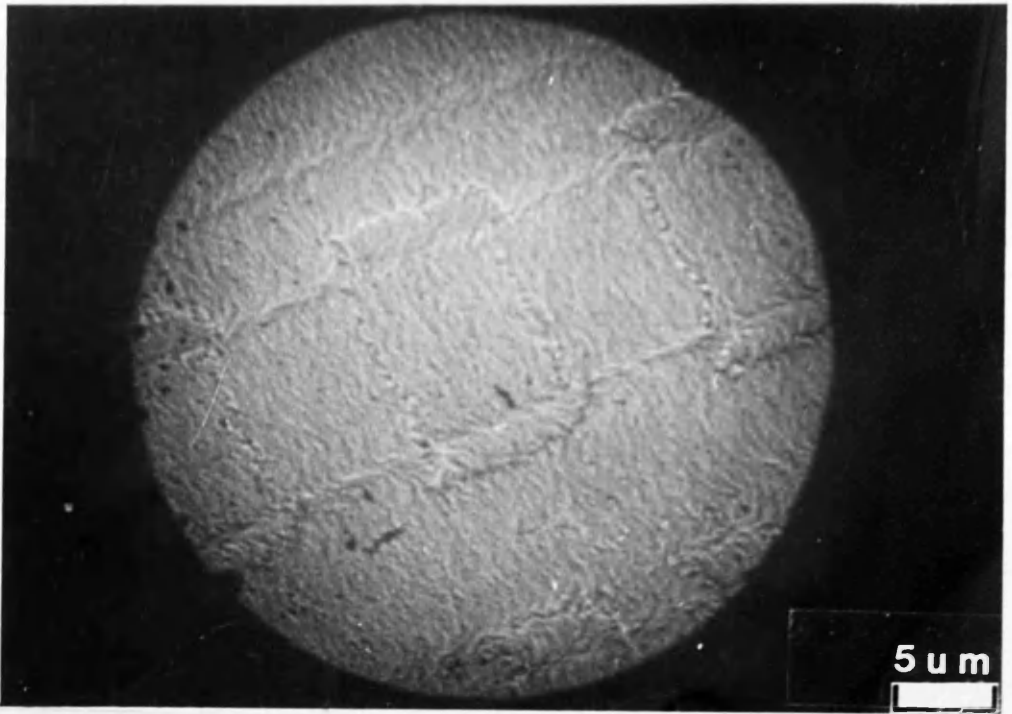


Figure 5.15 - A Fresnel image of track written on d.c. erased medium and the corresponding small angle diffraction intensity distribution.

where the medium magnetisation was recorded perpendicular to the write direction. This was consistent with the isotropic nature of the medium and differential phase contrast images of the virgin medium produced further evidence of this medium characteristic. Tracks written with non-saturating write currents allowed the deterioration of written bits to be observed as the current was decreased. These tracks were also seen to sensitively reflect the characteristics of the head design in their domain structures, revealing how a flaw in the particular head used for these write experiments could manifest itself in the form of the written magnetisation transition. Finally, small angle diffraction studies indicated the possibility that the virgin medium may exhibit a component of magnetisation directed out of the plane of the medium. A d.c. erasure of this medium then appeared to destroy this perpendicular component of magnetisation, constraining the magnetisation to lie strictly in the plane of the medium. Further, more extensive small angle diffraction studies are required to investigate this possibility further.

QUANTITATIVE ESTIMATION OF A.C. ERASED MEDIUM FLUX
NOISE POWER BY LORENTZ ELECTRON MICROSCOPY

6.1 INTRODUCTION

The property that ultimately determines the maximum areal recording density that a magnetic medium can support is the intrinsic noise generated by the medium magnetisation when data is read back. A more complete understanding of the relationship between the medium noise power and micromagnetisation is therefore of primary importance in evaluating recording media.

Lorentz electron microscopy allows the medium micromagnetics to be visualised, but as yet there has been little or no work undertaken to extract quantitative measurements of the medium noise from Lorentz images. The following two chapters describe the first such quantitative noise estimations using the iron cobalt chromium as a test recording medium.

This chapter concentrates on the initial development and evaluation of the noise estimation technique through the analysis of the most straight forward recorded signal, that of a.c. erasure. The success of the Lorentz derived noise measurements can be gauged from a comparison with noise power spectra measured electronically from the original hard disk by spectral analysis of the read back signal.

6.2 THE RELATIONSHIP BETWEEN THE MEDIUM MICROMAGNETISATION AND THE MEDIUM FLUX NOISE POWER

In chapter one the Reciprocity Model of the read process was introduced. The final expression given, equation (1.15), described the spatial relationship between the read signal $e(x_0)$ and the x component of the medium magnetisation $m_x(x, y, z)$ as

$$e(x_0) = -\mu_0 n \epsilon v \frac{\partial}{\partial x_0} \int_{-w/2}^{+w/2} dz \int_a^{d+b} dy \int_{-\infty}^{+\infty} dx h_x(x, y, z) \cdot m_x(x-x_0, y, z) \quad (6.1)$$

where n is equal to the number of head turns or windings, ϵ is the head efficiency, v is the head-medium velocity, μ_0 is the permeability of free space, and $h_x(x, y, z)$ represents the x component of the head sensitivity function. The remaining geometrical parameters are described in figure 1.10 which is copied overleaf - figure 6.1.

From this expression describing the spatial variation of the readback signal a relationship between the medium flux noise power and the medium magnetisation can be derived as follows [1]. Consider the correlation operation of two arbitrary functions $f(x)$ and $g(x)$, written as

$$c(x) = f(x) \bullet g(x) = \int_{-\infty}^{+\infty} f(x') \cdot g(x'-x) dx' \quad (6.2)$$

where \bullet denotes the correlation operator.

The standard result of the Fourier transform of the function $c(x)$ is

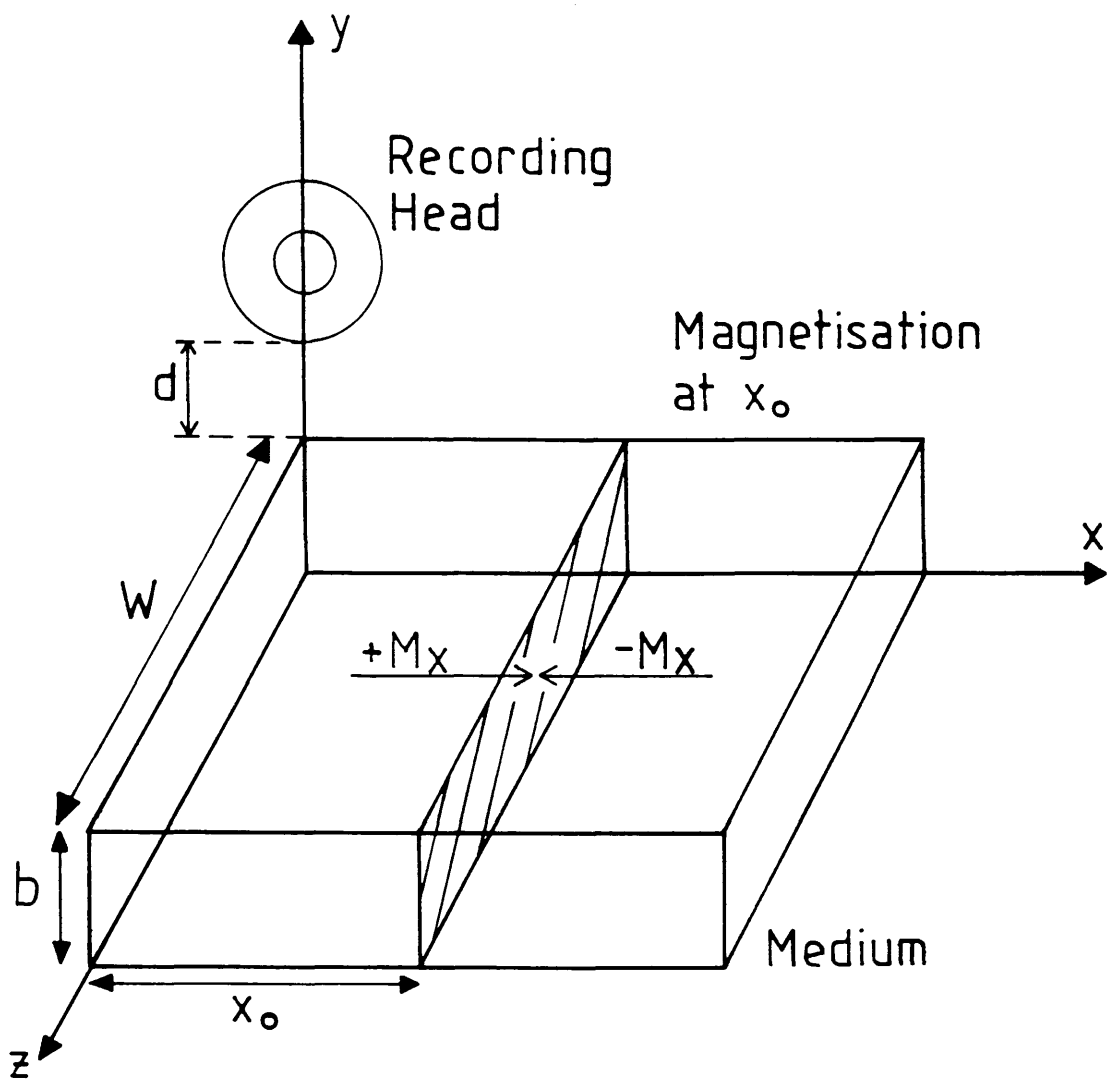


Figure 6.1 - The system geometry used in the Reciprocity Model derivation.

$$FT[c(x)] = C(k_x) = F(k_x) \cdot G^*(k_x) \quad (6.3)$$

where * denotes a complex conjugate.

A comparison between equations (6.1) and (6.2) shows that the read back signal is written in the form of a correlation integral between the head sensitivity function $h(x,y,z)$ and the medium magnetisation $m(x,y,z)$ with respect to x integration. Thus

$$e(x_0) = -\mu_0 n \epsilon v \frac{\partial}{\partial x_0} \int_{-w/2}^{+w/2} dz \int_d^{d+b} dy \{ h_x(x,y,z) \bullet m_x(x,y,z) \} \quad (6.4)$$

which, by equation (6.3), has a corresponding Fourier transform

$$E(k_x) = -\mu_0 n \epsilon v (ik_x) \int_{-w/2}^{+w/2} dz \int_d^{d+b} dy H(k_x, y, z) \cdot M^*(k_x, y, z) \quad (6.5)$$

where $H(k_x, y, z)$ and $M(k_x, y, z)$ are the Fourier transforms (with respect to the x direction) of $h_x(x, y, z)$ and $m_x(x, y, z)$ respectively.

Let the read back spectral power be defined as

$$\begin{aligned} P(k_x) &= E(k_x) \cdot E^*(k_x) \\ &= (\mu_0 n \epsilon v k_x)^2 \int_{-w/2}^{+w/2} dz \int_{-w/2}^{+w/2} dz' \int_d^{d+b} dy \int_d^{d+b} dy' \\ &\quad [H(k_x, y, z) \cdot H^*(k_x, y', z') \cdot M^*(k_x, y, z) \cdot M(k_x, y', z')] \end{aligned} \quad (6.6)$$

The partially Fourier transformed head sensitivity function $H(k_x, y, z)$ is assumed constant across the track width $[-W/2, +W/2]$, that is, $H(k_x, y, z)$ independent of z .

Equation (6.6) can then be written

$$\begin{aligned} P(k_x) &= (\mu_0 n \epsilon v k_x)^2 \int_{+w/2}^{d+b} dy \int_{+w/2}^{d+b} dy' H(k_x, y) \cdot H^*(k_x, y') \\ &\quad \cdot \int_{-w/2} dz \int_{-w/2} dz' M^*(k_x, y, z) \cdot M(k_x, y', z') \end{aligned}$$

(6.7)

For a single layer thin film recording medium, such as iron cobalt chromium, it is reasonable to believe that the magnetisation is uniform throughout the film thickness, $y=d$ to $d+b$. Then

$$\begin{aligned}
 P(k_x) &= (\mu_o n \epsilon v k_x)^2 \int_{d+w/2}^{d+b} dy H(k_x, y) \int_{d+w/2}^{d+b} dy' H^*(k_x, y') \\
 &\quad \int_{-w/2}^{d+w/2} dz M^*(k_x, z) \int_{-w/2}^{d+w/2} dz' M(k_x, z') \\
 &= \frac{(\mu_o n \epsilon v k_x)^2 \left| \int_d^{d+b} H(k_x, y) dy \right|^2}{F_E} \frac{\left| \int_{-w/2}^{+w/2} M(k_x, z) dz \right|^2}{F_I}
 \end{aligned}
 \tag{6.8}$$

This expression for $P(k_x)$ can be considered as a multiplication of two terms - F_I arising from contributions intrinsic to the medium and F_E from extrinsic contributions. F_I is solely dependent upon intrinsic medium qualities and hence characterises the reciprocal (k_x -space) response of the medium. The effect of F_E upon F_I is to shape the spectral response of the medium by the response of the read head and read channel. The medium spectral flux power is thus defined as

$$\begin{aligned}
 S(k_x) &= \frac{P(k_x)}{(\mu_o n \epsilon v k_x)^2 \cdot \left| \frac{1}{b} \cdot \int_d^{d+b} H(k_x, y) dy \right|^2} \\
 &= \left| b \cdot \int_{-w/2}^{+w/2} M(k_x, z) dz \right|^2
 \end{aligned}
 \tag{6.9}$$

or, normalising for the sample volume,

$$S(k_x) = \frac{\left| b \cdot \int_{-w/2}^{+w/2} M(k_x, z) dz \right|^2}{W \cdot b \cdot X}
 \tag{6.10}$$

where X is the length along the track or write

direction of the sample analysed.

The spectral power function $S(k_x)$ multiplied by the film thickness b was chosen as a measure of the medium noise since the electron microscope images are two-dimensional in the x - z plane. In the particular case of an a.c. erased medium the measured spectral flux power can be considered completely as noise since no signal was written. Hence the a.c. erased medium noise spectral flux power is given by

$$b.S(k_x) = \frac{\left| b \int_{-w/2}^{+w/2} M(k_x, z) dz \right|^2}{W.X} \quad (6.11)$$

From the above equation it is seen that the medium noise power can be estimated from an image or map of the medium micromagnetisation. To make quite clear how the noise can be calculated from a two-dimensional magnetisation map $m(x, z)$ (as determined from Lorentz electron microscopy) equation (6.11) was developed further.

The Fourier transform of the medium magnetisation with respect to x can be written as

$$M(k_x, z) = \int_{-\infty}^{+\infty} m(x, z) e^{-ik_x x} dx \quad (6.12)$$

The two-dimensional Fourier transform of the magnetisation, $M(k_x, k_z)$, is given by

$$M(k_x, k_z) = \int_{-\infty}^{+\infty} \int_{-\infty}^{+\infty} m(x, z) e^{-ik_x x} e^{-ik_z z} dx dz \quad (6.13)$$

Let

$$\begin{aligned} Q &= \int_{-\infty}^{+\infty} M(k_x, z) dz = \int_{-\infty}^{+\infty} \int_{-\infty}^{+\infty} m(x, z) e^{-ik_x x} dx dz \\ &= M(k_x, k_z=0) \end{aligned} \quad (6.14)$$

Thus,

$$b.S(k_x) = \frac{| b.Q |^2}{W.X} = \frac{| b.M(k_x, k_z=0) |^2}{W.X} \quad (6.15)$$

It is therefore seen that the medium spectral flux power can be estimated from a given sample by calculating the two-dimensional Fourier transform of the medium micromagnetisation $M(k_x, k_z)$ and extracting the set of points in reciprocal space defined by the line $k_z=0$.

Finally, equation (6.15) can be reduced to a one-dimensional analysis. Consider the magnetisation averaged across the z-direction, say over a track width W :

$$\overline{m}(x) = \frac{\int_{-W/2}^{+W/2} m(x, z) dz}{W} \quad (6.16)$$

Then

$$\begin{aligned} \overline{M}(k_x) &= (1/W) \cdot \int_{-\infty}^{+\infty} \int_{-W/2}^{+W/2} m(x, z) e^{-ik_x x} dz dx \\ &= (1/W) \cdot M(k_x, k_z=0) \end{aligned} \quad (6.17)$$

Thus, the one-dimensional equivalent of equation (6.15) is

$$b.S(k_x) = \frac{W \cdot | b. \overline{M}(k_x) |^2}{X} \quad (6.18)$$

In summary, the above analysis has produced expressions from which the medium flux noise power spectrum for the a.c. erased medium (that is, $b.S(k_x)$ against reciprocal frequency k_x) can be calculated using either the two-dimensional Fourier transform of the map of the medium micromagnetisation or else the one-dimensional Fourier transform of the magnetisation averaged across the z direction, which is perpendicular to the write

direction. These estimates can then be compared directly with the corresponding noise spectra measured electronically from analysis of the read back signal.

6.3 ELECTRONIC MEASUREMENT OF THE MEDIUM FLUX NOISE POWER

The measurement of the a.c. erased and track medium noise spectra were made by L.L.Nunnally [9] at the laboratories of the General Products Division of IBM. An eighteen turn thin film head was used for writing and reading at an interface speed of 38ms^{-1} relative to the iron cobalt chromium rigid disk. The noise power spectra at the output of the recording channel preamplifier were measured with a spectrum analyser. Measurements were taken from the a.c. erased medium and also from square wave written tracks with write frequencies from 1MHz to 20MHz. The thermal noise power spectrum from the head and amplifier was collected with the head unloaded from the disk. The noise from the medium alone was then obtained by subtracting quadratically the head and electronic noise from the total noise after the signal peaks (if present) had been suppressed numerically.

The noise power, $P(f)$, was corrected for amplifier gain and spectrum analyser bandwidth to give the noise power spectrum at the terminals of the head. The medium flux noise power per unit area, $b.S(k_x)$, was then obtained from the experimental $P(f)$ from the following

NOISE RISES DUE TO TYPICAL SIGNAL

* These electronic spectral estimates have a worst case uncertainty of between -40% and +70%.

The following table shows the results of the spectral analysis of the signal. The signal was analyzed using a spectrum analyzer with a resolution bandwidth of 100 Hz. The results are shown in the table below. The signal is a complex waveform and the results are given in dBm/Hz. The signal is a complex waveform and the results are given in dBm/Hz. The signal is a complex waveform and the results are given in dBm/Hz.

expression [1]

$$b.S(k_x) = \frac{P(f)}{2v(k_x \mu_o \varepsilon N)^2 W} \cdot \frac{1}{|H(k_x, d)|^2} \cdot \left(\frac{2 \cdot k_x \cdot b}{1 - e^{2k_x b}} \right) \quad (6.19)$$

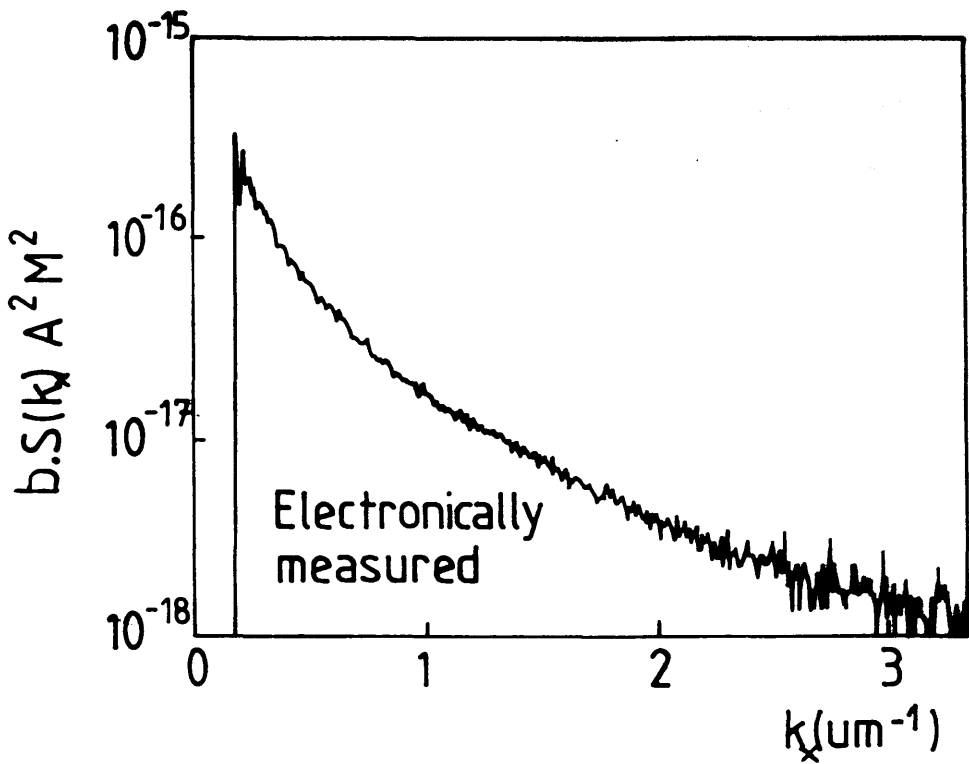
where $P(f)$ is the corrected measured noise power (V^2/Hz), f is temporal frequency (Hz), v is the interface velocity ($38ms^{-1}$), μ_o is the free space permeability, ε is the head efficiency (0.8), N is the number of head turns (18), W is the track width ($15\mu m$), d is the head to medium spacing ($\approx 0.28\mu m$), and b is the medium thickness. The head spectral response $H(k_x, d)$ is the Fourier transform of the head sensitivity function along the track at head to media spacing d . The medium flux noise power spectrum for the a.c. erased medium is shown in figure 6.2.*

6.4 PREPARATION OF MEDIUM MICROMAGNETISATION MAPS AND THE CALCULATION OF LORENTZ DERIVED NOISE SPECTRA BY FAST FOURIER TRANSFORM COMPUTATION

In this work digital image processing techniques have been employed both to produce representations of the medium magnetisation and in calculating the medium noise power from such images. The software used was the IBM IAX Image Processing system (IAX) which was operated on the IBM 3090 mainframe computer.

(A) MAPPING THE MEDIUM MICROMAGNETISATION

The iron cobalt chromium recording medium was chosen because of its high magnetic anisotropy. This



FLUX POWER SPECTRUM-AC-BULK ERASED

Figure 6.2 - A.C. erased medium flux noise power measured electronically over a track length of $\approx 10^5 \mu m$.

constrains the magnetisation to lie essentially parallel or anti-parallel to the easy axis with a magnitude equal to the saturation value $|M_s|$ [2]; this greatly simplifies the interpretation of the magnetisation within domains. With the a.c. erased micromagnetic structure the electron microscope beam deflection from the stray field effects above and below the medium can be neglected; the magnetic induction experienced by the electron beam then arises from the medium micromagnetisation alone. This allowed both differential phase contrast (DPC) and Fresnel Lorentz electron microscopy to be employed to visualise the medium micromagnetic domain structure. Binary magnetisation maps were then created from such Lorentz images on the assumption that the magnetisation lies parallel/anti-parallel in neighbouring domains.

DPC imaging on the VG HB5 scanning transmission electron microscope allowed an in-focus image of the medium micromagnetic domain structure to be acquired. Differentiating so that the image contrast was sensitive to the components of induction along the easy axis produced light and dark contrast in neighbouring domains, so revealing the domain geometry. Along with the magnetic contrast however contrast arising from the disk texturing process was imaged. In order to decrease its influence in the DPC images, the images were processed with the kernel operator described in figure 6.3. Thresholding the images now allowed binary contrast between intensities representing neighbouring domains to be established while simultaneously removing

0	0	0
1	1	1
0	0	0

Dimension: 3pels x 3pels
Divisor: 3
Boundary: leave

Figure 6.3 - This nine element kernel window reduced the striation contrast in differential phase contrast images when the texture ran vertically up the images. It assigns the three element horizontal average to the central pixel.

any trace of the physical striation contrast. The anisotropic behaviour of the medium has thus been fully incorporated into the medium magnetisation map obtained from the DPC image.

With Fresnel imaging the domain structure was delineated by light and dark contrast domain wall boundaries in the out-of-focus image of the specimen. The amount of de-focus was kept optimal in order to define accurately the medium micromagnetics. Large prints of these micrographs (for example, a $50\mu\text{m}$ by $30\mu\text{m}$ image printed 50cm by 30cm) were made from which the domain structures could be easily delineated. Oppositely magnetised domains were then differentiated in the prints by either colouring domains black and white or removing all domains that were magnetised in one of the two directions and placing the photograph on top of a sheet of paper to produce black and white contrast between the two differently magnetised sets of domains. The resultant photographs were stored digitally on computer using a digitizing camera to give images in which the oppositely magnetised domains could be distinguished by intensity thresholding. This last stage in the preparation of the Fresnel images produced the required binary magnetisation maps.

Although more tedious, the technique involving Fresnel imaging was superior in one important respect. The HB5 electron microscope was limited in its ability to image areas greater than approximately 400 square microns because of the degradation in the performance of the post-specimen de-scan electron optics at low

magnifications. Fresnel imaging on the other hand provided images of larger specimen areas from which the resulting analysis should be less sensitive to local structural inhomogenities.

(B) GRAPHICAL DEVELOPMENT OF COMPUTED FAST FOURIER TRANSFORM RESULTS

In order to evaluate the spectral noise power expressions of equations (6.15) and (6.18) a means of calculating the Fourier transform of the medium magnetisation had to be found. Employment of the fast Fourier transform algorithm was chosen as the solution [3,6,7,8].

A branch of Fourier theory describes how a continuous function or image can be represented by a discrete, finite set of data points (as with digital data) and how this data set can be transformed to produce a second discrete finite data set. This second set then describes the reciprocal spectrum of the first, and the transform is known as the discrete Fourier transform (dFt). The two data sets are identified as a dFt pair, one set approximating the continuous real function, the other the continuous Fourier transform (cFt) of the real function. The fast Fourier transform (FFT) is a computer program that calculates the dFt. The relationship between cFt and dFt pairs must be established if FFT results are to be correctly interpreted. A graphical description of this relationship is therefore presented here; a more extensive and mathematical treatment can be found in

Brigham [3], Bracewell [4], and Cordell and Grauch [5]. Consider figure 6.4, the left and right columns of this diagram represent real and reciprocal space. Figure 6.4a graphs a cFt pair $h(x)$ and $H(k)$. To calculate the discrete Fourier transform $H'(k)$ by FFT, $h(x)$ must first be modified for computation. A finite set of discrete data values is required as input. To this end $h(x)$ is sampled by multiplication with the function $\Delta_0(x)$ described in figure 6.4b, the product in figure 6.4c. At this stage the modified transform differs only from the continuous transform $H(k)$ if any reciprocal space overlap, or 'aliasing', arises from the sampling interval T of $\Delta_0(x)$. The Nyquist sampling condition [3] states that the sampling interval T must be chosen so that $1/T$ is at least twice the largest reciprocal frequency required to be measured from the transform spectrum; if T were chosen too large, frequencies of interest would be corrupted by aliasing - figure 6.4c shows the resulting overlap in reciprocal space.

The product function $\{h(x) \cdot \Delta_0(x)\}$ describes a sampled data set of infinite extent. For computational purposes it is necessary to truncate the data to, say, N points; this is accomplished by a second multiplication - $\{h(x) \cdot \Delta_0(x)\}$ by a truncation window $w(x)$, see figure 6.4d. Figure 6.4e illustrates the resulting transform pair, and now a second variation from the continuous $H(k)$ is apparent. The observed smoothing or averaging is produced by the convolution in reciprocal space of $\{H(k) \circledast \Delta_0(k)\}$ (where \circledast represents

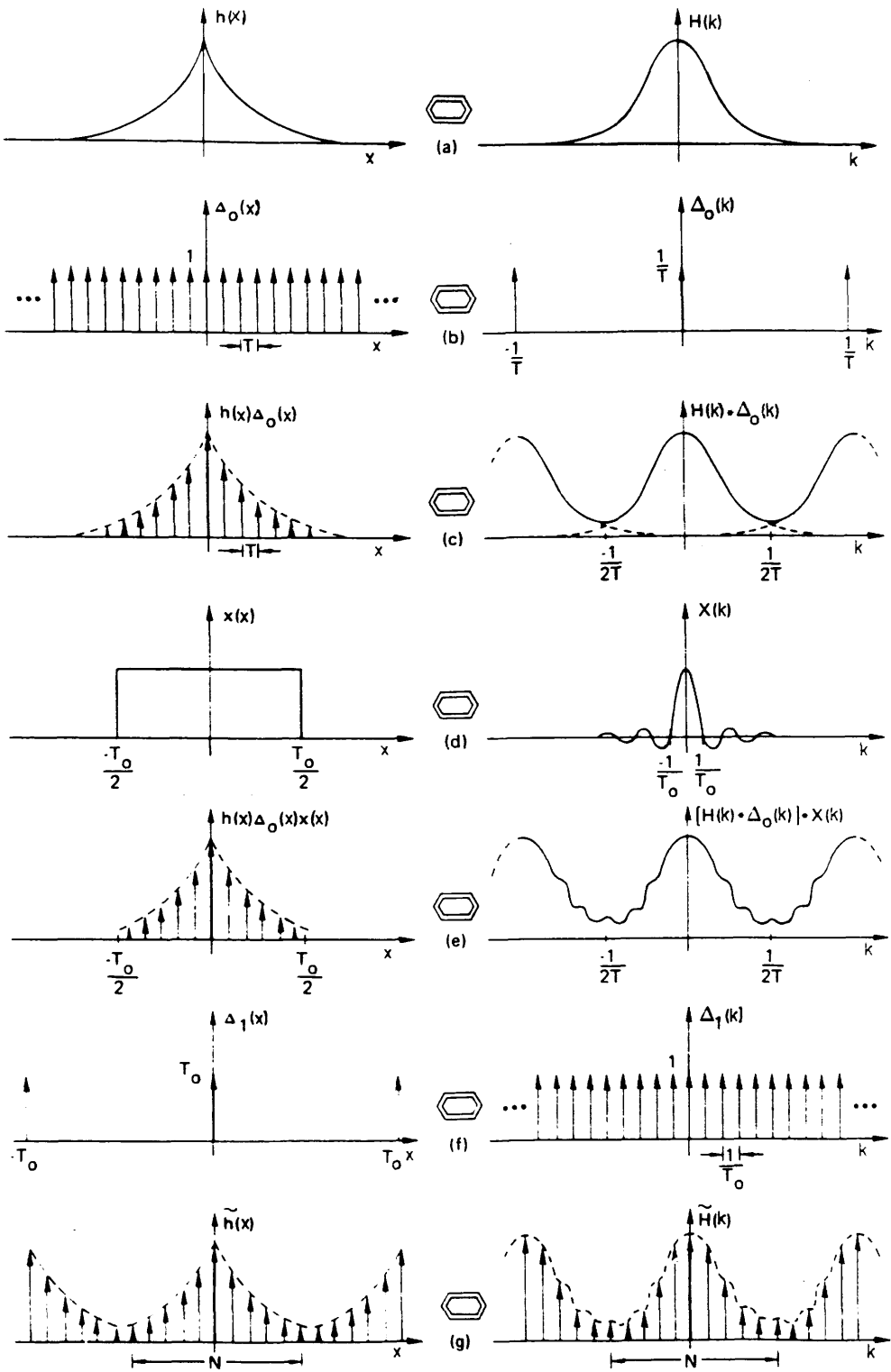


Figure 6.4 - Graphical development of the discrete Fourier transform (Brigham [3]).

the convolution operation) with the sinc function transform of the rectangular truncation window ($\sin[kT_0]/kT_0$). As the window increases in length the corresponding sinc function approaches an impulse function, hence this effect is reduced by maximising the truncation window length.

The real space input data is now in an acceptable form for machine computation, but the reciprocal space result remains continuous. A digital calculation must produce discretely sampled values of the frequency spectrum as output, hence the continuous spectrum must be sampled in reciprocal space - the sampling interval chosen as $1/T_0$ where T_0 is the truncation window length. Figure 6.4f describes this reciprocal space sampling; figure 6.4g illustrates the final FFT results.

Figure 6.4 has illustrated graphically the operations performed on the cFt pair, $h(x)$ and $H(k)$, to produce the dFt pair $h'(x)$ and $H'(k)$. The N discrete values representing $h'(x)$ are assumed to define a basic repeat of the continuous $h(x)$, see figure 6.4g. Digital FFT calculation of $H'(k)$ from $h'(x)$ is then seen to generate N discretely sampled points that define the discrete Fourier transform spectrum. In the analysis presented in this thesis aliasing can be ignored since the smallest real space sampling intervals T were chosen so that $1/T$ was almost an order of magnitude greater than the frequency range over which the medium spectral noise power was measured electronically. Regarding spectral feature definition in the FFT

calculation $H'(k)$, the resolution was 'altered' by 'padding' the real space input data with strings of zeros, see figure 6.5a. The truncation window was artificially elongated from T_0 , the length over which the non-zero input data $h'(x)$ extended, to (T_0+T') where T' defines the zero padding length. This increased the reciprocal space sampling to $1/(T_0+T')$ from $1/T_0$, an improvement factor of $(T_0+T')/T_0$. An example of how this enhances the information content of the FFT is shown in figure 6.5b. Without padding the effect of the truncation window sinc function convolution is overlooked, so distorting the interpretation of the output.

Finally, no matter how well the FFT algorithm is applied, it must be noted that the end result will always be a convolution of the required noise spectrum with the transform of the window function. In the case of a.c. erased medium the FFT calculated spectrum must be considered as

$$\{b.S_{ac}(k_x)\} \otimes W(k_x)$$

The absolute measurement is thus limited by an averaging process weighted by the window function $W(k_x)$.

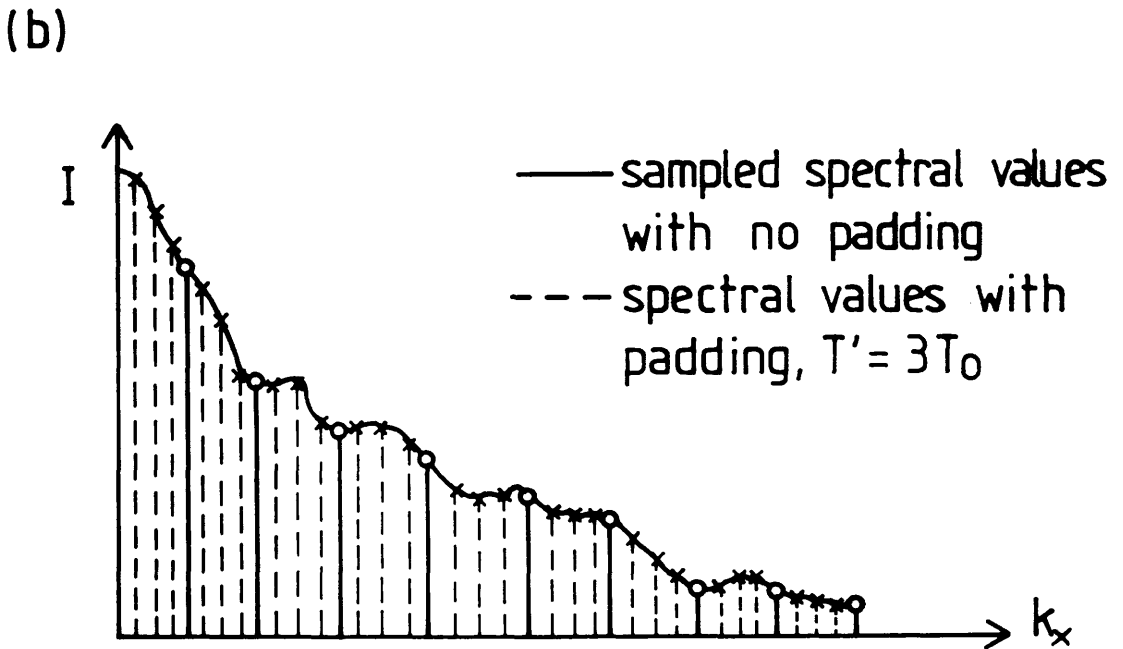
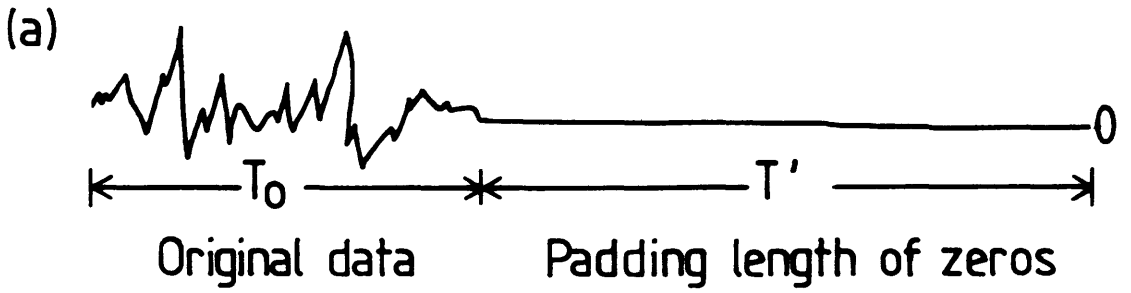


Figure 6.5 - An illustration of the extra resolution generated by padding with zeros. (a) padded function; (b) fast Fourier transform spectrum indicating the points resolved by padding.

6.5 ESTIMATION OF THE A.C. ERASED MEDIUM FLUX NOISE POWER SPECTRUM

As stated above, images obtained by both DPC and Fresnel Lorentz microscopy were used to estimate the iron cobalt chromium medium a.c. erased noise power spectrum. The following three examples illustrate the results of the analysis.

A DPC image, obtained on the VG HB5 STEM, is shown in figure 6.6a. This image illustrates the magnetic contrast within the specimen, but also contains the physical striation contrast. Figure 6.6b shows the processed binary representation of this DPC image upon thresholding. In this case the threshold pixel intensity value was set at the mean pixel value in the image after the kernel operation had reduced the 'visibility' of the texture contrast. The extent to which the binary data reproduced the domain structure in the DPC image was verified visually. The long axis of the needle-like domains in this image lies close to or along the easy axis. From the figure it can be seen that the easy axis does not run parallel to either of the two image edges or boundaries. To rotate this image, average the magnetisation across the image and pad with zeros for the fast Fourier transform calculation would prohibit the use of the full extent of the image data shown in figure 6.6. For this reason, and only for this image, the fast Fourier transform of the 256pixel by 256 pixel image was calculated and the appropriate data extracted from the

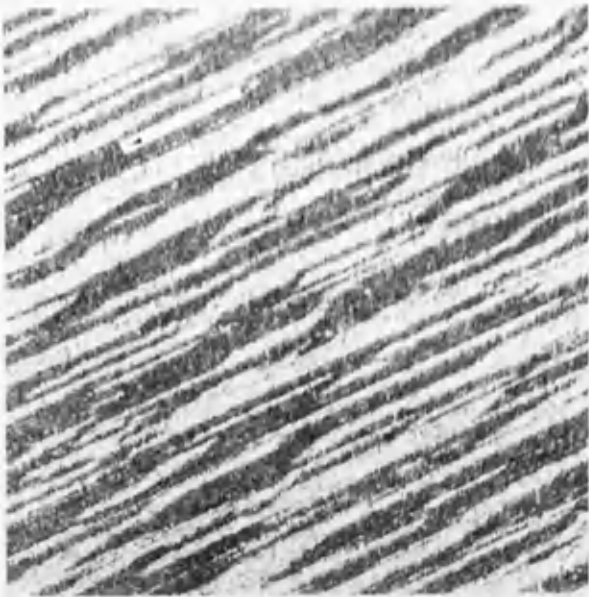


Figure 6.6 - Differential phase contrast image of the domains in an a.c. erased sample and the corresponding binary representation. The specimen area is 17 square micrometres.

two dimensional transform.

Two Fresnel images of the a.c. erased medium are shown in figures 6.7a and 6.8a; both were acquired on the JEOL 1200EX CTEM. The size of these images (approximately $40\mu\text{m}$ by $30\mu\text{m}$) and the complex a.c. erase micromagnetic domain structure made a direct visual comparison between the original images and the binary images difficult - thus inhibiting a visual determination of how accurate the thresholded data described the micromagnetisation. In order to set the thresholding pixel intensity value to produce accurate binary representations of the medium magnetisation it was assumed that with images of this size the two opposing magnetisations should be equally represented in the domain structure, hence the black to white contrast ratio in the binary images should be as close to 1:1 as possible. Threshold values for the artificially coloured photographs of these two images were then chosen to achieve such distributions. This produced magnetisation maps with binary percentages of 49.9% white : 50.1% black for image KAR; 47.2% white : 52.8% black for image MAR.

The binary representations of the medium micromagnetisation for images KAR and MAR are shown in figures 6.7b and 6.8b respectively. In calculating the fast Fourier transforms of this data the images were averaged in a direction perpendicular to the easy axis (that is, vertically in figures 6.7 and 6.8) and padded with zeros. The original data was padded from 1024 pixels to 16384 pixels with zeros.

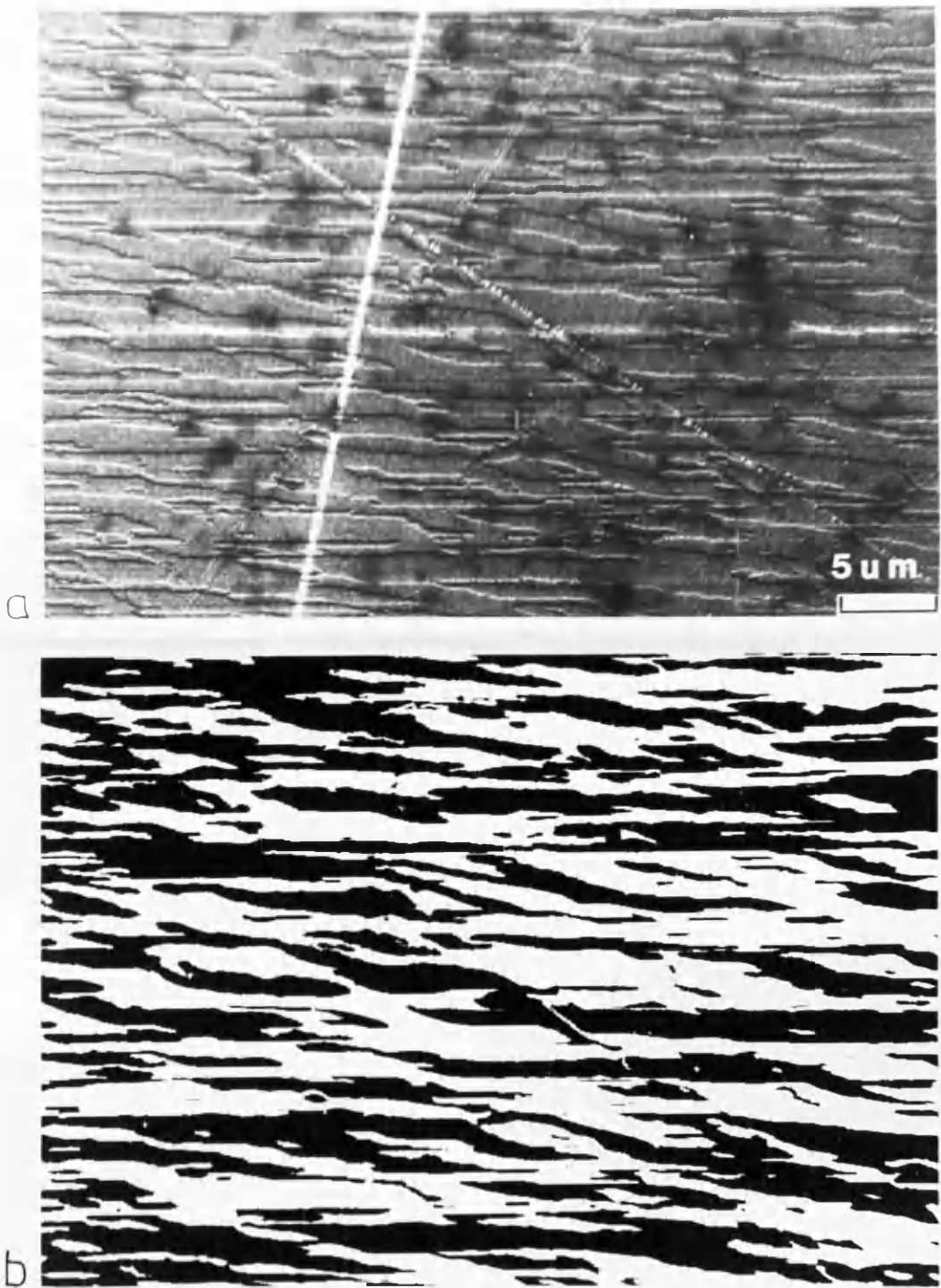


Figure 6.7 - (a) Fresnel image of the a.c. erased medium (Kar); (b) the corresponding binary representation.

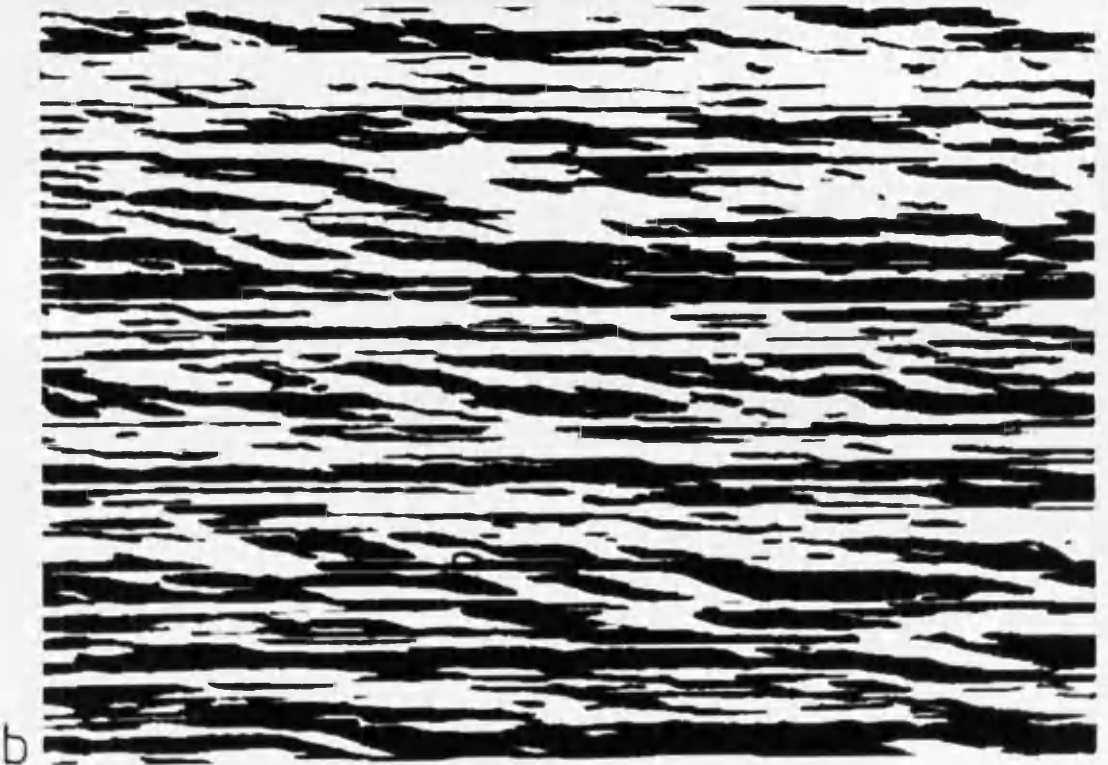
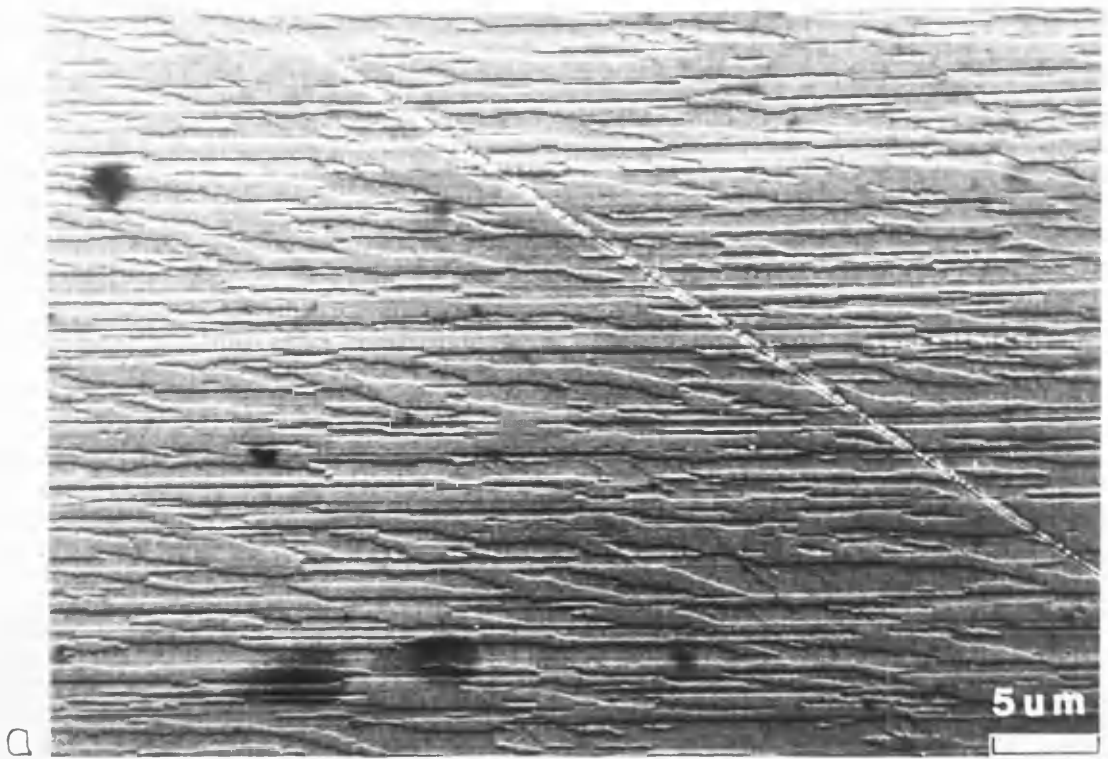


Figure 6.8 - (a) Fresnel image of the a.c. erased medium (Mar); (b) the corresponding binary representation.

In the thresholded images of figures 6.6b, 6.7b, and 6.8b binary intensity values of ± 127 were set to represent $\pm M_s \cdot b$ in oppositely magnetised domains. The actual value of the product of the saturation magnetisation and the film thickness was measured by both small angle diffraction and VSM as 2.3×10^{-2} in the S.I. unit system, hence a scaling factor of

$$\frac{127}{M_s \cdot b} = \frac{127}{2.3 \cdot 10^{-2}}$$

must be applied to the results computed from the binary magnetisation maps. Analysis by FFT itself introduces a scaling factor to the calculated output spectrum. Intrinsic to the FFT algorithm used was an amplitude scaling of $(n_1 \cdot n_2)^{1/2}$, where n_1 and n_2 represent the number of pixels along the two image dimensions. A final scaling factor necessary is that of the actual area described by the image (this arises from the derivation of $b \cdot S(k_x)$). The computed FFT amplitude spectra representing the medium flux noise power are thus scaled to give absolute values for direct comparison with the electronically measured noise spectra:

$$b \cdot S(k) = \frac{|\text{FFT Amplitude}|^2 \cdot (\text{Image Area})}{(n_1 n_2) \cdot (127/2.3 \cdot 10^{-2})^2} \quad (6.20)$$

All three binary representations of the a.c. erased medium magnetisation shown in figures 6.6b, 6.7b and 6.8b were used to calculate the Lorentz image derived a.c. erased medium flux noise power. Upon scaling the FFT calculations the resultant Lorentz derived noise spectra were plotted in figures 6.9, 6.10, and 6.11

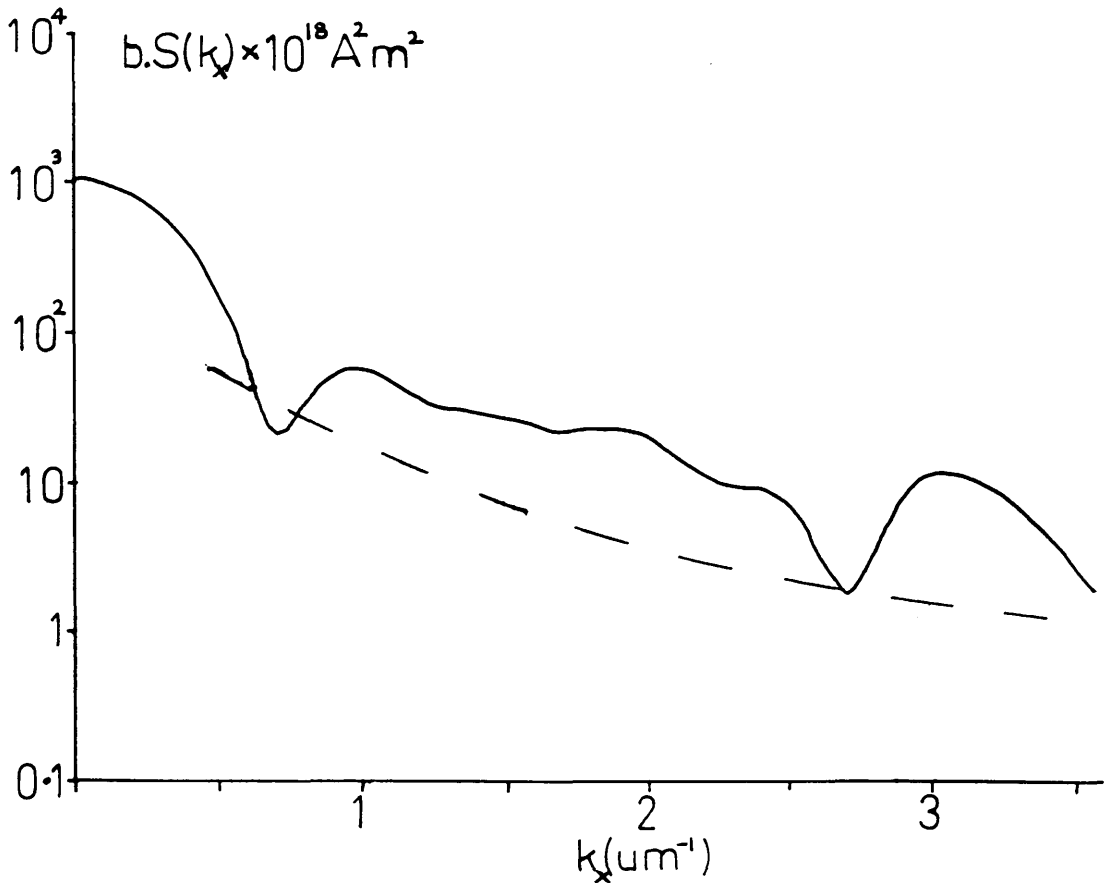


Figure 6.9 - A log10-linear graphical comparison of the Lorentz derived and electronically measured noise spectra for the DPC image. In this and subsequent figures describing noise power spectra the electronic data will be represented by a dashed line.

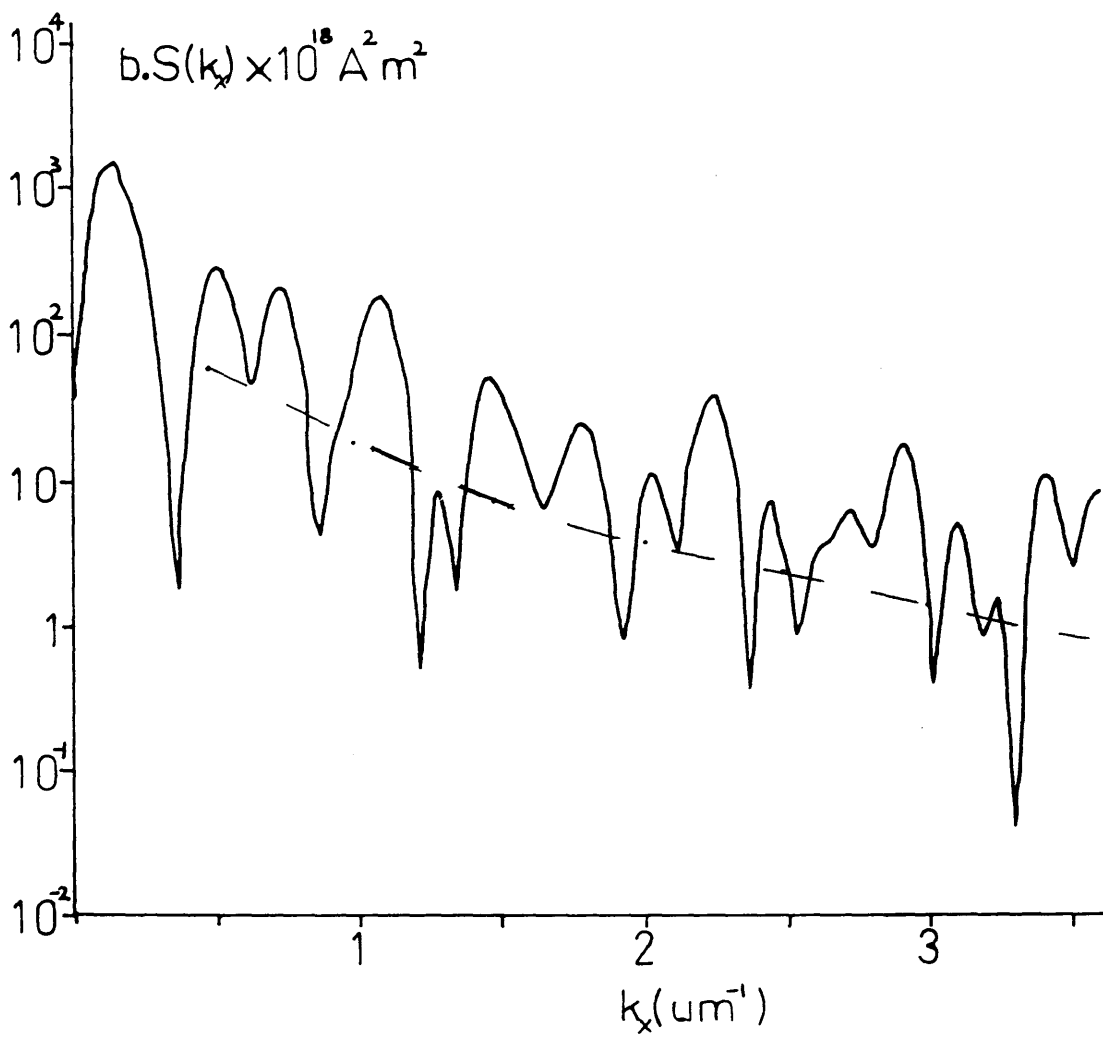


Figure 6.10 - A log10-linear graphical comparison of the Lorentz derived and electronically measured noise spectra for the Fresnel image Kar.

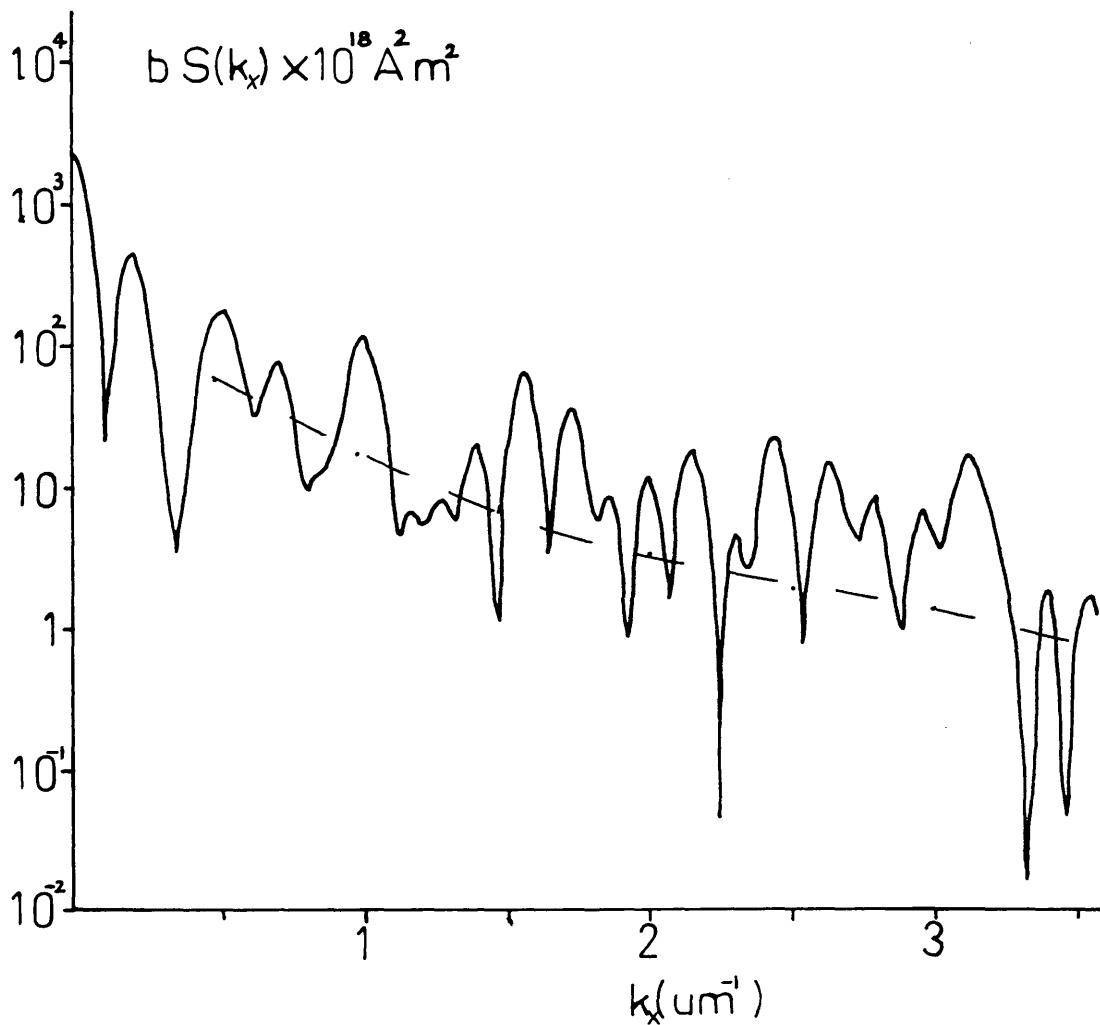


Figure 6.11 - A log10-linear graphical comparison of the Lorentz derived and electronically measured noise spectra for the Fresnel image Mar.

respectively. In each of the graphs of $b.S(k_x).10^{18}$ against reciprocal wave number k_x the electronically measured a.c. erase noise power data was plotted for comparison.

From these three graphs it can be seen that both the Lorentz and electronically derived noise spectra appear to decay at approximately the same rate with increasing frequency k_x , but that the Lorentz curve varies about that of the electronic noise spectrum. On comparing the data from the DPC and the Fresnel images it is noted that the above variation appears to be somewhat smaller in the DPC data, resulting in a smoother curve than those seen for the Fresnel images. This observation may be attributable to the smaller extent of the DPC image relative to the Fresnel images or more probably to the manner in which it is processed, possibly inhibiting the full resolution of the a.c. erased medium noise spectrum from this image because padding was not used. In any event, the spectral variation of the Lorentz image derived noise power about the electronically measured data must be explained to evaluate fully how well the two data sets actually compare.

With reference to the Fresnel derived spectra of figures 6.10 and 6.11 it was observed that the main discrepancy between the two spectral estimates (Lorentz and electronic) lies with this 'oscillatory' behaviour of the Lorentz data with respect to the electronic spectrum. This 'ripple' is believed to originate from two effects associated with the finite size of the

images analysed. Firstly, the convolution of the Lorentz derived noise with the sinc function (from the truncation window) was considered as a possible source capable of modulating the a.c. noise power in this manner. Figure 6.12 illustrates the sinc function associated with the spectra of figures 6.10 and 6.11. The magnitude and width of the secondary side-lobes and the close proximity of neighbouring positive and negative cycles suggested that this mechanism, although present in the spectra, may not be capable of producing the swings in magnitude observed in the Lorentz spectra.

A more likely source of this ripple in the a.c. noise power may in fact arise from the actual content of the real space area analysed. Figure 6.13 illustrates the selection of a data window from an infinitely long one-dimensional a.c. erased magnetisation profile. In the formalism of the fast Fourier transform the selected portion shown is then taken to be representative of a basic repeat describing the whole signal. If the window used contains any dominant local sinusoidal variations, as is the case in figure 6.13, the associated reciprocal frequencies will be emphasised in the resulting noise spectrum. Although this transform is perfectly correct for the finite length of signal analysed by FFT, it is not representative of the global behaviour of the a.c. erased signal. In this way it can be seen that each local window will have a corresponding noise spectrum signature in which associated local sinusoidal

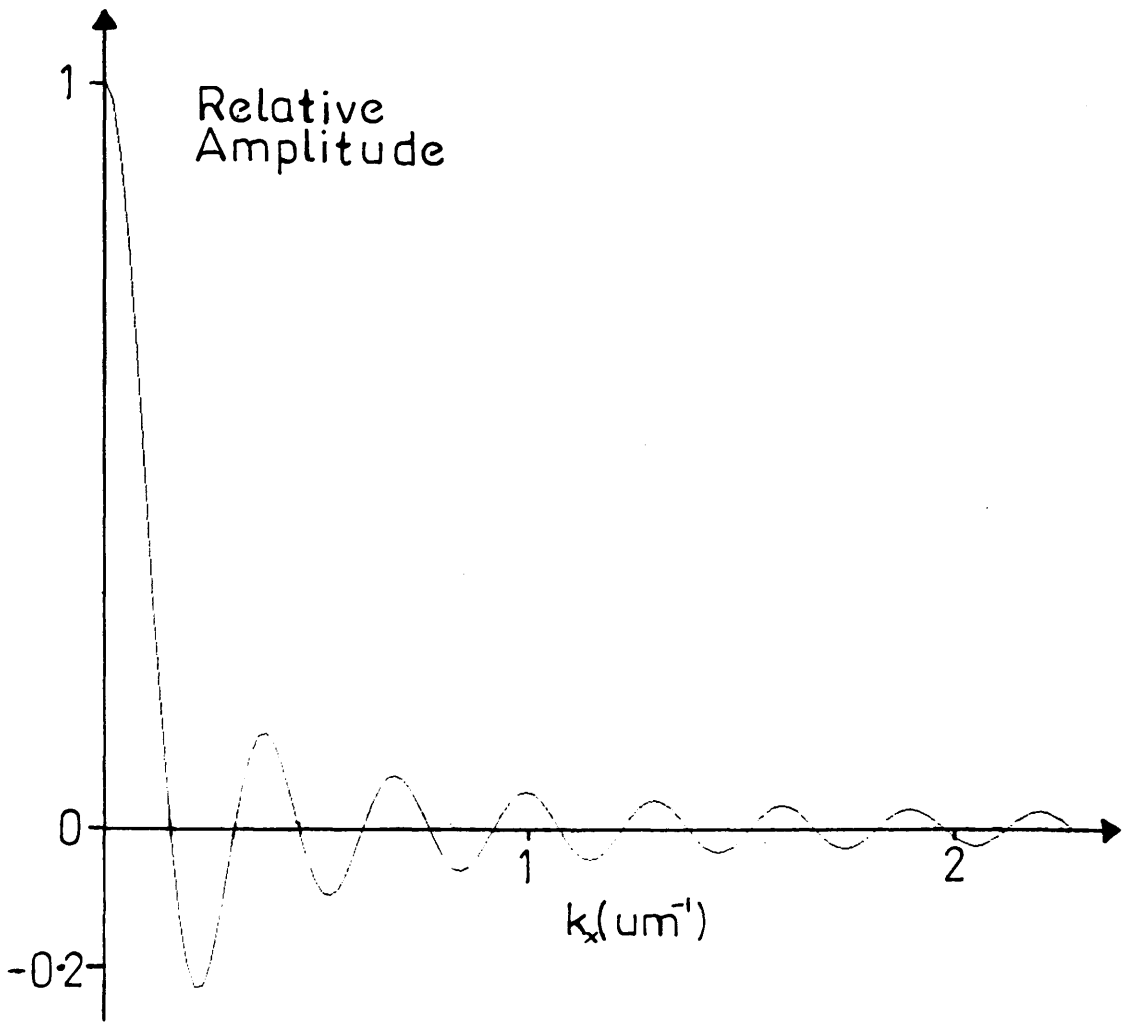
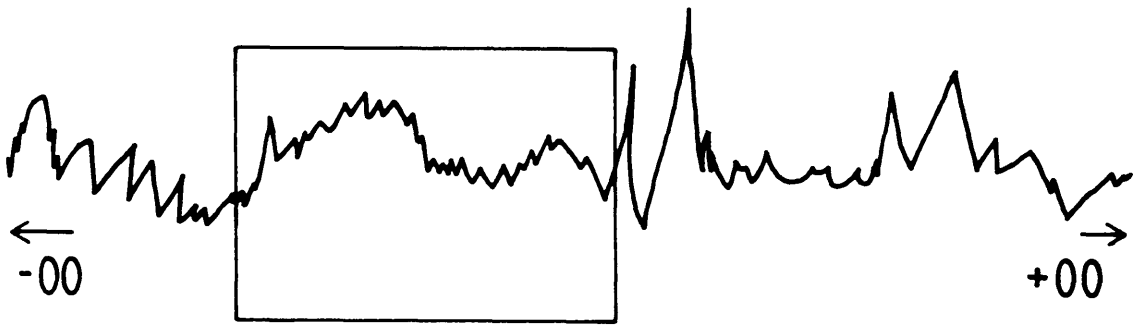


Figure 6.12 - The Fourier transform of the window function $w(x)$ applied to the Fresnel images Kar and Mar.



Selected portion of waveform



FFT

to estimate
noise power

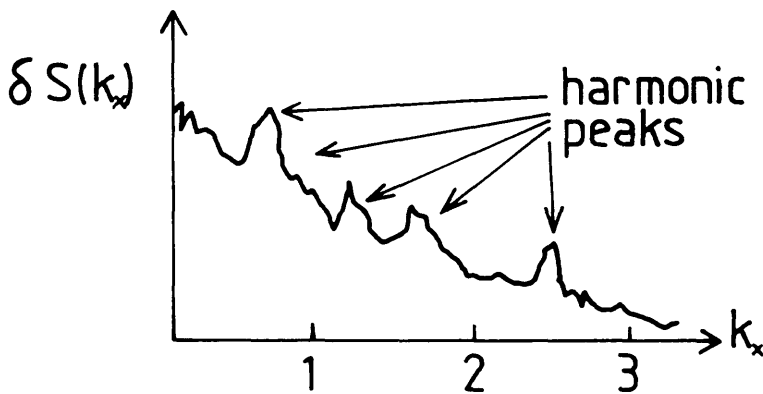


Figure 6.13 - A description of the selection of a section of a.c. erased signal from an infinite waveform.

frequencies may be emphasised. This would then explain the existence of the high magnitude peaks responsible for the Lorentz noise oscillation in the noise spectra analysed (figures 6.10 and 6.11).

In terms of perceiving the global behaviour of the a.c. noise spectrum an average over the two Fresnel derived spectra should give an improved representation of the a.c. noise relative to the individual local estimates. This is given in figure 6.14. It can be seen that the magnitude of the oscillation has in fact been reduced and that this mean curve is indeed a better quantitative fit to the electronic noise than either of the individual spectra. Further smoothing by averaging over yet more noise spectra obtained from images of the a.c. erased medium should reduce the ripple further, provided the Lorentz images used represent faithfully the more global behaviour of the a.c. medium, so reducing the effects of any locally dominant frequencies.

An alternative averaging approach involved segmenting the two-dimensional Fresnel images into strips with dimensions more appropriate to those of the read head. Both of the Fresnel images have approximate dimensions of $40\mu\text{m}$ by $30\mu\text{m}$, where these values represent the lengths parallel and perpendicular to the write direction or easy axis. Each digital image was halved to produce four $40\mu\text{m}$ by $15\mu\text{m}$ strips, the actual effective head width used being $15\mu\text{m}$. These four sections can then be considered as independent 'read back strips' from which legitimate estimates of the

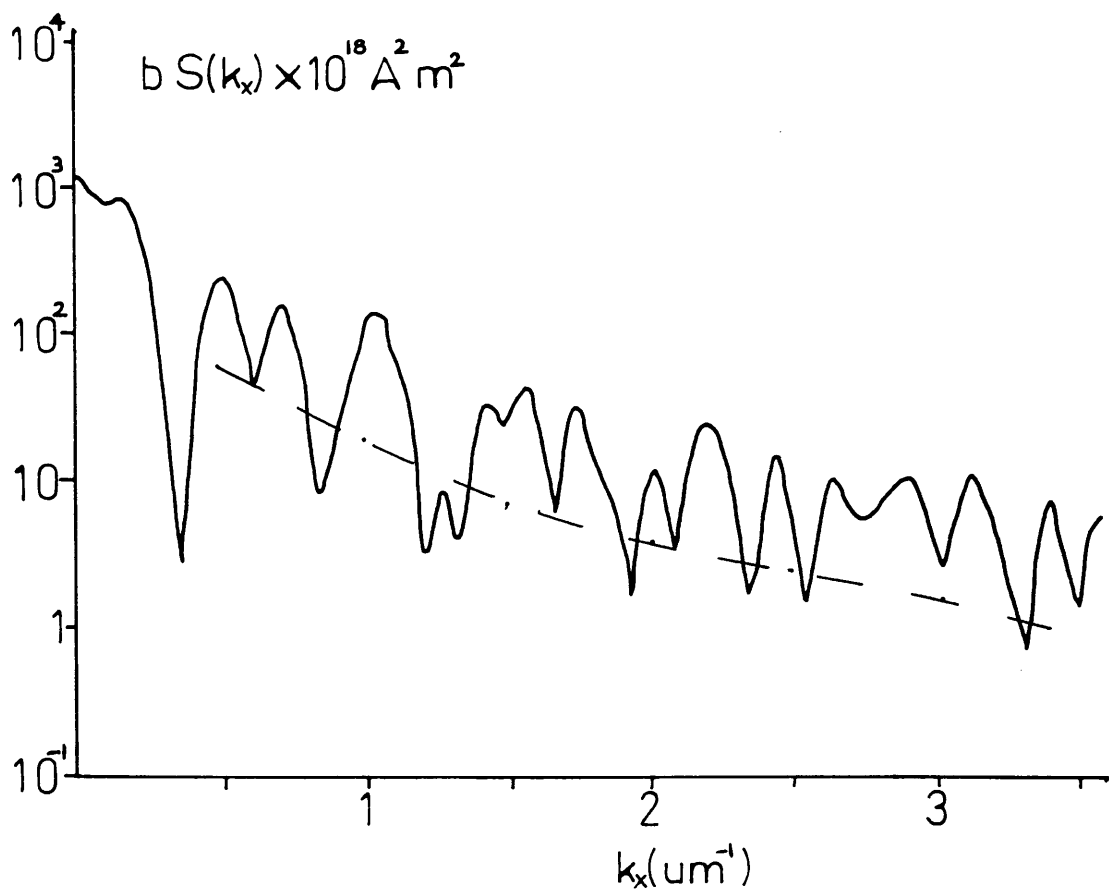


Figure 6.14 - A log₁₀-linear graphical comparison of the average of the Lorentz derived spectra graphed in figures 6.10 and 6.11 and the electronically measured noise spectrum.

a.c. erased medium flux noise can be calculated. Figure 6.15 graphs the the four individual spectra; figure 6.16 illustrates the comparison between the average of these spectra and the electronic data. With particular reference to figure 6.16 it can be seen that this method has indeed reduced further the oscillatory effects on the Lorentz derived noise spectrum, giving better agreement with the electronic measurement. When considering the limitations discussed regarding convolution effects, the introduction of disruptive 'sinusoidal' frequencies from local data windows, and the fact that the electronic data was acquired over a vastly greater readback length of a.c. erased medium (some $10^6\mu\text{m}$) the quantitative comparison between the Lorentz and electronically measured noise spectra of figure 6.16 is seen to be very good under the circumstances.

6.6 SUMMARY

In this chapter expressions for the medium spectral power in terms of the medium micromagnetisation have been presented, derived from the results of the Reciprocity Model of the read back process. A description of how the iron cobalt chromium medium magnetisation can be characterised using Lorentz electron microscopy has been detailed along with the digital computer FFT evaluation of the aforementioned medium flux power expressions.

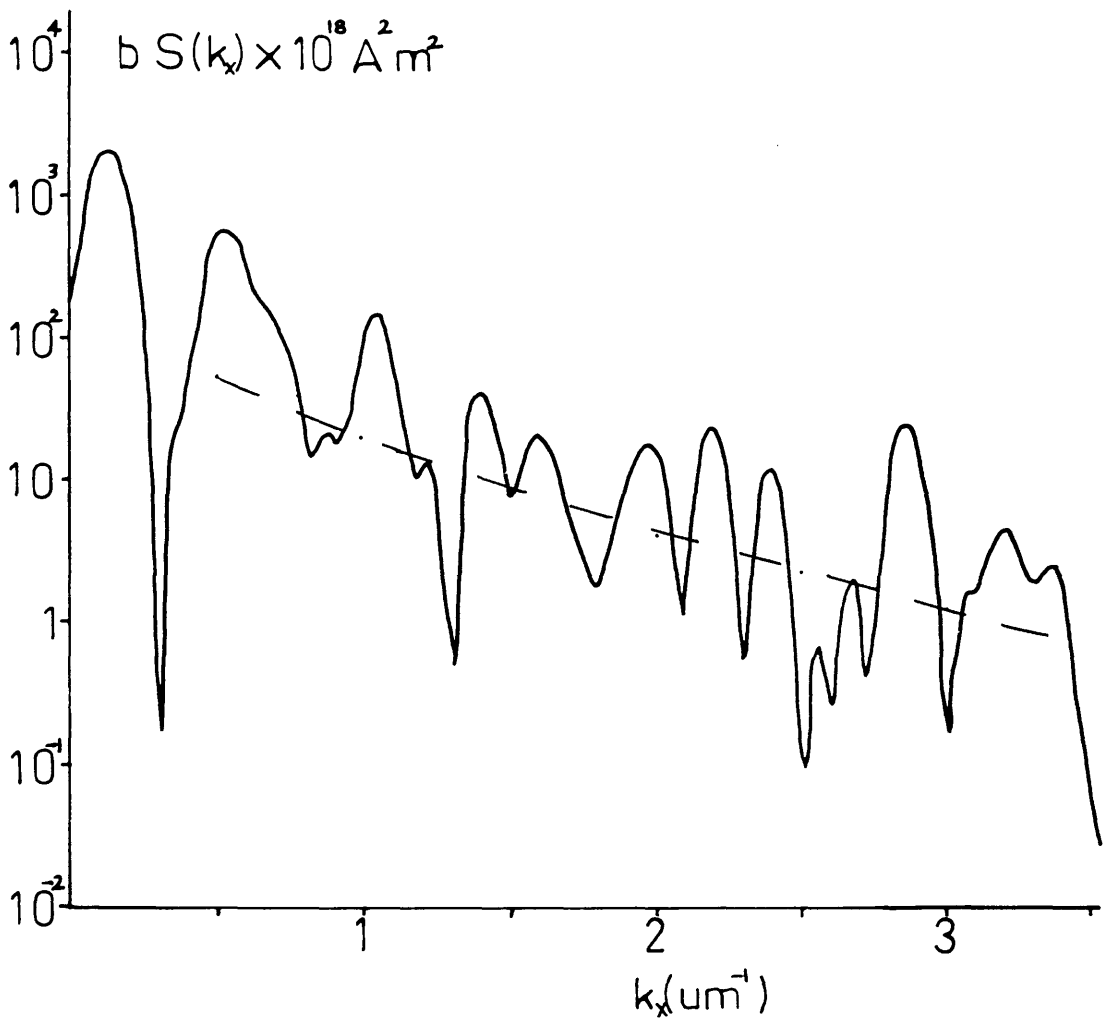
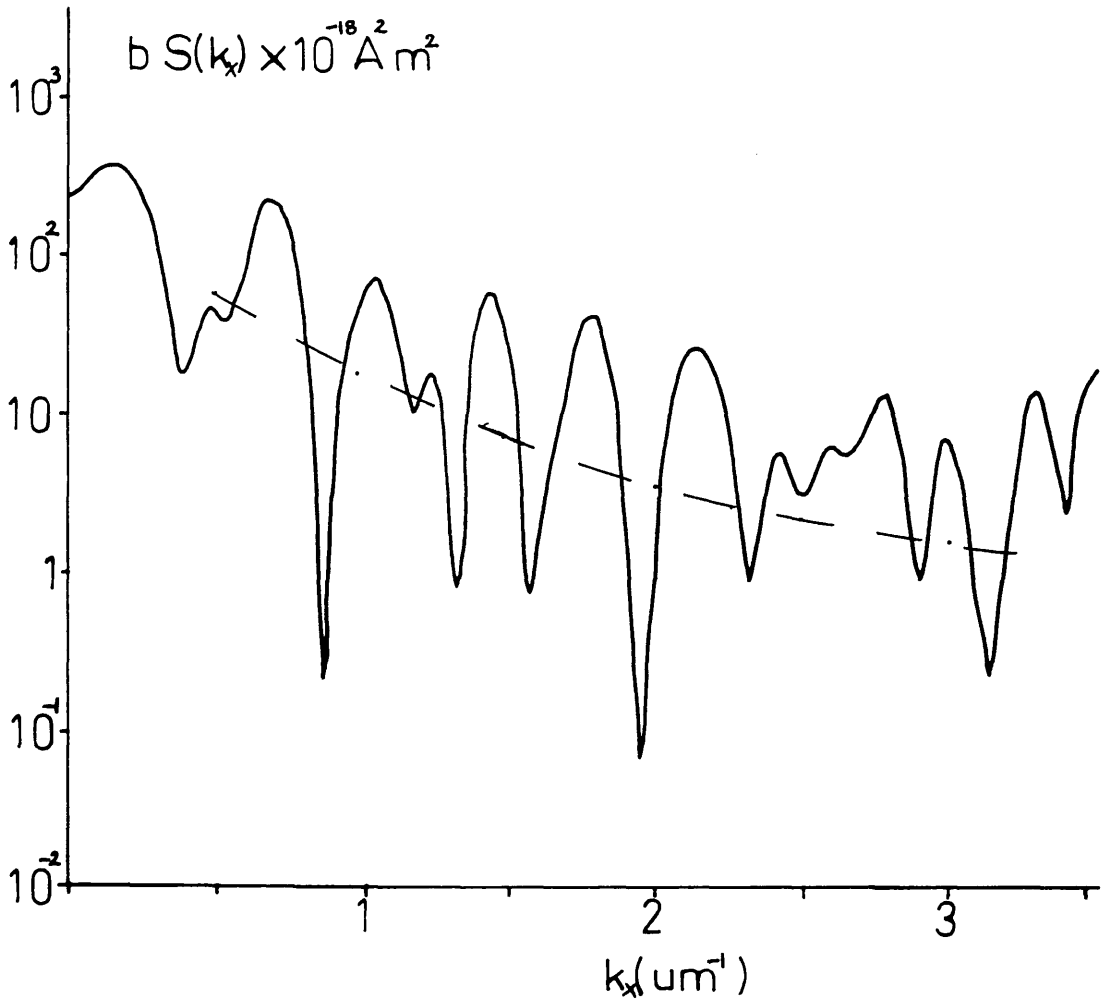
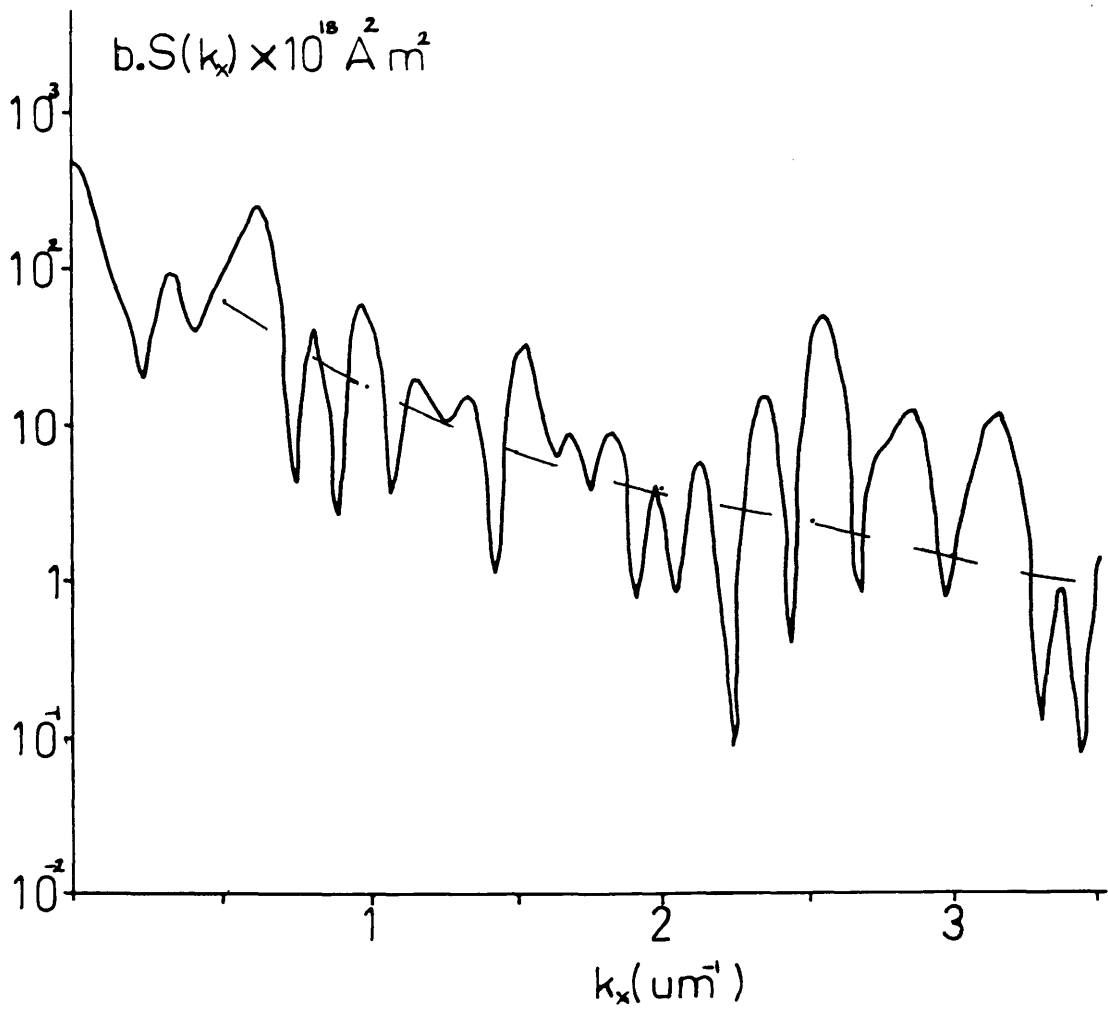


Figure 6.15 - The spectra obtained from the four 'readback strips' taken from Kar and Mar:

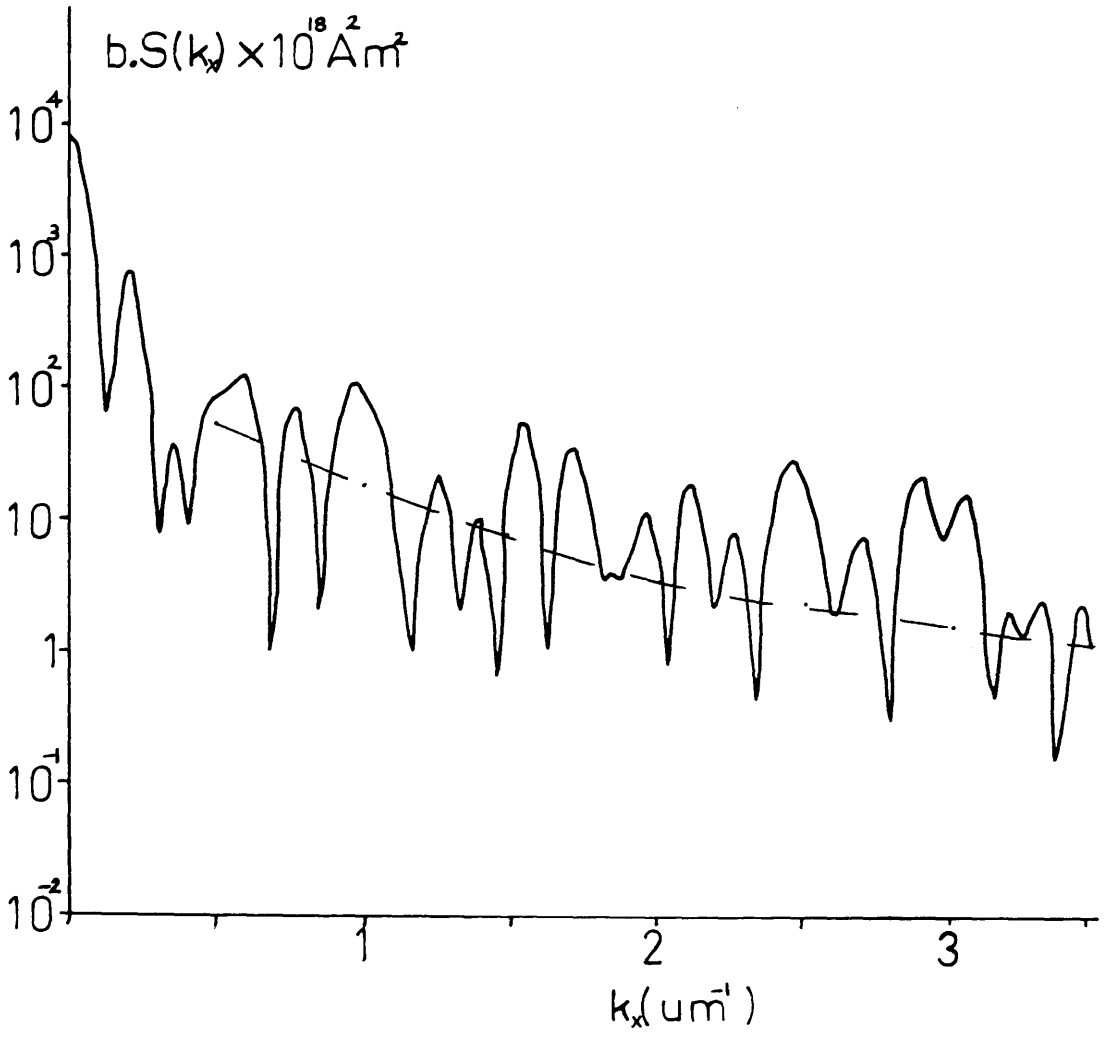
(a) the top half of Kar;



(b) the bottom half of Kar;



(c) the top half of Mar;



(d) the bottom half of Mar.

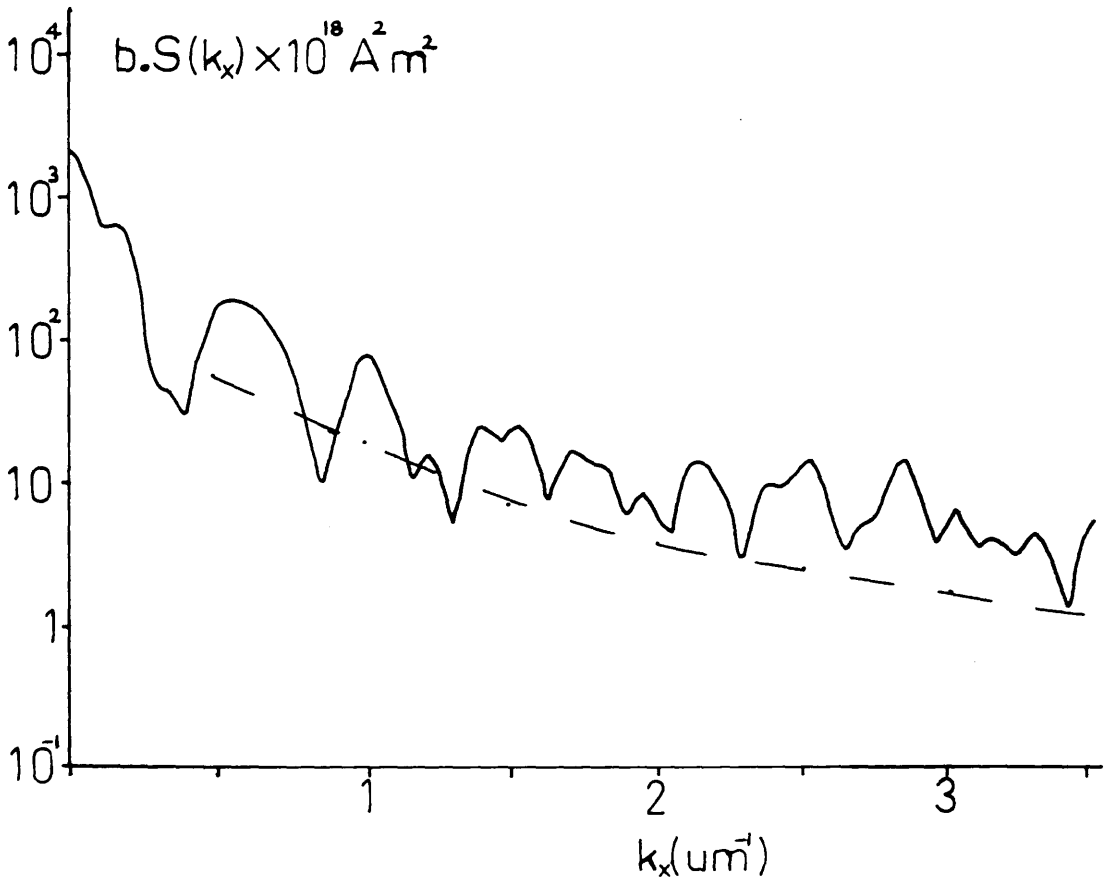


Figure 6.16 - A log10-linear comparison between the average of the noise spectra graphed in figure 6.15 and the electronically measured noise spectrum.

Preliminary use of this technique was then examined using a.c. erased iron cobalt chromium recording medium. Although inhibited by the finite extent of the Lorentz data analysed, good agreement between Lorentz derived and electronically measured data was achieved. From this first comparison the importance of understanding fully the computed FFT spectrum in terms of the sampled input image was highlighted.

The conclusion from this work was that the technique of quantitatively measuring medium flux noise power from Lorentz images of the iron cobalt chromium micromagnetic structure appeared to be valid, justifying a comparison with the electronically measured read back spectra.

CHAPTER SEVEN

INVESTIGATION OF TRANSITION NOISE FROM SQUARE WAVE WRITTEN TRACKS BY LORENTZ ELECTRON MICROSCOPY

7.1 INTRODUCTION

The overall objective of this chapter was to explore the micromagnetic nature of the noise power spectrum intrinsic to the written magnetisation transitions of square wave tracks.

Before this relationship between the micromagnetic structure and the recording performance of tracks written to a medium could be investigated, quantitative agreement had to be established between noise power spectra obtained from analysing Lorentz images and those measured electronically from the read back signal. The results given in the previous chapter indicate that this agreement has been achieved to a considerable degree for a.c. erased iron cobalt chromium; hence the same technique was employed as a basis to examine square wave tracks written on the same medium.

Two different computational approaches were used to study the transition noise by digital image processing of Lorentz derived images: a periodogram analysis [1,6,7] and a study of individual magnetisation transitions [2]. A periodogram is an image containing an integral number of wavelengths of a periodic signal, and the use of such images to describe written track

magnetisation forms the basis of the periodogram method. The single transition technique evolved directly from the results of the periodogram approach, being developed to remove the quantitative restrictions imposed upon the periodogram technique due to finite image sizes.

Although intimately related, the two techniques will be discussed separately in the subsequent text. In this way the systematic development from periodogram to single transition analysis is best stated, emphasising the advantages of the latter process. The form of the discussion for both techniques shall be similar - a comprehensive description of the magnetisation model and the considerations associated with the use of the fast Fourier transform, followed by a presentation of the important results obtained from each analysis.

7.2 ELECTRONIC MEASUREMENT OF TRANSITION NOISE POWER

The method used to measure the noise power spectra from written track readback signal was identical to that described in chapter six for the a.c. erased medium. Briefly, the track medium noise was isolated from the total electronically measured noise (medium + head + read channel) by subtracting quadratically the head and read channel contributions. Any signal peaks detected in the track power spectrum were numerically suppressed. Figure 7.1 illustrates the measured medium noise spectra for both the 3MHz ($\lambda=12.7\mu\text{m}$) and 6MHz ($\lambda=6.35\mu\text{m}$) square wave written tracks.

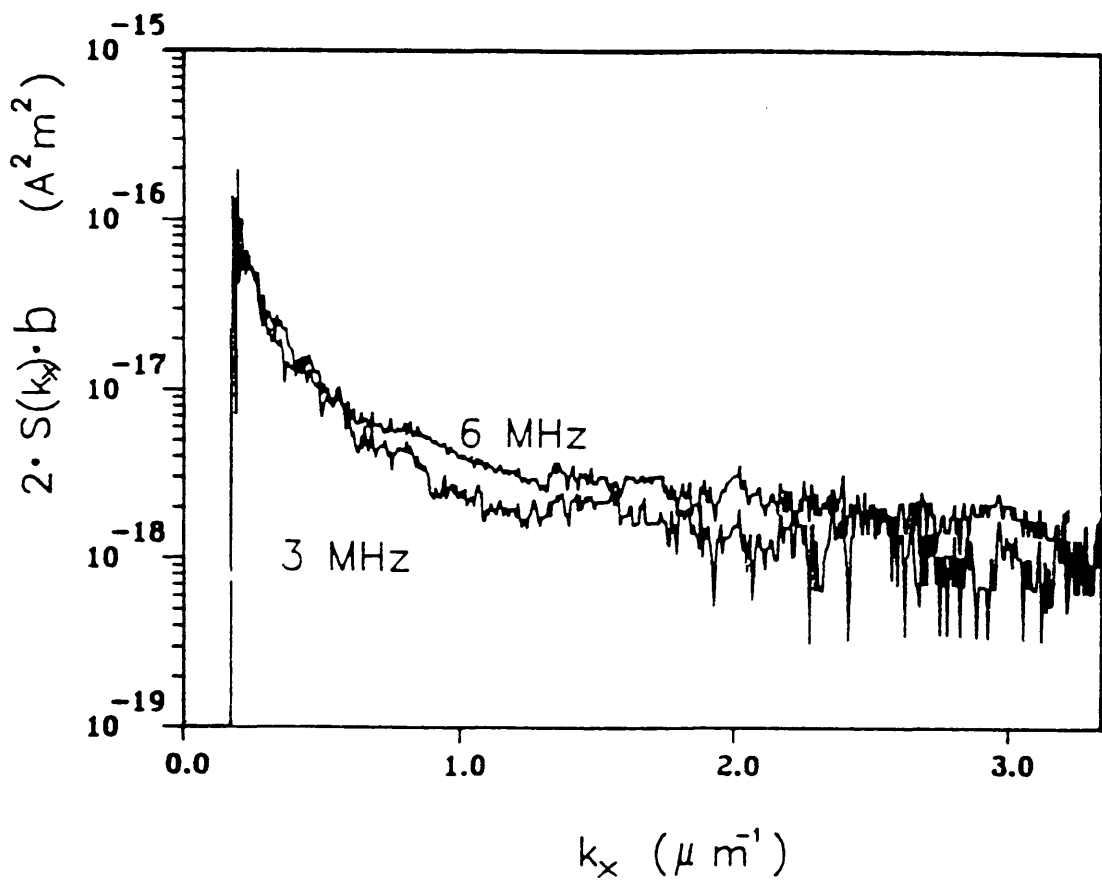


Figure 7.1 - The electronically measured transition noise power spectra for write frequencies of 3MHz and 6MHz. These were measured over a track length of $\approx 10^5 \mu m$.

7.3 BINARY REPRESENTATIONS OF THE MEDIUM MAGNETISATION FROM LORENTZ IMAGES

The assumptions used with the a.c. erased medium regarding the direction of the magnetisation in neighbouring domains within the highly oriented iron cobalt chromium were taken to apply equally well to a written square wave track. Although there may be some small amount of flux closure at the transition boundaries, this should be small and the magnetisation can still be considered to lie parallel or anti-parallel to the easy axis with a magnitude equal to the saturation magnetisation.

Unlike the a.c. erased medium the micromagnetic structure of recorded tracks produces large de-magnetising stray fields above and below the specimen. For a good recording medium these fields will cancel to first order the electron deflection from the medium induction within domains and therefore will, to some unknown extent, contribute to the Lorentz image contrast. In DPC imaging the result of this cancellation is a reduction in the contrast difference between oppositely magnetised domains which can impair the resolution of the domain characteristics. Fresnel imaging will also be susceptible to this effect since this technique involves resolving intensity features generated by the medium induction. However, unlike the DPC technique that produces domain contrast, Fresnel imaging delineates domain boundaries by the

convergence/divergence of electrons traversing oppositely magnetised domains. These boundaries will therefore always be well defined in an out-of-focus Fresnel image so long as the medium induction is not completely cancelled.

Two Fresnel images depicting both the 3MHz ($\lambda=12.7\mu\text{m}$) and 6MHz ($\lambda=6.35\mu\text{m}$) square wave written tracks were used to produce two independent binary representations of the tracks. The technique described in the previous chapter was used, but a different way of estimating the binary threshold value was operated. For each individual track an integral number of periods was selected which should then contain approximately equal amounts of each magnetisation. A threshold value was then chosen to produce an equal number of pixels of each state of magnetisation for the individual track images. In this way two independent binary representations of both the 3MHz and 6MHz tracks were created, the two 3MHz sections being six periods long while the 6MHz track periodograms were 10 wavelengths in length. Figure 7.2 illustrates original Fresnel and processed binary images for 3MHz and 6MHz track periodograms.

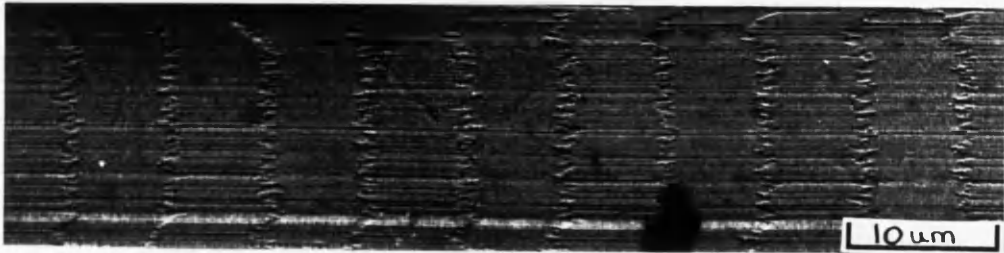
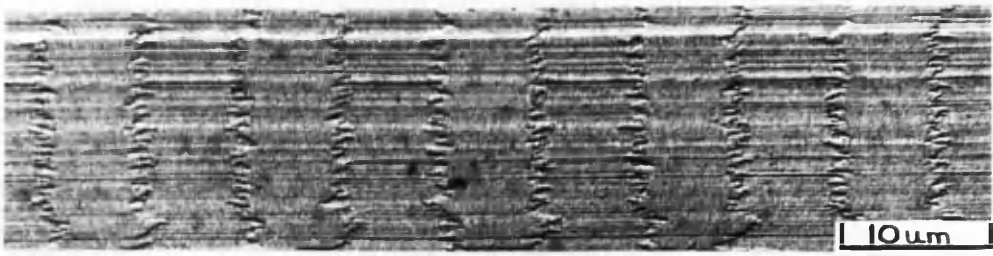
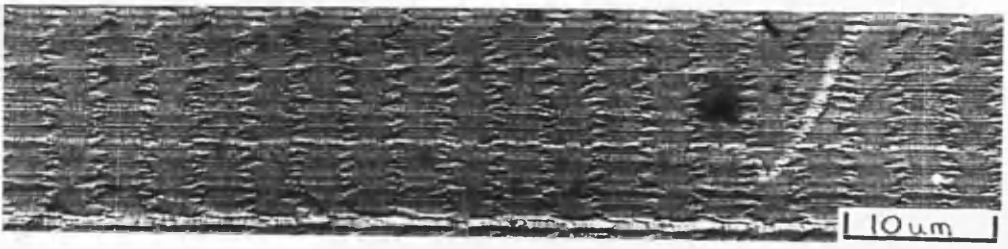
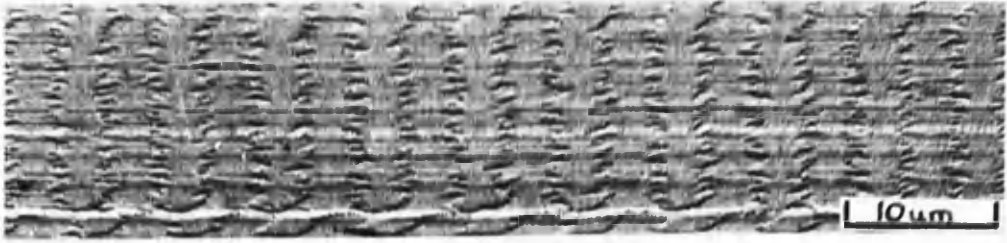


Figure 7.2 - Comparison between the original Fresnel images and their binary representations for (a) 3MHz track;



(b) 6MHz track.

7.4 PERIODOGRAM TECHNIQUE OF ESTIMATING TRANSITION NOISE POWER

7.4.1 FAST FOURIER TRANSFORM COMPUTATIONS INVOLVING PERIODIC SIGNALS

The previous chapter contained a general discussion of the relationship between the continuous Fourier transform and the discrete Fourier transform calculated by the fast Fourier transform (FFT) algorithm. Further consideration must now be given to the specific properties of discrete power spectra generated from finite images of a periodic signal, such as the binary representations of the iron cobalt chromium track magnetisation under discussion. As an example, a graphical description of the operations applied to the continuous cosine function Fourier transform pair to produce the corresponding discrete Fourier pair was taken from Brigham [3] and given graphically in figure 7.3.

From figure 7.3e it can be seen that the discretely sampled real space function was truncated to exactly define one period of the continuous cosine signal. The effects of this truncation on the reciprocal spectrum are clearly illustrated, the convolution generating secondary maxima and minima as well as broadening the impulse spectrum of figure 7.3a. This effect is termed 'frequency leakage'.

The expanded schematic diagram of this convolution between the cosine spectrum and the rectangular

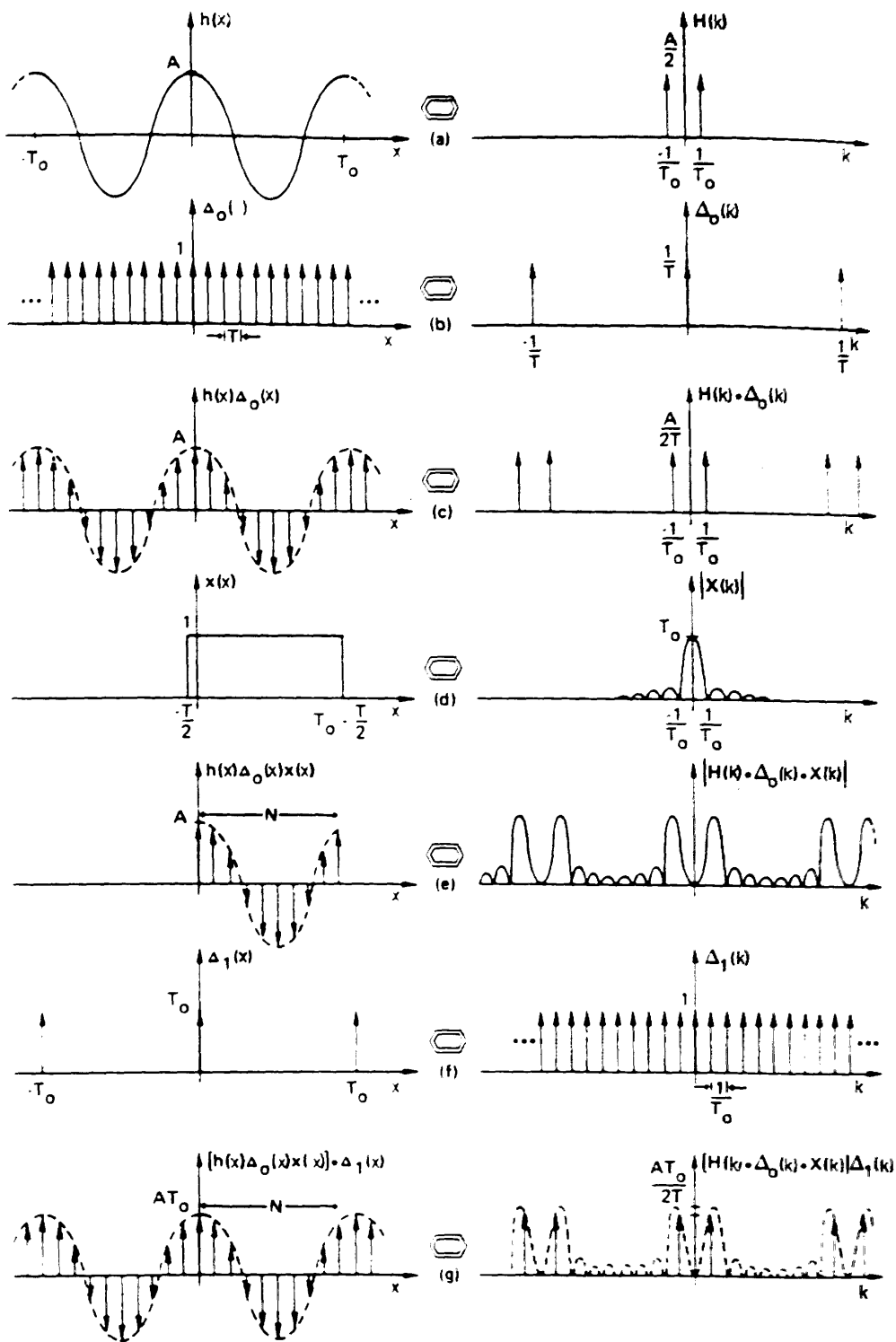


Figure 7.3 - Discrete Fourier transform of a cosine waveform: truncation interval equal to one period (Brigham [3]).

truncation window sinc function given in figure 7.4 serves to illustrate the manner in which the fast Fourier transform algorithm produces sampling in reciprocal space that avoids this frequency leakage. The composite frequency spectrum can be seen to be sampled at intervals of $1/T_0$, coincident with the zero value positions of the sinc function leakage distribution. It is only at the cosine signal frequencies of $\pm 1/T_0$ that the sampling produces non-zero values for the discrete Fourier transform. A comparison of the spectra described in figures 7.3a and 7.3g shows that the discrete FFT calculated spectrum is, apart from a scaling factor, identical to the continuous transform of the cosine function.

If the window length was extended to $n.T_0$, for some integer n , the reciprocal sampling interval and the form of the sinc function would both change - but the above sampling behaviour would be maintained. Sampling would be increased to a resolution of $1/n.T_0$ while the sinc function would contract, with zero values at $\pm 1/n.T_0$ (but not at $\pm 1/T_0$). These two changes combine to sample the spectrum again at the zero frequencies of the sinc function leakage distribution, yielding non-zero values again only at $\pm 1/T_0$. This illustrates that defining a basic repeat of the original continuous periodic function by the N sampled values of the discrete real space approximation has ensured that no secondary frequency leakage is sampled in reciprocal space.

An extension of this discussion is the treatment of

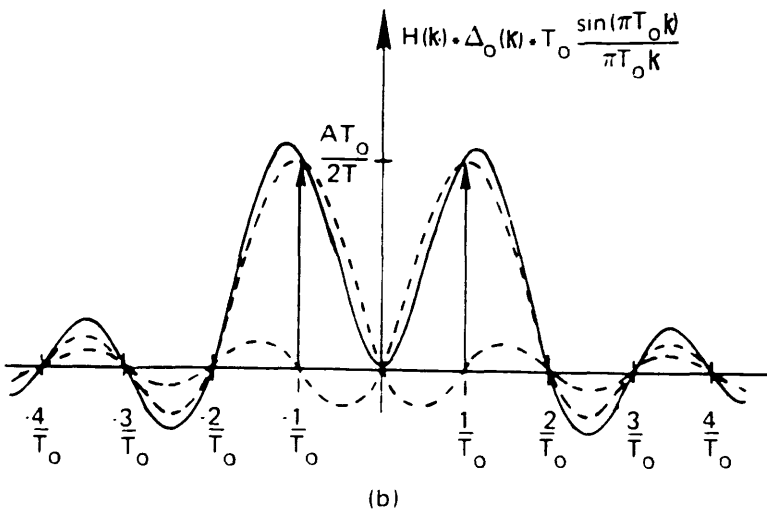
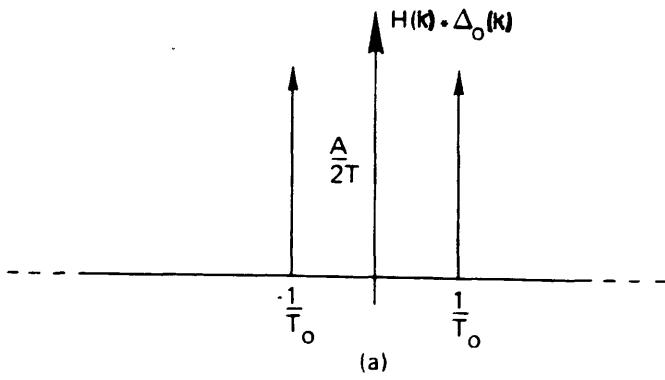


Figure 7.4 - Expanded illustration of the convolution of figure 7.3e (Brigham [3]).

zero padding described in figure 7.5. The discrete real space data describes a period of a continuous periodic function of length T_0 by N discrete points. This was then padded to $8N$ by a row of $7N$ zeros, giving a padded window length $8T_0$. Fast Fourier transforming now produces a sinc function leakage distribution with zeros every $1/T_0$ (but not at $\pm 1/T_0$) and a reciprocal sampling interval of $1/8T_0$. Figure 7.5 illustrates the resultant spectrum in which the padding has allowed the resolution of the complete frequency leakage structure from which the complete discrete transform can be obtained.

To illustrate the effect of mis-sampling in reciprocal space, figure 7.6 describes graphically the situation where the truncation of the discrete real space data does not describe a basic repeat of the continuous periodic function. In this circumstance the sampled values of the spectrum and the positions of the zero values of the sinc function leakage distribution are no longer coincident. Instead of sampling non-zero amplitudes only at frequencies defined by the periodic signal, the frequency leakage is mistakenly interpreted as the correct estimate of the discrete Fourier transform. Comparison between figures 7.6a and 7.6g now shows major discrepancies between the continuous and discrete Fourier transform pairs as a direct result of real space truncation not defining a basic signal repeat. Padding with zeros in this case would allow the complete frequency leakage spectrum to be viewed, but at sampled points that again do not exactly

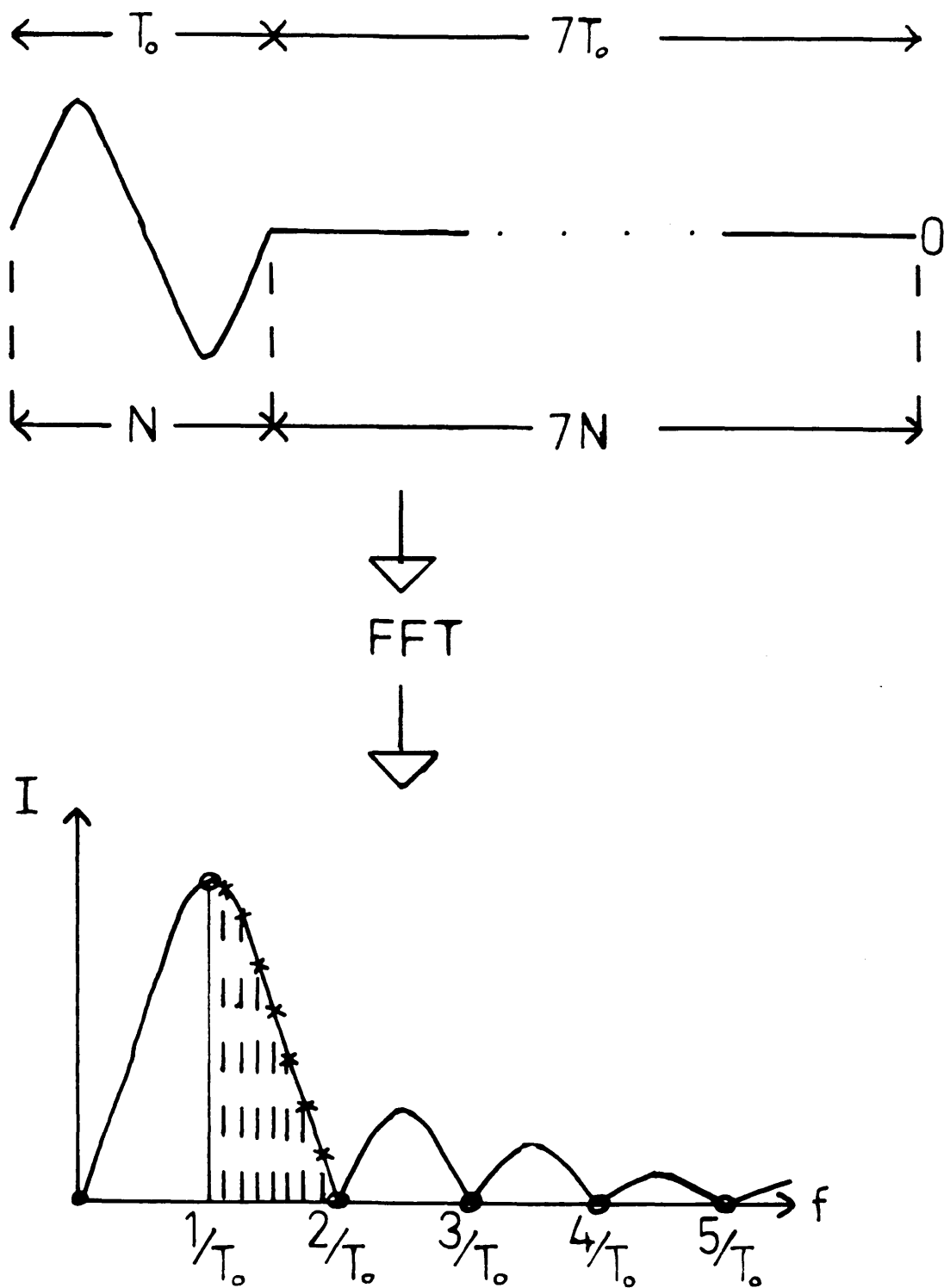


Figure 7.5 - An illustration demonstrating the extra resolution obtained by zero padding.

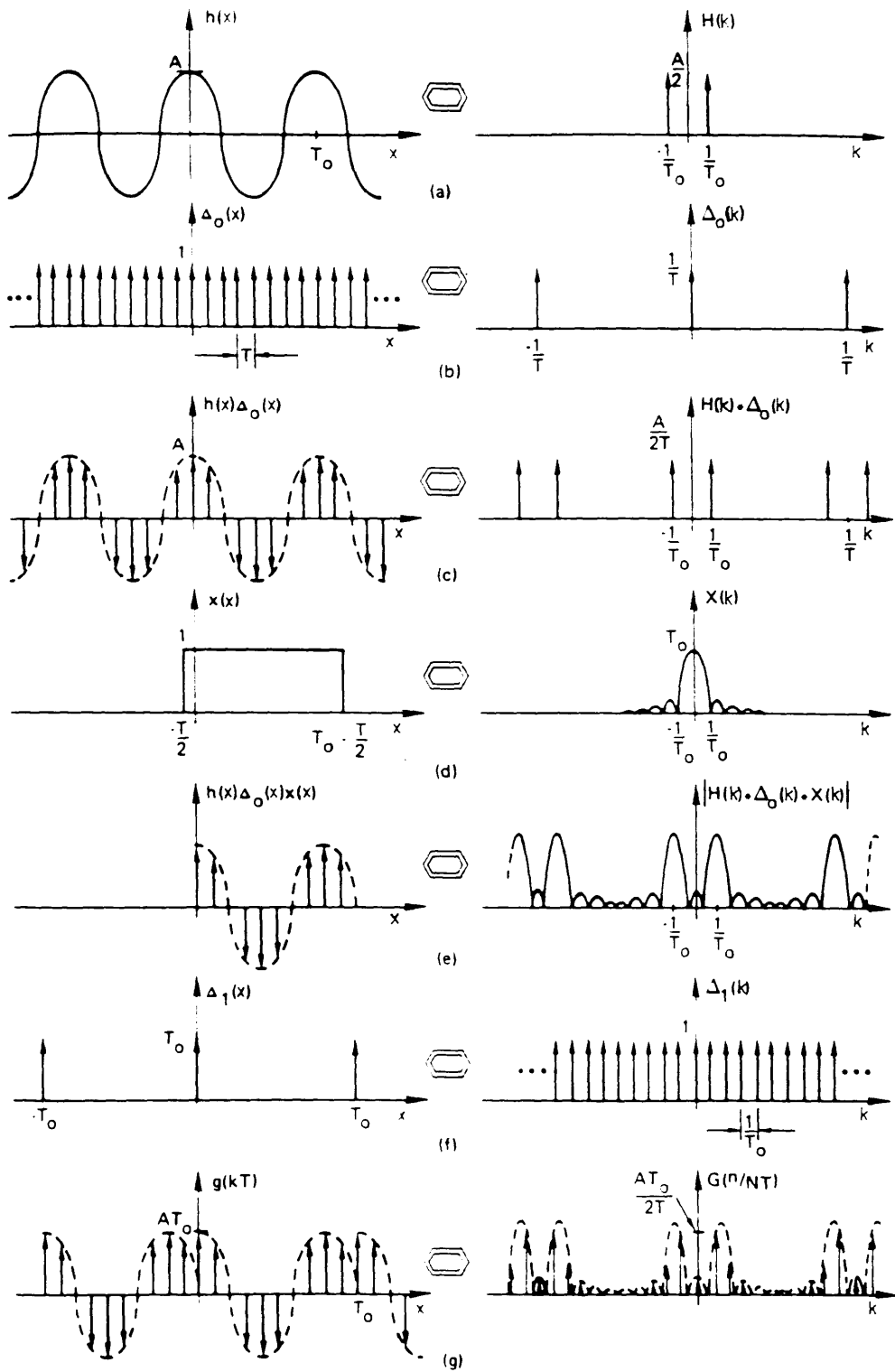


Figure 7.6 - Discrete Fourier transform of a cosine waveform: truncation interval not equal to an integral number of wavelengths (Brigham [3]).

coincide with the zeros of the sinc function transform of the truncation window. The better the truncated real space function approximates a periodogram, the closer the reciprocal frequency sampling will approach the zeros of the sinc function.

In summary, the above discussion has illustrated how critical a role the truncation window, and in particular its length T_0 , plays in the correct application of the FFT algorithm to analysing periodograms, defining

- (1) the reciprocal sampling interval $1/T_0$;
- (2) the exact form of the distribution of the frequency leakage intensity in reciprocal space. The graphical examples have shown how crucial the accuracy to which an exact periodogram can be defined is to producing a good approximation of the continuous Fourier transform by fast Fourier transform computation.

7.4.2 MEDIUM FLUX NOISE POWER FROM TRACK PERIODOGRAMS

Equation (6.18) expressed the medium flux power per unit area ($b.S(k_x)$) in terms of the Fourier transform of the medium magnetisation averaged across the track $M(k_x)$:

$$b.S(k_x) = \frac{W \cdot |b.M(k_x)|^2}{X} \tag{6.18}$$

Here W , X , and b represent the track width and length (along the easy axis) and the film thickness respectively.

In the case of track magnetisation the function $M(k)$ is

composed of the spectral contributions from both the written signal and the transition noise. In order to separate the noise contribution from that arising from the periodic track in equation (6.18) the following model of the average track magnetisation profile $m(x)$ was used

$$m(x) = \left\{ \sum_{j=-\infty}^{+\infty} \delta(x-x_j) \right\} \otimes f_B(x) + n(x) \quad (7.1)$$

where x is along the write direction or easy axis, $n(x)$ represents the intrinsic transition noise from the track medium, $f_B(x)$ is the basis repeat function describing an ideal track wavelength, the delta-function summation distributes the basis function along the waveform, and \otimes denotes the convolution operation.

In the terms previously used when discussing FFT calculated spectra, equation (7.1) describes the infinitely long, continuous real function. In practice, setting the pixel resolution when digitising and selecting the image size by computer processing defines the sampling and the rectangular truncation window length respectively. The digital representation of the magnetisation profile can thus be described in real space as

$$m_D(x) = w(x) \cdot \left[\left\{ \sum_{j=-\infty}^{+\infty} \delta(x-x_j) \right\} \otimes f_B(x) + n(x) \right] \quad (7.2)$$

where $w(x)$ is the rectangular window function defined by

$$\begin{aligned} w(x) &= 1 && \text{for } -T_0/2 \leq x \leq T_0/2 \\ &= 0 && \text{elsewhere} \end{aligned} \quad (7.3)$$

Equation (7.2) represents a real space function in a

form compatible with FFT computation, producing the discrete Fourier transform pair

$$w(x) \cdot \left[\left\{ \sum_{j=-\infty}^{+\infty} \delta(x-x_j) \right\} \otimes f_B(x) + n(x) \right] \xrightarrow{\underline{dFt}} \\ W(k_x) \otimes \left[\left\{ \sum_{j=-\infty}^{+\infty} e^{i k_x x_j} \right\} \cdot F_B(k_x) + N(k_x) \right] \quad (7.4)$$

that approximates the following continuous Fourier transform pair

$$\left\{ \sum_{j=-\infty}^{+\infty} \delta(x-x_j) \right\} \otimes f_B(x) + n(x) \xrightarrow{\underline{cFt}} \\ \left\{ \sum_{j=-\infty}^{+\infty} e^{i k_x x_j} \right\} \cdot F_B(k_x) + N(k_x) \quad (7.5)$$

The differences between the two Fourier pairs of equations (7.4) and (7.5) arise solely from the process of data truncation, manifesting spectrally in the form of the $W(k)$ convolution. To utilise the FFT data the effects of this truncation must therefore be examined. The signal and noise contributions to the discrete reciprocal spectrum of equation (7.4) can be separated by re-writing the expression as

$$\frac{W(k_x) \otimes \left[\left\{ \sum_{j=-\infty}^{+\infty} e^{i k_x x_j} \right\} \cdot F_B(k_x) \right]}{F_s(k_x)} + \frac{W(k_x) \otimes N(k_x)}{F_n(k_x)} \quad (7.6)$$

From this expansion it is seen that the measurement of the medium flux noise power spectrum is limited to the convolution function $F_n(k_x)$, and that in order to obtain measurements of $F_n(k_x)$ the form of the signal contribution $F_s(k_x)$ must be taken into account. We write $F_s(k_x)$ as:

$$F_s(k_x) = W(k_x) \otimes \left[\left\{ \sum_{j=-\infty}^{+\infty} e^{i k_x x_j} \right\} \cdot F_B(k_x) \right] \\ = \left[W(k_x) \otimes \left\{ \sum_{j=-\infty}^{+\infty} e^{i k_x x_j} \right\} \right] \cdot F_B(k_x) \quad (7.7a)$$

$$= FT \left(\left[w(x) \cdot \left\{ \sum_{j=-\infty}^{+\infty} \delta(x-x_j) \right\} \right] \otimes f_B(x) \right) \quad (7.7b)$$

Written in this form the action of the truncation

window can be interpreted as limiting the number of periods of signal present in the image, or equivalently the range of the j index. This in turn restricts the number of exponential terms permitted in the reciprocal space summation of equation (7.7a). For a periodogram truncation window allowing exactly J periods equation (7.7a) can be re-written by expanding the exponential terms of this summation

$$F_s(k_x) = \left\{ \sum_j e^{i k_x x_j} \right\} \cdot F_B(k_x)$$

$$= \left\{ 2 \cdot \sum_{j=1/2}^{+(J-1)/2} \cos(k_x x_j) \right\} \cdot F_B(k_x) \quad J \text{ even} \quad (7.8a)$$

$$= \left\{ 1 + 2 \cdot \sum_{j=1}^{+(J-1)/2} \cos(k_x x_j) \right\} \cdot F_B(k_x) \quad J \text{ odd} \quad (7.8b)$$

Figure 7.7 illustrates graphically the form of the trigonometric functions in the above equations for several values of J .

Whether J is odd or even the function by which $F_B(k_x)$ is multiplied has a well defined set of frequencies $\{k_1\}$ at which it is zero, that is, the signal contribution to the FFT calculated spectrum, $F_s(k_x)$, is zero. Hence, at these frequencies the computed FFT spectra yield the noise contribution alone,

$$M(k_1) = W(k_1) \otimes N(k_1) \quad \text{for all } \{k_1\} \quad (7.9)$$

This equation defines the frequencies at which a weighted average of the medium flux noise power for the square wave written track can be estimated from an FFT calculation of the power spectrum obtained from a Lorentz derived binary periodogrammic image of the track magnetisation. The accurate measurement of the noise power spectrum at these frequencies is therefore the essence of the periodogram technique.

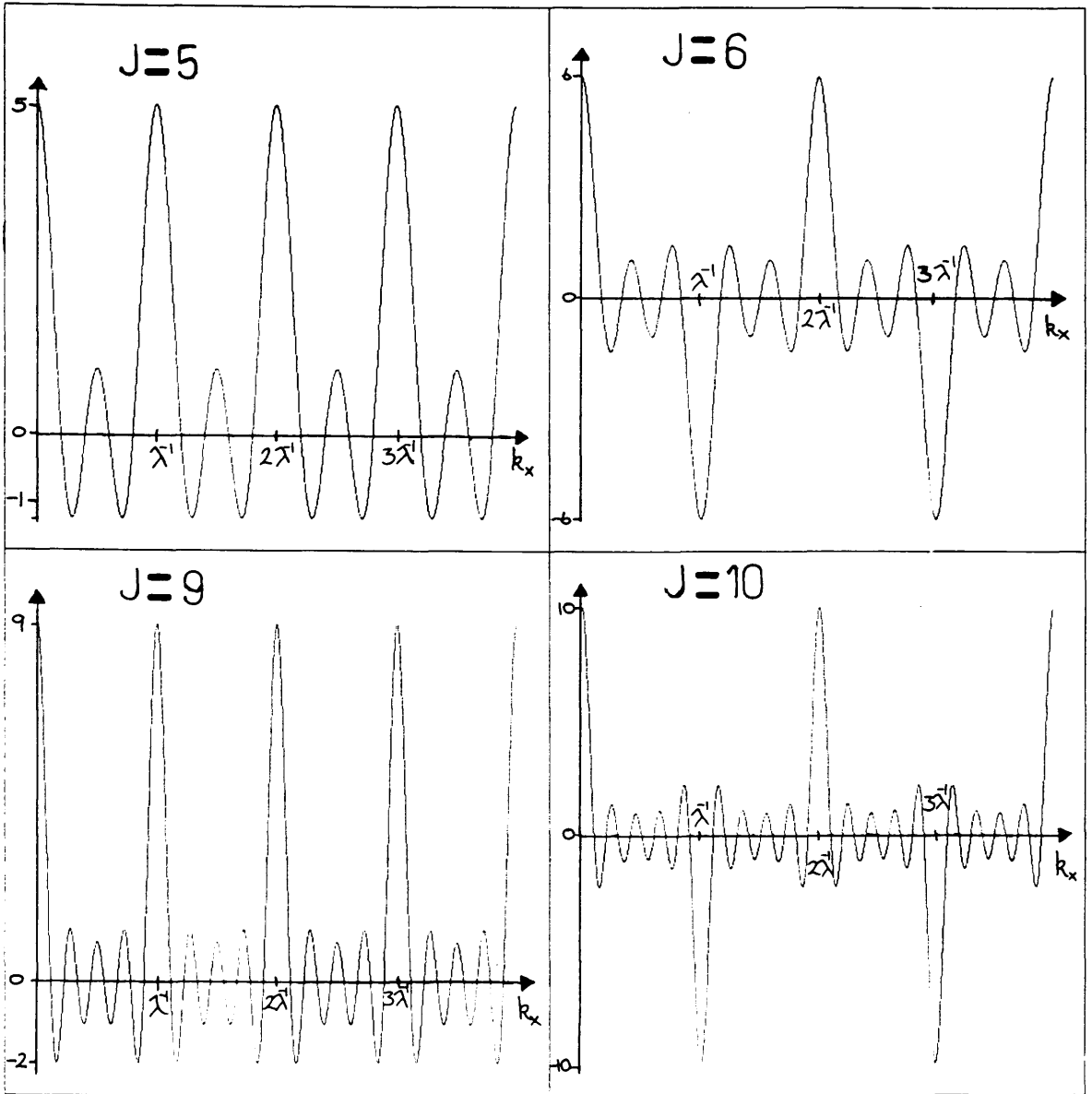


Figure 7.7 - Graphical illustration of the form of the trigonometric terms in equations (7.8a) and (7.8b) for $J=5, 6, 9,$ and 10 . The frequency of the track is given by λ^{-1} where λ is the track wavelength.

7.4.3 RESULTS OF THE PERIODOGRAM APPROACH

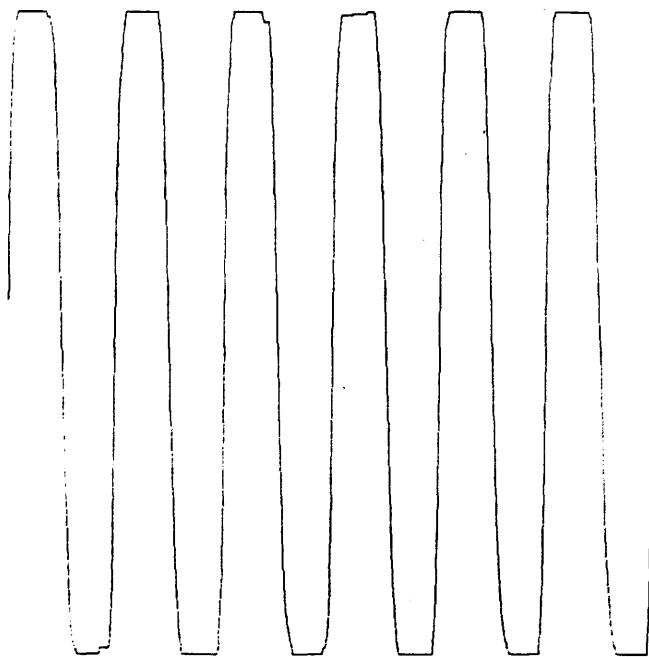
Periodograms of both the three and six megahertz square wave written tracks were used to calculate the transition noise power spectra for comparison with the electronically measured data. In each case the magnetisation averaged across the written track was employed in the fast Fourier transform, but padded with zeros from 1024 pixels in length to the maximum permitted size on the IBM 3090 mainframe of 16384 pixels. The pixel precision was set at 32 bits per element, floating point number.

(A) THREE MEGAHERTZ TRACK

Two binary periodograms were created from Fresnel images of the 3MHz square wave written track, each six periods long. The average magnetisation taken across these track sections are shown in figure 7.8.

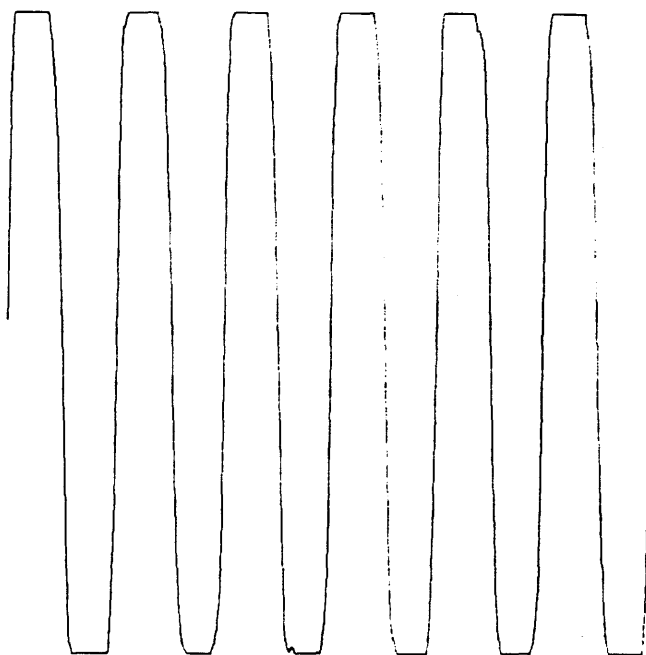
The use of the word periodogram to describe these waveforms is not strictly accurate. By definition a periodogram contains an exact integer number of periods; the magnetisation profile is a composite of the perfectly periodic waveform recorded to the medium (represented by the basis function in equation (7.1)) and a transition noise function intrinsic to the medium. Therefore, it is not possible to define exactly a periodogram of the track profile, only an approximation to such a function can be made.

$+M_s$



$-M_s$

$+M_s$



$-M_s$

Figure 7.8 - Magnetisation profiles for the two 3MHz periodograms.

The determination of where best to truncate a magnetisation waveform in order to obtain a 'periodogram' sample of the track profile was accomplished by discarding all data before the point on the first transition at which the value of the average magnetisation was closest to zero, as in figure 7.8. Moving along the waveform a given number of periods, say six for instance, then defines the periodogram length. The last pixel was chosen in the locality of the end of the sixth wavelength at one point before the position where the value of the magnetisation profile was again closest to zero. (This then defines the 'periodogram' length in a basic manner).

For both 3 MHz periodograms the trigonometric function generated by the convolution in reciprocal space of the truncation window sinc function with the written magnetisation signal can be written for six periods using equation (7.8a) with J=6:

$$T = 2 \cdot \sum_{j=1/2}^{5/2} \cos(k_x x_j) \quad (7.10)$$

This is illustrated graphically in figure 7.7 from which it can be seen that between the signal harmonic frequencies of $0.5\mu\text{m}^{-1}$, $1.0\mu\text{m}^{-1}$, $1.5\mu\text{m}^{-1}$, and so on there will be five frequencies at which the value of the noise spectra from the periodogram can be measured free from any signal contributions.

The power spectra from the two independent periodograms are shown in figures 7.9a and 7.9b. The presence of the five minima between harmonics is clearly seen, as are the signal side-lobe effects arising from window

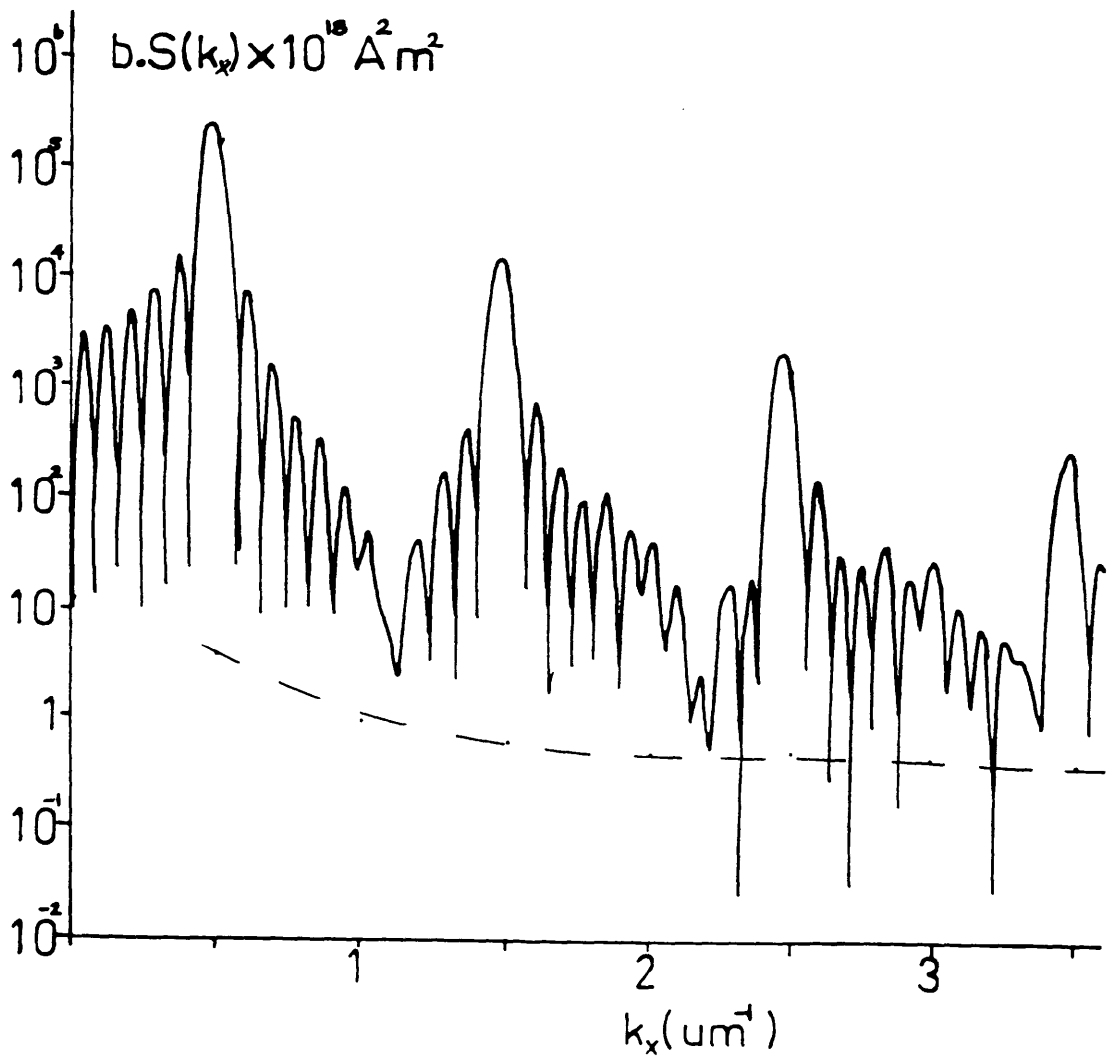
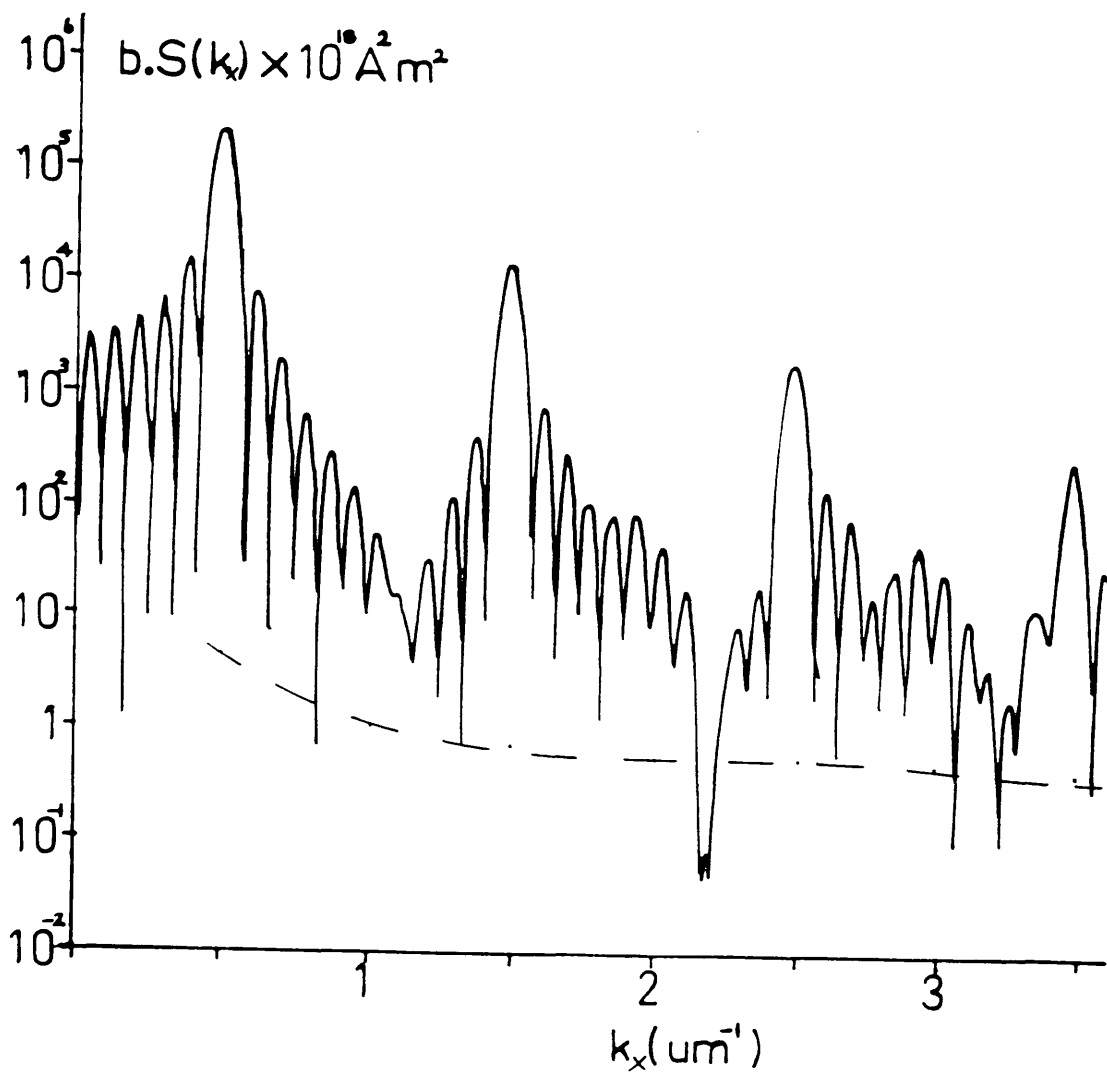
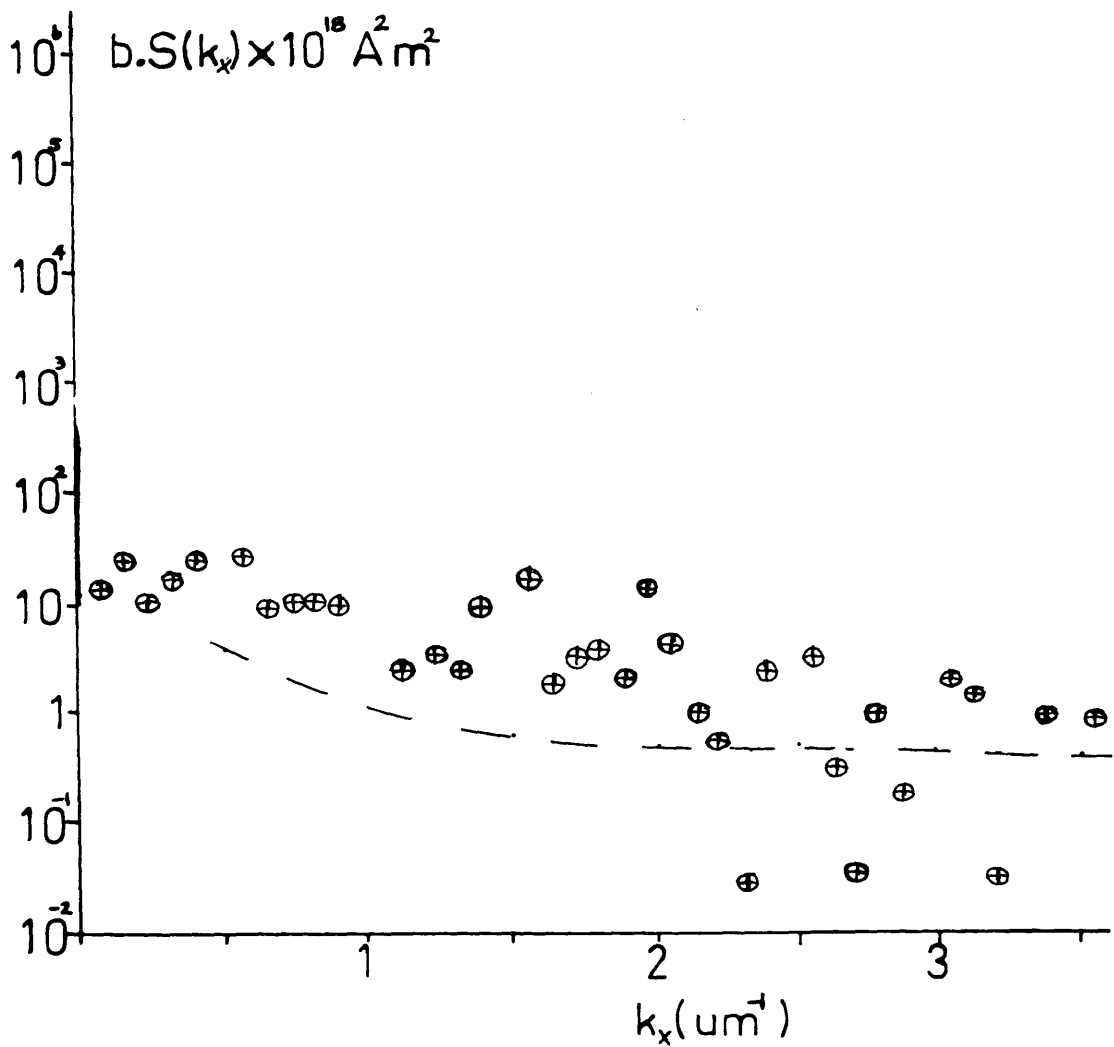


Figure 7.9 - (a) Log10-linear graphical comparison of the noise spectrum generated from the data of figure 7.8a and that measured electronically for the 3MHz track.

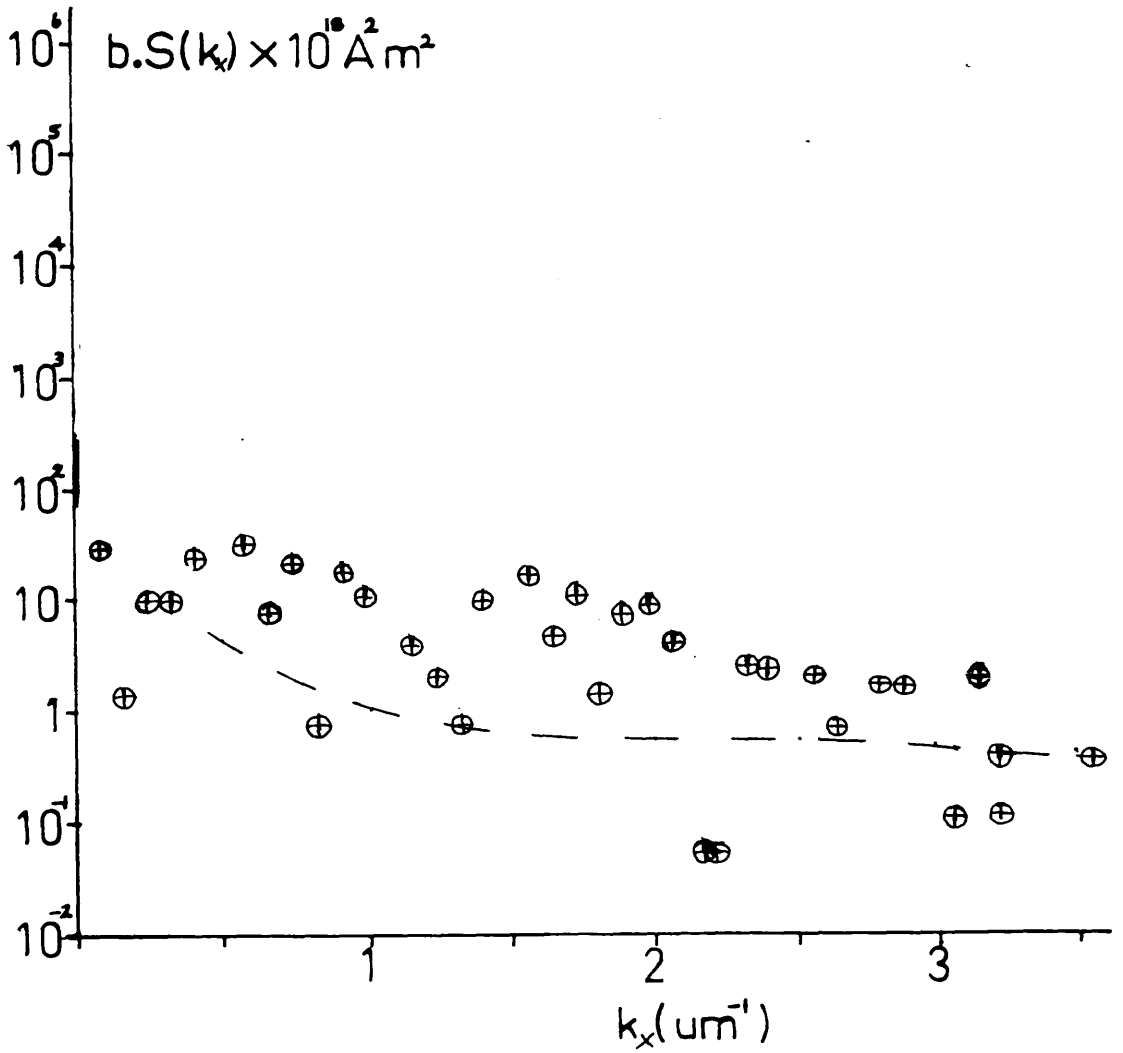


(b) Log10-linear graphical comparison of the noise spectrum generated from the data of figure 7.8b and that measured electronically for the 3MHz track.

truncation. The values of the power spectra in figures 7.9a and b at the minima frequency positions correspond to the noise power values free from signal contributions and are plotted in figures 7.9c and d respectively. It was observed that while many of the minima values lay close to the line representing the electronically measured noise, there were discrepancies - particularly in the vicinity of the recorded signal peaks. In any explanation of the differences between the Lorentz and electronic spectra the weighted averaging of the Lorentz derived noise spectrum caused by real-space truncation and the possibility of some local spectral signature associated with a particular periodogram must be accounted for when comparison is made with the more global electronic measurement. However, the other effects inherent in the digital fast Fourier transform calculation are more probably responsible for the major discrepancies between the two spectra. We shall discuss these and how they limit the accuracy at which the noise power values can be sampled at the minima frequencies defined by equation (7.9). Although a technique has been used that estimates periodogrammic lengths from magnetisation profile waveforms, the resultant periodograms will almost certainly be incorrect by very small amounts. Then, as was seen for the cosine signal of figure 7.6 which was not truncated to an integral number of periods, the sampling interval in reciprocal space cannot exactly evaluate the noise spectrum at precisely the frequencies where the convoluted signal contribution is



(c) The minima values taken from figure 7.9a and plotted for comparison with the electronic data.



(d) The minima values taken from figure 7.9b and plotted for comparison with the electronic data.

zero. Instead an estimate of the noise plus some secondary signal leakage amplitude is sampled very close to the true minima frequency. In this way the minima in the spectra of figures 7.9c and 7.9d can be considered as the best estimates of the points that define the transition noise spectrum which can be obtained from the approximation to a periodogram.

(B) SIX MEGAHERTZ TRACK

A pair of independent magnetisation profiles representing the 6MHz track were analysed in the same manner as the 3MHz track described above, these are illustrated in figure 7.10. For this recorded frequency both periodograms were ten periods in length, allowing the trigonometric function of equation (7.8a) to be evaluated with $J=10$:

$$T = 2 \cdot \sum_{j=1/2}^{9/2} \cos(k_x x_j) \quad (7.11)$$

Figure 7.7 graphs this function, indicating that there are nine equidistant minima frequencies between the harmonic frequencies ($1\mu\text{m}^{-1}$, $2\mu\text{m}^{-1}$, $3\mu\text{m}^{-1}$, etc) at which the noise power spectrum can be measured alone. Figures 7.11a and 7.11b graph the power spectrum calculated from the two 6MHz periodograms while figures 7.11c and d graph the minima intensity values observed in figures 7.11a and b respectively.

From figure 7.11 it is again seen that the inherent uncertainty in perfect periodogrammic truncation impairs the resolution of the true noise power values. Several extremely low minima values were observed in

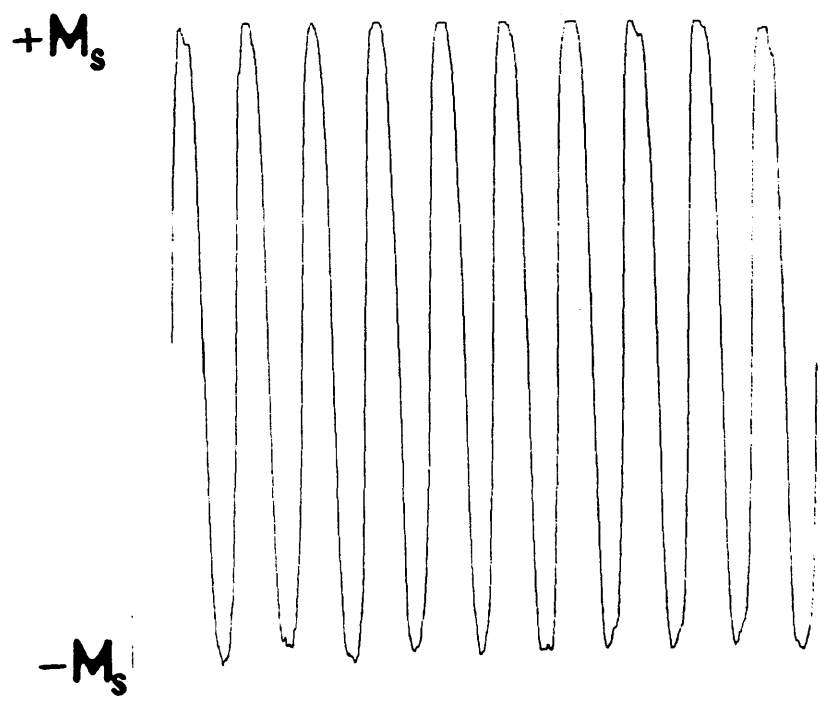
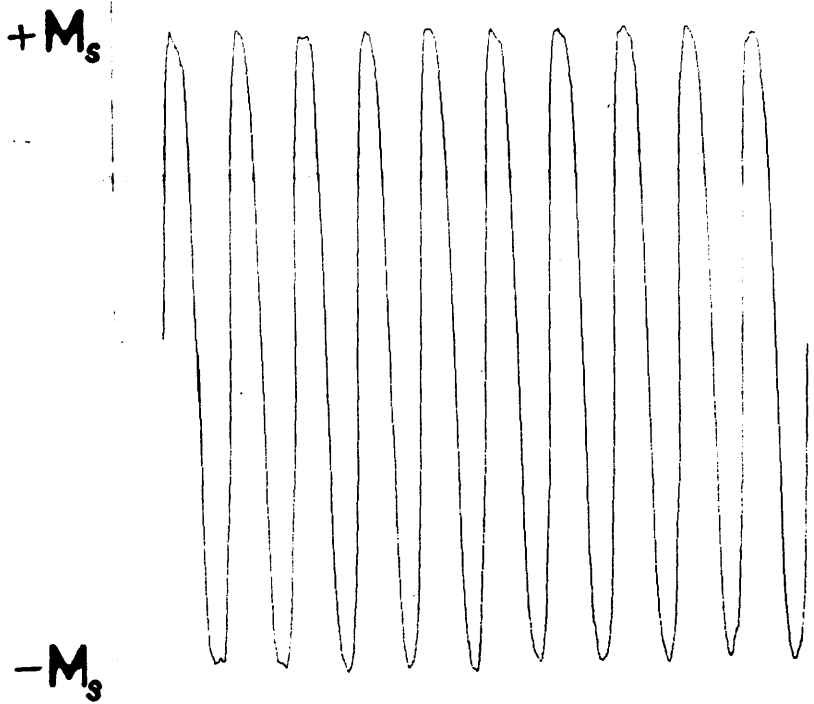


Figure 7.10 - Magnetisation profiles for the two 6MHz periodograms.

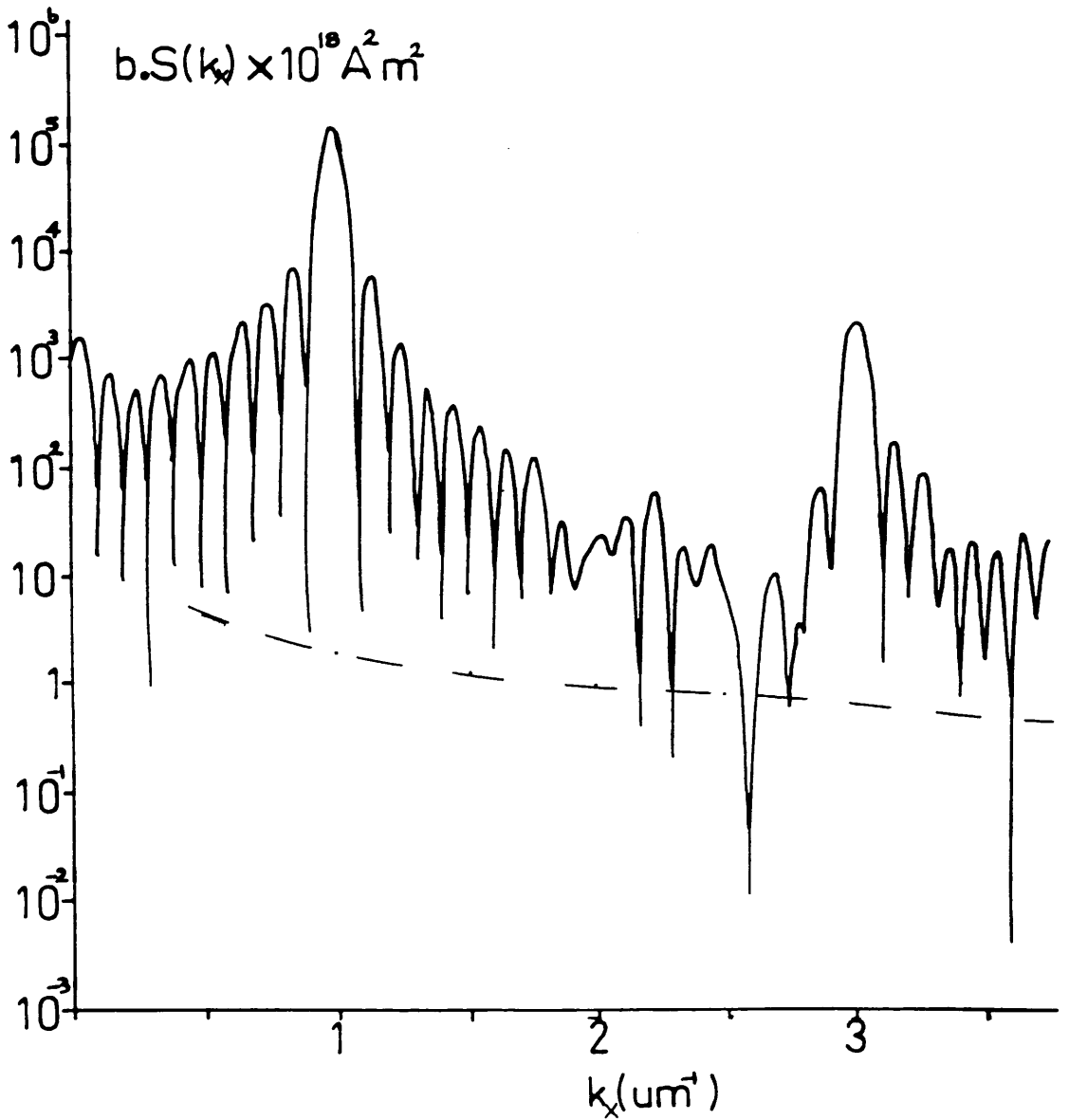
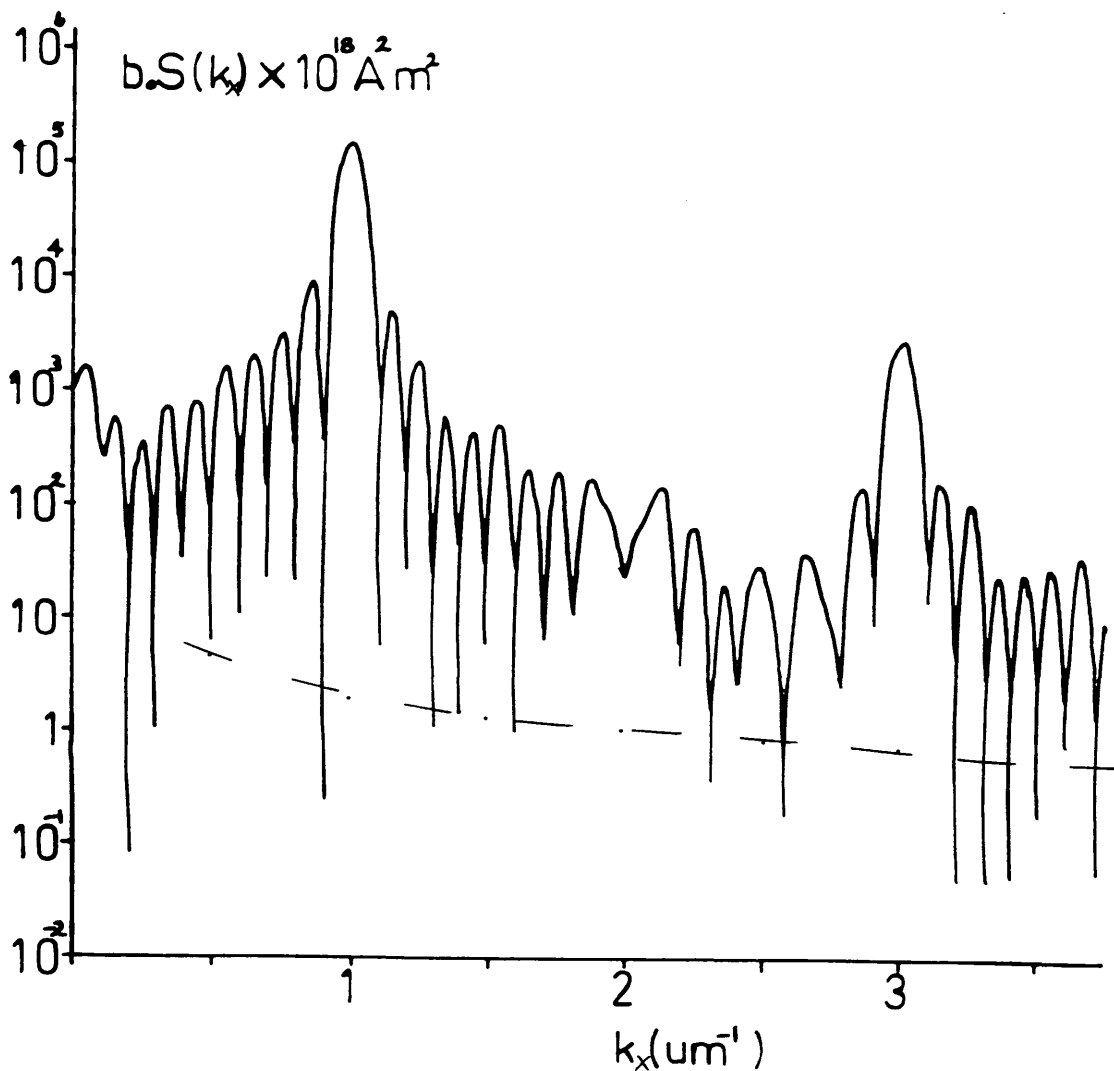
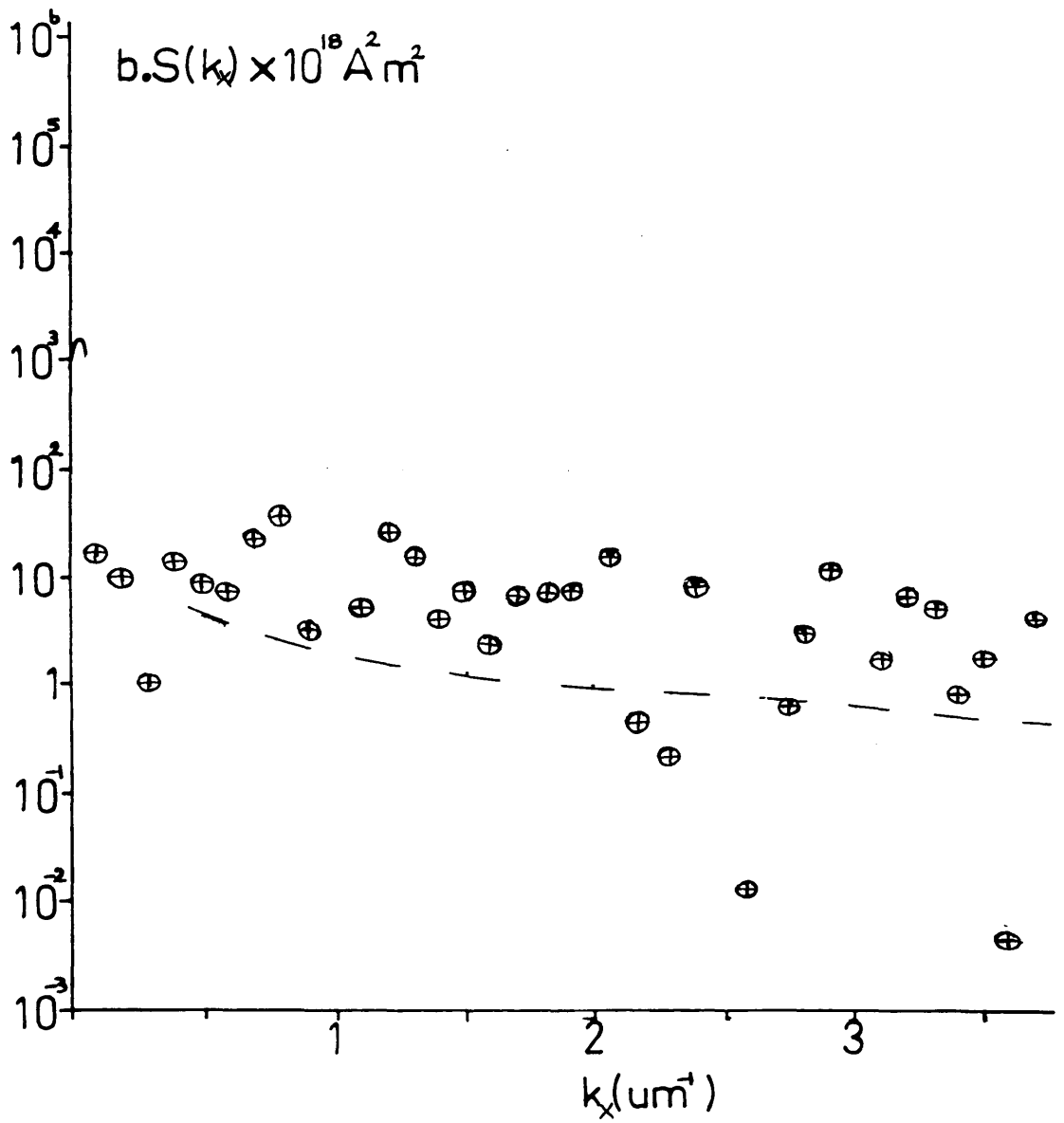


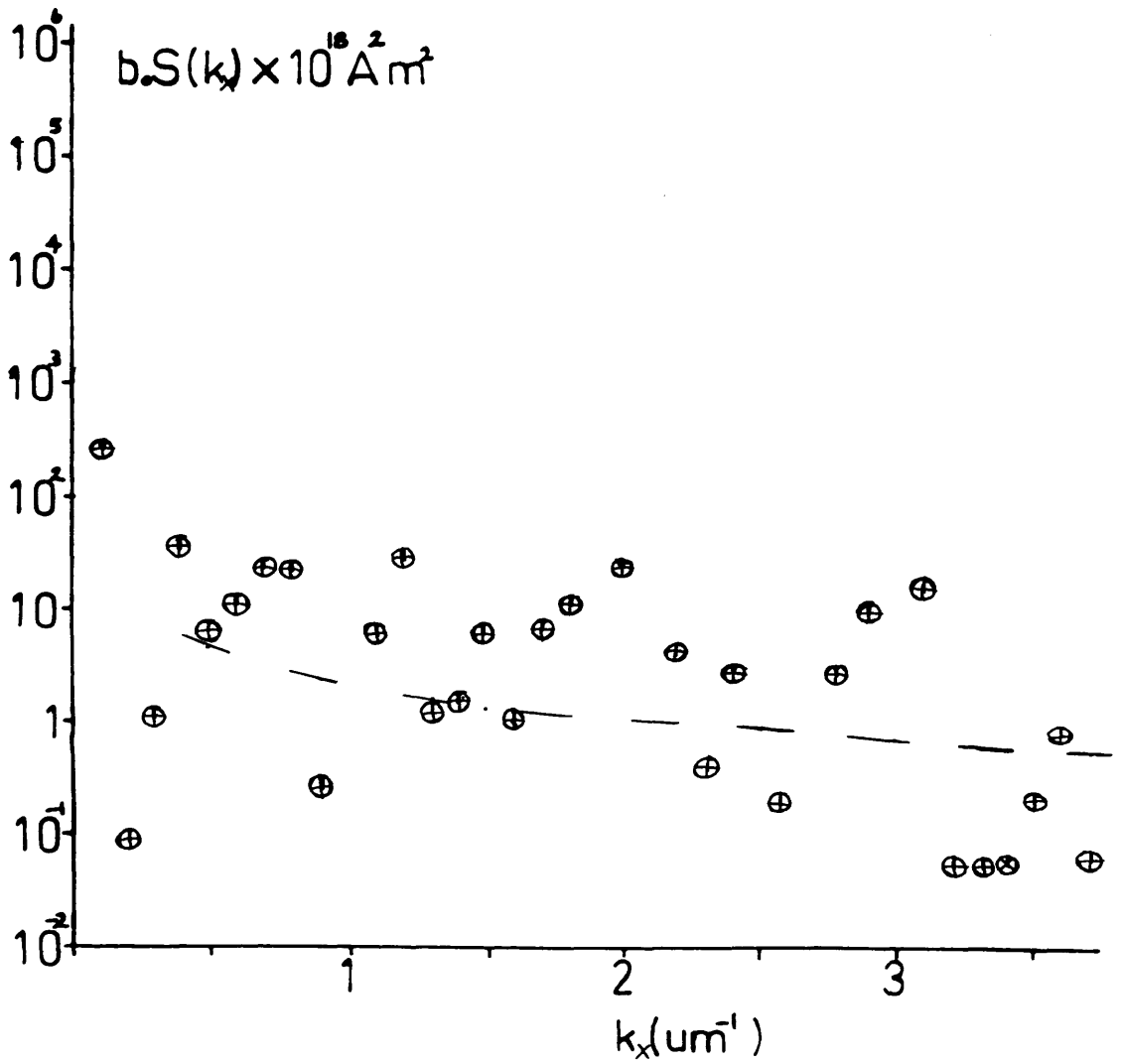
Figure 7.11 - (a) Log10-linear graphical comparison of the noise spectrum generated from the data of figure 7.10a and that measured electronically for the 6MHz track.



(b) Log10-linear graphical comparison of the noise spectrum generated from the data of figure 7.10b and that measured electronically for the 6MHz track.



(c) The minima values taken from figure 7.11a and plotted for comparison with the electronic data.



(d) The minima values taken from figure 7.11b and plotted for comparison with the electronic data.

the low frequency region of the Lorentz derived power spectrum in figure 7.11d. These may arise from effects generated by the amplitude convolution between the truncation window and the track signal profile.

The average of the two 3MHz and the average of the two 6MHz noise profiles are graphed separately in figures 7.12a and 7.12b for comparison with the corresponding electronically measured spectra. Generally the agreement is seen to be better for the respective averages than from any of the individual periodograms.

(C) PERIODOGRAM ROTATION

It was observed for an exact integral number of periods of a synthesised square wave that the depth of the minima observed upon fast Fourier transforming with zero padding varied significantly depending upon the end-point values of the truncated real space sample. Whether the data began or ended close or far from the binary remanent magnetisation value of ± 127 appeared to have a definite effect upon the calculated spectrum. The experimental verification with the square wave is summarised schematically in figure 7.13.

A quantitative understanding of this computational observation is beyond the scope of this discussion. Instead this effect was incorporated empirically in the following way: the original periodogram image data of length 1024 pixels was taken and cycled within the 1024 pixel window. In practice a group of pixels were taken from the beginning and added to the end in sections corresponding to $\lambda/20$; this procedure was repeated

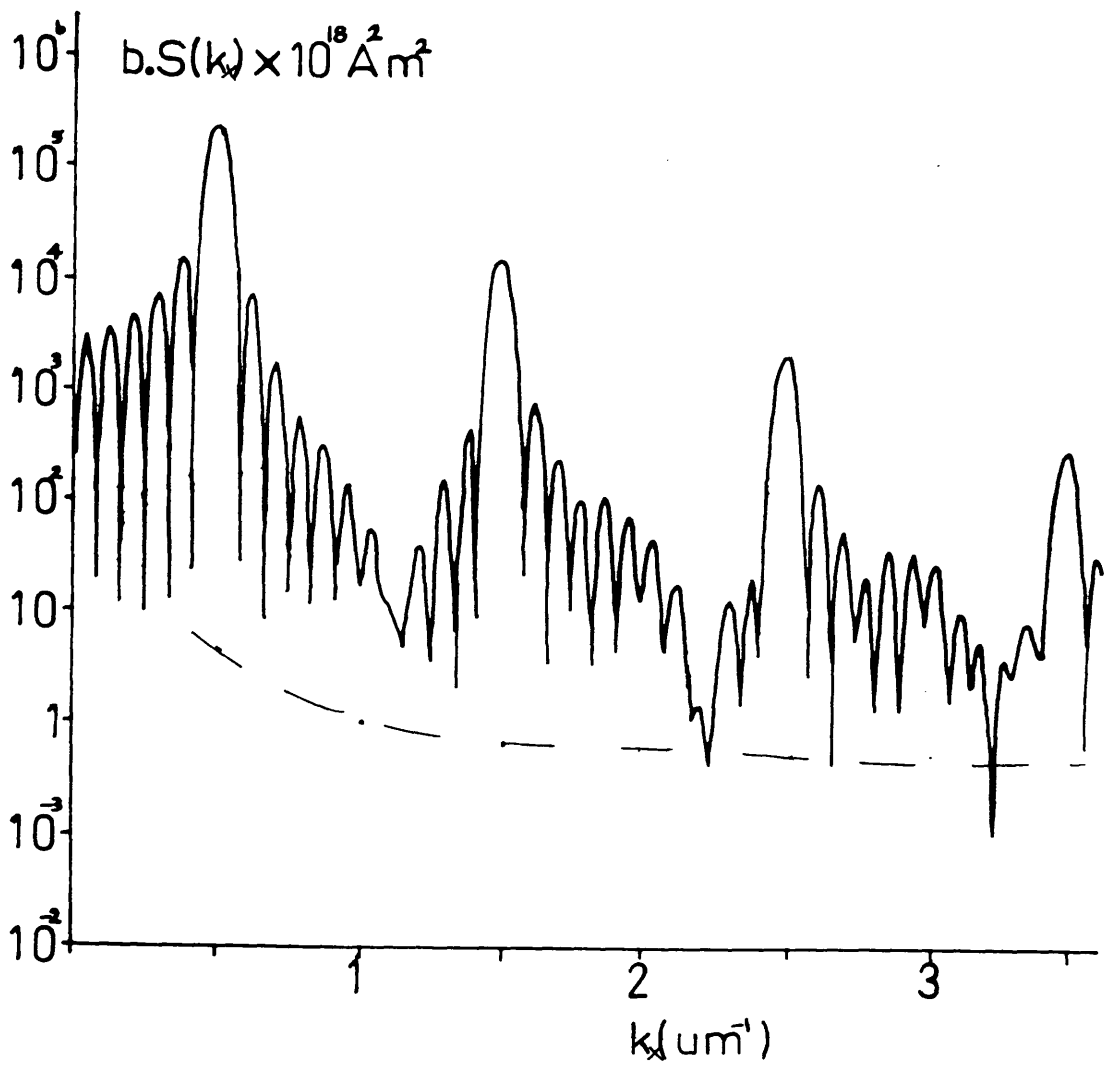
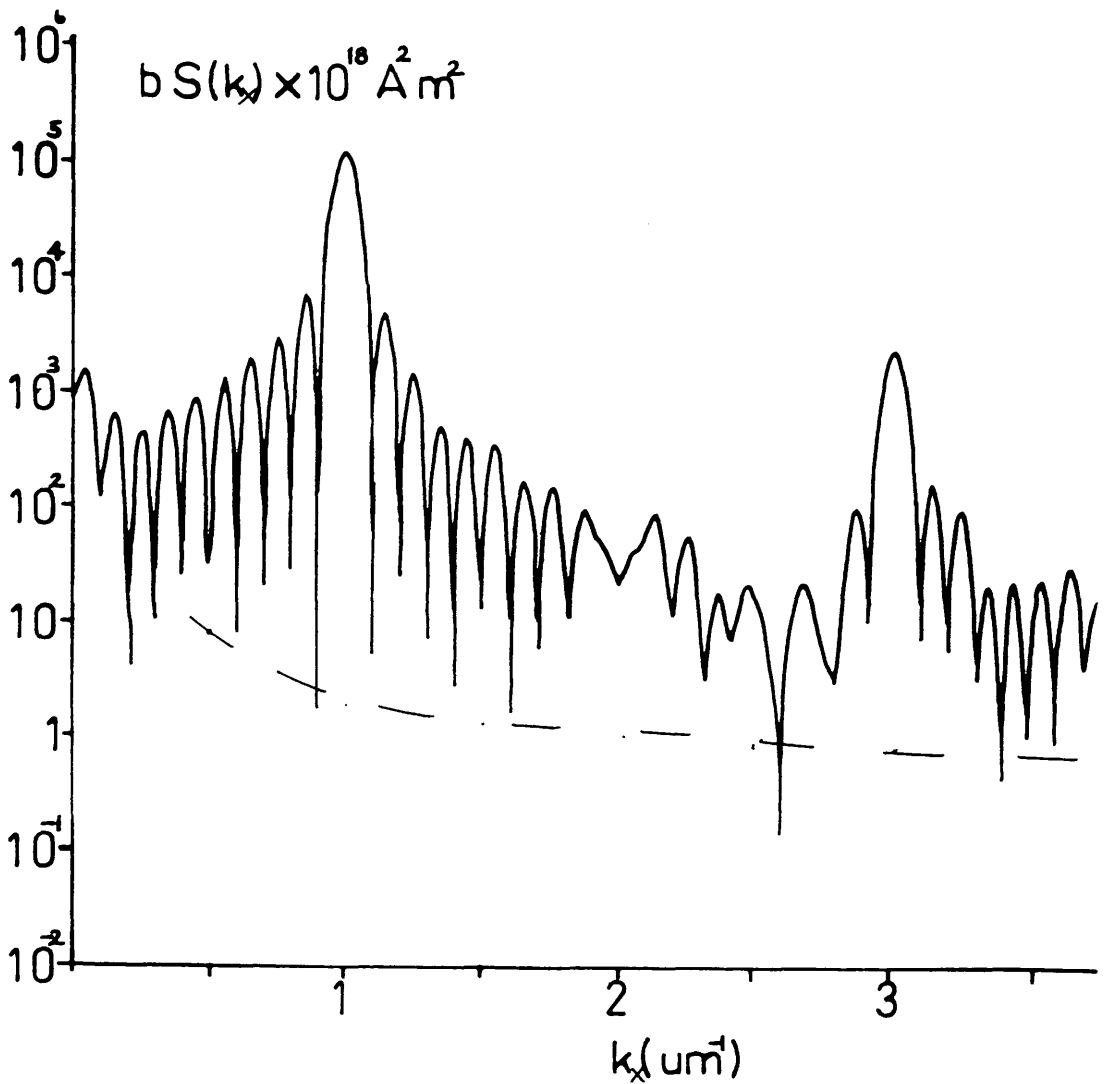
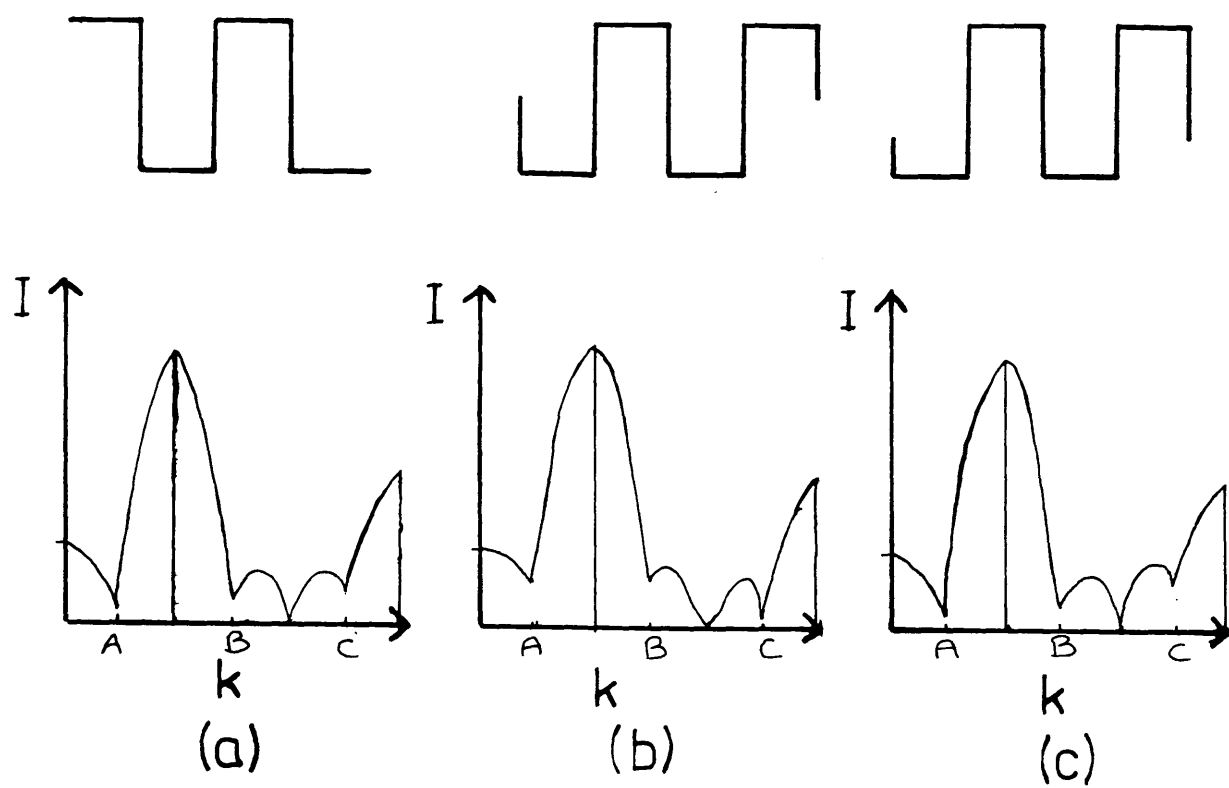


Figure 7.12 - (a) A Log10-linear graphical comparison between the average of the Lorentz derived spectra graphed in figure 7.9 and the 3MHz electronic data.



(b) A Log10-linear graphical comparison between the average of the Lorentz derived spectra graphed in figure 7.11 and the 6MHz electronic data.



Minima Values A,B, & C.

Figure 7.13 - The three Fourier transform pairs (a), (b), and (c) qualitatively illustrate how the k-space minima intensity values were seen to depend on the end-point values of the square waves in real space.

until the data had been rotated through approximately half a period. At each stage the data was padded with zeros to a length of 16,384 pixels and then fast Fourier transformed. The values of the minima were then determined for each of the individual spectra, and the median magnitude at any particular k-value was selected to represent the noise power at that point. The analysis was performed on the two independent sets of 5 period 3MHz data. The average of the noise power obtained from these is shown in figure 7.14, together with data derived from the electronic measurement. A similar exercise was performed for two independent sets of 11 period 6MHz images. The results of averaging the noise power derived from these are plotted in figure 7.15. For both frequencies the noise spectra minima of figures 7.14 and 7.15 may show slightly better agreement with the electronically measured noise power than the corresponding figures of 7.9 and 7.11. Thus, the data rotation procedure possibly proved marginally beneficial.

While the general agreement between the Lorentz and electronic data sets in figure 7.14 is generally good, residual signal effects are still observed in the vicinity of the signal peaks in figure 7.15. One possible method of reducing the effects of the signal would be to use alternative window functions to the rectangular form imposed by the way our image data is defined. Much has been written on such windows (for example references [4,8,9]) but they are designed in general to discern signal in the presence of

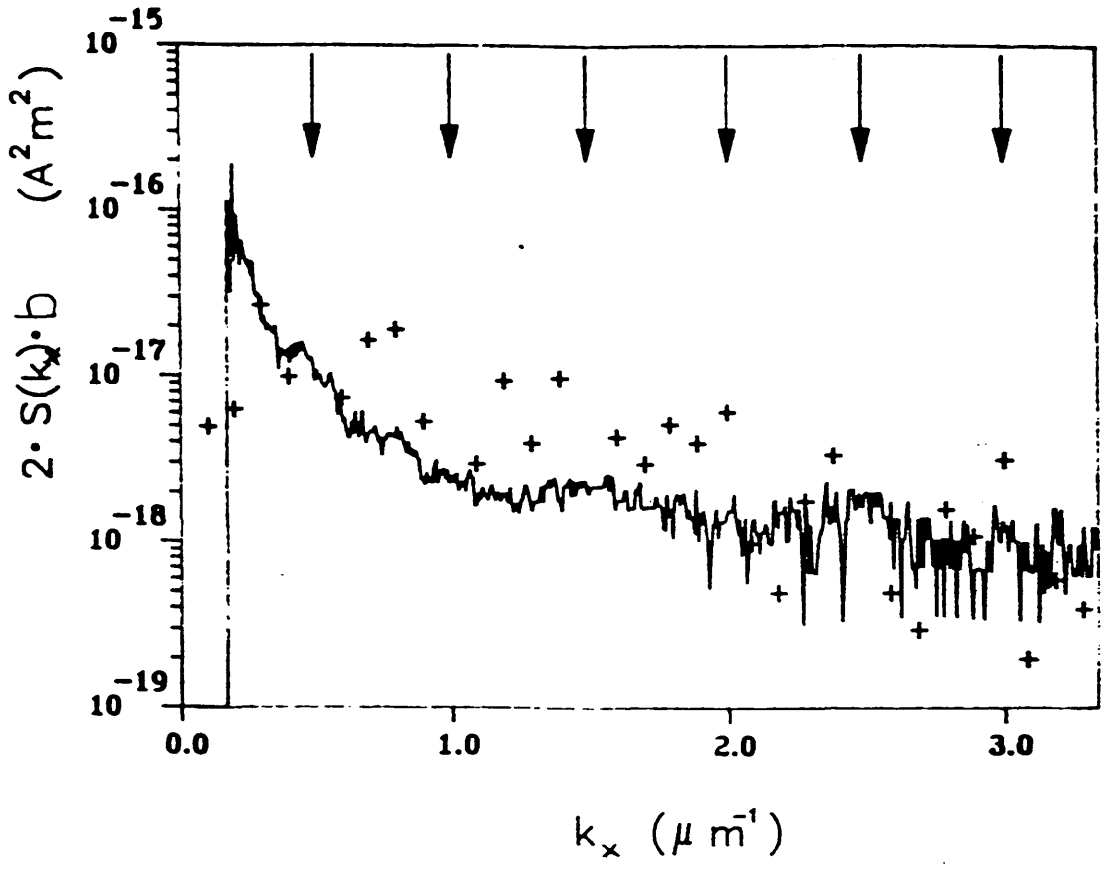


Figure 7.14 - Log10-linear graphical comparison of the Lorentz derived and electronically measured noise spectra when data rotation was applied to the 3MHz periodograms.

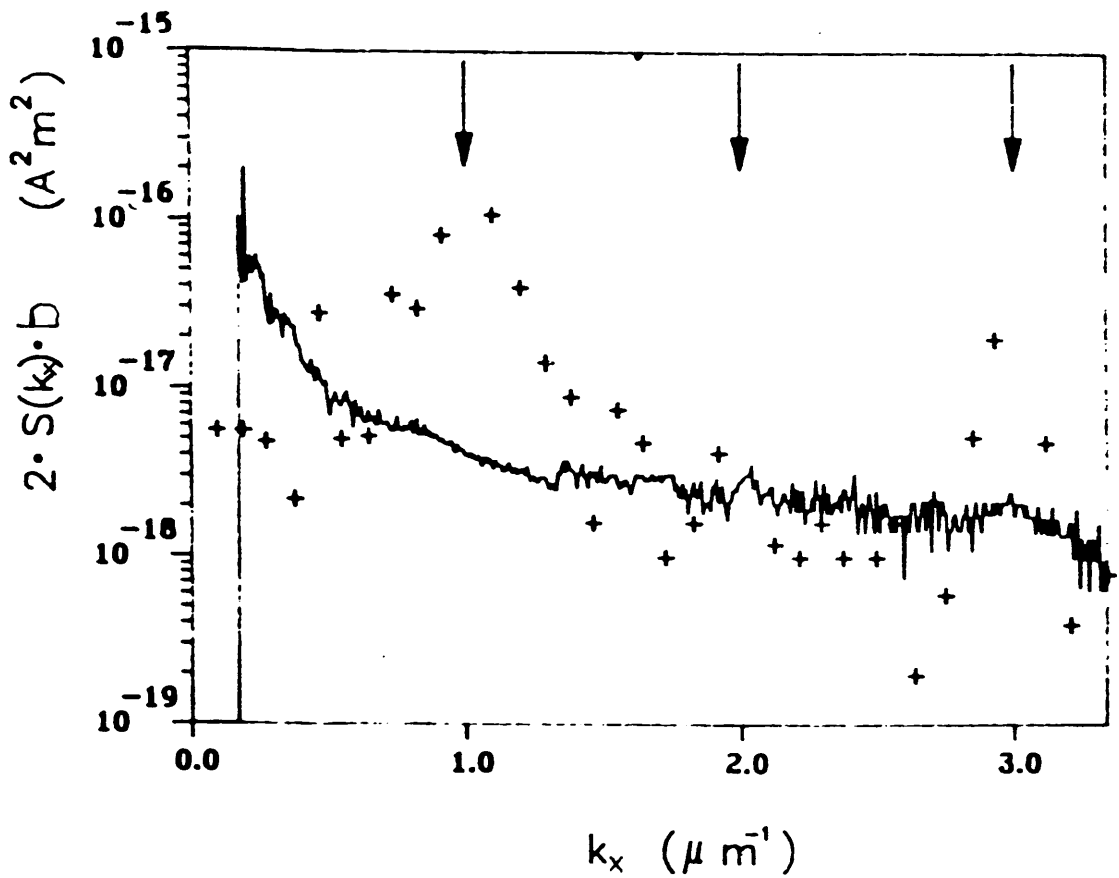


Figure 7.15 - Log10-linear graphical comparison of the Lorentz derived and electronically measured noise spectra when data rotation was applied to the 6MHz periodograms.

significant noise and they achieve this by suppressing the signal side-lobes at the expense of an increased signal peak width. In our case we are involved in the much rarer procedure of extracting noise in the presence of large signal peaks and it is not yet clear the role that these alternative window functions can play in improving our analysis procedures. In the case of the 3MHz comparison illustrated in figure 7.14, any influence of the signal peaks in the Lorentz image derived noise spectrum appear reduced when compared to figure 7.9, and the agreement between the two sets of noise data is reasonably good.

7.4.4 SUMMARY

From the results of the periodogram approach it was seen that quantitative transition noise estimation in the presence of the dominant track signal by fast Fourier transform analysis is restricted in effectiveness by sample truncation phenomena:

- (1) the actual noise measurement attainable is 'blurred' by the convolution with the Fourier transform of the truncation window function;
- (2) this convolution limits the number of frequency values at which the noise can be measured uncorrupted by signal contributions;
- (3) accurate frequency domain sampling in the fast Fourier computation, critical to quantitative estimation, was seen to be susceptible to corruption

from non-integral periodogram representations used in the practical application of written track magnetisation;

(4) end-point effects intrinsic to fast Fourier transform calculations introduce further uncertainty to the final result.

These effects combine to corrupt the absolute intensity minima values associated with many of the frequencies where the signal contribution is zero, thus greatly limiting this technique of noise power estimation.

7.5 ANALYSIS OF INDIVIDUAL MAGNETISATION TRANSITIONS

As stated above, limitations associated with the periodogram approach were exposed when it was employed to examine written track transition noise. These limitations were all seen to be related to the periodogram length and convolution effects. The solutions to the problems posed by these observations requires the elimination of the window function from the noise calculations, or at least a substantial reduction in its influence on the extraction of quantitative data. A development of this idea brought about a markedly different approach to transition noise estimation from the Lorentz images, that of examining individual flux transitions and their departure from an average magnetisation reversal profile. This method was seen as capable of yielding greater insight into

the origins and nature of transition noise than the periodogram treatment could afford.

7.5.1 A TRACK MODEL IN TERMS OF INDIVIDUAL MAGNETISATION TRANSITIONS

As with the a.c. erased medium and the periodic track the relationship through which the noise power per unit area ($b.S(k_x)$) can be calculated from the magnetisation averaged across the track $m(x)$ is

$$b.S(k_x) = \frac{W. |b.M(k_x)|^2}{X} \quad (6.18)$$

where $M(k_x)$ is the Fourier transform of $m(x)$, b is the medium thickness, W is the track width, and X is the length of track analysed.

In terms of the individual flux transitions that constitute a written track the following model for $m(x)$ was used. The j 'th magnetisation reversal $P_j(x)$ was assumed to be composed of a basis step function $f_B(x)$ plus a local transition noise contribution $n_j(x)$

$$P_j(x) = f_B(x) + n_j(x) \quad (7.12)$$

The one-dimensional magnetisation profile along the write direction x can then be written as

$$m(x) = f_{B+} \otimes \sum_{j=-\infty}^{+\infty} \delta(x-x_{j+}) + \sum_{j=-\infty}^{+\infty} \{ n_{j+}(x) \otimes \delta(x-x_{j+}) \} \\ + f_{B-} \otimes \sum_{j=-\infty} \delta(x-x_{j-}) + \sum_{j=-\infty} \{ n_{j-}(x) \otimes \delta(x-x_{j-}) \} \quad (7.13)$$

where the + and - subscripts denote step up ($-M_s$ to $+M_s$) and step down ($+M_s$ to $-M_s$) magnetisation reversals. The step up and step down transitions shall

be treated identically but separately. Equation (7.13) shows clearly the separation of the signal (represented by the basis function) and the noise contributions, allowing the Fourier transform of the noise to be described alone by

$$\begin{aligned} M(k_x) &= \text{FT} \left[\sum_{j=-\infty}^{+\infty} \{ n_j(x) \otimes \delta(x-x_j) \} \right] \\ &= \sum_{j=-\infty}^{+\infty} \{ N_j(k_x) \cdot e^{i k_x x_j} \} \end{aligned} \quad (7.14)$$

In equation (6.18) it is the modulus squared of $M(k_x)$ that is calculated, hence from above

$$\begin{aligned} |M(k_x)|^2 &= \left| \sum_{j=-\infty}^{+\infty} \{ N_j(k_x) \cdot e^{i k_x x_j} \} \right|^2 \\ &= \sum_{j=-\infty}^{+\infty} |N_j(k_x)|^2 + \sum_{\substack{i, j=-\infty \\ i \neq j}}^{+\infty} \{ N_i(k_x) \cdot N_j^*(k_x) \cdot e^{i k_x x_i} \cdot e^{-i k_x x_j} \} \end{aligned} \quad (7.15)$$

The real space equivalent of the second term in the above equation can be expanded as

$$\begin{aligned} \text{FT}^{-1} \left[\sum_{\substack{i, j=-\infty \\ i \neq j}}^{+\infty} \{ N_i(k_x) \cdot N_j^*(k_x) \cdot e^{i k_x x_i} \cdot e^{-i k_x x_j} \} \right] \\ &= \text{FT}^{-1} \left[\sum_{\substack{i, j=-\infty \\ i \neq j}}^{+\infty} \{ N_i(k_x) \cdot e^{i k_x x_i} \cdot N_j^*(k_x) \cdot e^{-i k_x x_j} \} \right] \\ &= \sum_{\substack{i, j=-\infty \\ i \neq j}}^{+\infty} \{ \delta(x-x_i) \otimes n_i(x) \} \otimes \{ \delta(x-x_j) \otimes n_j^*(x) \} \\ &= \sum_{\substack{i, j=-\infty \\ i \neq j}}^{+\infty} \{ n_i(x-x_i) \otimes n_j^*(x-x_j) \} \end{aligned} \quad (7.16)$$

If the noise functions $n(x)$ are assumed uncorrelated then the infinite summation of equation (7.16) should contain as many positive as negative contributions over all x , reducing this spectral term to zero in equation (7.15), hence

$$|M(k_x)|^2 = \sum_{j=-\infty}^{+\infty} |N_j(k_x)|^2 \quad (7.17)$$

Individual $n_j(x)$ can be calculated from the magnetisation profiles $P_j(x)$ by subtracting the basis

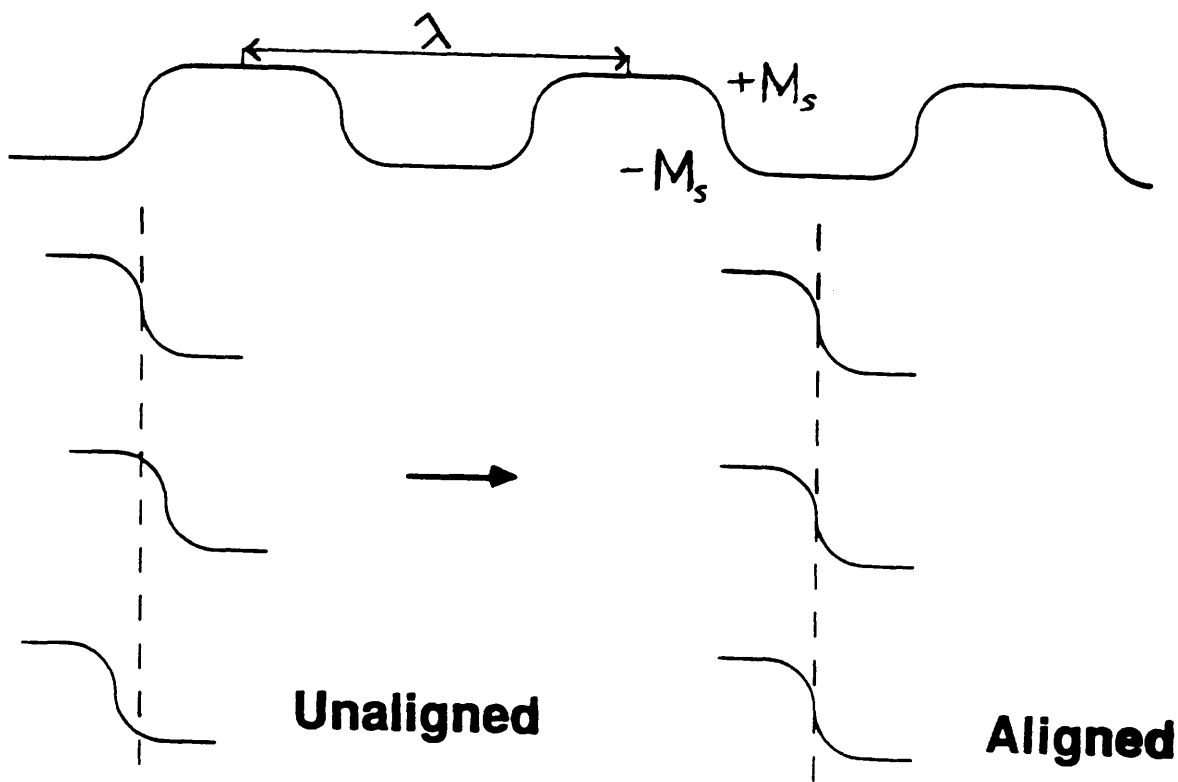
function $f_B(x)$ (equation (7.12)). An estimate of $f_B(x)$ was obtained from periodograms by averaging over the magnetisation transitions $P_j(x)$ in the following way. A set of profiles $\{P_j(x)\}$ was produced by sectioning the track magnetisation $m(x)$ into samples one half wavelength long, see figure 7.16. The mean over the set $\{P_j(x)\}$ then yields an approximation for $f_B(x)$. This process, however, assumes each transition is correctly placed periodically along the track waveform and this need not necessarily be the case. Profile alignment has therefore to be ensured by shifting the transition profile sections laterally by amounts calculated from a recursive, weighted minimisation of profile differences, producing the aligned set $\{P_j^\wedge(x)\}$. Alignment of the profiles in this way was based upon minimising the profile difference parameter Δ :

$$\Delta = P_k(x) - \frac{\left(\sum_{j=0}^{N-1} P_j^\wedge(x) \right) + P_k(x)}{N}$$

$$= \frac{(N-1)}{N} \cdot \left[P_k(x) - \frac{1}{(N-1)} \cdot \left(\sum_{j=0}^{N-1} P_j^\wedge(x) \right) \right]$$

$$\propto^{a1} \left(P_k(x) - P_j^\wedge(x) \right) \quad (7.18)$$

where $P_k(x)$ is a profile that is being aligned with the set of $N-1$ aligned profiles $\{P_j^\wedge(x)\}$. Minimising Δ by shifting $P_k(x)$ laterally allows any number of profiles to be aligned relative to each other by this method. Experimentally it was found that over, say, twelve transition profiles a second iteration of the minimisation was unnecessary and that the final aligned set of transitions was independent of the order in which the profiles were aligned. The final expression



$$f_B(x) = (1/N) \cdot \sum P_j^A(x)$$

Figure 7.16 - The magnetisation waveform (top) was sectioned into half wavelength sections ($\lambda/2$) to produce the set of profiles shown on the left hand side. Alignment of these profiles using equation (7.18) yields an aligned set from which the basis function $f_B(x)$ can be estimated.

for the basis function is then

$$f_B(x) = \frac{\sum_{j=0}^N P_j^\wedge(x)}{N} \quad (7.19)$$

for N magnetisation profiles, allowing the individual local transition noise functions to be estimated by

$$n_j(x) = P_j^\wedge(x) - f_B(x) \quad (7.20)$$

7.5.2 FFT EFFECTS WITH ISOLATED TRANSITION NOISE FUNCTIONS

The effects of transforming $n_j(x)$ by FFT to evaluate the noise power spectrum $b.S(k_x)$ (equation (6.18)) are considered here by studying the form of equation (7.20). Both $P_j^\wedge(x)$ and $f_B(x)$ extend from negative (positive) saturation magnetisation through a transition to positive (negative) saturation for a step up (down) magnetisation reversal. Any difference between them, $n_j(x)$, is seen to be non-zero over an extent smaller than the half wavelength dimension of $P_j(x)$ and $f_B(x)$. Hence, for these data, real space truncation of $n_j(x)$ by multiplication with a window function $w(x)$ will have no effect on the FFT calculated spectrum provided that $w(x)$ equals unity over a length greater than the non-zero extent of $n_j(x)$, that is

$$w(x).n_j(x) = n_j(x)$$

$$\text{if } w(x) = 1 \quad \text{for } -T_0/2 \leq x \leq T_0/2$$

$$= 0 \quad \text{elsewhere}$$

and $n_j(x)$ does not fall off to zero for $-T/2 \leq x \leq T/2$ where $T_0 \geq T$.

In this way the limitations of the periodogram approach related to the truncation window $w(x)$ are overcome. Fast Fourier transforming $n_j(x)$ produces spectra $N_j(k_x)$ that can be substituted directly into equations (7.17) and (6.18) to estimate the transition noise power per unit area of track $b.S(k_x)$.

7.5.3 THE FORM OF THE TRACK MAGNETISATION AND THE ASSUMPTIONS OF THE READ MODEL

The Fresnel images and associated two-dimensional binary representations of sections of 3MHz track are given in figure 7.2. If these binary images are examined closely it is seen that the zig-zag transitions change character near the edges of the track and shift relative to the central track region. This was attributed to head edge writing effects (chapter three) and it can be assumed that in this region the head response function will be different from that over the central part of the track, but by some unknown factor. Since in the noise analysis it is assumed that the head sensitivity function is constant we must take this into account. The starting point for the data processing was to evaluate the magnetisation distribution averaged across the track and this was now done in two ways. For the first computation only the central 10 μm section of the track was used to compute the average magnetisation and the noise and then scaled to the full track width. In the second approach the

magnetisation 'wings' were incorporated before proceeding as before; this is equivalent to ignoring any change in the head sensitivity function. Figure 7.17 contains graphs of individual step-up and step-down magnetisation transitions with and without the wing structure.

7.5.4 RESULTS OF THE SINGLE TRANSITION ANALYSIS

The two independent periodograms depicting the 3MHz track that were used in the periodogram technique were also used to analyse transition noise by studying the the individual magnetisation reversals that make up these periodograms. The examination of the data with and without wings was carried out separately in each case, but in both cases the step-up and step-down transitions were isolated from the periodogram profile by dividing the track into half-wavelength sections, each beginning and ending in the magnetically saturated regions of written bits. From the two 3MHz periodograms, each six periods long, twelve step-up and twelve step-down magnetisation transitions were isolated.

As was described in the preceding sections, the basis function $f_g(x)$ from the model proposed for the track magnetisation $m(x)$ in equation (7.13) was obtained by averaging over the aligned profiles taken from the periodograms. With these functions, the local transition noise $n_{,\pm}(x)$, can be estimated from the

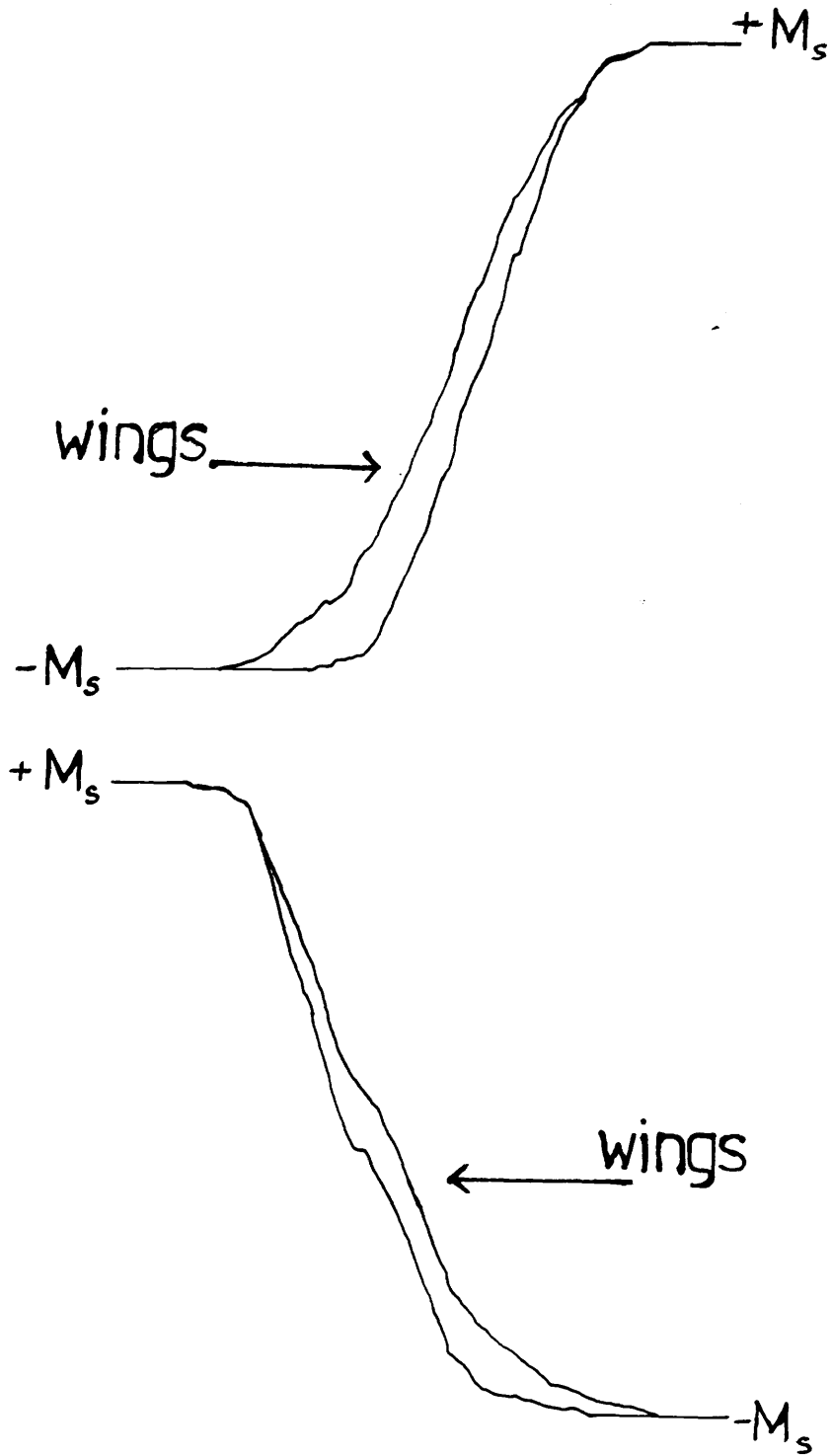


Figure 7.17 - (a) A step-up magnetisation profile measured with and without the wing structure; (b) a step-down magnetisation profile measured with and without the wing structure.

individual aligned transition profiles $P_j^{\wedge}(x)$:

$$n_j(x) = P_j^{\wedge}(x) - f_B(x) \quad (7.21)$$

Figure 7.18 depicts a typical noise function, with and without wings, for the 3MHz track. The figure illustrates the greater non-zero extent of the 'winged' data.

Equations (6.18) and (7.17) can be combined to describe the relationship between the set of transition noise profiles $\{n_j(x)\}$ and the transition noise power density $b.S(k_x)$,

$$b.S(k_x) = \frac{W \cdot b^2 \cdot \sum_j |N_j(k_x)|^2}{X} \quad (7.22)$$

where $N_j(k)$ represents the Fourier transform of the noise $n_j(x)$, b is the magnetic layer thickness, W is the track width, and X is the length of track studied ($\lambda/2$). This equation can be used to calculate the noise power spectra from the sets of twelve magnetisation reversal profiles obtained from sectioning the periodograms, analysing them with and without wings.

Figure 7.19 illustrates some typical noise spectra obtained from individual step-up transitions. They vary quite significantly in magnitude (a factor in range of ≈ 8) but all exhibit the same characteristic 'peaked' shape at $\approx 3.5 \mu\text{m}^{-1}$. The noise spectra $b.S(k)$ calculated from the set of transition noise bursts $\{n_j(x)\}$ obtained from the 3MHz data are depicted in figure 7.20. Here the step up and down transitions have been graphed separately for both winged and non-winged data. An examination of the individual

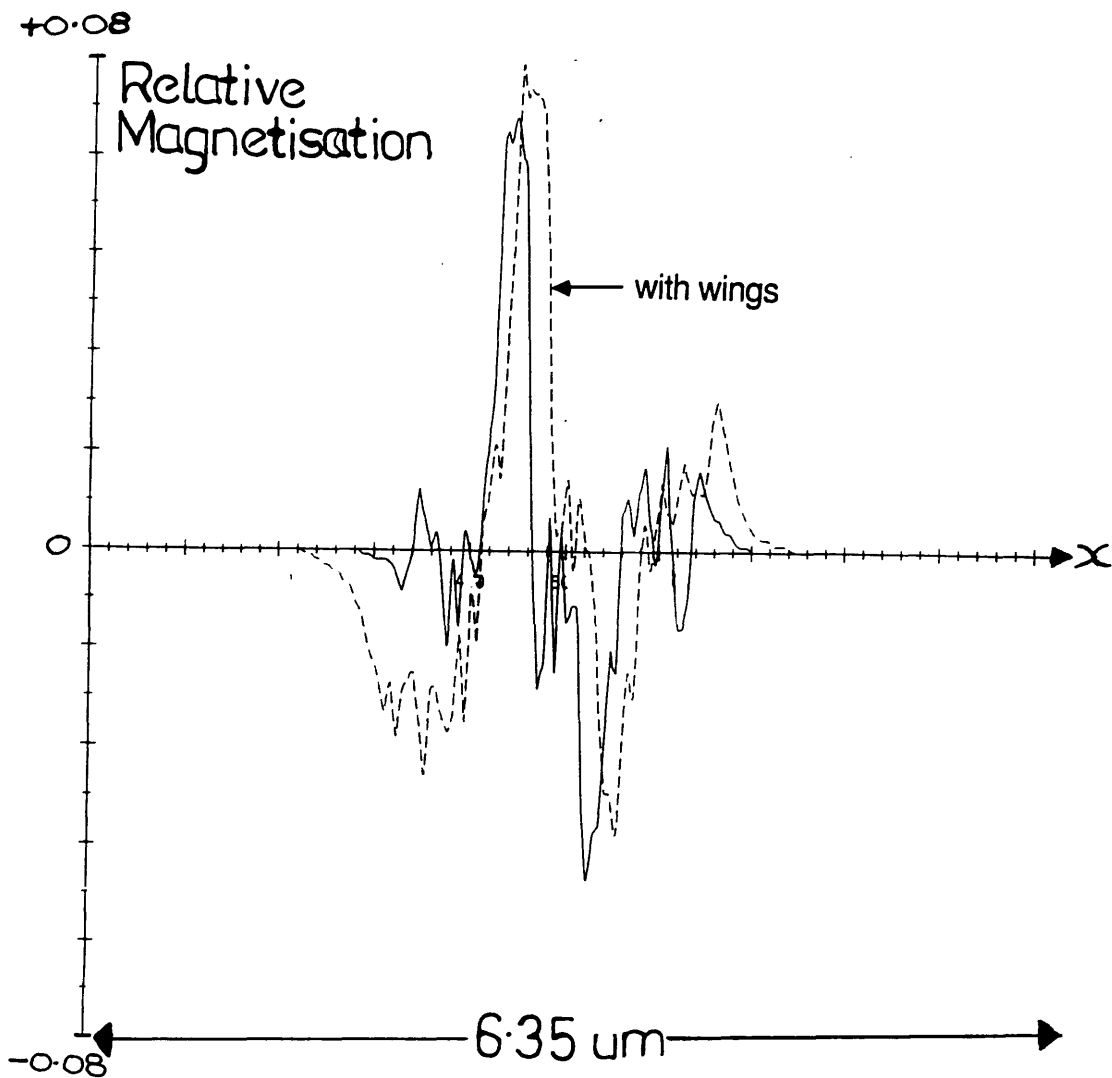


Figure 7.18 - A typical magnetisation transition noise function $n_j(x)$ from 3MHz track.

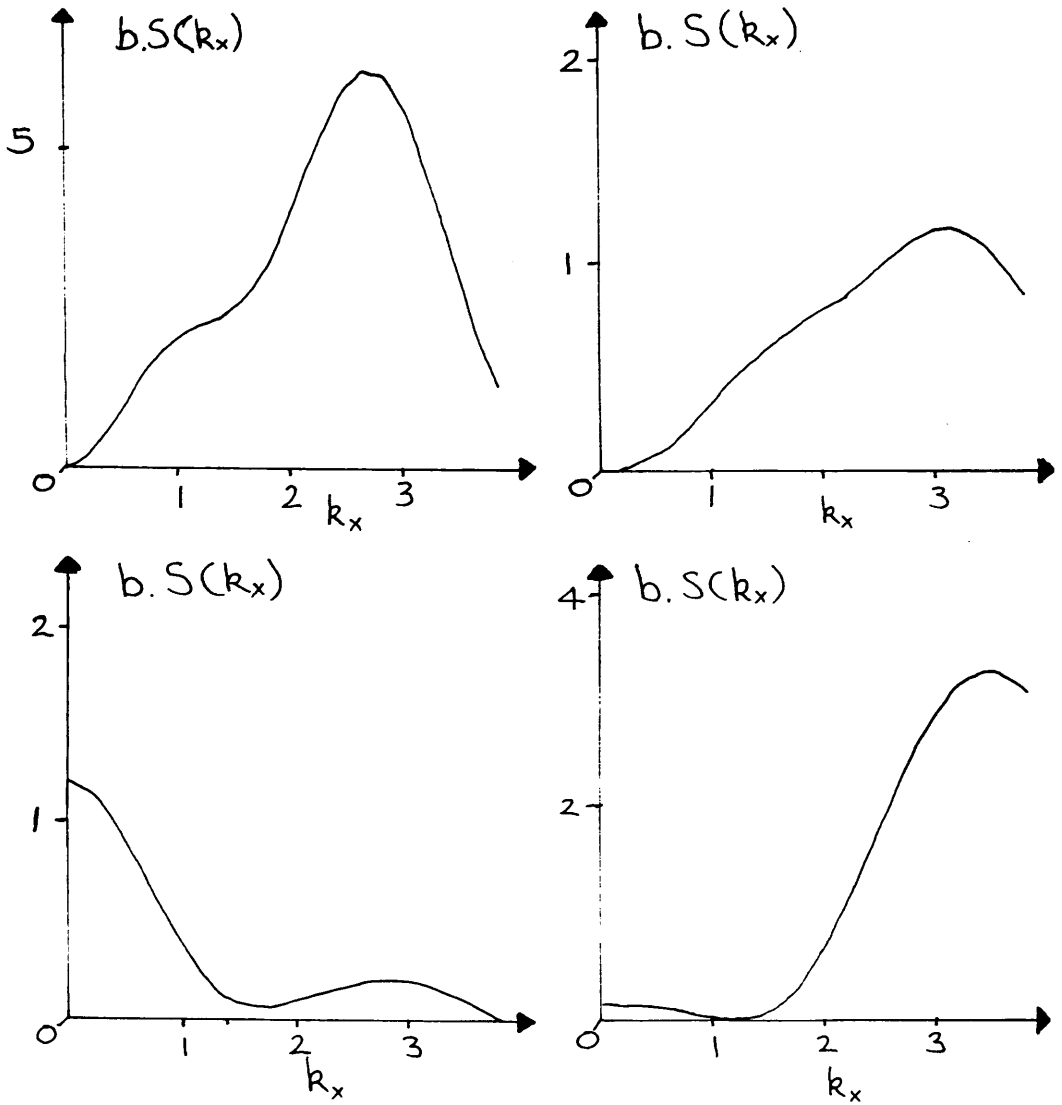


Figure 7.19 - Four noise power spectra obtained from different noise functions $n_j(x)$ help illustrate the variation in the noise calculated from different transitions.

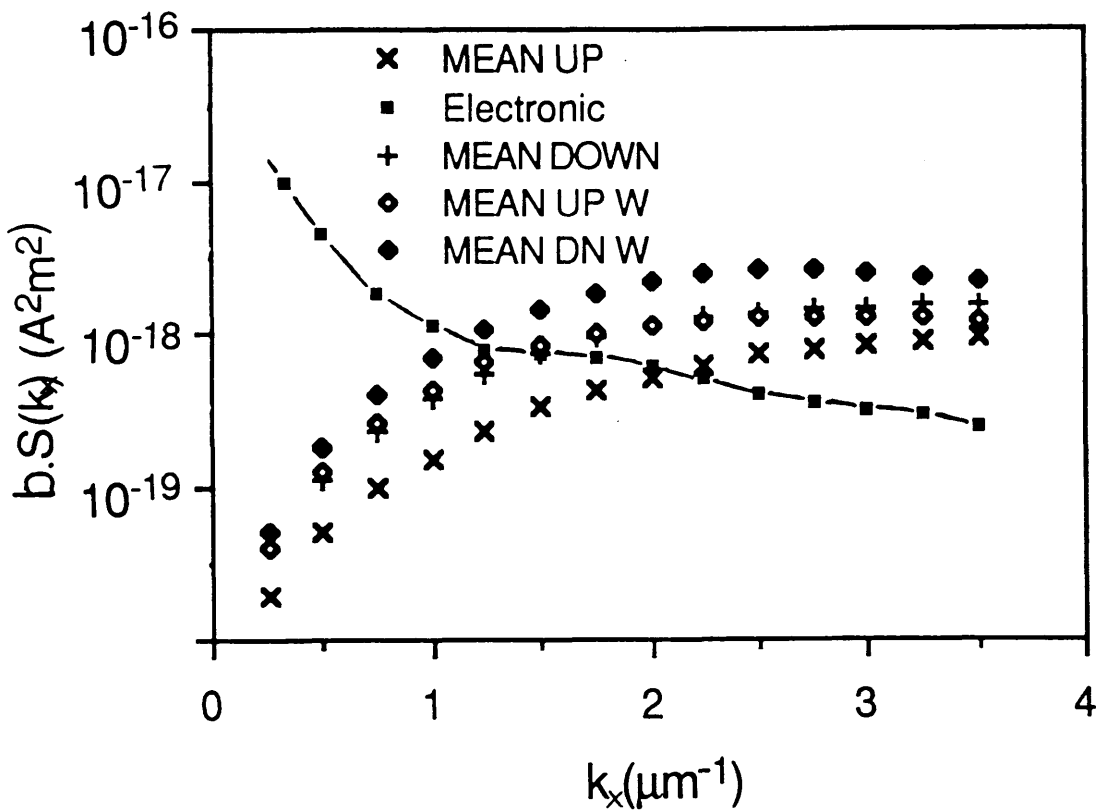


Figure 7.20 - Average noise spectra for the step up and down transitions with wings (mean upw and mean dnw) and without wings (mean up mean down) graphed on a log10-linear scale for comparison with the electronic spectrum.

noise spectra peak values at $\approx 3.5\mu\text{m}^{-1}$ showed that for the step up transitions two profiles produced values greater than 3 standard deviations larger than the mean. In computing the average noise profiles of figure 7.20 we ignored these since, with the small number of profiles used, their inclusion would give them undue weight.

On the assumption that the individual noise functions $n_j(x)$ are uncorrelated (equation (7.17)) the average noise curves represent the collective noise spectrum from the two track sections. The general spectral shape is quite different from that measured electronically, although they are of the correct order of magnitude. The spectra calculated from the data containing the wings were seen to produce slightly higher peak noise values than their counterparts computed from the central track data, and that for both data sets, with and without wings, it was observed that the step-up ($-M_s/+M_s$) noise function was smaller in peak noise magnitude. The differences seen for noise with and without wings are understandable from the micromagnetic structure and its influence on the transition profiles. The difference between step up and step down was very interesting and may be due to the fact that the track analysed was d.c. erased prior to recording, possibly inducing subtle changes in the form of the flux reversal regions depending on the sense of magnetisation change. There is some evidence for this from previous work [5], and analysis of tracks written on an a.c. erased medium would provide an

interesting comparison. This is proposed as part of future noise models.

In so far as the analysis up to this point has measured the noise produced from profiles $P_j^{\wedge}(x)$ derived from an aligned basis function, it has taken no account of how variations in the location of magnetisation reversals about a perfectly periodic placement can influence spectral noise. The contribution from this effect can be investigated by shifting a profile from its position of periodic alignment by some small value ξ , and this section discusses the results of such an analysis.

A shift of a magnetisation reversal from its position of perfect periodicity along the signal waveform can be considered as introducing a second local noise function at the site of the transition

$$n_{\xi}(x) = f_b(x \pm \xi) - f_b(x) \quad (7.23)$$

where $f_b(x)$ and $f_b(x \pm \xi)$ represent the aligned basis function and the basis function shifted laterally by $\pm \xi$ respectively. The basis functions calculated were used to estimate the size of this 'shift' noise in real space; these can then be fast Fourier transformed and substituted into equation (7.17) to estimate the corresponding reciprocal space noise spectrum. A comparison of $n_{\xi}(x)$ calculated with and without the wing magnetisation is given in figure 7.21 for a 3MHz step-down transition. The wings broaden the noise, as was seen with the transition measurements, but the overall maximum peak height is reduced. The noise power spectra for the up and down transitions were observed to be essentially similar, hence in figure

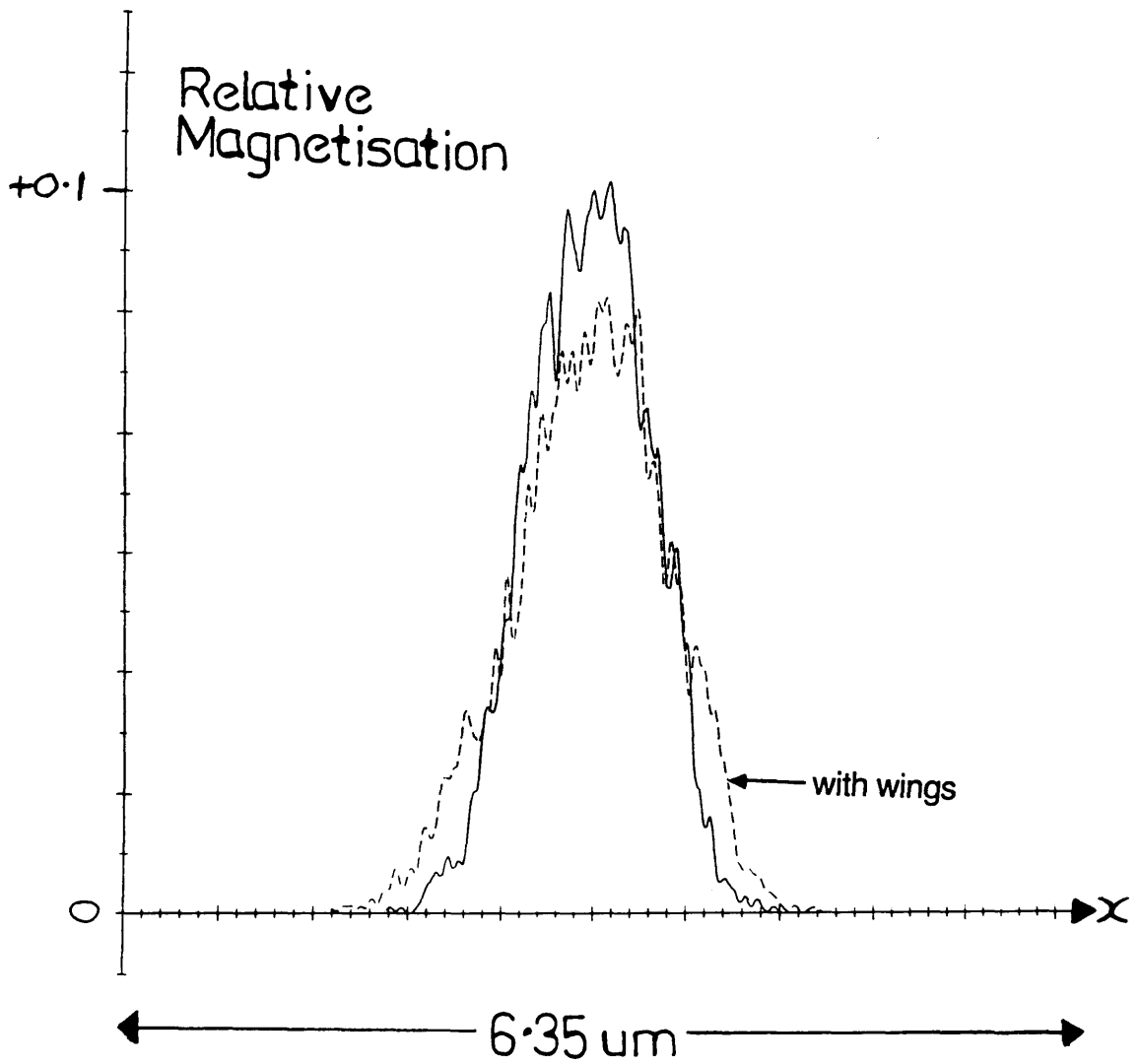


Figure 7.21 - The shift noise function $n_{\xi}(x)$ measured with and without wing structure. $\xi=50\text{nm}$.

7.22 we show for the wing data three spectra for different values of shift: 12.5nm, 25nm and 50nm. For comparison the spectrum for a 50nm shift calculated without the wing magnetisation is also shown. This figure illustrates that the wing data sharpens the noise spectrum relative to that calculated without any wing structure, maintaining the low frequency noise while attenuating that at high frequencies; this is consistent with the real space data. Compared to the transition noise the 'shift' spectra are much closer in shape to the electronically derived spectrum. This suggests the noise associated with departures from the perfect periodic placement of magnetisation transitions may contribute significantly to the overall noise performance measured from the track. The composite medium transition noise would then be a combination of both 'transition only' and 'shift' noise: the variation of the transition profiles from an aligned basis function influencing the high frequency noise, the shift of the transitions from positions of perfect periodicity dominating the noise characteristic at low frequencies.

If it is assumed that each transition has a total real space noise composed of both transition and shift components then the 'transition-shift' noise for profile j shifted ξ from alignment can be written as

$$n_{j\xi}(x) = n_j(x) + n_\xi(x) \quad (7.24)$$

For individual transitions specific amounts of shift noise $n_\xi(x)$ were combined with the transition noise $n_j(x)$ and figure 7.23 illustrates the typical best fits

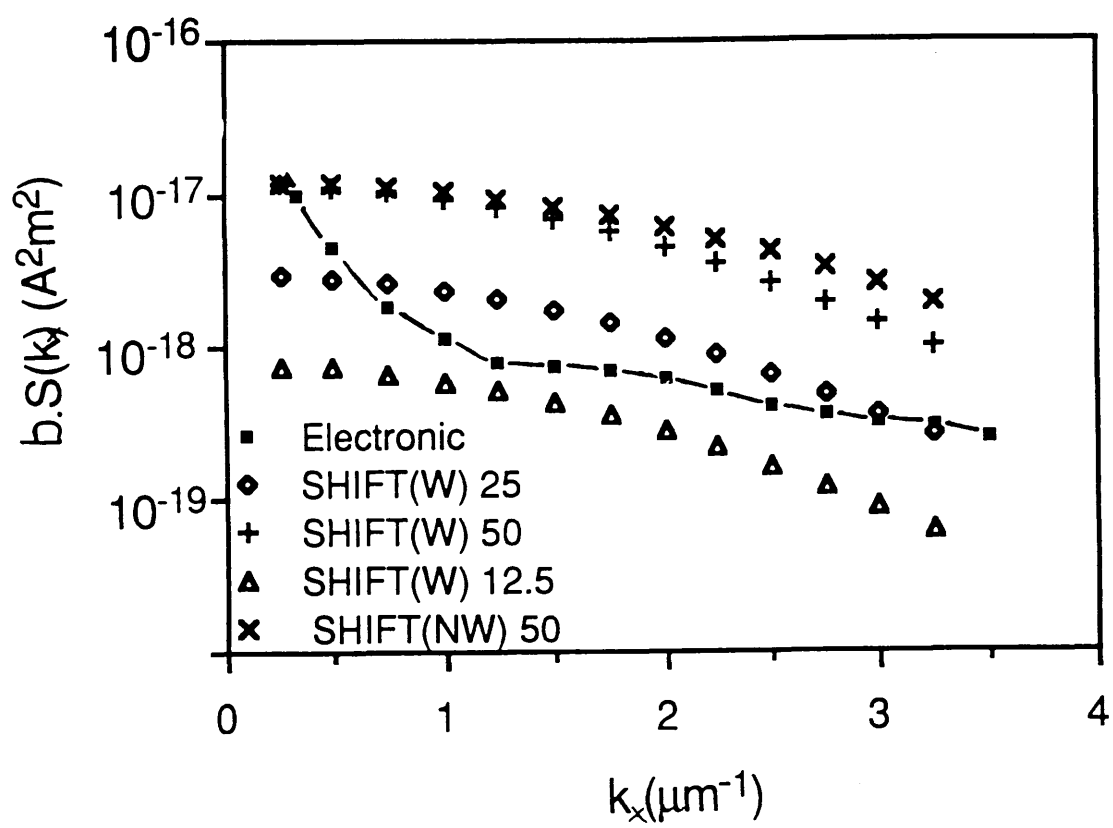


Figure 7.22 - Log10-linear graphical comparison of the shift noise spectra with and without the wing structure. The electronically measured noise spectrum is also graphed for comparison.

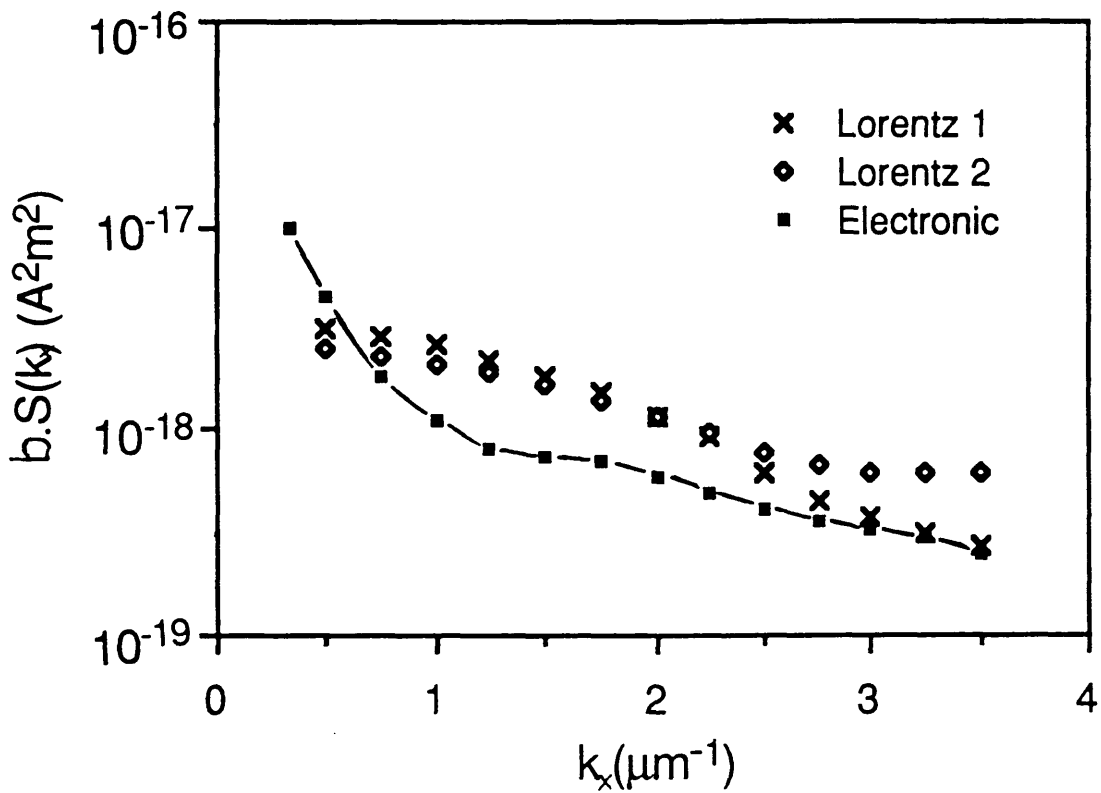


Figure 7.23 - Log10-linear graphical comparison of two 'transition-shift' noise spectra with the electronically measured data.

that can be achieved between the Lorentz and electronically measured data. For reciprocal frequencies $k > 0.75 \mu\text{m}^{-1}$ the agreement between data sets is excellent, both qualitatively in shape and quantitatively in magnitude, the Lorentz data being some factor < 2 greater than the electronic data. Below $\sim 0.75 \mu\text{m}^{-1}$ the electronic curve rises rapidly compared with the Lorentz data; currently no explanation for this behaviour can be given.

7.5.5 SUMMARY

The analysis of the Lorentz derived images of square wave written track magnetisation by both 'periodogram' and 'individual transition' techniques in order to estimate the iron cobalt chromium transition noise has been described in this chapter. Transition noise measurement by the periodogram approach was observed to be severely limited in its ability to access the noise power spectra generated by fast Fourier transforming the periodograms. Spectral effects associated with the window function that defines the periodogram hinder the estimation of the noise power by this technique.

As a direct consequence of the results obtained from and the limitations discovered about the periodogram approach, the technique of studying individual magnetisation reversals was developed as a means of trying to overcome these problems. By computing the noise power spectra from finite non-zero length noise

functions local to the magnetisation reversals excellent spectral agreement was achieved between the Lorentz and electronic power functions, revealing details of the relationship between the medium micromagnetics and noise performance. It was observed that the distribution and shape of the zig-zag domain walls that make up the written magnetisation transition within the iron cobalt chromium medium produce two contributions to the noise power spectrum. The first appeared to be the deviation of the transition from an ideal basis transition written to the track. A second arises from the magnetisation reversal appearing to be sited off its respective position of perfect periodicity along the track waveform. It is suggested that some complex combination of these two spectral contributions may be ultimately responsible for the spectral noise performance measured electronically from the medium.

CHAPTER EIGHT

CONCLUSIONS AND FUTURE WORK

The bias in this concluding chapter lends itself to the discussion of the possible avenues down which future investigations could be pursued. However, the results presented do allow several important conclusions to be drawn with regard to the preparation and characterisation of the thin film recording medium.

Preparation of both the iron cobalt chromium and the cobalt nickel chromium media was seen to be successful and efficient. The techniques employed were seen not to impeach the integrities of either of the media whilst producing thin film specimens of thicknesses useful for electron microscope observation ($\leq 100\text{nm}$). Improvements could be made however to both methods. For the iron cobalt chromium a more sophisticated way of removing the nickel phosphate layer may reduce the amount of stress the specimen are subjected to; this may then reduce the physical degradation of the specimen and allow the rhodium overcoat thickness to be reduced below 20nm without encountering the observed de-magnetising effects. Specimen debris observed in the images of the cobalt nickel chromium thin film were identified as unreacted silicon substrate. A more clinically developed etching of this substrate material could eradicate this debris. A further improvement to the preparation of these specimen could be achieved by the reduction or removal of the carbon layer by some form of organic incineration (for example, carbon

ashing) or the use of a thinner silicon nitride layer in the disk construction. One final comment regarding the successful preparation of this isotropic medium from the silicon based hard disks is that it now paves the way for the characterisation of other thin film recording media by electron microscopy.

From the prepared specimens of the iron cobalt chromium alloy the medium was seen to be body centre cubic crystalline structure with a lattice parameter of $\approx 2.56\text{\AA}$. As discussed, this estimate of the lattice parameter involved a 5% correction because of a slight difference in the calibrated camera length and the actual value applicable to the recording medium due to thin film specimen deformation. A more rigorous execution of this experiment would provide confirmation of the lattice parameter estimate given above. Images of the medium grain structure showed micro-cracks running parallel to the easy axis in contours produced by the texturing of the nickel phosphate substrate. These were proposed as an explanation of the observed increase in the ratio between the easy and hard axes coercivities when texturing is applied. A more extensive study may better characterise these observations and substantiate this claim.

A presentation of the various domain structures of tracks written along the easy axis of the iron cobalt chromium medium was given in chapter four. This illustrated the wide variation in track structures that can be written to the medium:

(i) as the write frequency was increased the written

bits were seen to change from a whole domain into a collection of lozenge-shaped domains; this effect reduced the clarity with which the individual written transitions could be observed;

(ii) as the write current was reduced from a saturation value the integrity of the written track domain structure was degraded;

(iii) a distinct change between the two frequencies used in the over-write experiments was observed by Lorentz microscopy.

On all of these images the domain wall transition was seen to be zig-zag with the teeth pointing along the easy axis and the domains themselves contained no magnetic ripple. This was also seen to be the case when the tracks were written at some angle ψ ($0^\circ \leq \psi \leq 90^\circ$) to the easy axis, indicating that the medium magnetisation consistently lies along the easy axis irrespective of the write angle ψ . Fresnel images of tracks written off the easy axis indicated a re-distribution of the zig-zag around written bits as ψ increased from 0° to 90° . The zig-zag structure was seen to gradually re-locate itself from lying perpendicular to the write direction ($\psi=0^\circ$) to lying parallel to the write direction ($\psi=90^\circ$). A variation such as this implied an associated variation in free magnetic poles and therefore stray field around the written bit. Small angle diffraction supplemented these images by identifying changes in the induction in the locality of the medium which allowed a qualitative model of the behaviour of the induction to be proposed.

This model was confirmed by a differential phase contrast analysis which showed that the component of stray field perpendicular to the easy axis increased as the write angle ψ increased from zero to some maximum value at an intermediate value of ψ before decreasing to zero for $\psi=90^\circ$. A precise determination of write angle at which the maximum value of this component of perpendicular stray field is created could be made using differential phase contrast microscopy and/or small angle diffraction. Possibly some mathematical model of the dynamics of the stray field rotation could supplement such an experiment.

Chapter five was introduced as containing the first electron microscope images of the isotropic cobalt nickel chromium medium prepared from hard disk. Analysis of the physical microstructure should now be undertaken in a form similar to that presented for the iron cobalt chromium medium, that is: higher magnification images of the grain structure to investigate further the regularity of the grain structure and orientation; a determination of the crystal structure of the medium and corresponding lattice parameters. In terms of the micromagnetic characterisation of this medium the most prominent initial investigations should include:

- (i) a more intensive study of the micromagnetic domain and magnetisation transition structure by Lorentz electron microscopy;
- (ii) the development of a computational technique which utilises the observed magnetic ripple to synthesize

images that describe a 'first estimate' of the medium magnetisation map;

(iii) a study of the nature of the perpendicular component of magnetisation observed by small angle diffraction;

(iv) an examination of the potential for the study of head structure using this isotropic medium.

The first quantitative estimates of medium flux noise power from Lorentz images of a.c. erased medium were presented in chapter six. Good agreement was obtained between the Lorentz derived spectrum and that measured electronically from a spectral analysis of the readback signal from the hard disk. This agreement was seen to be improved when the data was analysed in sections of similar dimensions to the readback strips associated with the head width since any sensitivity in the noise spectra to localised real space characteristics in the magnetisation image was reduced through averaging. This observation implied that further improvement could be attained by analysing more of the same sized sections of medium or, in fact, longer sections.

An identical noise analysis was applied in the examination of Lorentz images of square wave written track to estimate the transition noise power spectra from track magnetisation. The analysis showed that the finite length of the real space image of the track magnetisation inhibited the measurement of the noise spectra: (i) the noise can only be estimated free from signal contributions at a limited number of frequencies defined by the number of periods described by the

periodogram of the track; (ii) because absolute accuracy cannot be obtained in defining periodograms of the track magnetisation, precise sampling in frequency space of the noise power cannot be made at the set of frequencies at which the signal contribution is zero; (iii) end-point values of the track magnetisation periodograms effect directly the values of the noise estimates.

The combination of these constraints detracted from the overall effectiveness of this technique. To overcome these difficulties the track periodograms were instead analysed in terms of the local noise associated with individual transitions.

By calculating the noise attributable to each transition an estimate of the transition noise power spectrum was made. The results appeared to indicate that the distribution of the transition zig-zag wall across the track width manifests itself spectrally in two ways. The deviation of a transition from an idealistic basis transition written at every magnetisation reversal dominated the high frequency region ($\geq 1.75\mu\text{m}^{-1}$) of the noise spectrum; the displacement of the transition from its position of perfect periodicity along the track was seen to most strongly influence the low frequency region of the spectrum. The analysis of the transition noise presented here shall be superseded in the future by the implementation of a computer algorithm that will produce estimates of both the 'transition' and 'shift' noise contributions at each magnetisation reversal.

T.C. Arnoldussen of the General Product Division of IBM developed the core of this new analysis.

Indications from the transition only noise measurements presented in the second half of chapter seven suggested that there may be subtle differences in the form of the magnetisation transitions written with or against an originally d.c. erased medium. A similar analysis of tracks written on a.c. erased medium would substantiate this possibility.

The global summary conclusion from the work of this Ph.D. study appears to be that Lorentz electron microscopy is an enormously powerful tool for both the physical and micromagnetic characterisation of thin film magnetic recording media, and that there does appear to be a quantitative method through which the relationship between micromagnetic features and the recording performance of a medium can be better understood.

REFERENCES

CHAPTER ONE

- 1 P.Weiss, J.Phys., 6, 661 (1907).
- 2 W.Heisenberg, Z.Physik, 49, 619 (1928).
- 3 F.Bloch, Z.Physik, 74, 295 (1931).
- 4 L.Nèel, Compt. Rend., 421, 533 (1955).
- 5 L.L.Nunnelley, D.E.Heim, and T.C.Arnoldussen, IBM Technical Report TR02.1343 (1986).
- 6 P.Lorrain and D.Corson, 'Electromagnetic Fields and Waves', Freeman.
- 7 C.D.Mee and E.D.Daniel, 'Magnetic Recording Volume I: Technology', McGraw Hill.
- 8 R.White, 'Introduction to Magnetic Recording', IEEE Press.
- 9 F.Jorgensen, 'The Complete Handbook of Magnetic Recording', Tab Books Inc..
- 10 C.Kittel, 'Introduction to Solid State Physics', Wiley.

CHAPTER TWO

- 1 G.Thomas and M.Goringe, 'Transmission Electron Microscopy of Materials', Wiley.
- 2 J.N.Chapman, J.Phys D: Appl. Phys., 17,623 (1984).
- 3 J.P.Jakobovics, Electron Microscopy in Materials Science, Vol.4 ed U.Valdre and E.Ruedl (Brussels: Commision of the European Communities), 1303 (1975).
- 4 R.P.Ferrier, Advances in Optical and Electron Microscopy, 155 (1965).
- 5 Y.Aharonov and D.Bohm, Phys. Rev, 115, 485 (1959).

- 6 N.H.Dekkers and H. de Lang, *Optik*, **41**, 452 (1974).
- 7 J.N.Chapman, P.E.Batson et al, *Ultramicrosc.*, **3**, 203 (1978).
- 8 E.M.Waddell and J.N.Chapman, *Optik*, **54**, 83 (1979).
- 9 G.R.Morrison and J.N.Chapman, *Optik*, **64**, 1 (1983).
- 10 E.M.Waddell, Ph.D Thesis, University of Glasgow (1978).
- 11 G.R.Morrison, Ph.D Thesis, University of Glasgow (1981).
- 12 I.R.McFadyen, Ph.D Thesis, University of Glasgow (1986).

CHAPTER THREE

- 1 E.M.Rossi, G.McDonough et al, *J. Appl. Phys.*, **55**(6), 2254 (1984).
- 2 T.C.Arnoldussen, E.M.Rossi et al, *IEEE Trans. Magn.*, Vol. **MAG-20**, No.5, 821 (1984).
- 3 R.P.Ferrier, F.J.Martin et al, *IEEE Trans. Magn.*, Vol.24, No.6, 2709 (1988).
- 4 T.Chen and T.Yamashita, unknown at present.

CHAPTER FOUR

- 1 P.S.Alexopolous and R.H.Geiss, *IEEE Trans. Magn.*, **MAG-22**, 566 (1986).
- 2 T.C.Arnoldussen, E.M.Rossi et al, *IEEE Trans. Magn.*, Vol. **MAG-20**, No.5, 821 (1984).
- 3 E.M.Rossi, G.McDonough et al, *J. Appl. Phys.*, **55**(6), 2254 (1984).
- 4 H.C.Tong, R.P.Ferrier et al, *IEEE Trans. Magn.*, **MAG-20**, 1831 (1984).

5 T.C.Arnoldussen and H.C.Tong, IEEE Trans. Magn., MAG-22, 889 (1986).

6 L.L.Nunnelley et al, IEEE Trans. Magn., MAG-23, 1767, (1987).

CHAPTER FIVE

1 T.Chen and T.Yamashita, unknown at present.

2 T.C.Arnoldussen, L.L.Nunnelley et al, Proceedings of the MMM conference, San Diego (1990). To be published in the Journal of Applied Physics.

CHAPTER SIX

1 L.L.Nunnelley, D.E.Heim, and T.C.Arnoldussen, IBM Technical Report TR02.1343 (1986).

2 R.P.Ferrier, F.J.Martin et al, IEEE Trans. Magn., Vol.24, No.6 (1988).

3 E.O.Brigham, 'The FFT and Its Applications', Prentice Hall.

4 R.Bracewell, 'The Fourier Transform and Its Applications', McGraw Hill.

5 L.Cordell and V.J.S.Grauch, Geophysics, Vol.47, No.2 (February 1982), p.237-243.

6 J.W.Cooley and J.W.Tukey, Math. Comp., 19, 297-301 (1965).

7 W.T.Cochran and J.W.Cooley, et al, Electroacoustics, AU-15(2), 45-55 (1967).

8 R.C.Young, Report No. THEMIS-UM-69-6, Contract No. ONR-N00014-68-A-0146-6.

9 L.L.Nunnelley et al, IEEE Trans. Magn., MAG-23, 1767, (1987).

CHAPTER SEVEN

- 1 R.P.Ferrier and F.J.Martin et al, IEEE Trans. Magn., MAG-25, 3387 (1989).
- 2 R.P.Ferrier and F.J.Martin et al, IEEE Trans. Magn., MAG-26, 1536-1538 (1990).
- 3 E.O.Brigham, 'The FFT and Its Applications', Prentice Hall.
- 4 F.J.Harris, Proc. IEEE, 66, 51 (1978).
- 5 H.C.Tong et al, IEEE Trans. Magn., MAG-20, 1831 (1984).
- 6 P.D.Welch, IEEE Trans. on Audio and Electroacoustics, Vol. AU-15, No.2, 1967.
- 7 Technical Note, Journal of Computational Physics, 61, 186-193 (1985).
- 8 N.C.Geckinli and D.Yavuz, IEEE Trans. on Acoustics, Speech, and Signal Processing, Vol. ASSP-26, No.6, 1978.
- 9 A.H.Nuttall, IEEE Trans. on Acoustics, Speech and Signal Processing, Vol. ASSP-29, No.1, 1981.